Optimization of Direct-Contact-Spray-Coolers

By

Mohamed S. El-Morsi

A dissertation submitted in partial fulfillment of the requirements for the degree of

DOCTOR OF PHILOSOPHY
(Mechanical Engineering)

at the

UNIVERSITY OF WISCONSIN-MADISON
2002

Dedication

To
my parents and my beloved ones
for their patience and support

Acknowledgements

Several people have made significant contributions to this work. The Professors in the Solar Energy Laboratory have always provided technical and scholastic inputs. I have greatly profited from advice, generously bestowed through interactions and discussions with my advisors, Professors S. Klein, and Professor D. Reindl. They always provided candid and critical comments that assisted me in assembling this work in a presentable way. Their patience and continuous encouragement helped me get along the way. My cordial thanks are due to Professor Farrell and Professor Shedd. Discussions with both of them helped a lot to figure out some of the difficult points in spray imaging. Professor Farrell made available to me the high speed flash. Professor Shedd generously made available to me his lab facilities (CCD cam, triggering box, computer, and laser). Without using their lab facilities, I couldn't have gotten the images necessary to complete the experimental part of my thesis.

I also want to express my appreciation to my Egyptian colleagues who contributed with either inspirational or actual work with this research effort. Special thanks are due to Dr. El-Sayed Mogahed and Dr. Ahmad Essmat for their support. I am much indebted to Sherif Abdullah and Essam El-Hanouny for their help and support. Credit is also due to my former and current Solar Lab fellows. Some of the many students whom I wish to thank: Amr Abdou, Helge Klocko, Janeen Ault, Lars Vicum, Mark Richler, and Rob Brawn. I am also indebted to Dave Bradley, for his participation in the review of my prelim exam .

I would particularly wish to thank the members of the ME Machine-Shop for their help. Special thanks are due to Rick Proctor, Richard Williams and John Robinson. Without their help a lot of effort would have been expended in building the experimental test rig. Their comments, ideas and questions greatly enhanced or improved building the test rig.

Last but not least, I would like to acknowledge the financial support offered by the Egyptian Government, Missions Department, and the University of Wisconsin-Madison.

Table of Contents

List of Figures

List of Tables

Chapter 1 Introduction

Air conditioning is the simultaneous control of humidity, temperature, cleanliness, and distribution of air within enclosed spaces. The classic definition for air conditioning by Carrier [1] is:

> *"Air conditioning is the control of the humidity of air by either increasing or decreasing its moisture content. Added to the control of humidity are the control of temperature by either heating or cooling the air, the purification of the air by washing or filtering the air, and the control of air motion and ventilation."*

Modern air conditioning started in the early 1900s and was mainly initiated by the textile industry needs to control the humidity levels in the work environment [2]. Textile fibers, like paper, must retain a minimum amount of moisture to prevent its physical/structural damage. Therefore, humidity control was a necessary to achieve a good final product and easy operation with the minimum breakage and static electricity. Air conditioning, initially, depended on the use of air-washers, in which large quantity of water is sprayed into direct-contact with an air stream using nozzles to form a fine mist. These air-washers were able to produce the required amount of humidity with a nominal amount of cooling. Unsatisfied by their performance, Willis H. Carrier improved air washer performance by using counter flow systems and modifying the mist eliminators. In 1902 when Carrier designed his first

dehumidifier for a printing plant using cooling coils, he observed that as dehumidification was taking place. Carrier noted that the process air apparently came in contact with water on the cooling coil surface,

> *"in other words we had the apparent paradox of reducing the moisture in air by bringing it into contact with moisture. Of course the explanation was simple. The temperature of water [inside the coil] was below the dew point or condensation temperature of the entering air. Why should we not, then, spray the cold water into the air stream, thus increasing the surface contact and reducing the resistance to air flow."* [2]

Carrier concluded that air-washers could be used to simultaneously cool and dehumidify a moist air stream. By 1909, use of air-washers expanded well beyond the textile industry to the tobacco industry, paper industry, steel industry and others [1]. The use of air-washers systems for cooling and dehumidification was also common for air-conditioning movie theaters starting in the 1920s. Providing a conditioned indoor environment for its patrons resulted in economic boom for the theater and movie industry, since they were previously forced to close during the summer.

Apart from the early applications of direct-contact cooling systems, there were several attempts at using cooling coils to cool and dehumidify the air. The cooling process was achieved by circulating well water or cold brine through the coils. In 1896 an ammonia brine chiller was installed to cool the US senate chamber [2]. A combination of well water/ammonia brine chiller was used to cool air for a theater in Cologne, Germany about

1903-1904 [2]. A very elaborate system of cooling coils and controls, using carbon dioxide as a refrigerant, was installed in 1907 to condition the Gold room of Chicago's Congress hotel [3].

In the period from 1904-1924, air conditioning was almost entirely accomplished without refrigeration and was almost entirely confined to industrial applications [3]. Thus, except for the sporadic use of refrigeration, artificial cooling of air was practically unheard of before World War I. Despite the fact that air-washers were bulky and sometimes encountered nozzle clogging problems, they were the preferred approach because of their increased effectiveness over cooling coils. Advances in manufacturing technology, driven by refrigeration for household and automotive uses, led to the development of smaller and thinner tubing configured as heat exchangers with plate-finned enhanced surfaces. These new heat exchanger designs helped to downsize the indirect cooling coils and make them more effective, further paving the road for cooling coils to become more compact, more effective, and finally to overtake the air-washer technology. The aforementioned compact size of cooling coils compared to air-washers comes at the expense of power requirements (due to increased pressure drop on the airside) and capital costs.

The current state-of-the-art in air conditioning technologies rely on the use of chilled water cooling coils for cooling and dehumidifying supply air. The result is a system with a high operating cost due to the high air-side pressure drop and cooling losses due a finite approach

temperature[1] in addition to fouling on both the air and water-sides. Today's air conditioning system alternatives do not have the ability to simultaneously cool and dehumidify the supply air with low operating cost. With a renewed interest in energy conservation and enhanced indoor air quality, direct-contact spray-coolers deserve another look due to their effectiveness and capacity to control the temperature and humidity of supply air. The success of spray coolers to compete or commercially replace indirect cooling coils is, however, hampered by the fact that they tend to be bulky and expensive. Consequently, their economic viability demands a renewed effort on refining and improving the technology. Studying the performance of spray coolers is crucial for their optimization.

A detailed study of water sprays used for cooling and dehumidification is carried out to furnish groundwork for any further study in this topic. The objective of this study is to focus on developing methods that can predict and optimize the heat and mass transfer characteristics of the cooler. This investigation can be considered a first brick toward paving the road for future studies in the field of optimal control of spray coolers and in the field of using sprayed ozonated water for sanitizing and air conditioning the supply air. With recent acts of terrorism that involve the dispersion and dissemination of biological agents (e.g. anthrax), systems that can effective abate such pathogens would be in great demand.

In the following chapters a review of the previous work, research objectives, and experimental and numerical analysis necessary to study the cooling and dehumidification in

[1] The approach temperature is the difference in temperature between the coldest fluid entering the coil and the leaving air dry bulb temperature.

direct contact air coolers are presented. Chapter 2 presents a review of the relevant work in the area of spray cooling. In Chapter 3, the experimental investigation conducted to study the heat and mass transfer characteristics of a water spray cooler is presented. The purpose of the experiments is to evaluate the performance of the spray cooler and study its ability to cool and dehumidify the air at a given ambient condition. Chapter 4 illustrates the methods used to experimentally measure both the droplet size and spray cone angle. A brief description of each method is given along with the merits and drawbacks of technique. Chapter 5 presents the numerical simulations performed to assess the impacts of changing the spray cooler initial speed-ratio and droplet diameter on the performance of the spray cooler. The numerical analysis included both zero-dimensional as well as two-dimensional models. The two-dimensional model relied on the use of a commercial software package, FLUENT [4], to investigate the behavior of the spray cooler. It is then validated by running numerical simulation under the same inlet conditions of the laboratory experiments. A parametric study is then conducted to investigate the effect of the droplet diameter and initial speed-ratio on the performance of the spray cooler. Chapter 6 presents the semi-analytical models that predict the hydrodynamics and thermal performance of the cooler. These models predict the spray tip penetration length, the overall heat transfer coefficient, the interfacial area, and the effectiveness of the spray cooler. Finally, Chapter 7 presents the conclusions and recommendations for this work.

1.1 References

1 M. Ingels, “Father of Air Conditioning”, Country Life Press, 1952

2 Nagengast, B., “The First 80 Years of Air-Conditioning”, ASHRAE Journal, Vol.34, No.1, pp.S164-S175, 1992.

3 Fleisher, W., “How Air-Conditioning has developed in fifty Years”, Heating Piping and Air-Conditioning, January, pp.120-123, 1950

4 Fluent Incorporated Network Services, 10 Cavendish Court, Lebanon, NH 03766-1442, www.fluent.com.

Chapter 2 Literature Review

Water sprays are extensively used in many agricultural and engineering applications, such as, dust control, fire fighting, spray drying and gas turbine combustor cooling. In the field of heating ventilation and air conditioning they are used in cooling towers, evaporative cooling, and air washers. Air washers are used for dust removal and can also be optimized for either evaporative cooling or for cooling and dehumidifying. In a typical air washer, water droplets are brought into direct contact with the air. Consequently, heat and mass are transferred from/to the water droplets. If the water temperature is below the dew point temperature, moisture from the air will condense onto the water droplets. In this complex multiphase three-dimensional system, an understanding of the drop-air interaction dynamics is important for optimizing the process.

A review of the literature shows that the analytical and experimental studies conducted on liquid sprays can be divided into two categories. The first category considers the heat and mass transfer to a single droplet. The second category deals with full field spray models and configurations.

In the former category, Chung and Ayyaswamy [1] used a similarity solution to solve the system of partial differential equations describing the interaction of an air stream with a single droplet in a condensing regime. Sundararajan and Ayyaswamy [2] used a similarity solution technique to model the heat and condensation mass transfer associated with a single

drop. Huang and Ayyaswamy [3] solved a system of partial differential equations to determine the time-dependent behavior of an individual droplet's temperature, heat flux, condensation velocity, and aerodynamic drag. Ruckensten [4] solved the time-dependent convective diffusion equations for mass transfer between a drop and a continuous phase. Ford and Lekic [5] studied the growth of drops during condensation in direct contact between liquid drops and vapor. A review of the techniques and models used in these gas-particle type flows is given by Crowe [6]. In spray coolers, the problem is more complicated owing to the large number of water droplets interacting with each other. The single droplet models do not take into account the effect of the drop-to-drop interaction that may include droplet breakup or coalescence.

In the latter category, the droplet trajectories and their temperature history throughout the flow field are studied, assuming that the gas flow field is weakly affected by the presence of drops. The Lagrangian or Eulerian frames of reference are used to formulate the governing equations. The drawback of the Eulerian formulation is that it consists of a system of partial differential equations, which makes it mathematically difficult to solve when compared to the Lagrangian approach, which involves ordinary differential equations that are easier to solve. Various equations involved in Lagrangian motion analysis are mentioned in Yeung [7] and Crowe et al. [8]. Yeung [9] also presented a similarity analysis of liquid spray systems. A three-dimensional model has been given by Palaszewksi et al. [10]. Moussiopoulous [11] developed a numerical model for predicting the thermal performance of a circular spray-cooling pond. A study of one and two dimensional water sprays was performed by Ghosh and Hunt [12]. Kachhwaha et al. [13] developed a two-dimensional numerical model for

predicting the heat and mass transfer in hollow cone water sprays in a parallel flow arrangement. Frediani and Smith [14] considered the behavior of a single spray and extended their results to a system of sprays. Chen and Trezek [15] adopted the single unit approach in analyzing the performance of a spray system. Reindl [16] developed numerical models for three direct contact spray configurations; parallel flow, cross flow and counter flow using chilled water sprays. Ryan and Myers [17] reviewed various techniques for predicting the performance of spray models for power plant heat rejection. The models reviewed are primarily zero dimensional (global) type models. Details of the above references are discussed hereinafter.

2.1 Single Droplet

Chung and Ayyaswamy [1] studied the laminar condensation heat and mass transfer in the vicinity of the forward stagnation point of a spherical cold water droplet. They presented numerical solutions to the nonlinear, coupled boundary layer equations governing this laminar condensation problem. The environment surrounding the droplet is composed of a condensable vapor (steam), a non-condensable non-absorbable gas (air), and a third component, which is an absorbable non-condensable species (e.g. elemental iodine). Effects due to the presence of hydrodynamic and thermal boundary layers inside the drop are included. Also, the effect of viscosity on the internal core motion and the consequent reduction in the vortex strength inside the drop is accounted for. The most significant conclusion is that for laminar condensation on a freely falling droplet, for a given thermal

driving force and noncondensable gas concentration, the dimensionless heat transfer decreases with increasing saturation temperature of the outside medium.

Sundararajan and Ayyaswamy [2] evaluated the condensation heat and mass transfer to a liquid drop moving in a laminar flow of a mixture of noncondensable gas (air) and saturated vapor. The quasi-steady, coupled, boundary layer equations for the flow field and the transport in the gaseous phase are simultaneously solved. A similarity solution valid for the vicinity of the forward stagnation point, and a series solution that is applicable for the entire boundary region are obtained. In the series solution, the fluid flow and thermodynamic variables are expanded in terms of Legendre polynomials and associated variables. The resulting non-linear, ordinary differential equations are solved by the series truncation technique. On the other hand, the transient heat-up of the drop interior is evaluated using a Crank-Nicolson procedure. Figure 2-1 depicts a comparison between the analytical results for the non-dimensional droplet bulk temperature, $\bar{\theta}_b = \dfrac{T_b - T_o}{T_\infty - T_o}$, and Kulic and Rhodes [18] experimental data. Kulic and Rhodes [18] recorded the time history of a water drop experiencing condensation in a forced flow of air-steam mixture for two situations; both are summarized in Table 2-1. Figure 2-1 shows that the predictions and the experimental data are in good agreement.

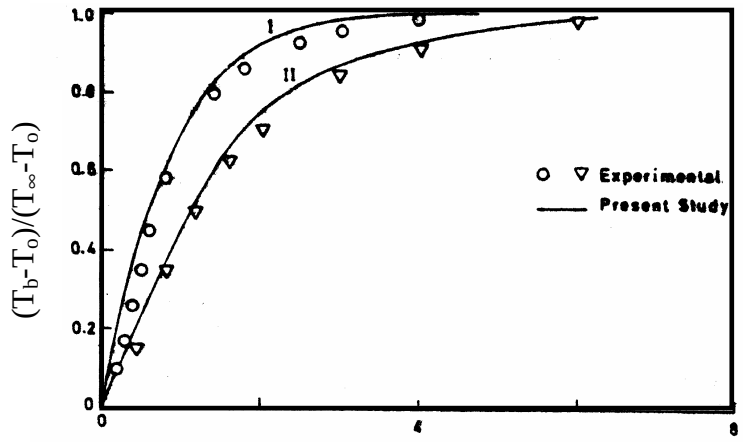

Figure 2-1 Variation of the non-dimensional drop bulk temperature, $\overline{\theta}_b$, with time [2]

Table 2-1 Parameters investigated by Sundararajan et al. [2]

	Initial Conditions		**I**	**II**
Saturated mixture	Temperature, T_∞	[°C]	80	72.5
	Pressure, P_∞	[bar]	1	1
Water Side	Temperature, T_o	[°C]	16	18
	Radius, R_o	[mm]	1.45	1.4
	Velocity, U_∞	[m/s]	1.91	1.68

Haung and Ayyaswamy [3] investigated the time-dependent hydrodynamics and heat/mass transfer associated with condensation on a spray drop for low Reynolds number. The drop environment is a mixture of saturated vapor and non-condensable gas (air). The formulation entails solution of the partial differential equations that describe the flow field and transport phenomena in the gaseous and liquid phases. The trajectory of the droplet is established by solving the relevant force balance equations. In the analysis, the effects of non-condensable

accumulation, liquid circulation and external-flow separation have been taken into account in the development of the results. A Crank-Nicolson procedure is used to evaluate the transient heat-up of the drop. The non-linear, algebraic difference equations are solved iteratively until the relative error between successive iterations is less than 0.1%. Figure 2-2 shows the effect of initial droplet spray angle, β_o, on the rate of rise in bulk temperature, $\overline{\theta}_b = \dfrac{T_b - T_o}{T_\infty - T_o}$, and the droplet vertical-height for the conditions summarized in Table 2-2. It can be noticed from Figure 2-2 that the rate of rise in bulk temperature of a liquid drop is insensitive to the droplet spray angle. However, the drop vertical-fall height, before thermal equilibrium is achieved, changes significantly with the spray angle.

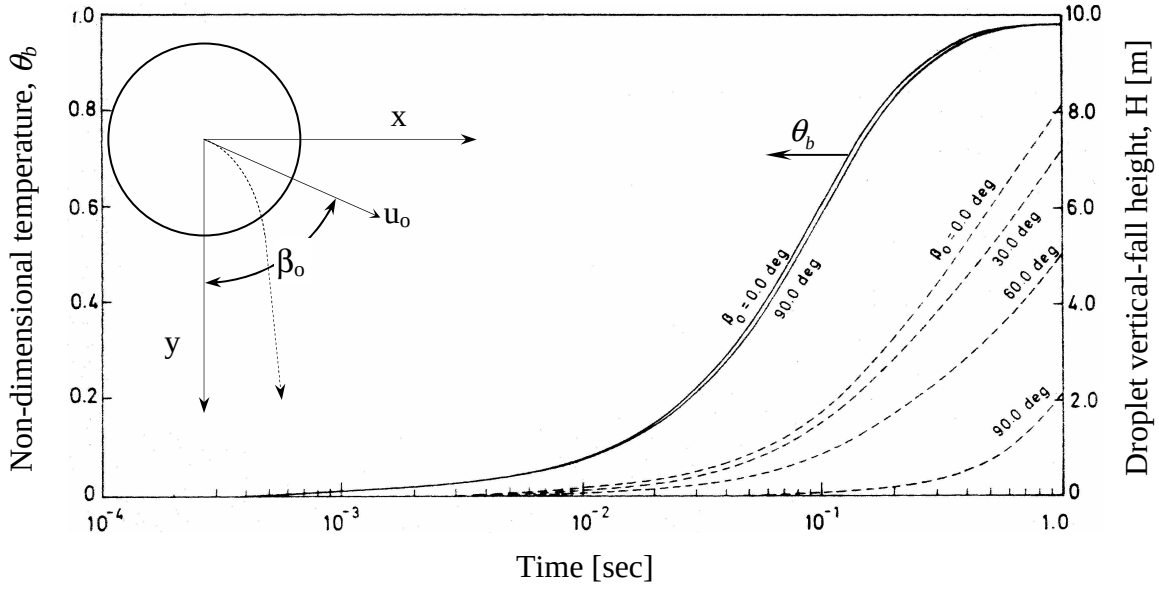

Figure 2-2 Effect of droplet spray angle on the variation of bulk temperature and drop vertical-fall height [3]

Table 2-2 Parameters investigated by Haung and Ayyaswamy. [3]

	Initial Conditions		
Saturated mixture	Temperature, T_∞	[°C]	120
	Pressure, P_∞	[kPa]	300
Water Side	Temperature, T_o	[°C]	37
	Radius, R_o	[μm]	250
	Velocity, U_o	[m/s]	15

Ruckensten [4] solved the time dependent convective diffusion equations for mass transfer between a spherical droplet and a continuous phase. The exact analytical solution is obtained based on the assumption that the depth of diffusion by penetration is very small. Consequently, the distribution of concentration in the vicinity of the interface of the drop is approximated by that for semi-infinite fluids. The similarity solution is presented for two cases: the first is for small Reynolds numbers, while the second is of potential flow. There method is based on a similarity variable which enables the transformation of the equations into ordinary differential equation for the concentration for each of the two species.

Ford and Lekic [5] studied the growth of water droplets during the direct contact condensation of steam. An approximate correlation for this process based on theoretical considerations is obtained and compared to experimental data. They treated the process of vapor condensation as unsteady–state heat transfer to a solid sphere, with negligible resistance at the interface and obtained an expression which approximates the rate of droplet growth. In his study, Ford and Lekic [5] performed an experimental investigation of condensation steam on water drops of three different diameters, 1.51, 1.67 and 1.76 mm

diameter, and with different initial sub-cooling below the saturation temperature of steam. High speed photography, 2000-5000 frames/sec, is used to analyze the growth rate of drops during condensation. Figure 2-3 shows that the measured of drop diameters as a function of time are in good agreement with that predicted by the approximate correlation.

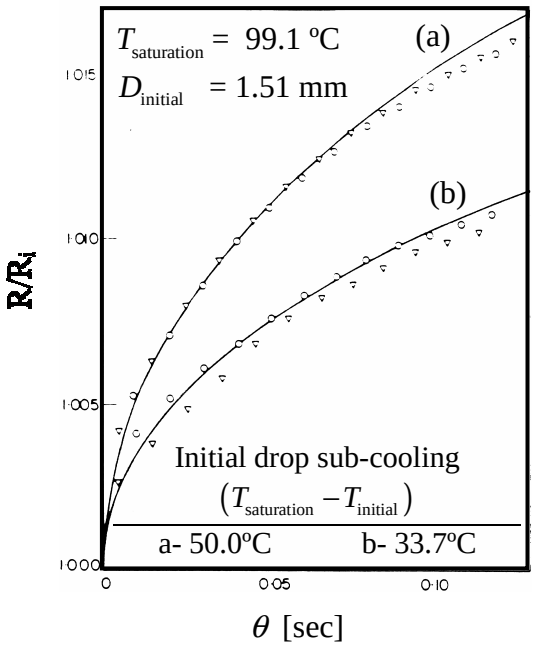

Figure 2-3 Dimensionless radius of drop during condensation [5]

2.2 Full field sprays

Yeung [7] presented a general formulation for the dynamics of a liquid spray in an incompressible gas phase and neglected the mass transfer. Crowe et al. [8] studied a steady two-dimensional, parallel flow, spray-cooling problem using the Particle-Source-In-Cell model (PSI-Cell). In this model the droplet is considered a source of mass, momentum and energy to the gaseous phase. The continuum flow field is analyzed utilizing the Eulerian

approach and the entire flow-field solution is obtained by solving the system of algebraic equations constituting the finite-difference equations for each cell. The droplet trajectories, size and temperature history are obtained by integrating the equations of motion for the droplets in the gas flow field and utilizing expressions for the droplet-gas mass and heat transfer rates. Solving for the droplet velocity, size and temperature along particle trajectories is done using the Lagrangian approach. Recording the mass, momentum and energy of the droplets on crossing cell boundaries provides the droplet source terms for the gas flow equations. The governing equations are solved using an iterative technique. The complete solution for a gas-droplet flow field is executed by first assuming no droplets are present in the flow field.

The model was used to analyze the velocity and temperature fields in a spray cooling vertical configuration, shown in Figure 2-4. The droplets are sprayed in the downstream direction with a spray angle ranging between 25 and 35 degrees, and the mass flow rate of the droplets is 10 times that of air. The initial droplet size distribution was assumed to consist of three discrete diameters, 740 μm, 1000 μm and 1380 μm. The main values for the parameters considered are summarized in Table 2-3

.

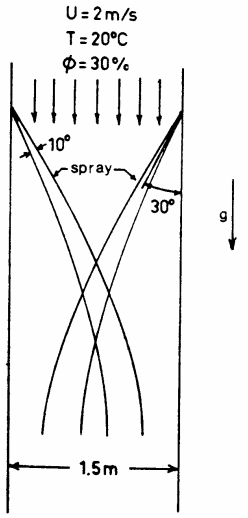

Figure 2-4 Cooling spray system [8]

Table 2-3 Parameters investigated by Crowe and Sharma [8]

	Air Side	Water Side
Inlet Temperature [°C]	20	60
Relative humidity [%]	30	-
Initial velocity [m/s]	2	2

The simulations show that the larger droplets penetrate the greatest distance and cool the slowest owing to their large inertia and thermal capacity. These results aSre consistent with the observations made in this study. A reduction of the axial velocity of the gas stream near the injection port was also observed. This reduction in axial speed was attributed to the aerodynamic drag since the initial axial velocity of the droplets is the less than that for the gas.

Yeung [9] investigated similarity solutions for the liquid dispersed region of flat (two-dimensional) and conical (axisymmetric) spray systems. In the analysis Yeung followed the classical Schlichting [19] approach for turbulent jet analysis in which both the gravity and interfacial drag are neglected. Furthermore, the droplets were treated as solid spheres with a constant mean diameter following straight-line trajectories. Two different cases are considered; the first corresponds to the situation where the drag forces influence the droplet

motion. In this case, no compatible similarity solutions were possible. In the second case both the gravity and interfacial drag are neglected. The similarity solution for the conical spray produced unrealistic results. On the other hand, the similarity solutions for flat sprays are compared to the experimental results reported by Chuah et al. [20], revealing that the analytical solutions over predicted the experimental results, due to uncertainty in the mean droplet diameter.

Palaszewski et al. [10] developed a three-dimensional numerical model for predicting the detailed flow and thermal characteristics of circular spray cooling ponds. The model predicts the local variation in the dry bulb temperature, absolute humidity, and the air streamlines through the flow field encompassing the spray umbrella and the effect of this local variation on drop cooling. The conservation equations are written in the Lagrangian form where the droplets are treated as a spatially varying source of mass, momentum and energy. In the analysis the authors assumed that the pressure field is uniform and the turbulent transport is of the boundary layer type. Consequently, the differential equations for the air-vapor phase change from elliptic to parabolic. The kinematics problem involving the spatial distribution of the droplets and the time duration of the droplet in air in solved separately and the results are stored. The spray is assumed to be mono-dispersed and the initial droplet diameter is obtained by varying the droplet diameter until the single particle momentum equation yielded the experimentally measured trajectory. The numerical model is capable of handling wind speeds not less than 0.1 m/s. The lowest order solution for the iterative technique adopted, for the droplet velocities, locations, temperatures and sizes, is based on the ambient conditions. The first order air-vapor solutions yield a correction to the local environment of

the drops, and utilized in the next iteration. The iteration procedure is repeated until the convergence criteria, $\frac{\dot{Q}_k - \dot{Q}_{k-1}}{\dot{Q}_{k-1}} \le \varepsilon$, is satisfied. In the previous equation $\dot{Q}_k$ and $\dot{Q}_{k-1}$ are the rate of heat transfer from a spray unit at different iterations, and ε is the prescribed tolerance for convergence of spray heat transfer from successive iterations. The model is compared against experimental data obtained for the Spraco nozzle as given by Chen [21]. The sprayed water is collected in catch pans where the collected water temperature is measured. The measured temperature is corrected to account for heat transfer from the pan. Five discrete droplet diameters from the measured size distribution, their discharge angle, and the mass fraction for the total spray flow rate for each size are used as inputs to the model. In the model, droplets are discharged from ten sites around the nozzle perimeter. All five droplet sizes are discharged from each site. Figure 2-5 depicts a comparison between the model and the experimental results for the non-dimensional cold spray temperature, $T_C^* = \frac{T_C - T_{\mathrm{wb}_\infty}}{T_{\mathrm{do}} - T_{\mathrm{wb}_\infty}}$, and the non-dimensional distance, $y^* = \frac{yg}{v_o^2}$. Where T_C is the spray cold water temperature at canal re-entry, T_{do} is the spray supply temperature, T_{wb_∞} is the ambient wet-bulb temperature, y is the horizontal space coordinate in the wind direction, g is the gravitational acceleration, and v_o is the initial speed of the mean size drop. The numerical simulations presented in this figure are for two cases. The first case is for the no-interaction theory where the environment of the drops during its entire time flight is maintained at the ambient condition at all times. Thus, the no-interaction theory gives the maximum amount of cooling that can be experienced by the droplets. The second case is the interaction case

where the environment of the drops varies along its path. Figure 2-5 shows that the theoretical predictions of the model compare favorably with the experimental data.

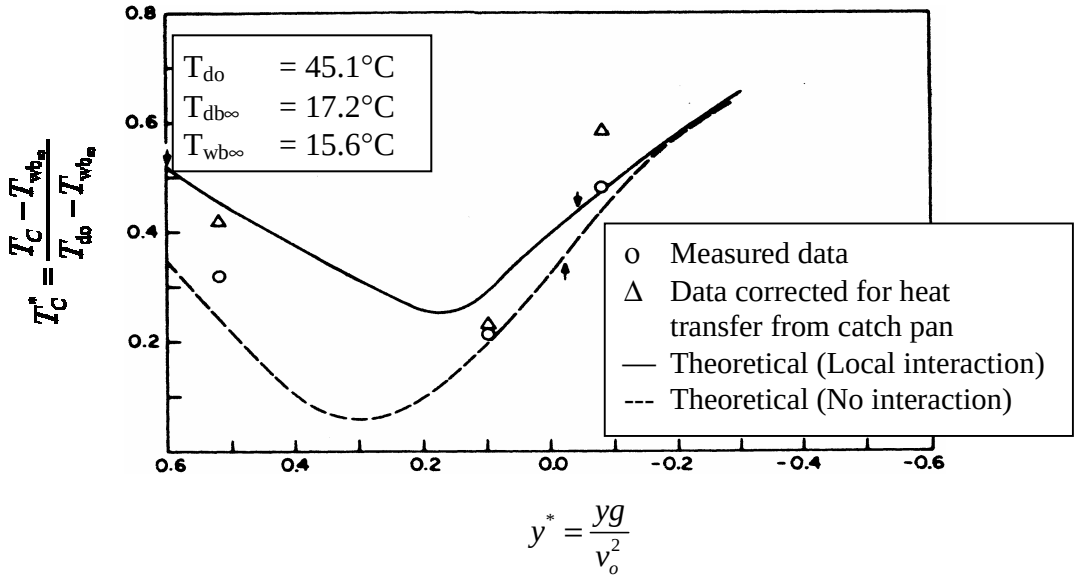

Figure 2-5 Centerline droplet return temperature for Sparco nozzle (U_{2m_∞} = 2.88 m/s) [10]

Moussiopoulos, N. [11] presented a two-dimensional model for predicting the performance of circular spray cooling ponds for the critical case of zero wind velocity. The airflow is described by partial differential equations for the vorticity and the stream function. Turbulence is taken into account by a modified $k-\varepsilon$ model. Temperature and humidity of air are obtained by solving the appropriate transport differential equations. The governing equations are solved using the ADI (Advanced Direction Implicit) method with numerically optimized under relaxation factors. The author assumed that the experimental values reported by Hebden and Shah [20] for a 2 m/s wind velocity are representative for their case

of zero velocity. The analytical results are in good agreement with the experimental measurements.

Ghosh and Hunt [12] studied one and two dimensional water sprays in air. The spray induced air velocity field for a spray emerging into a quiescent environment is analytically calculated. Contrary to Yeung [9], they show that a two-dimensional fan spray and a one-dimensional axisymmetric spray can be mathematically modeled as a line source of momentum due to which surrounding air behind the jet is drawn towards the spray centerline. The predictions of the study are in good agreement with the Binark and Ranz [22] measurements. In the experiments, they visualized the air flow using smoke and also obtained air velocity measurements using a pitot probe inside the spray and a hot-wire probe outside the spray. The liquid discharge rate is 0.14 gpm and initial droplet velocity of 26.5 m/s.

Kachhwaha et al. [13] developed a two-dimensional numerical model for predicting the heat and mass transfer in hollow cone water sprays in a parallel flow arrangement. The model inputs include drop size distribution, and velocities at nozzle spray angle; inlet dry-bulb temperature and humidity ratio. The drop volume mean diameter at break up is measured from still photographs of the spray and these data are used in the model. The set of conservation equations, mass momentum and energy of air and water, are time marched numerically and local conditions at various downstream locations are computed. In the analysis, the authors assumed that the air pressure is constant throughout the duct, the momentum exchange between the air and the water drops is negligible. Simulations are

performed using four mean drop diameters, 15% and 30% larger, 15% and 30% smaller than the measured mean drop diameter. Experimental data are obtained for a horizontal once through wind tunnel at three air velocities with each nozzle, 3.2 and 4.8 mm outlet diameter, at three pressures in parallel and counter flow configurations. The main values for the parameters considered are summarized in Table 2-4.

Table 2-4 Parameters investigated by Kachhwaha et al. [13]

		Air Side	**Water Side**
Inlet Temperature	**[°C]**	35-42	26-33
Relative humidity	**[%]**	22-60	-
Initial velocity	**[m/s]**	0.8-2.5	12-22

Figure 2-6 presents a comparison between the predictions and experimental values for 3.2 mm nozzle diameter. Figure 2-6 shows that the temperature predictions are within ±30%, and ±15% for the humidity ratio. This deviation was attributed to the uncertainty in the drop size measurements.

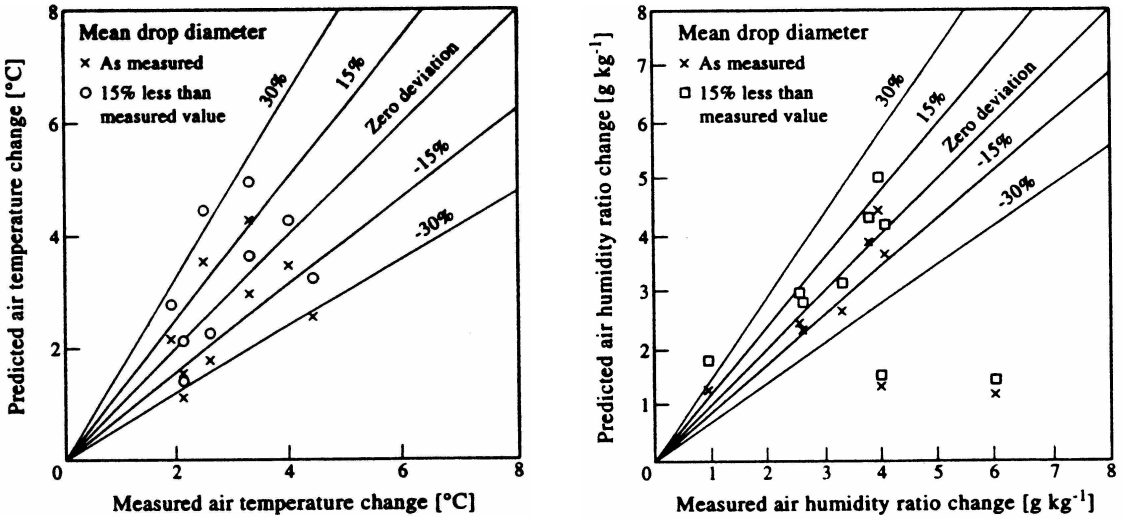

(a) (b)

Figure 2-6 Comparison of experimental data and model predictions of air dry-bulb change and air humidity ratio change [13]

Frediani and Smith [14] developed a mathematical model that describes large-scale spray cooling systems. The continuity and energy equations are developed for a cellular model representing a single spray in a system of arrays. The equations are solved using a finite-difference solution along a drop trajectory for both water and air parameters. The cellular method consists of dividing the spray into a number of non-interacting identical cells, each of which is a volume of air containing a representative drop of water. The effective drop diameter is varied until agreement between the predictions and the experimental data is satisfied. The radius and volume of a sphere of air surrounding the drop is calculated by setting the ratio of the volumes of the drop and the air sphere to the ratio of the flow rates of water and air. In order to satisfy continuity, the volumetric flow of air to form air cells is set equal to the product of air velocity and the cross sectional area of the spray. The rate of formation of air cells is set equal to the rate of formation of water drops. The number of

water drops per second is derived from knowing the flow rate of water volume per drop. The model is applied towards solution of large systems involving multiple passes of sprays operating in conjunction with power stations. The agreement between data and the predictions was reasonable over a range of parametric variations, including wind velocity and air-water temperatures.

Chen and Trezek [15] adopted the single unit approach, semi-empirical, in analyzing a spray system performance. In their work they addressed the effect of three basic parameters, the droplet heat transfer coefficient, the local wet bulb temperature, and the size distribution of the spray droplet on the spray system performance. Three common relations for the heat transfer are considered; Ranz and Marshall correlation [23], a modified Ranz and Marshall correlation [24], and solid spheres correlation. Moreover, for the humidity calculations they used three approaches; at zero or low wind conditions, the local humidity is obtained by solving the diffusion equation neglecting the convective effects, for high wind speeds (greater than the rate of evaporation) the local air vapor humidity is taken as that of the ambient, and an average value is taken for the intermediate range. The results of their investigation are shown in Figure 2-7. The figure shows that the highest and lowest values for the heat transfer coefficient are given by the solid sphere and the modified Ranz and Marshall correlation. The quantitative evaluation of the applicability of the different correlations is carried assuming that the wet bulb temperature is either equal to the ambient value, T_{wb_∞} or equal to the arithmetic mean value of the initial, T_{wb_∞}, and the final, T_{wb_f}, wet-bulb temperatures as deduced from the test data [25]. Thus, the final wet-bulb temperature

change across the spray is obtained from laboratory tests. The results are shown in Figure 2-8 as $\frac{T_{sp}^{'} - T_{sp}}{T_{co} - T_{sp}}$ versus wind speed, where $T_{sp}^{'}$ and T_{sp} are the predicted and experimental spray temperature at the end of the trajectory, and T_{co} is the spray temperature at the nozzle. The results indicated that, for a drop size less than 6 mm, the Ranz-Marshall heat-mass correlation yields a valid prediction of the thermal performance provided that the proper values of wet bulb temperature and spray distribution function are used.

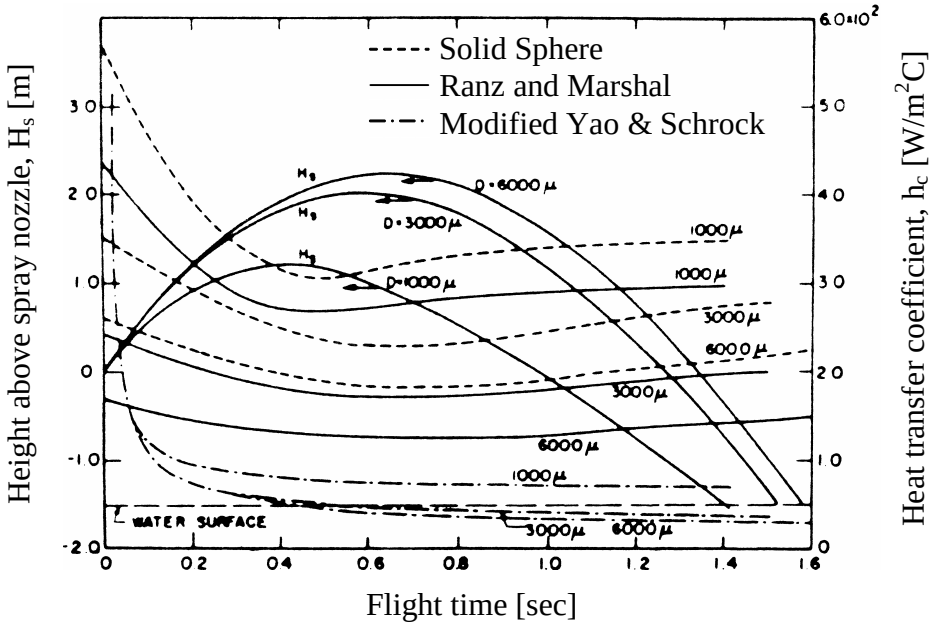

Figure 2-7 Variation of heat transfer along the drops' trajectories [15]

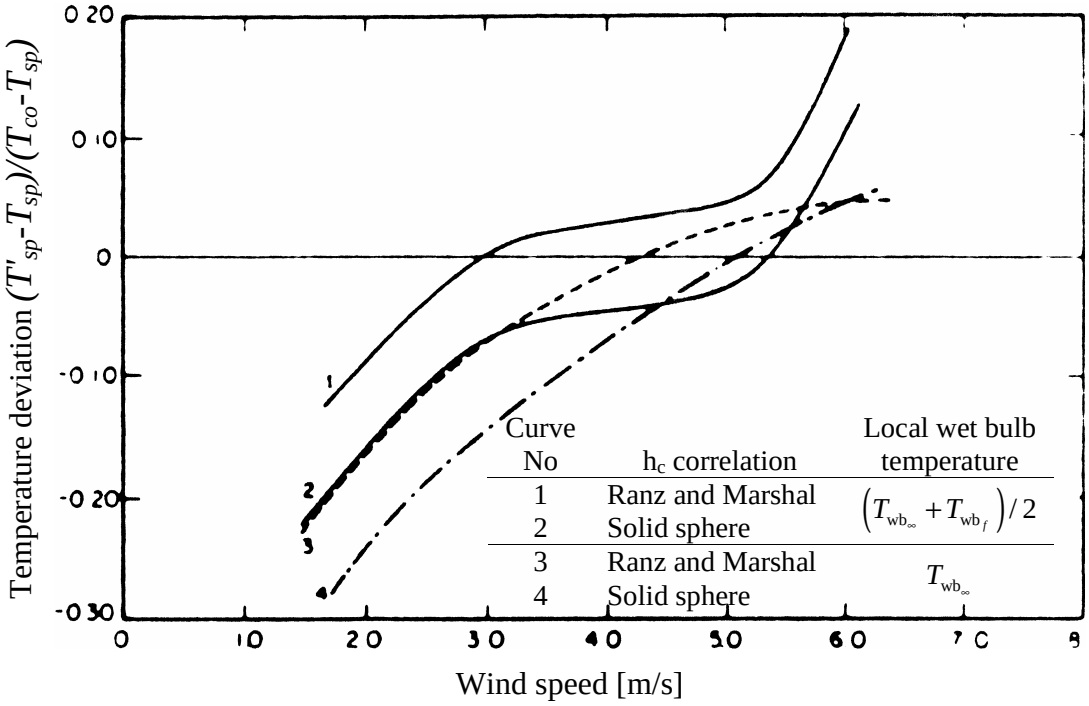

Figure 2-8 Predicted final spray temperature, T'_{sp}, deviation for different heat transfer coefficients and local wet-bulb temperatures [15]

Reindl [16] studied the heat and mass transfer to chilled water sprays. The author developed numerical models for three direct contact spray configurations; parallel flow, cross flow and counter flow. The model inputs include physical characteristics for the spray chamber, the surface to volume ratio, a, the overall mass transfer coefficient, $\bar{h}_D a$, and the inlet conditions for air and water, (temperature and mass flow rate). The magnitude of the overall mass transfer coefficient-specific surface area product, $\bar{h}_D a$, is evaluated experimentally, experimental conditions are presented in Table 2-5. For parallel flow systems the governing equations are solved using a fourth-order Runge-Kutta method. On the other hand, for the cross-flow and counter-flow cases a second order finite difference scheme using central

difference is implemented to solve the system of ordinary differential equations for the dry bulb temperature, air humidity ratio, water mass flow rate and water temperature. For the cross flow configuration the convergence criterion is satisfied when the root mean square error, e, for the air humidity ratio, air enthalpy, water temperature, and water mass flow rate is less than 10^{-5}. The author concluded that the cooling capability of the considered spray chamber, for the given conditions, is relatively insensitive to the water-side flow.

Table 2-5 Parameters investigated by Reindl [16]

		Air Side	**Water Side**
Inlet Temperature	**[°C]**	35	0.6
Wet bulb temperature	**[°C]**	24	-
Air discharge	**[cfm]**	1120	-
Water discharge	**[gpm]**	-	10-50

The aforementioned literature review shows that a significant amount of research has been conducted on the heat and mass transfer to a single droplet, and full field sprays. However, there have been very few attempts to study the problem of cooling and dehumidification in air coolers. The only available study conducted by Reindl [16] presents a global type model approach to characterize the heat and mass transfer in a condensing regime. Moreover, the effect of important parameters, such as droplet diameter and spray-cooler initial velocity-ratio, on improving the effectiveness of spray coolers has not been addressed in any of the previous studies. The review also reveals that no simple semi-analytical models that can predict the thermal performance of a direct-contact spray-cooler have been developed.

2.3 Research Objectives

In an effort to complete and extend some of the previously reported results of heat and mass transfer in chilled water direct contact spray coolers, an experimental and numerical investigation of a water spray system is conducted. The numerical model is performed with a commercial software package FLUENT [26]. A theoretical analysis of the spray cooler is also performed by developing analytical and semi-analytical models. The purpose of the current research work is to develop methods that allow control and optimization of the heat and mass transfer characteristics for direct-contact spray coolers. The specific goals of the research are:

1. Gain insight into the fundamental physics of mass and heat transfer in direct contact spray coolers.
2. Identify relevant parameters that control the heat and mass transfer in spray coolers.
3. Build appropriate numerical models to simulate the cooling and dehumidification in direct contact spray coolers.
4. Validate numerical results by physical experiments.
5. Establish general guidelines for designing direct-contact spray coolers.
6. Conduct a feasibility study for using direct-contact spray coolers.
7. Explore different methods to optimize the heat and mass transfer characteristics of spray coolers.

For the spray cooler under consideration the following parameters are varied; water flow rate, droplet diameter, and initial-velocity ratio. The effect of each of these parameters on the spray cooler performance and its ability to meet different loading conditions are investigated.

2.4 Nomenclature

g	Gravitational acceleration	m/s^2
$\dot{Q}_k$	Rate of heat transfer from a spray unit at a given iterations	
R	Droplet radius at any time	mm
R_i	Initial droplet radius	mm
T_b	Drop bulk temperature	°C
T_C	The spray cold water temperature at canal re-entry	
T_C^*	Non-dimensional cold spray temperature	
T_{co}	Spray temperature at the nozzle	
T_{do}	The spray supply temperature	
$T_{initial}$	Solid sphere initial temperature	°C
T_o	Water-side temperature	°C
$T_{saturation}$	Steam condensation temperature	°C
T_{sp}	Experimental spray temperature at the end of the trajectory	
$T_{sp}^{'}$	Predicted spray temperature at the end of the trajectory	
T_{wb_∞}	The ambient wet-bulb temperature	
T_{wb_f}	Final wet-bulb temperature	
T_∞	Saturated mixture temperature	°C
u_o	Initial droplet velocity	m/s
v_o	Initial speed of the mean size drop	
y	Horizontal space coordinate in the wind direction	
y^*	Non-dimensional distance	

2.4.1 Greek Symbols

$\overline{\theta}_b$	Non-Dimensional droplet bulk temperature [2]	
θ	Time	s
β_o	Initial droplet spray angle	deg
ε	prescribed tolerance for convergence of spray heat transfer from successive iterations	

2.5 ReferencesS

1 Chung, J. N. and Ayyaswany, P. S., “Laminar Condensation Heat and Mass Transfer to a Moving Drop”, AIChE Journal, 1981, Vol. 27(3), pp. 372-377.

2 Sundararajan, T., and Ayyaswamy, P. S., “Heat and Mass Transfer with Condensation on a Moving Drop: Solutions for Intermediate Reynolds Number by a Boundary Layer Formulation”, ASME Journal of Heat Transfer, 1985, Vol.107, pp. 409-416.

3 Huang, L., and Ayyaswamy, P. S., “Heat and Mass Transfer Associated with a Spray Drop Experiencing Condensation: A Fully Transient Analysis”, Int. Journal of Heat and Mass Transfer, 1987, Vol.30 (5) pp. 881-891.

4 Ruckenstein. E, “Mass Transfer between a Single Drop and a Continuous Phase”, International Journal of Heat and Mass Transfer, vol. 10, 1967, pp. 1785-1792.

5 Ford, J. D. and Lekic, A., “Rate of Growth of Drops During Condensation”, International Journal of Heat and Mass Transfer, vol. 16, pp. 61-64, 1973.

6 Crowe, C. T., “Review-Numerical Models for Dilute Gas-Particle Flows”, Journal of Fluids Engineering, 1982, Vol. 104, pp.297-303.

7 Yeung, W. S., “Dynamics of Gas Liquid Spray Systems”, Encyclopedia of Fluid Mechanics, 1986, Vol. 3, chapter 12, pp. 281-300.

8 Crowe, C. T., and Sharma, M., “The Particle Source-In-Cell (Psi-Cell) Model for Gas Droplet Flows”, ASME Journal of Fluids Engineering, 1977, Vol.99, pp. 325-352.

9 Yeung, W. S., “Similarity Analysis of Gas Liquid Spray Systems”, Transactions of the ASME Journal of Applied Mechanics, pp. 687-690, Vol. 49, 1982.

10 Palaszewski, S. J., “Three-Dimensional Air Vapor Droplet interaction Model”, Journal of Heat and Mass Transfer, 1981, Vol.103, pp. 514-521.

11 Moussiopoulos, N., “Numerical Simulations of Spray Cooling Pond Performance”, Transactions of the ASME: Journal of Fluids Engineering, 1987, Vol. 109, pp. 179-185.

12 Ghosh, S. and Hunt, J. C. R., “Induced Air Velocity Within Droplet Driven Sprays”, Proceedings of the Royal Society of London A, 1994, Vol. 444, pp. 105-127.

13 Kachhwaha, S. S., Dhar, P. L. and Kale, S. R., “Experimental Studies and Numerical Simulation of Evaporative Cooling of Air with a Water Spray-I. Horizontal Parallel Flow”, Int. Journal of Heat and Mass Transfer, 1998, Vol. 41, No. 2, pp. 447-464.

14 Frediani, H. A. and Smith, N., “Mathematical model of spray cooling systems”, Journal of engineering for power, pp279-283, April 1977.

15 Chen, K. H. and Trezek, G. J., “The Effect of Heat Transfer Coefficient, load Wet Bulb Temperature and Droplet Size Distribution Function on the Thermal Performance of Sprays”, Journal of Heat Transfer, vol. 99, no. 3, pp. 381-385.

16 Reindl, D. T., “Combustion Turbine Inlet Air Cooling Using Direct-Contact Sprays”, Electric Power Research Institute Final Report RP3890-02.

17 P. Ryan, D. Myers, “Spray cooling: a review of thermal performance models”, Proceedings of the American power conference, pp1473-1481, Vol. 38, 1976.

18 Kulic, E. and Rhodes, E., “Direct Contact Condensation from Air-Steam Mixtures on a Single Droplet”, Can. J. Chem. Engrg., 1977, Vol. 55, pp. 131-137.

19 Schlichting, H., “Boundary Layer Theory”, 7th ed. McGraw Hill, New York, 1979.

20 Chuah, Y. K., Yeung, W. S. and Fisher, E. N., “Measurement of Air Velocity in a Plane Turbulent Spray” Report, Thayer School of Engineering, Dartmouth College, Hanover, N. H. 03755, Nov. 1980.

21 Chen, K., “Heat and Mass Transfer from Power Plant Spray Cooling Ponds”, Doctoral Dissertation, University of California, Berkeley, 1975.

22 Hebden, W. E., and Shah, A. M., “Effects of Nozzle Performance on Spray Ponds”, Proceedings of the American Power Conference, 1976, Vol. 38, pp. 1449-1457.

23 Ranz, W. E. and W.R. Marshall, “Evaporation from drops”, Chemical Engineering Progress, vol. 48, no.3 & 4, 1952, pp 141-146, 173-180.

24 Yao, S-C., and Schrock, V.E., “Heat and Mass Transfer from Freely Falling Drops”, Journal of Heat Transfer, Trans, ASME, Series C, Vol.98, No.1 Feb.1976.

25 Chen, K. H., “Heat and Mass Transfer of Multi-Sray Unit Cooling System in Open Atmosphere”, Ph.D. dissertation, University of California, Berkeley, 1976.

26 Fluent Incorporated Network Services, 10 Cavendish Court, Lebanon, NH 03766-1442, www.fluent.com.

Chapter 3 Experimental Analysis

The current state-of-the art in air conditioning technologies has long relied on chilled water finned cooling coils. Cooling coils provide cooling and dehumidification but their operation incurs losses due to fouling on both the air- and water-sides in addition to a relatively high pressure drop. Thermodynamically, a better alternative would be direct-contact spray coolers where the chilled water is brought into intimate contact with the warm, moist air to be cooled. Spray coolers are however bulky and expensive and hence require development in order to compete with cooling coils on a commercial level.

Studying the performance of spray coolers is an indispensable requirement to their development. Experimentation is very reliable in revealing the physical processes and accurate in predicting their performance. In addition, experimental methods are still a quintessential scientific research technique for a number of reasons. First, experiments provide a foundation for asserting strong conclusions about research hypotheses. Second, the experimental results offer an optimum method to test the validity of competing hypotheses. Finally, appropriately designed experiments can provide answers to surprisingly complex questions.

This chapter introduces the experimental setup used for studying the heat and mass transfer characteristics of water sprays to directly condition supply air for indoor environments. Then the procedures and results of the experiments are presented. The purpose of these

experiments is to evaluate the performance of a spray cooler and study its ability to effectively cool and dehumidify air at different ambient conditions. The apparatus consists of a blower, wind tunnel, test section, water supply system, spray system, and necessary transducers for measuring dry-bulb, wet-bulb, and dew-point temperatures. The air-side pressure drop and volume flow rate are measured. The water injection pressure, inlet and exit temperatures, and volume flow rate are also measured. A schematic of the test rig is shown in Figure 3-1, also photographs for the test rig are given in Appendix-I.

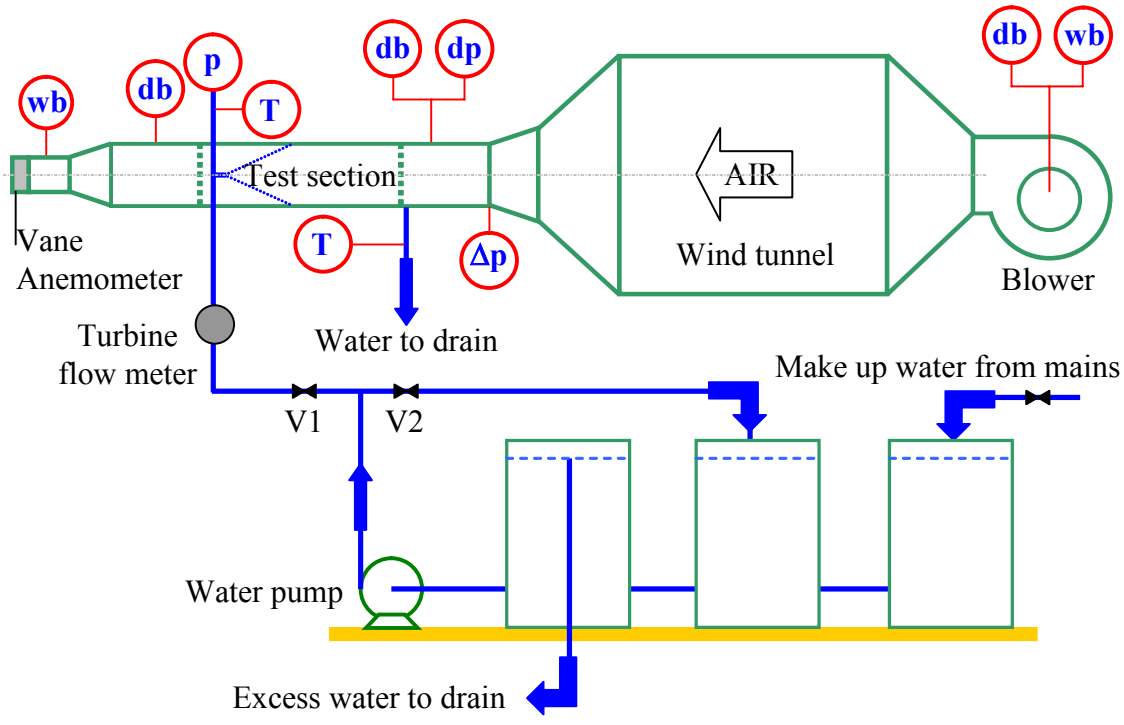

Figure 3-1 Schematic for the test apparatus

A constant volume flow rate of air enters the test section through the wind tunnel. Chilled water is sprayed in a counter flow configuration to cool and dehumidify (conditions

permitting) the air. The flow rate of air is measured with a vane anemometer at the duct exit and the pressure drop across the test section is measured using a micro-manometer. While entering and leaving dry-bulb, dew-point and wet-bulb temperatures are measured at the inlet and exit sections to determine the psychometric states of air. In addition to air-side measurements, water-side measurements are performed to check that the energy-balance is satisfied. Entering water flow rate, injection pressure and temperature are measured in a station prior to reaching the spray nozzle. The injection pressure is measured with a pressure transducer and flow rate is measured using a turbine flow meter. Return water temperature is also measured, thus allowing the water-side rate of energy gain to be compared with the air-side rate of energy loss. All measurements are taken under quasi-steady state conditions. Quasi-steady state condition is achieved when the deviation of the air-side and water-side temperatures, over a five minute period, is within ±0.02 ºC from their average values. Quasi-steady state is verified by continuous logging of air and water-side temperatures in accordance with the previously mentioned criteria. The following sections discusses in detail the test rig and the experimental procedure.

3.1 Test Section

The motor driven blower draws in room ambient air and delivers it to the test section via the wind tunnel. A set of parallel blade dampers on the blower inlet-side is manually adjusted to establish a target fixed volume flow rate of air to the test section. Two copper-constantan thermocouples are fixed after the dampers to measure the entering air dry-bulb and wet-bulb temperatures. The test section is an insulated stainless steel circular duct 0.2 m in diameter

and 3.48 m long. The section is inclined downwards in the water flow direction to facilitate draining of water from the test section. The test section can conceptually be divided into three zones, an inlet zone, a spray chamber, and an exit zone, as shown in Figure 3-2. The diameter of the duct is chosen to be 0.2 m for the following two reasons:

1. Cost and handling
2. The experiments need to be realistic; scaling up the results from a too small experiment is not reliable.

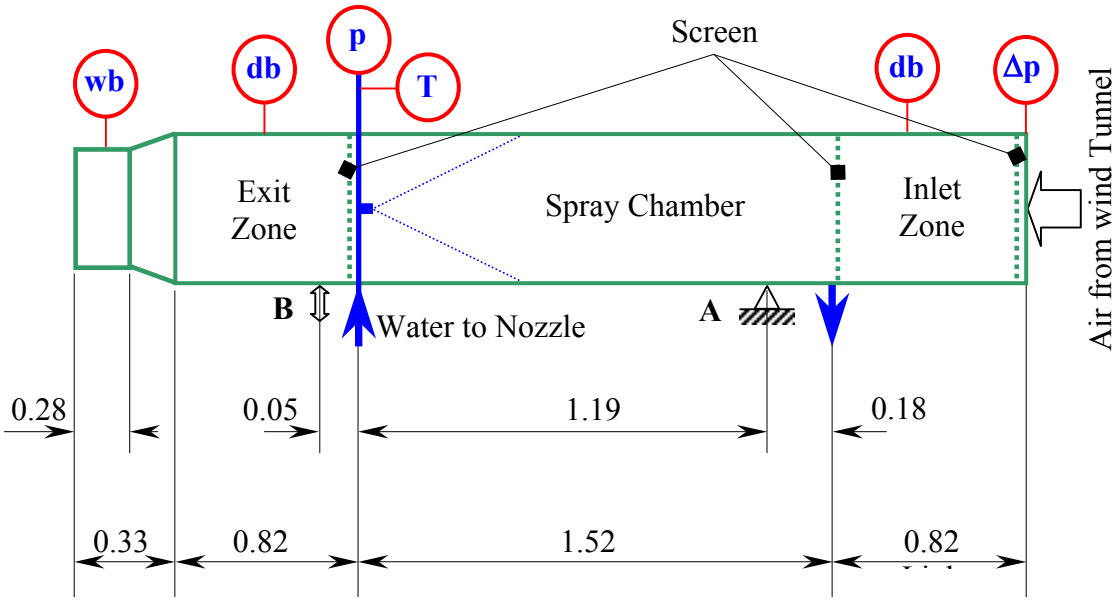

Figure 3-2 Schematic for the test section

3.1.1 Inlet zone

The inlet zone, which directly follows the wind tunnel, is 0.82 m long and 0.2 m in diameter. A flow straightener is fixed on the upstream side to ensure that parallel airflow is supplied to

the instrumentation located in the inlet section. Also, another flow straightener is fixed on the downstream side of the inlet zone to ensure parallel airflow through the spray chamber, that follows this zone. In this zone, the average dry-bulb and the dew point temperatures are measured using thermocouples and a dew point hygrometer, respectively. Eighteen copper-constantan thermocouples, connected in parallel (a thermopile arrangement), are used to measure the average dry bulb temperature, in accordance with the ANSI/ASHRAE Standard 111-1988 [1].

3.1.2 Spray Chamber

The spray chamber, which is the middle zone of the test section, is 1.52 m long and 0.2 m in diameter. In this zone, water and air come into direct contact with each other. Water is sprayed in a counter-flow direction into the air stream via a circular pattern full cone spray nozzle. The nozzle is fixed on the exit side of the spray chamber. The sprayed water is drained from the spray chamber inlet side via an exit port. On the exit side, a screen is positioned within the duct to ensure parallel flow through the exit zone and to act as a drift eliminator.

The spray nozzle tip; model QLH-SS-25 [2], produces a full cone spray pattern with spray angles ranging from 61º to 67º depending on the capacity, details on its performance are shown in Table 3-1. The nominal orifice diameter of the nozzle is 4.8 mm (3/16 in). The spray nozzle is composed of two parts, a “Quick FullJet” spray nozzle tip and a “Quick FullJet” body. The body; model QJJL [2], has a ½" BSPT. The tips are easily installed into

or removed from the body. This design provides ease, convenience, and speed of replacement if a different spray nozzle tip size is required.

Table 3-1 Performance data for Quick FullJet spray nozzle tip QLH-SS-25 [2]

	Inlet Pressure [kPa]									
	34.5	48.3	68.9	137	206	275	423	551	689	1034
Capacity [l/min]	6.81	7.9	9.5	13.2	15.9	18.2	22.0	25.4	28.0	33.7

Table 3-1 continued

	Inlet Pressure [kPa]		
	48.3	137	551
Spray Angle	64º	67º	61º

3.1.3 Exit Zone

The exit zone is divided into two segments; the first segment is 0.82 m long and 0.2 m in diameter. In this location, the average dry-bulb temperature is measured by eighteen thermocouples arranged and connected in a similar manner as those in the inlet zone. The second segment is down stream of the first one and is 0.33 m long and 0.15 m in diameter. The wet-bulb temperature is measured in this segment using a wetted copper-constantan thermocouple. The diameter of this section is reduced to increase the air velocity; thereby ensuring that the air velocity past the thermocouple always exceeds the lower recommended limit of 4.6 m/s required to obtain accurate wet bulb temperature readings [3]. The measurement of wet-bulb temperature is performed downstream of the dry-bulb temperature to prevent biasing of the dry-bulb temperature measurements by the air that passes the wet-bulb, and is thereby cooled by the evaporation [3].

3.2 Water Supply System

The water supply system consists of three interconnected containers, 0.0757 m^3 (20 gallons) each, water pump, filter, necessary piping, fittings and valves, turbine flow meter, and a spray nozzle, as shown in Figure 3-1. The three containers store thermal energy in the form of ice for capacity while running the experiment using chilled water. Water is added from the mains to the containers to compensate for the water injected into the spray chamber. The water height is maintained constant by an overflow pipe. This design ensures a constant head imposed on the supply water pump; thereby, stabilizing the water flow rate delivered during its operation.

Varying the position of the two ball valves connected to the water supply line serves to modulate the water mass flow rate. The function of the first valve, V1, is to circulate water from the pump suction back to the storage tanks. The second valve, V2, controls both the flow rate of water and pressure supplied to the nozzle. The positions of both valves are adjusted at the start of an experimental run to maintain a desired constant pressure at the nozzle inlet. This is necessary because the nozzle capacity, the spray drop sizes and spray cone angle, are greatly affected by the supply water pressure to the nozzle. A pressure transducer continuously monitors the inlet pressure to the spray nozzle.

3.3 Measuring Instrumentations

This section presents the data acquisition system and the necessary transducers used for measuring dry-bulb, wet-bulb, dew-point temperatures, water inlet and exit temperatures, air and water volume flow rates, injection pressure, and air-side pressure drop. Copper-

constantan thermocouples are used for dry-bulb temperatures, wet bulb temperatures, and water inlet temperature and exit temperature. A dew-point hygrometer is used for measuring the entering air dew-point temperature. The air volume flow rate is measured by a vane anemometer, while a turbine flow meter is used to measure the water flow rate. The injection pressure is measured by a pressure transducer, while the air-side pressure drop is measured with a digital micro-manometer. The measuring locations and measured variables are summarized in Table 3-2. Details on these measurements and their accuracy are discussed in what follows.

Table 3-2 Measuring locations

Location	**Measurement**	***Unit***
Blower Inlet	Dry-bulb temperature Wet-bulb temperature	*°C* *°C*
Inlet zone	Dry-bulb temperature Dew-point temperature Air-side pressure	*°C* *°C* *Pa*
Exit Zone	Dry-bulb temperature Wet-bulb temperature Air-side volume flow rate	*°C* *°C* *cfm*
Nozzle inlet	Water temperature Water volume flow rate Injection pressure	*°C* *°C* *psig*
Water outlet	Temperature	ºC

3.3.1 Temperature Measurements

The main components for temperature measurements involve transducers (thermocouples and hygrometer), and extension wires. Fixing the psychrometric state of air requires three independent properties. In addition to the prevailing atmospheric pressure, two other air properties are required to fix the state. Three types of temperature measurements are

performed to determine these two additional properties to fix the psychrometric state of the air; dry-bulb temperatures, wet-bulb temperatures, and dew point temperatures. All temperature measurements (dry-bulb and wet-bulb) are carried out using copper-constantan thermocouples [4], ANSI symbol T (American National Standards Institute). Shielded extension cables, thermocouple grade [4], are used to connect the thermocouples to a multiplexer. Compared to other thermocouples, copper-constantan have the best uncertainty characteristics, as shown in Table 3-3. The copper-constantan thermocouple with a blue positive copper wire and a red negative copper-nickel wire has the following advantages:

i. Accuracy of ±1ºC
ii. Good performance for measuring temperatures in humid atmospheres
iii. Relatively inexpensive

Table 3-3 Comparison between different thermocouple types

Thermocouple type	**ANSI symbol**	**Limits of uncertainty**	**emf at 100°C [mV]**
Iron vs. Copper-Nickel	J	±2.2°C	5.268
Nickel-Chromium vs. Nickel-Aluminum	K	±2.2°C	4.095
Nickel-Chromium vs. Copper-Nickel	E	±1.7°C	6.317
Copper vs. Copper-Nickel	T	±1.0°C	4.277
Platinum-13%Rhodium vs. Platinum	R	±1.5°C	0.647

3.3.1.1 Dry-bulb measurements

Two sets of thermocouples are used to measure the dry-bulb temperature at the inlet and exit zones. Each set has eighteen copper-constantan thermocouples connected in parallel (a thermopile arrangement). The eighteen thermocouples, are divided into six groups, sixty degrees apart, as shown in Figure 3-3.

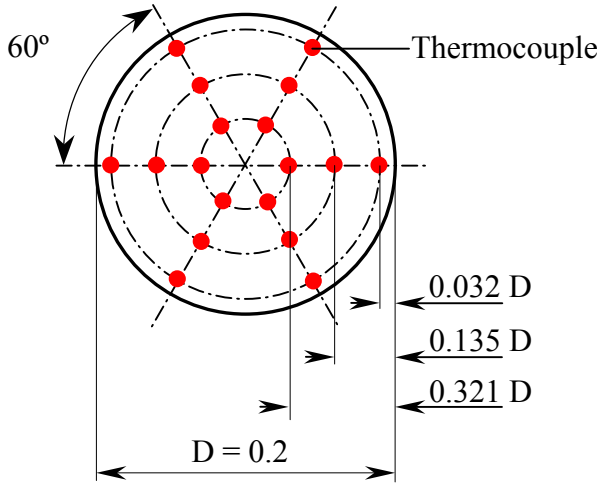

Figure 3-3 Arrangement of thermocouples for dry-bulb measurements, [1]

The test section, as shown in Figure 3-2, is designed to accommodate the demands of the ANSI/ASHRAE Standard 111-1988 which requires the following conditions for measuring the dry-bulb temperature:

i. Regular duct cross section

ii. Straight duct 5 (10 preferred) diameters upstream

iii. Straight duct 1 (3 preferred) diameters downstream

iv. Traverse plane should be perpendicular to air flow

v. Uniform velocity throughout plane

Velocity measurements are conducted using hot wire anemometer at inlet and exit sides of the spray chamber, to check for the uniformity of the velocity profiles. These measurements are conducted at six radial locations (A, B, C, D, E, F) at different radii, as shown in Figure 3-4. The figure presents the normalized velocity measurements that are performed on the

exit side of the spray chamber. This figure shows that the deviation from the uniform flow assumptions is generally within 8-10%.

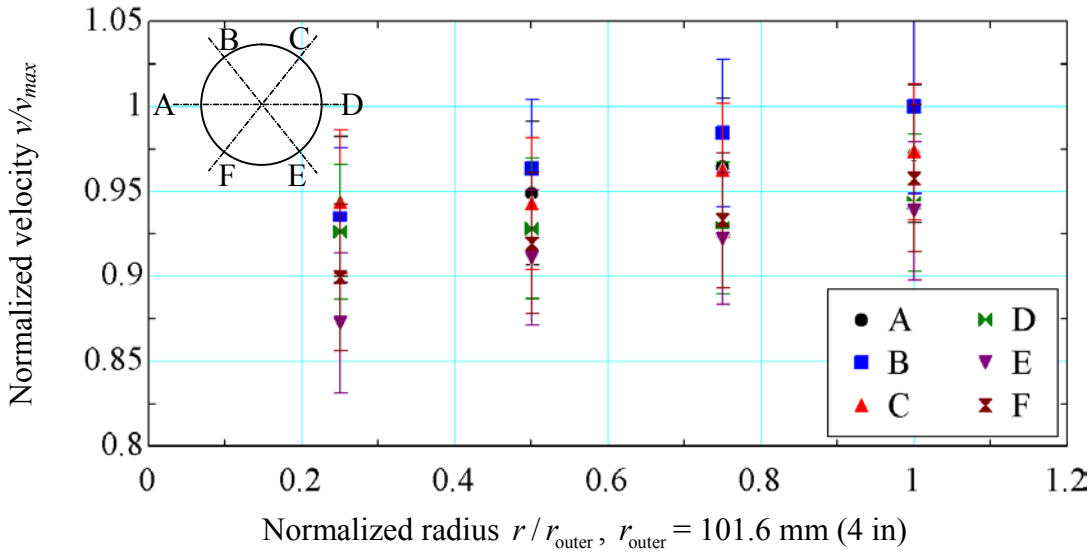

Figure 3-4 Normalized velocity measurements in the spray chamber

3.3.1.2 Wet-bulb temperature measurement

The wet-bulb thermocouple is covered with a wick, as shown in Figure 3-5, to retain a film of water on the thermocouple, thus ensuring that the true wet-bulb temperature is reached. Cotton is used as the wick material due to its excellent water-absorbent property [3]. The wick covers more than 25 mm of the thermocouple wire, measured from the thermocouple bead, to minimize bias of temperature measurements by reducing "stem losses" i.e. conduction of heat away from the junction [3]. Distilled water, supplied at a temperature close to the true wet-bulb temperature, is used for moisturizing the cotton wick. Distilled water is used since the presence of contaminants or dissolved salts in the wick water will change the saturation vapor pressure leading to erroneous wet-bulb readings [3].

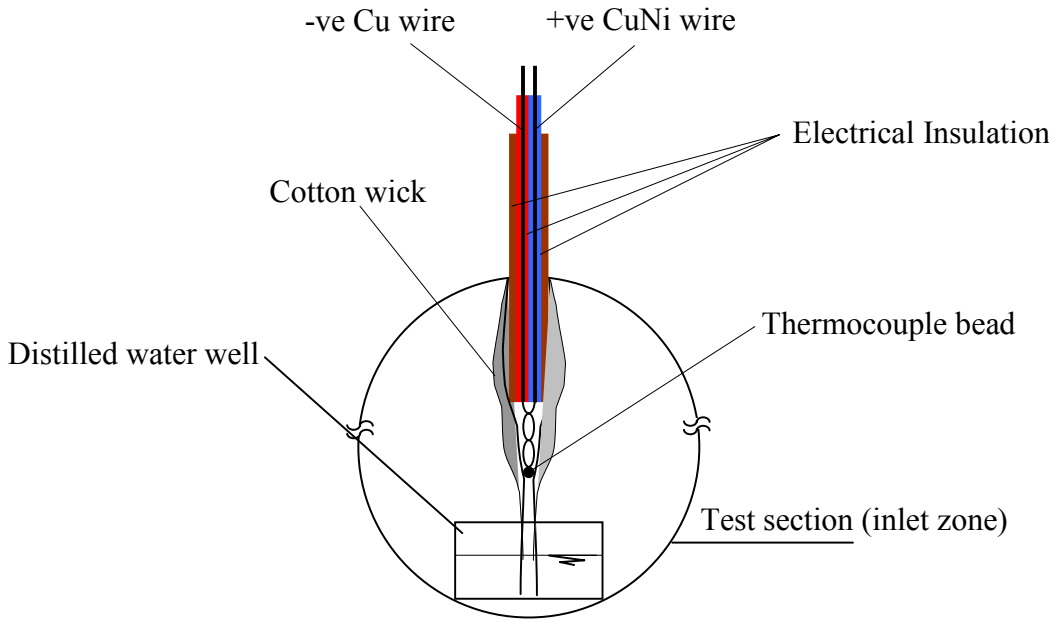

Figure 3-5 Wet-bulb temperature measurement

3.3.1.3 Dew-point temperature measurement

The dew-point temperature is measured at the test section inlet zone using a dew-point hygrometer [5]. This is a general-purpose optical condensation dew-point hygrometer that provides a measurement range of –75ºC to 95ºC with an accuracy of 0.2 ºC. The dew-point temperature is measured by detecting the condensation on a chilled mirror, which is cooled by a thermoelectric cooler. The mirror temperature is measured with a platinum resistance thermometer.

Figure 3-6 shows a schematic for the dew point hygrometer that illustrates its principle of operation. The condensate detection mirror is illuminated with a high intensity, solid state, light emitting diode, LED. A photo-detector monitors the light reflected from the mirror. A separate LED and photo-detector are used to compensate for any thermally induced changes in the optical components. The photo-detectors are arranged in an electrical bridge circuit so

that the specular detector is fully illuminated when the mirror is clear of dew. An optical offset is designed into the bridge, causing a large bridge output whenever the mirror is dry. The bridge output is amplified and used to drive the thermoelectric cooler current, causing the mirror to cool towards the dew point.

Condensation on the mirror decreases the light received by the photo-detector. As a result, the bridge is driven from its set point leading to a decrease in the bridge output. This decrease in bridge output decreases the cooling of the thermoelectric cooler. A rate feedback loop within the amplifier ensures critical response, and the system stabilizes at a condition where a thin dew or frost layer is maintained on the mirror surface. The dew point hygrometer is calibrated against dew point standards that are traceable to the National Institute of Standards and Technology, NIST [5].

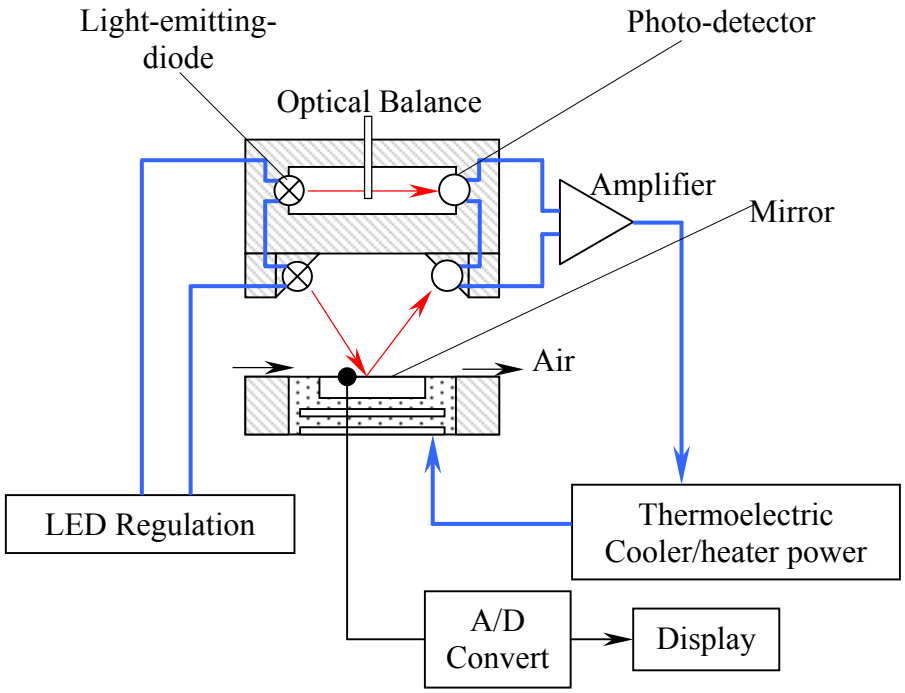

Figure 3-6 Dew point detection in optical condensation hygrometer [5]

3.3.1.4 Flow measurements

Two flow measurements are performed, airflow measurement and water flow measurement. The average velocity of air is determined by measuring air velocity in ft/min using a rotating vane anemometer [6] and time with a stop watch. The vane anemometer has a resolution of 5 ft. The volume flow rate can then be calculated knowing the cross-sectional area of the duct section with an accuracy of ±1 cfm. The volume flow rate of water is measured in gpm using a turbine flow meter, model FTB-4000 [4], with an accuracy of ±1.5-2% of the reading. The turbine flow meter is connected to one of the control I/O ports of the data logger, C1-C8, as shown in Figure 3-7. The meter produces a square wave signal; the pulses of this signal are converted by the data logger to the corresponding flow rate in gpm.

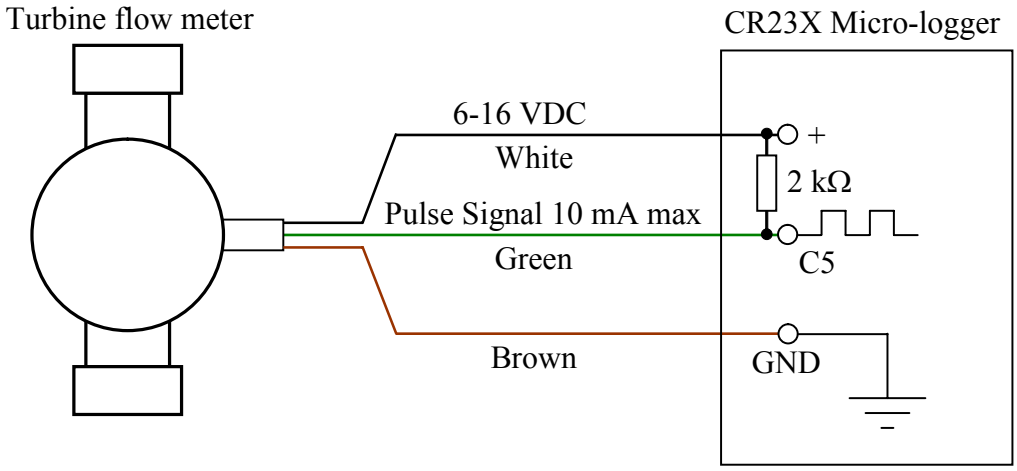

Figure 3-7 Schematic showing the wiring of the turbine flow meter to the data logger

3.3.1.5 Pressure measurements

Two pressure measurements are performed, air-side pressure drop measurement and water injection pressure measurement. The air-side pressure drop across the test section is measured in kPa by a digital micro-manometer; model DG-2 [7]. The manometer has two

ranges, -199.9 to +199.9 Pa with a resolution of 0.1 Pa, and -1999 to +1999 Pa with a resolution of 1 Pa. The spray nozzle injection pressure is measured in psig by a pressure transducer model; PX 304-050A V [4] with an accuracy of ±0.5% of the reading. The transducer is connected to one of the analog inputs of the data logger, 1-12, as shown in Figure 3-8.

3.3.1.6 Data acquisition system

The data acquisition system consists of a solid state multiplexer, a data-logger and a computer. The solid state multiplexer, model AM25T, is connected to the CR23X micro-logger [8]. The data logger is connected via an RS-232 port to a serial port of the computer. The computer is used for programming the data logger, data retrieval, and storage. The data-logger is supplied with a 12 VDC current. It has several analog input ports that can accept single ended measurements as well as differential measurements. It also has several analog output ports and digital I/O ports. The data-logger has also regulated power outputs with 5 and 12 VDC.

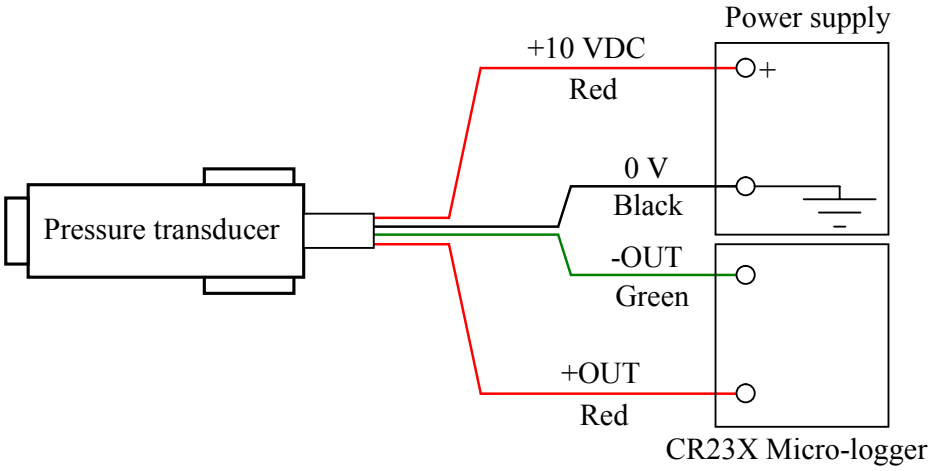

Figure 3-8 Schematic showing the wiring of the pressure transducer to the data logger

The data logger is programmed, using software PC208W provided by Campbell Scientific [8], to measure the water volume flow rate, injection pressure, and the air-side dry-bulb and wet-bulb temperatures. The data logger is also used to calculate the effectiveness of the spray cooler. The data-logger program is divided into three tables (sections). The whole program is written in one table (table 1). Additional information and programs can be stored in Table 2 and 3 if needed. The program is divided into 25 modules, each consisting of one procedure, and the program is executed every one second. The first four modules instruct the data-logger to collect data from all peripherals. The modules that follow instruct the data-logger where to store the data and how to post process them, if needed. In module 1 a reference voltage for the thermocouples is received from an internal thermistor built into the data-logger to provide a reference temperature. The voltage drops across the thermocouples are measured in module 2. All thermocouple readings have a range of 10 mV and a 60 Hz rejection to suppress noise from the power supply. In module 3, the voltage difference across the pressure transducer is measured with a range of a 200 mV and a 60 Hz rejection. Finally, the output from the turbine flow meter is measured in module 4. In modules, 5-11, the data are averaged over a time period of 1 minute and stored. Modules 12-19 are used to calculate the effectiveness of the spray cooler. The remaining modules, 20-25, are used to calculate the flow rate from the given injection pressure based on the manufacturer's data and compare the output to the experimental measurement. The complete code is listed in Appendix-II.

3.4 Calibration and Confirmation

Calibration is simply the comparison of an instrument performance to a standard of dependably known and unvarying accuracy. It may simply involve this determination of deviation from nominal or include correction (adjustment) to minimize the errors. Calibrated equipment provides confidence in the presented results. Calibration also assures consistency and that measurements are compatible with those made elsewhere. This section presents the methods used to calibrate the thermocouples and the pressure transducer, and the results of this calibration process.

3.4.1 Thermocouple calibration

The calibration process of the thermocouples is performed twice. First, it is performed before installing the thermocouples in the test rig. The calibration during this stage begins by placing all thermocouples in an agitated constant temperature water bath [9]. The data logger reading is compared to a reference temperature measurement device–mercury in glass thermometer [10] with 0.1ºC divisions. The calibration equations are summarized in Table 3-4. Three points are used for comparison, ice point, boiling point, and room temperature, as shown in Figure 3-9. A second calibration is conducted after installing the thermocouples in the test section, before each experiment. In this process, the read out of the thermopiles is compared to the same thermometer used in the previous calibration to compensate for any drifts in the output.

Table 3-4 Temperature calibration equation

$T_{\text{actual}} = a_o + a_1 T_{\text{measured}}$		
Location	a_o	a_1
Dry-bulb test section inlet	-0.0089388	*1.0088*
Dry-bulb test section exit	-0.31032	*1.0225*
Wet-bulb test section exit	0.051444	*1.0050*
Water inlet temperature	0.06888	*1.1014*
Water exit temperature	-0.1717	1.0150

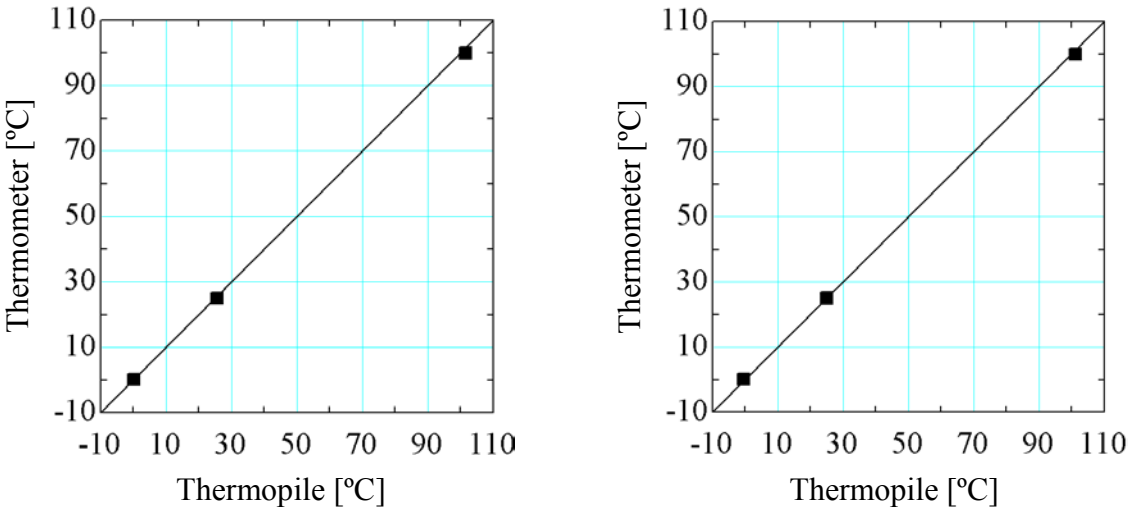

Figure 3-9 Results of thermocouples calibration

3.4.2 Pressure transducer

A dead weight pressure tester is used to calibrate the pressure transducer. A weight supplies a known force on a piston with a known diameter. Weights are added, the known pressure and the corresponding voltage drop, in mV, across the transducer are recorded. The calibration procedure is done in an ascending and descending order. Finally, a calibration curve is constructed, as shown in Figure 3-10, and the coefficients are plugged into the data-

logger program. The pressure transducer and the piston are maintained at the same level to avoid additional static pressure due to height difference and the weight of the transmitter fluid.

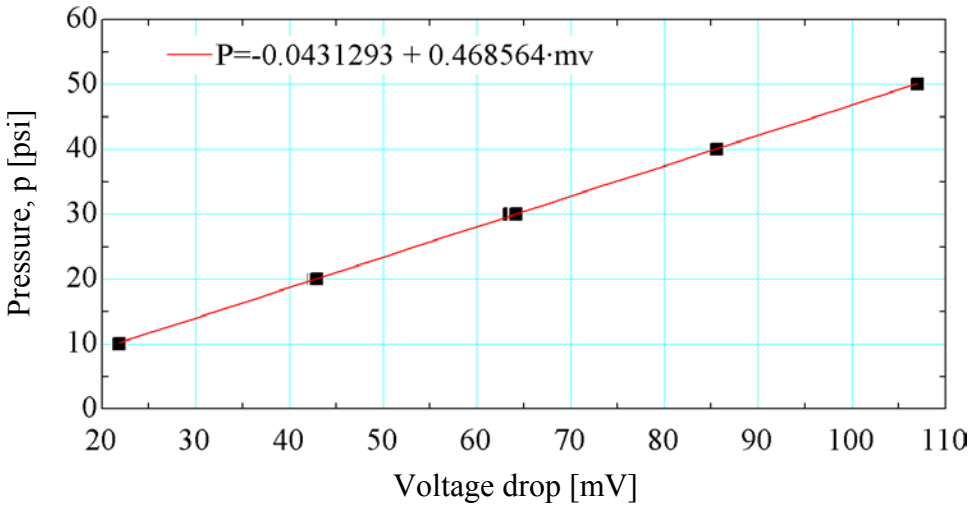

Figure 3-10 Results of pressure transducer calibration

3.5 Experimental Methods and Procedure

The experiment starts by turning on the measuring and controlling equipment an hour prior each experiment for the measuring instruments to warm up. After the warm up period the following chronological procedure is followed for each experimental run:

1. The injection pump is turned on to inject water from the containers to the nozzle. Water temperature, pressure and flow rate at nozzle inlet are measured and recorded.
2. Valves V1 and V2 are adjusted and tuned to achieve a specific water flow rate and injection pressure.
3. Continuous logging of air and water-side temperatures is performed to check for quasi-steady state.

4. Data are collected and stored via the data-logger.
5. To cover a range of water volume flow rates steps 2 to 4 are repeated.
6. Stored data are then transferred from the data-logger to the computer, for post processing.

3.6 Results and Discussion

The results of the experimental investigation conducted to evaluate the performance of the spray cooler and study its ability to effectively cool and dehumidify the air are presented in this section. The measured variables are volume flow rate of water in gpm, air exit velocity in ft/min, air inlet temperature in ºC (dry bulb and dew point), air outlet temperature (dry bulb and wet bulb) in ºC, water inlet and exit temperatures in ºC, water inlet pressure in psig and test section pressure drop in Pa. The temperature measurements and flow rate measurements are used to calculate the enthalpy and mass flow rates for each stream, and consequently the rate of energy transfer and the effectiveness of the spray cooler are calculated. Energy balances are examined to check if the First Law of thermodynamics is satisfied. Also, the effect of the uncertainties in air and water measurements on the rate of energy transferred from the air-side to the water-side and the effectiveness of the spray cooler are analyzed.

Two sets of experiments are performed. In the first set of experiments the spray cooler is working as an evaporative cooler. The main objective these experiments is to evaluate the performance of the spray cooler at different water mass flow rates. The objective of the second set is to study the ability of the spray cooler to effectively cool and dehumidify the

air. In all the experiments the air velocity inside the spray chamber is maintained below 2.54 m/s (500 ft/min) to prevent carry-over of water droplets [11]. All measurements are taken under quasi-steady state conditions.

3.6.1 Mass flow rate calculations

The measurements of the volume flow rate of water and air allow the calculation of the mass flow rate for both streams as follows:

$$\dot{m}_{\text{water}} = \left(\left(\dot{V}_{\text{water}} \Big|_{\text{in}} \right) 0.000063 \frac{m^3/s}{gpm} \right) \rho_{\text{water}} \tag{3.1}$$

where $\dot{m}_{\text{water}}$ is the water mass flow rate in kg/s, $\dot{V}_{\text{water}}\Big|_{\text{in}}$ is the water volume flow rate in gpm and ρ_{water} is the density of water in kg/m^3 evaluated using the injection pressure and water inlet temperature. For the air-side, the mass flow rate is calculated as follows:

$$\dot{m}_{\text{air}} = \left(\left(\dot{V}_{\text{air}} \Big|_{\text{out}} \right) 0.00047 \frac{m^3/s}{cfm} \right) \rho_{\text{air}} \Big|_{\text{out}} \tag{3.2}$$

where $\dot{m}_{\text{air}}$ is the air mass flow rate in kg/s and $\rho_{\text{air}}\Big|_{\text{out}}$ is the density of moist air in kg/m^3 evaluated using the dry-bulb and wet-bulb temperatures at the air-side exit and assuming a pressure of 101.325 kPa. $\dot{V}_{\text{air}}\Big|_{\text{out}} = Au$ is the air volume flow rate in cfm, where u is the cross sectional average velocity of air at exit in fpm and A is the cross sectional area of the exit zone of the test section which is also equal to the vane anemometer cross sectional area. The amount of condensate is calculated as follows:

$$\dot{m}_{\text{cond}} = \dot{m}_{\text{air}} \left(\omega_{\text{in}} - \omega_{\text{out}} \right) \tag{3.3}$$

where $\dot{m}_{\text{cond}}$ is the rate of condensation or evaporation in kg/s, and ω_{in} and ω_{out} are the humidity ratios at inlet and exit, respectively.

3.6.2 Enthalpy Calculations

The enthalpies of the air-side and the water-side are calculated from the temperature measurements and mass flow rates as follows:

$$\dot{H}_{\text{air}}\Big|_{\text{in}} = \dot{m}_{\text{air}}\, h_{\text{air}}\Big|_{\text{in}} \tag{3.4}$$

$$\dot{H}_{\text{air}}\Big|_{\text{out}} = \dot{m}_{\text{air}}\, h_{\text{air}}\Big|_{\text{out}} \tag{3.5}$$

$$\dot{H}_{\text{water}}\Big|_{\text{in}} = \dot{m}_{\text{water}}\, h_{\text{water}}\Big|_{\text{in}} \tag{3.6}$$

$$\dot{H}_{\text{water}}\Big|_{\text{out}} = \left(\dot{m}_{\text{water}} + \dot{m}_{\text{cond}} \right) h_{\text{water}}\Big|_{\text{out}} \tag{3.7}$$

$$\dot{H}_{\text{cond}} = \dot{m}_{\text{cond}} h_{\text{cond}} \tag{3.8}$$

where $\dot{H}_{\text{air}}\Big|_{\text{in}}$ and $\dot{H}_{\text{air}}\Big|_{\text{out}}$ represents the enthalpy, in kJ/s, of moist air at the inlet and exit sections, respectively. $\dot{H}_{\text{water}}\Big|_{\text{in}}$ and $\dot{H}_{\text{water}}\Big|_{\text{out}}$ are the enthalpies, in kJ/s, of water at inlet and exit , respectively. $\dot{H}_{\text{cond}}$ is the enthalpy of the condensed water, in kJ/s, evaluated at the air exit dry-bulb temperature and atmospheric pressure. Two other enthalpies for the air-side are needed to calculate the sensible and latent heat loads, and the effectiveness. These enthalpies are calculated as follows.

$$\dot{H}_{\text{air}}\Big|_{\text{x}} = \dot{m}_{\text{air}}\, h_{\text{air}}\Big|_{\text{x}} \tag{3.9}$$

$$\dot{H}_{\text{air}}\Big|_{\text{min}} = \dot{m}_{\text{air}}\, h_{\text{air}}\Big|_{\text{min}} \tag{3.10}$$

$\dot{H}_{\text{air}}\Big|_{\text{x}}$ is the enthalpy of moist air in kJ/s at the air exit dry-bulb temperature and humidity ratio evaluated at the inlet conditions. $\dot{H}_{\text{air}}\Big|_{\text{min}}$ is the enthalpy of moist air in kJ/s at the water inlet temperature and 100% relative humidity.

3.6.3 Effectiveness Calculations

At this stage the enthalpies for both streams at inlet and exit are known. Consequently, the thermal performance of the spray chamber, presented as sensible heat ratio, SHR, and the sensible, $\varepsilon_{\text{sensible}}$, effectiveness, can be evaluated

$$\text{SHR} = \frac{\dot{Q}_{\text{sensible}}}{\dot{Q}_{\text{air}}} = \frac{\dot{H}_{\text{air}}\Big|_{\text{in}} - \dot{H}_{\text{air}}\Big|_{\text{x}}}{\dot{H}_{\text{air}}\Big|_{\text{in}} - \dot{H}_{\text{air}}\Big|_{\text{out}}} \tag{3.11}$$

$$\varepsilon_{\text{sensible}} = \frac{\dot{Q}_{\text{sensible}}}{\dot{Q}_{\text{sensible}}\Big|_{\text{max}}} = \frac{\dot{H}_{\text{air}}\Big|_{\text{in}} - \dot{H}_{\text{air}}\Big|_{\text{x}}}{\text{C}_{\text{min}}\left(T_{\text{air}}\Big|_{\text{in}} - T_{\text{water}}\Big|_{\text{in}}\right)} \tag{3.12}$$

where $\dot{Q}_{\text{sensible}}$ is the sensible load in kW, and $\dot{Q}_{\text{air}}$ is the rate of energy transferred from the air-side in kW. $\dot{Q}_{\text{sensible}}\Big|_{\text{max}}$ is the maximum possible sensible load in kW, and C_{min} is the minimum thermal capacitance rate in kW/ºC.

3.6.4 Performance Evaluation Experiment

This section presents the results of the experimental investigation conducted to evaluate the performance of the spray cooler. Table 3-5 summarizes the inlet and exit conditions of both

streams, air and water. The table also gives the results of these experiments. The inlet and exit states of the air-side are shown on the psychrometric chart, Figure 3-11. In this experiment the effect of changing the mass flow rate of water on the spray cooler pressure drop and effectiveness is investigated. The volume flow rate of water is varied over the range 0.08-0.17 liters/s (1.3-2.7 gpm). The average sensible heat ratio for the four runs is $SHR=0.53\pm0.02$. Figure 3-12 depicts the variation of water temperature and air enthalpy with time throughout the experiment. The figure also shows the time and duration over which the averaging process takes place. The peaks in water temperatures after each run, at t= 166, 352 and 533 min, are due to the experimental adjustments conducted to prepare for the following run.

Table 3-5 Summary of the performance evaluation experiment

		Run 1	**Run 2**	**Run 3**	**Run 4**
Air-Side	Inlet Dry-bulb [ºC]	27.34±0.05	27.36±0.05	26.35±0.05	24.79±0.05
	Inlet Dew-point [ºC]	9.1±0.2	9.1±0.2	8.5±0.2	8.9±0.2
	Exit Dry-bulb [ºC]	22.32±0.05	18.28±0.05	16.02±0.05	15.03±0.05
	Exit Wet-bulb [ºC]	16.39±0.05	16.0±0.05	15.38±0.05	14.6±0.05
	Volume flow rate [cfm]	181.2	152.3	123.2	107.1±1
	Rate of energy transfer [W]	14.54±28.6	107.6±24.4	85.55±19.3	136.4±17.1
Water Side	Inlet Temperatures [ºC]	14.83±0.05	14.57±0.05	14.7±0.05	14.07±0.05
	Exit Temperatures [ºC]	14.83±0.05	14.72±0.05	14.84±0.05	14.29±0.05
	Volume flow rate [gpm]	1.301	1.844	2.423	2.746±2%
	Rate of energy transfer [W]	7.03±24.2	77.01±34.4	90.67±45.2	159.8±51.2
Sensible Heat Ratio		0.50	0.53	0.52	0.56
Effectiveness		0.40	0.71	0.89	0.91

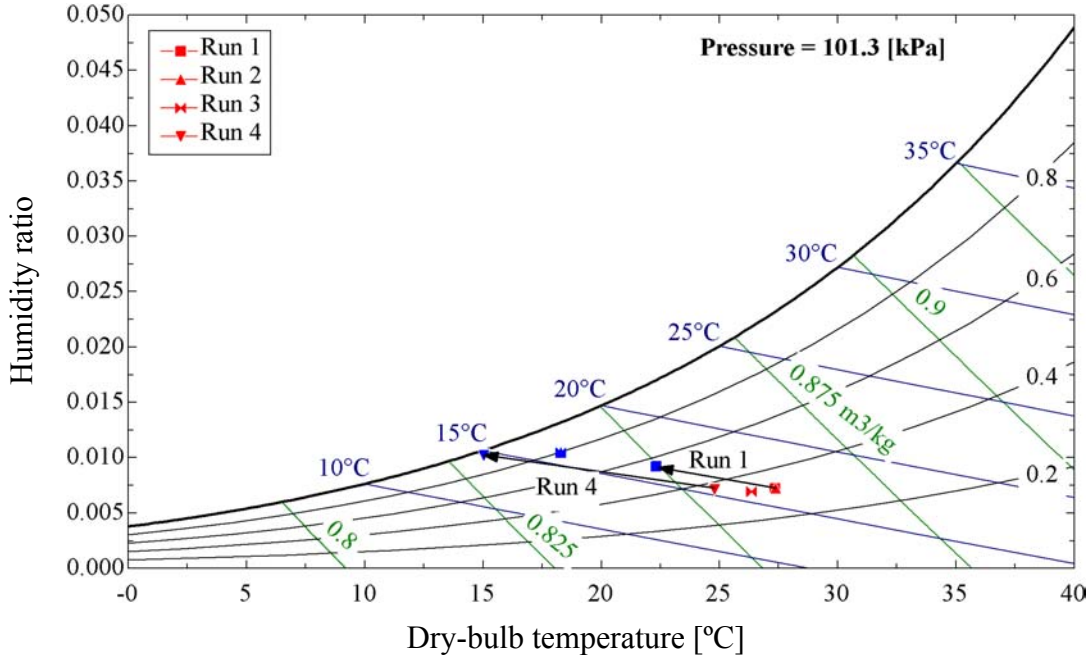

Figure 3-11 Air-side psychrometrics

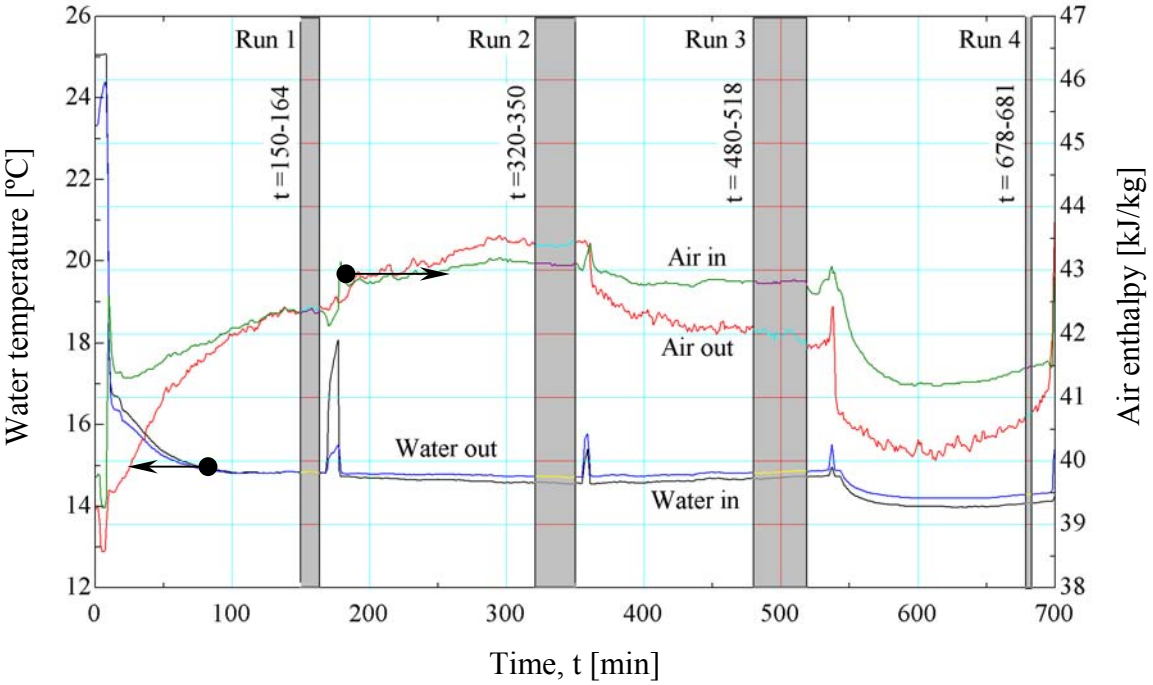

Figure 3-12 Temporal variation in water-side temperature and air-side enthalpy

Figure 3-13 illustrates the effect of changing the water discharge rate on the air-side pressure drop through the spray zone. This figure shows that increasing the water flow rate increases the air-side pressure drop. This increase in pressure drop results in a decrease in air flow rate, as shown in Figure 3-14.

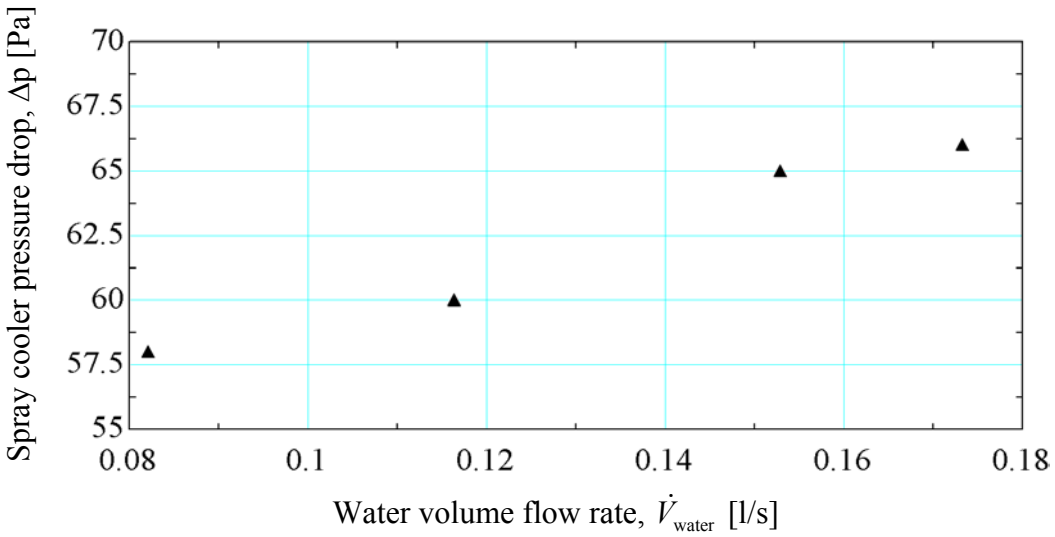

Figure 3-13 Effect of water volume flow rate on the spray cooler pressure drop

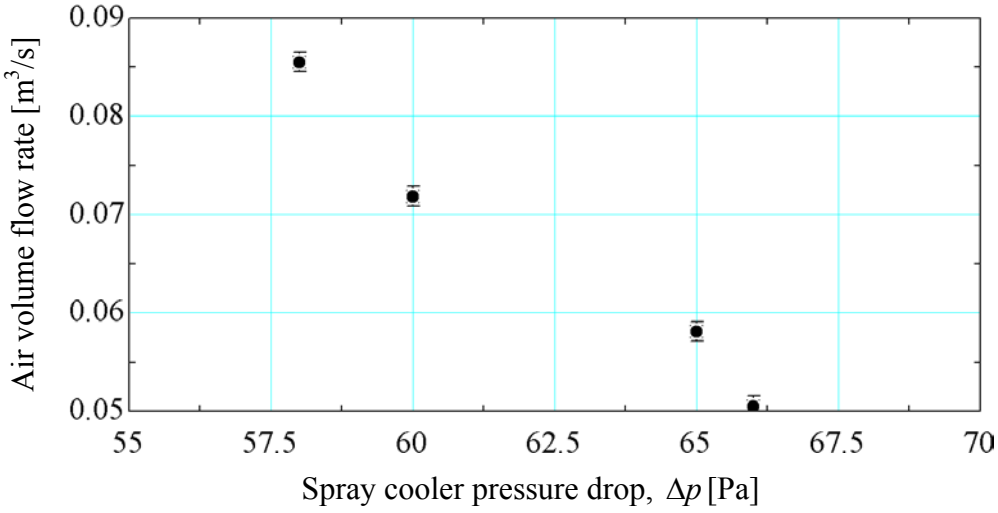

Figure 3-14 Effect of spray cooler pressure drop on the air volume flow rate

Figure 3-15 shows the effect of increasing the water flow rate on the spray cooler effectiveness and $h_{air}|_x$. As the water flow rate increases the effectiveness of the spray cooler increases, while $h_{air}|_x$ decreases. Referring to equation (3.12), the effectiveness increase is due to the reduction in $h_{air}|_x$ which increases $\dot{Q}_{sensible}$. Increasing the mass flow rate of water also increases the rate of energy transfer between the air-side and water side. Consequently, the dry-bulb temperature of air at exit decreases. Accordingly, the enthalpy $h_{air}|_x$ decreases.

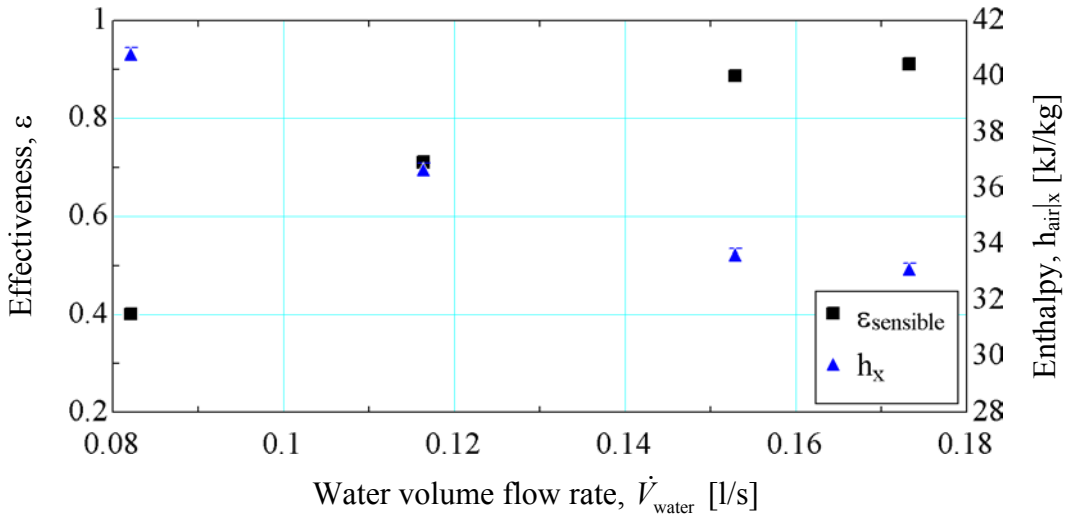

Figure 3-15 Effect of water volume flow rate on the spray cooler effectiveness

3.6.4.1 Uncertainty

The spray cooler is insulated and consequently, assumed to be adiabatic. Accordingly, the air and water streams exchange energy with one another at steady state as follows

$$\dot{Q}_{air} = \dot{Q}_{water} \tag{3.13}$$

$$\left(\dot{H}_{air}|_{in} - \dot{H}_{air}|_{out}\right) - \dot{H}_{cond} = \left(\dot{H}_{water}|_{out} - \dot{H}_{water}|_{in}\right) - \dot{H}_{cond} \tag{3.14}$$

For each experimental run the energy balance, equation (3.13), is checked. Moreover, the effect of the uncertainty in temperature and mass flow rate measurements on $\dot{Q}_{\text{air}}$ and $\dot{Q}_{\text{water}}$ is investigated, to make sure that both quantities match within the uncertainties in the temperature measurements. Figure 3-16 to Figure 3-18 show the effect of the uncertainty in the different temperature measurements on the rate of energy transfer for both the air and water sides. Figure 3-16-a and Figure 3-17-a show that rate of energy transfer from the air side is almost insensitive to the uncertainty in the measured dry-bulb temperature at inlet and exit, respectively. However, as shown in Figure 3-16-b and Figure 3-17-b, the uncertainty in the measured dew-point temperature at inlet and wet-bulb temperature at exit, respectively, greatly affects the calculation of the rate of energy transfer for the air-side. On the other hand, Figure 3-18 shows that uncertainty in the measured water temperatures at inlet and exit has a minor effect on the uncertainty in calculating the rate of energy transfer for the water-side. Finally, Figure 3-19 shows that the uncertainty in the measured flow rates has a minor effect on the uncertainty in calculating the rate of energy transfer. Despite the fact that the uncertainty in each measured variables has a minor effect on the energy balance, the cumulative effect of the uncertainty in all measured variables greatly affects the energy balance, as shown in Figure 3-20. Figure 3-20 shows that both quantities, rate of energy transfer for the air-side and water-side, match when the uncertainties in all of the measured variables are considered.

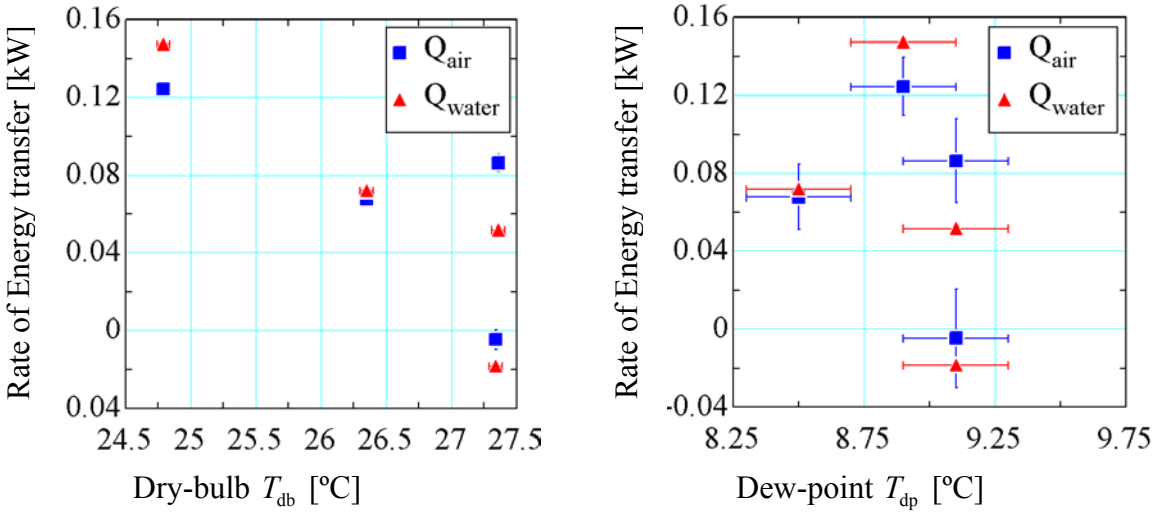

a- Inlet dry-bulb temperature b- Inlet dew-point temperature

Figure 3-16 Effect of uncertainty in air-side inlet temperature on the rate of energy transfer for the air-side and water-side

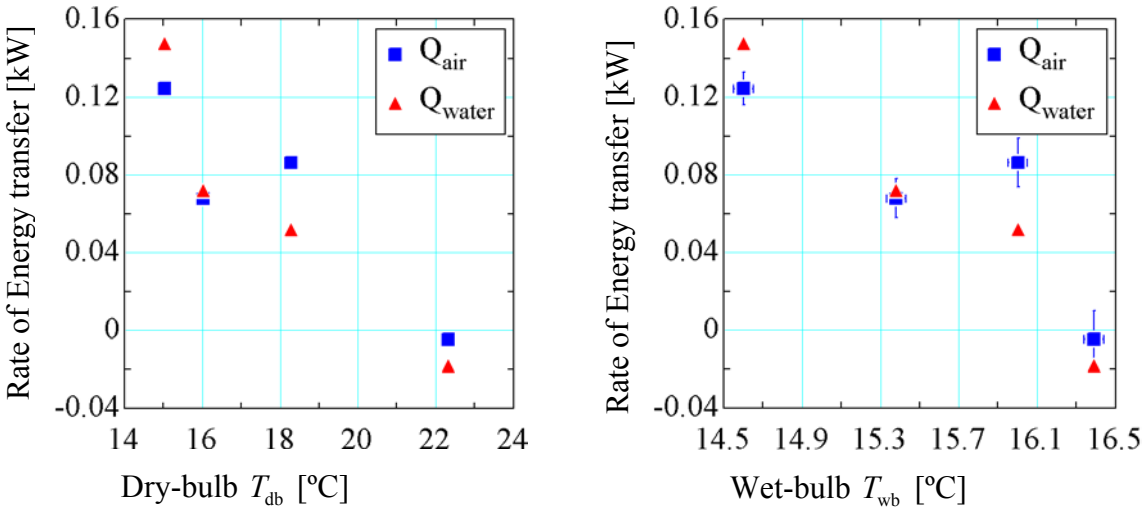

a- Exit dry-bulb temperature b- Exit wet-bulb temperature

Figure 3-17 Effect of uncertainty in air-side exit temperature on the rate of energy transfer for the air-side and water-side

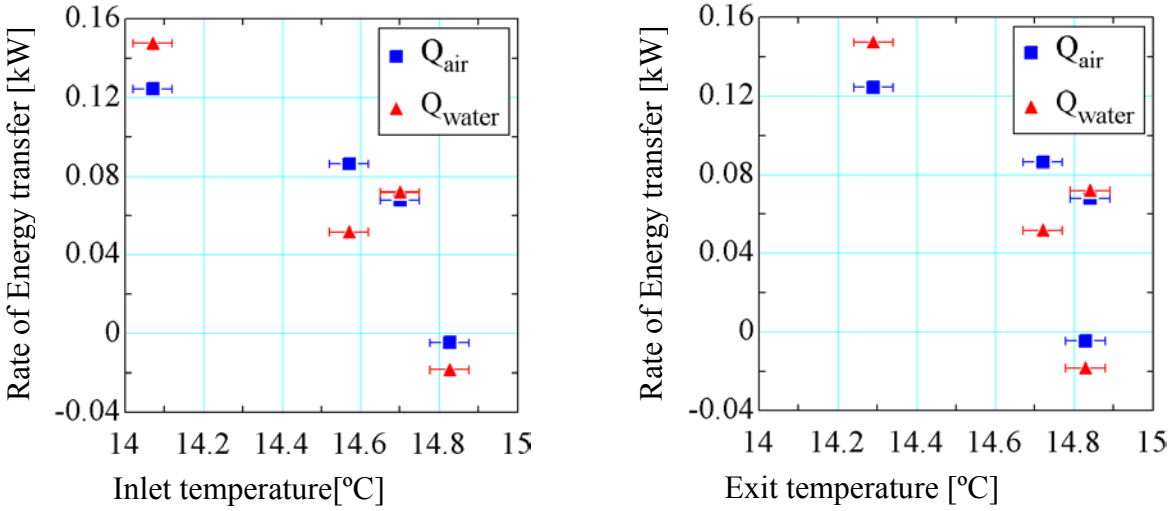

a- Inlet water temperature

b- Exit water temperature

Figure 3-18 Effect of uncertainty in water-side exit temperature on the rate of energy transfer for the air-side and water-side

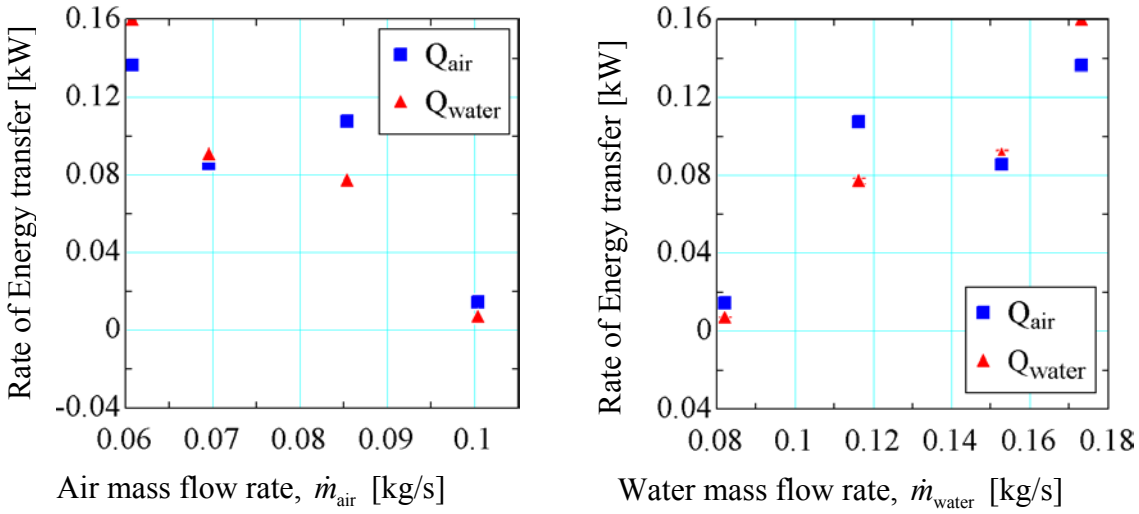

a- Air mass flow rate

b- Water mass flow rate

Figure 3-19 Effect of uncertainty in air and water-side mass flow rates on the rate of energy transfer for the air-side and water-side

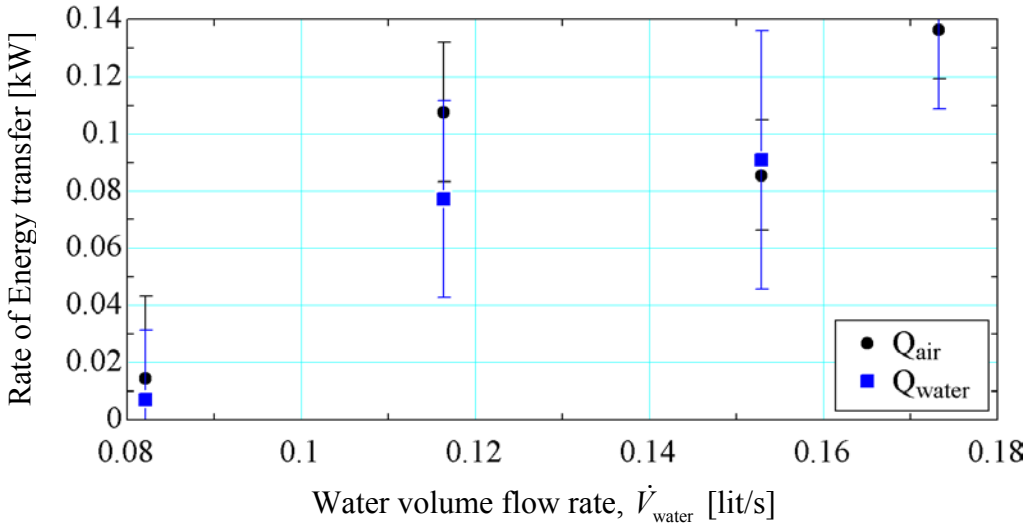

Figure 3-20 Effect of total uncertainties in temperature measurements on the rate of energy transfer at different water flow rates

3.6.5 Cooling and Dehumidification Experiment

This section presents the results of the experimental investigation conducted to study the spray cooler ability for effective cooling and dehumidification. Table 3-6 summarizes the inlet and exit conditions for both streams, air and water. The table also gives the results of this experiment. The inlet and exit states of the air-side are shown on the psycrhometric chart, Figure 3-21. Figure 3-22 depicts the variation of water temperature and air enthalpy with time throughout the experiment. The figure also shows the time and duration over which the averaging process takes place. The results show that the latent load comprises only 7.5% of the total load. Hence, the spray cooler can be considered as a principally sensible cooler under this operating condition. If the latent load were to be neglected the effectiveness of the spray chamber will be 0.44 (10% higher) and the exit dry-bulb temperature would be 17.27 ºC (1.29 ºC lower).

Table 3-6 Summary of the cooling and dehumidification experiment

Air-Side	Inlet Dry-bulb [ºC]	30.52±0.05
	Inlet Dew-point [ºC]	17±0.2
	Exit Dry-bulb [ºC]	18.56±0.05
	Exit Wet-point [ºC]	17.21±0.05
	Volume flow rate [cfm]	193.1
	Rate of energy transfer [kW]	1.419±0.05
Water Side	Inlet Temperatures [ºC]	0.58±0.05
	Exit Temperatures [ºC]	3.37±0.05
	Volume flow rate [gpm]	1.96
	Rate of energy transfer [kW]	1.46±0.04
Sensible Heat Ratio		0.92
Effectiveness		0.4

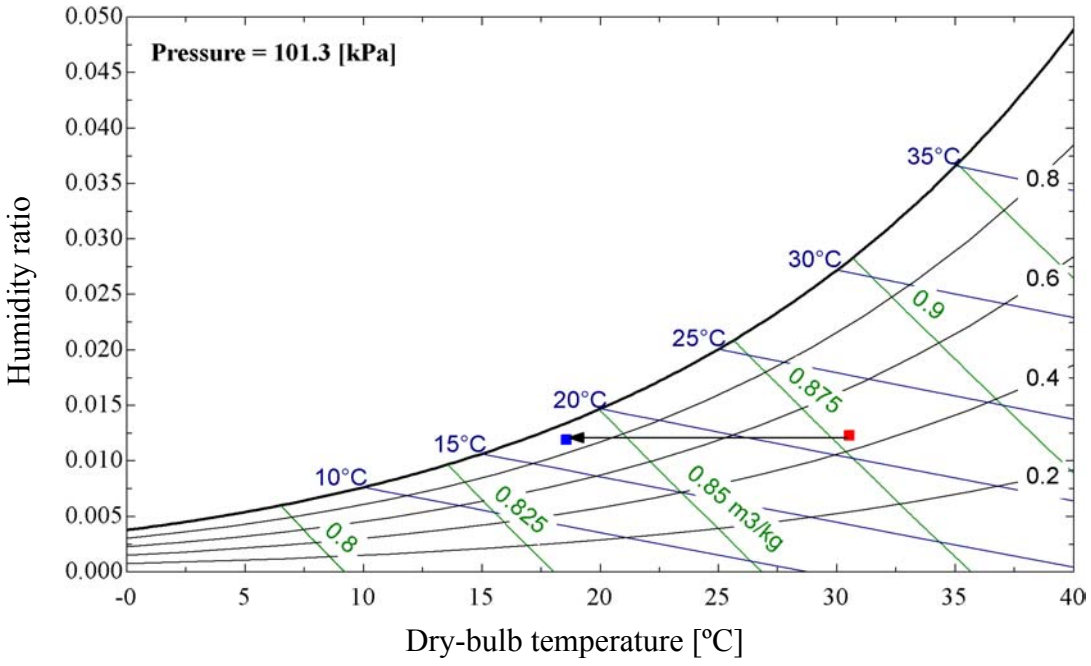

Figure 3-21 Air-side psychrometrics

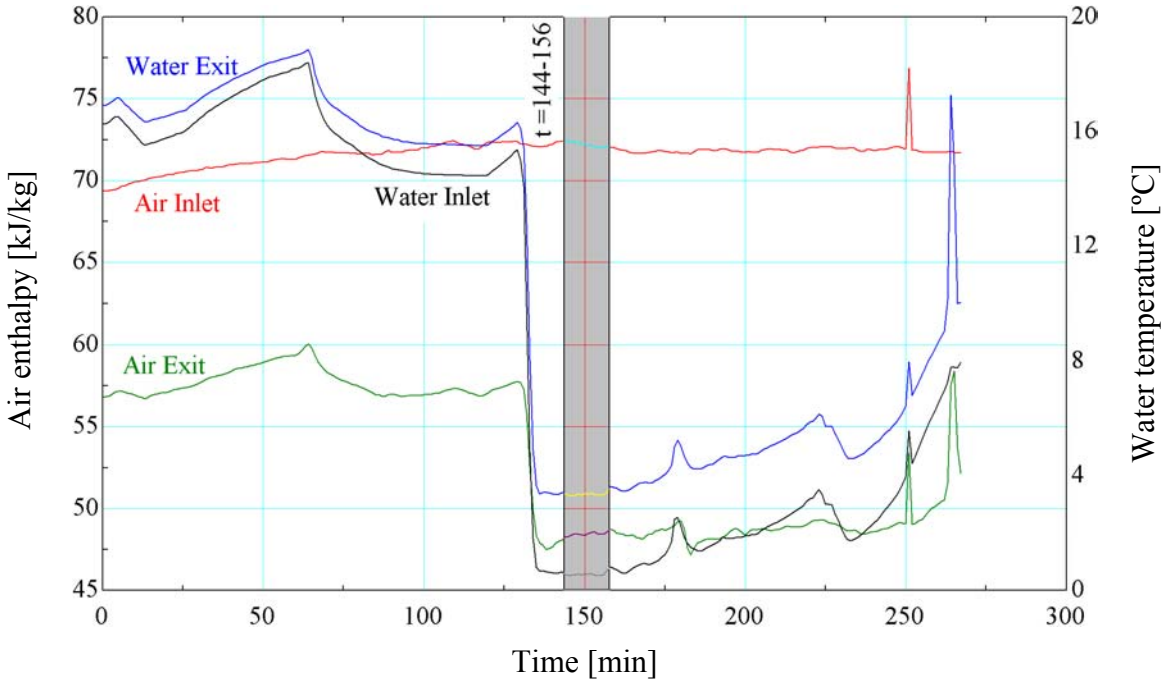

Figure 3-22 Temporal variation in water-side temperature and air-side enthalpy

3.7 Summary

This chapter introduces the experimental investigation conducted to study the heat and mass transfer characteristics of a water spray cooler. The purpose of these experiments is to evaluate the performance of the spray cooler and study its ability to effectively cool and dehumidify air at different ambient conditions. The chapter starts by giving a detailed description of the test rig used and the methods adopted to calibrate the instrumentation. This is then followed by an illustration of the procedures followed in the experiments. Finally, the results of the experiments are presented. The measured variables are volume flow rate of water, air exit velocity, air inlet temperatures, air outlet temperature, water inlet and exit temperatures, water inlet pressure and test section pressure drop. The temperature measurements and flow rate measurements are used to calculate the heat transfer rate and

hence the effectiveness. The results show that increasing the water flow rate increases the air-side pressure drop and the effectiveness of the spray cooler. The results of the cooling and dehumidification experiment show that the latent load comprises only 7.5% of the total load for the experimental conditions investigated. Hence, the cooler can considered as a sensible cooler for the given operating condition. If the latent load were to be neglected the effectiveness of the spray chamber will be 10% higher and the exit dry-bulb temperature would be 1.29 ºC lower (7%).

3.8 Nomenclature

A	Cross sectional area of the vane anemometer	Ft^3
C_{min}	Minimum capacitance rate	kW/ºC
$\dot{H}_{air}\|_{in}$	Enthalpy of moist air at inlet	kJ/s
$\dot{H}_{air}\|_{out}$	Enthalpy of moist air at exit	kJ/s
$\dot{H}_{air}\|_{min}$	Enthalpy of moist air at water inlet temperature and 100% relative humidity	kJ/s
$\dot{H}_{air}\|_{x}$	Enthalpy of moist air at the air exit dry-bulb temperature and humidity ratio evaluated at the inlet conditions	kJ/s
$\dot{H}_{cond}$	Enthalpy of the condensed water	kJ/s
$\dot{H}_{water}\|_{in}$	Enthalpy of water at inlet	kJ/s
$\dot{H}_{water}\|_{out}$	Enthalpy of water at exit	kJ/s
$h_{air}\|_{in}$	Specific enthalpy of moist air at inlet	kJ/kg
$h_{air}\|_{out}$	Specific enthalpy of moist air at exit	kJ/kg
$h_{air}\|_{min}$	Specific enthalpy of moist air at water inlet temperature and 100% relative humidity	kJ/kg
$h_{air}\|_{x}$	Specific enthalpy of moist air at the air exit dry-bulb temperature and humidity ratio evaluated at the inlet conditions	kJ/kg
h_{cond}	Specific enthalpy of the condensed water	kJ/kg
$h_{water}\|_{in}$	Specific enthalpy of water at inlet	kJ/kg
$h_{water}\|_{out}$	Specific enthalpy of water at exit	kJ/kg
$\dot{m}_{air}$	Dry-air mass flow rate	kg/s
$\dot{m}_{cond}$	Rate of condensation or evaporation	kg/s

$\dot{m}_{water}$	Water mass flow rate	kg/m^3
$\dot{Q}_{air}$	Rate of energy transferred from the air-side	kW
$\dot{Q}_{sensible}$	Sensible load	kW
$\dot{Q}_{sensible}\big\vert_{max}$	Maximum possible sensible load	kW
$\dot{Q}_{water}$	Rate of energy transferred to the water-side	kW
r	Radial	m
r_{outer}	Duct outer radius	m
SHR	Sensible heat ratio	
$T_{air}\big\vert_{in}$	Air-side inlet dry-bulb temperature	ºC
$T_{water}\big\vert_{in}$	Water-side inlet dry-bulb temperature	ºC
u	Velocity of air at exit in	ft/min
$\dot{V}_{air}\big\vert_{out}$	Air volume flow rate	cfm
$\dot{V}_{water}\big\vert_{in}$	Water volume flow rate	gpm
v	Axial velocity	m/s
v_{max}	Maximum axial velocity	m/s

3.8.1 Greek Symbols

$\rho_{air}\big\vert_{out}$	Density of moist air	kg/m^3
ρ_{water}	Density of water	kg/m^3
ω_{in}	humidity ratios at inlet	kg/kg
ω_{out}	humidity ratios at exit	kg/kg
$\varepsilon_{sensible}$	Spray cooler sensible effectiveness	

3.9 References

1 ANSI/ASHRAE Standard 111, "Practices for Measurement, Testing, Adjusting and Balancing of Building Heating, Ventilation, Air-Conditioning and Refrigeration Systems", 1988.

2 Spraying Systems, Co., North Ave. at Schmale Rd., P.O. Box 7900, Wheaton, IL60189-7900.

3 Arnold Wexler and W. G. Brombacher, "Methods of Measuring Humidity and Testing Hygrometers", US National Bureau of Standards, NBS Circular 512, 1951.

4 Omega Engineering, Inc., One Omega drv., P.O. Box4047, Stamford, CT 06907-0047, www.omega.com.

5 General Eastern Instruments, 20 Commerce Way, Woburn MA 01801.

6 Keuffel and Esser Co.

7 The Energy Conservatory, Minneapolis, MN.

8 Campbell Scientific, Inc., 815W. 1800N. Logan, Utah 84321-1784, www.campbellsci.com.

9 Blue M, A Unit of General Signal, Blue Island, IL 60406.

10 Fisher Scientific, 600 Business Center Dr. Pittsburgh, PA 15205-9913, www.fisher1.com.

11 Watt, J., Brown, W., "Evaporative Air Conditioners Hand Book", The Fairmont press. Inc., 1997, ISBN 0-88173-193-5.

Chapter 4 Spray Droplet Analysis Experiments

Numerical simulations of heat and mass transfer processes to/from water sprays require information about the macroscopic and microscopic spray structure. In particular, droplet diameter, droplet distribution, and spray cone angle must be known. This chapter presents methods used in the current research to experimentally measure both droplet size and spray cone angle for water flowing through a full cone nozzle. The chapter starts with defining the most commonly used median droplet diameters, followed by an overview of the most commonly used spray structure measuring techniques available in the literature. A brief description of each method is presented, along with the drawbacks and merits of each technique for the present task as well as sources of errors that can affect the results. Thereafter, a detailed description of the test facility constructed for sizing the water droplets and measuring the spray cone angle is presented. Finally, the methods used for analyzing the experimental data are discussed.

4.1 Median Diameters

In practice, atomizing nozzles do not produce sprays of uniform liquid drop size, owing to the heterogeneous nature of the atomization process. In many calculations of heat and mass transfer and flow processes, it is convenient to work with mean or average diameters instead of the complete drop size distribution. A median diameter characterizes the spray by number, length, surface area, volume, or mass. In some cases, a particular median diameter

is selected to emphasize meaningful characteristics, such as the total surface area of the spray. The concept of mean diameter has been generalized and its notation standardized by Mugele and Evans [1], as shown by equation (4.1)

$$D_{ab} = \left[\frac{\int_{D_0}^{D_m} D^a \left(\frac{dN}{dD} \right) dD}{\int_{D_0}^{D_m} D^b \left(\frac{dN}{dD} \right) dD} \right]^{1/(a-b)} \tag{4.1}$$

where D_{ab} is the median diameter, a and b are assigned values corresponding to the effect investigated. The sum $a+b$ is called the order of the mean diameter. Median diameters are determined from cumulative distribution curves according to the following equation:

$$D_{ab} = \left[\frac{\sum N_i D_i^a}{\sum N_i D_i^b} \right]^{1/(a-b)} \tag{4.2}$$

where i denotes the size range considered, N_i is the number of drops in the size range considered, and D_i is the middle diameter of size range i. Thus, for example, D_{10} is the linear average value of all drops in the spray; D_{20} is the diameter of a drop whose surface area, if multiplied by the total number of drops, equals the total surface area of the sample; D_{32} is the diameter of the drop whose ratio of volume to surface area is the same as that for the entire spray. In liquid fuel-fired combustion systems, for example, and other applications involving heat and mass transfer to liquid drops, Sauter mean diameter is often preferred. Table 4-1 describes a number of important median diameters with their fields of application as suggested by Mugele and Evans [1].

Table 4-1 Mean diameter and their application [2]

Symbol	Name of Median Diameter	Expression	Application
D_{10}	Length	$D_{10}=\left(\frac{\sum N_i D_i}{\sum N_i}\right)$	Comparisons
D_{20}	Surface Area	$D_{20}=\left(\frac{\sum N_i D_i^2}{\sum N_i}\right)^{1/2}$	Surface area controlling
D_{30}	Volume	$D_{30}=\left(\frac{\sum N_i D_i^3}{\sum N_i}\right)^{1/3}$	Volume area controlling
D_{21}	Surface area-length	$D_{21}=\left(\frac{\sum N_i D_i^2}{\sum N_i D_i}\right)$	Absorption
D_{31}	Volume-length	$D_{31}=\left(\frac{\sum N_i D_i^3}{\sum N_i D_i}\right)^{1/2}$	Evaporation, molecular diffusion
D_{32}	Sauter (SMD)	$D_{32}=\left(\frac{\sum N_i D_i^3}{\sum N_i D_i^2}\right)$	Mass transfer, reaction

4.2 Droplet-Size-Measurement Methods

Methods used for droplet-size-measurement can be classified into three techniques; mechanical, electrical, and optical. Mechanical methods include drop collection on slides or in cells, cascade impactors, molten-wax and frozen-drop techniques. In droplet capturing and cascade impactor techniques, a sample of the spray is collected by exposing the slide or the impactor to the spray, on a slide or collected in a cell containing a suitable immersion liquid. The immersion liquid is of a density slightly less than that of the sprayed liquid. It has a lower viscosity and surface tension to prevent droplet evaporation and drop breakup,

respectively. The collected droplets are then sized using a microscope fitted with a traversing scale.

In the molten-wax technique, molten wax is injected into the atmosphere. The molten wax droplets rapidly cool and solidify soon after they leave the nozzle. The wax droplets are then separated into size groups and weighed to obtain the volume or mass fraction in each size range. The frozen drop technique is an extension to that of the molten-wax technique. In this case freezing solidifies spray droplets as soon as they leave the nozzle. Freezing of spray droplets is achieved by spraying them into a fluid maintained at a temperature significantly lower than the freezing temperature of the sprayed liquid, e.g. liquid nitrogen. The frozen droplets are then analyzed in a manner similar to the molten-wax technique.

Mechanical methods have the advantages of being simple and inexpensive. However, obtaining a sufficient representative sample of the spray is not an easy task. The collection of too many droplets on a slide leads to errors due to droplet overlap. Also, small droplets tend to follow the air stream around the slide instead of impacting on to the surface of the slide. Moreover, the breakup of large droplets on impingement will bias the actual droplet distribution to a smaller size. A correction factor is also required to convert the flattened diameter to the actual diameter. In the hot-wax technique the effect of surface tension and viscosity on the atomization process should be considered if the wax properties are different from those of the liquid being simulated. In the freezing technique, a correction factor is required to account for the change in the droplet size due to freezing.

Electrical methods include Wicks-Duckler technique [3], charged wire probe, and hot wire anemometer. The Wicks-Duckler technique is based on counting the pulses produced by drops bridging a gap as they momentarily make contact between two sharp needles across which there is a potential difference. In the charged-wire probe, an electrically charged wire is discharged as a drop impinges the wire. The amount of discharge depends on the droplet size. The hot-wire technique depends on the cooling effect when a droplet attaches to the wire. The local cooling by the drop reduces the resistance in proportion to the drop size. When measuring large drops the hot-wire can operate only at flow velocities around 10 m/s to avoid droplet breakup upon impacting the wire.

Electrical methods are more accurate compared to mechanical methods, owing to their ability to measure a larger sample size. They are also characterized by having short response time. In the hot-wire method, as an example, the response time can be 2 ms. However, electrical methods have the problem of being intrusive, which disturbs the original flow. They also provide local information at a particular point, which makes them unsuitable for cases where spatial sampling or averaging is required. Being dependent on the conductivity and the flux of droplets, as in the charged-wire technique, liquids of low conductivity produce pulses of long duration. This leads to counting errors due to overlap of successive impingements [4].

The third method used for droplet-size-measurement is the optical method that incorporates imaging and non-imaging methods. Imaging methods include photography, and holography. Examples of non-imaging methods are single-particle counters, Phase Doppler Anemometry (PDA), and the Malvern particle analyzer. Photography involves taking a picture with the

aid of a high intensity light source for a very short time duration e.g. 750 ns. The flash duration depends on the light source intensity and the film sensitivity. In more general terms, photography is a point-to-point recording of the image of the object, droplets, in a very short interval of time. In the holography method, a coherent beam of light is split into two beams, a reference beam and an object beam, as shown in Figure 4-1.

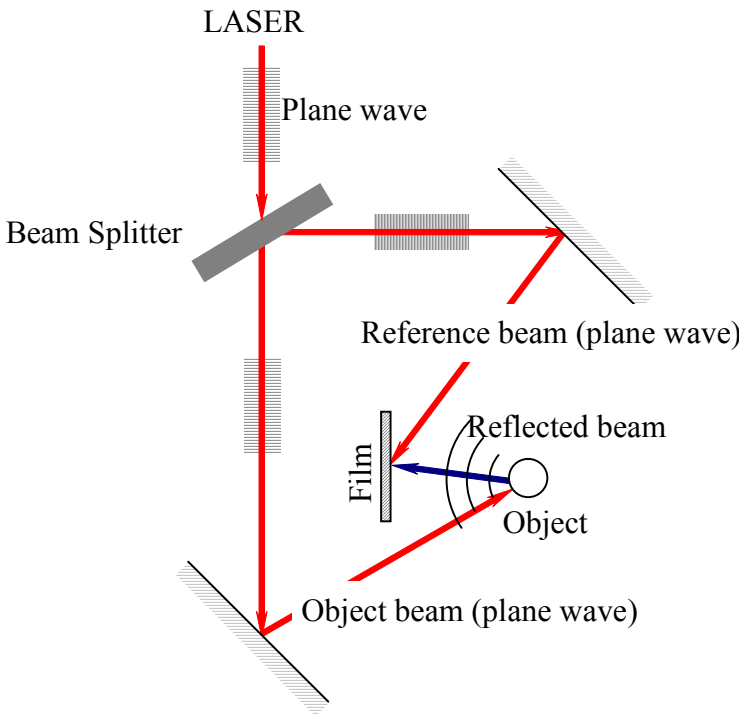

Figure 4-1 Schematic diagram of a laser holographic system

Once the object beam strikes an object such as a droplet, it is modulated in phase and amplitude according to the physical characteristics and dimensions of the object. After being reflected by the object, the modulated beam reaches the film at an intensity and phase different from the reference beam. At the holographic plate or film, the two beams interfere with each other and a hologram, composed of regions of high and low intensity, is recorded.

In other words, holography is a recording of the interface between the coherent light that hits the object and a reference beam. If the plate is illuminated with the same reference beam at the same angle, a 3-D image of the spray is reconstructed on the film surface. Consequently, holography is a technique that does not require calibration, but it is only limited to dilute sprays. Photography requires calibration and is applicable to dense sprays. Imaging techniques provide valuable information about droplet sizes and distribution without interfering with the flow field. Since photography and holography are instantaneous methods, errors that arise from droplet evaporation after sampling are eliminated. However, photography and holography encounter difficulties when analyzing the acquired images. Images are analyzed either manually (which can be tedious) or automatically (using image analysis software). In either case, the results obtained for image analysis are dependent on the skill and discretion of the analyst.

Most of the non-imagining techniques depend on analyzing the light scattered when a light beam strikes on an object. The phenomenon of light scattering can be visualized by ray tracing as shown in Figure 4-2. The light that is incident on a droplet is partially reflected at the surface and partially transmitted and refracted in both forward and backward directions after one internal reflection.

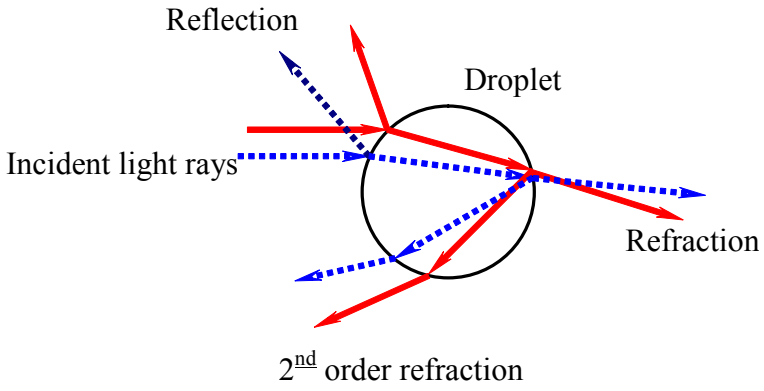

Figure 4-2 Ray tracing for a two monochromatic beams falling on a droplet

One example of a non-imaging droplet measurement approach is Phase Doppler Anemometry (PDA). In a PDA, measurements are made at the intersection of two parallel beams of monochromatic coherent light from a laser. As a particle passes through the point of intersection, it scatters the light thereby creating an interference fringe pattern. A receiving lens projects a portion of this fringe pattern onto two detectors, as shown in Figure 4-3. Each detector produces a signal. The phase shift between these signals is proportional to the size of the droplet. The particle velocity is calculated from the Doppler frequency of the signal from any one of the detectors.

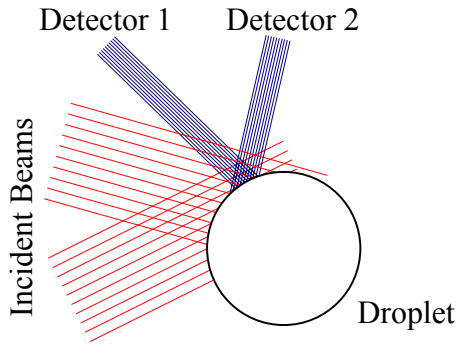

Figure 4-3 Schematic showing the PDA and the position of the 2 detectors

The Malvern particle analyzer is another example of the non-imagining measuring techniques. The optical system is schematically shown in Figure 4-4. In this system, the droplet size measurement depends on measuring the diffraction of light when a parallel beam of light interacts with a drop. The diffraction pattern produced is of the Fraunhofer form; i.e., a series of alternate dark and light concentric rings, the spacing of which depends on the droplet diameter. In a polydispersed spray, a series of overlapping diffraction rings are formed, each is associated with a characteristic drop size range. A Fourier transform lens focuses the diffraction pattern onto a multi-element photo-detector that measures the light energy distribution. The photo detector comprises 31 semicircular photosensitive to a particular small range of drop sizes. The output of the photo-detector is multiplexed through an analog-to-digital converter. Interpretation of the measured light energy distribution as a drop size distribution is then carried out by a computer.

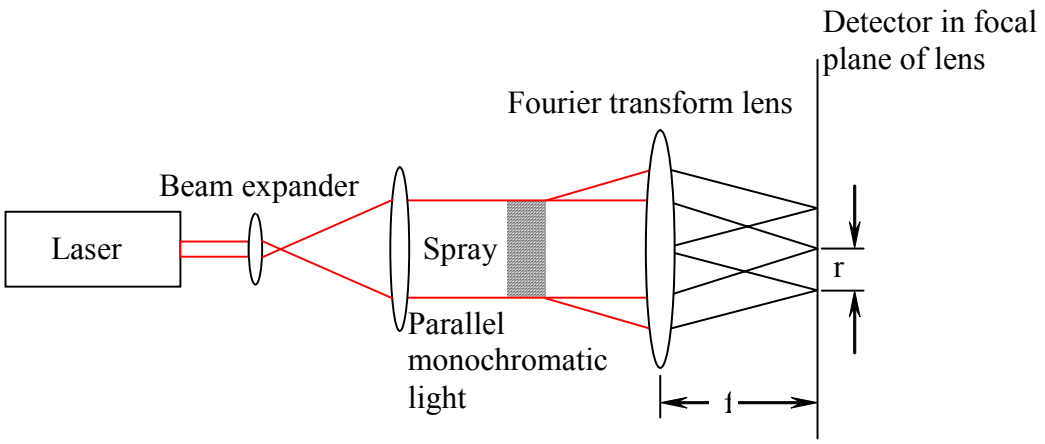

Figure 4-4 Optical arrangement employed in Malvern particle analyzer [2]

The main advantage of the non-imagining techniques, other than being non-intrusive, is the speed at which data can be accumulated and analyzed to characterize a spray. The principle disadvantage of non imaging methods lies in the limited range of spray densities over which these methods are functional. In dense sprays, multiple scattering becomes significant and can affect the interpretation of the data acquired. Moreover, the Malvern particle analyzer is limited to particles less than 850 μm. Owing to their nature, these techniques provide local information at a particular point, which makes them unsuitable for cases where spatial sampling is required. These techniques are also limited to spherical droplets of known refractive index.

The aforementioned discussion shows that there are a variety of methods that can be used for droplet sizing, Table 4-2 summarizes the key advantages and disadvantages of each method. It is worthwhile noting that, all these methods are susceptible to several kinds of error. These errors are discussed in detail in the following section.

Table 4-2 List of the measuring techniques for droplet size

Method	Advantages	Disadvantages
Mechanical Methods		
1. Drop collection on slides or in cells 2. Cascade Impactors 3. Molten-Wax 4. Frozen-drop technique	1. Simple 2. Low cost	1. Intrusive 2. Difficult to extract and collect representative spray samples

Table 4-2 continued

Method	Advantages	Disadvantages
Electrical Methods		
1. Charged-wire technique 2. Hot-wire technique	1. Accurate 2. Short response time	1. Intrusive 2. Depends on conductivity and flux of droplets
Optical		
1. Imaging a. Photography b. Holography 2. Non-imaging a. Single-particle counter b. PDA c. Malvern particle analyzer	1. Instantaneous 2. Non-intrusive	1. Multiple scattering due to high spray densities. 2. PDA assumes circular droplets. 3. Malvern is limited to a maximum diameter of 850μ.

4.3 Sources of Errors

In droplet-size-measurements, different sources of errors affect the results. Sources of these errors include sampling method and location, drop coalescence, drop evaporation, and sample size [2]. Sampling can be spatial or temporal. Spatial sampling describes the measurements of drops contained within a fixed control volume during short interval in time. Spatial sampling is advantageous in some applications, such as combustion, where ignition and burning rates depend on the population of droplets in a given volume [5]. On the other hand, temporal sampling describes the measurements of drops over a specific time period. Temporal sampling is advantageous in applications, such as herbicides, where the distribution of droplets on the ground over time is crucial [2].

Another source of error comes from collision of drops traversing through a sprays. Based on the relative velocity between drops, droplets diameter, and the collision angle, drop coalescence or breakup can take place. Drop coalescence results in an increase in drop size while breakup results in a decrease in drop size. Coalescence is more likely to occur in dense sprays when sampled at large distances from the atomizer [2].

Phase change can also influence droplet size measurements. Evaporation or condensation from droplets during sampling can bias the readings. In a mono-dispersed spray, evaporation causes a mass loss which in turn leads to a decrease in the mean drop size. On the other hand, in a spray that contains a wide range of droplets, evaporation might cause an increase in the mass median diameter. This phenomenon is discussed by Chin et al [6], where they have injected kerosene into air at 2 MPa and 2000 K. This increase can be attributed to the loss of fine droplets and the weighting effect of larger diameter droplets, as can be explained further with the aid of the Figure 4-5. Figure 4-5 depicts a drop size histogram for a spray before and after evaporation. In this figure, evaporation results in the loss of the 30 droplets falling in the range between 17-51 μm that have existed before evaporation. Despite of this loss of droplets, there is an increase in the mean diameter from 119 μm to 120.8 μm due to the weighting effect of the larger droplets.

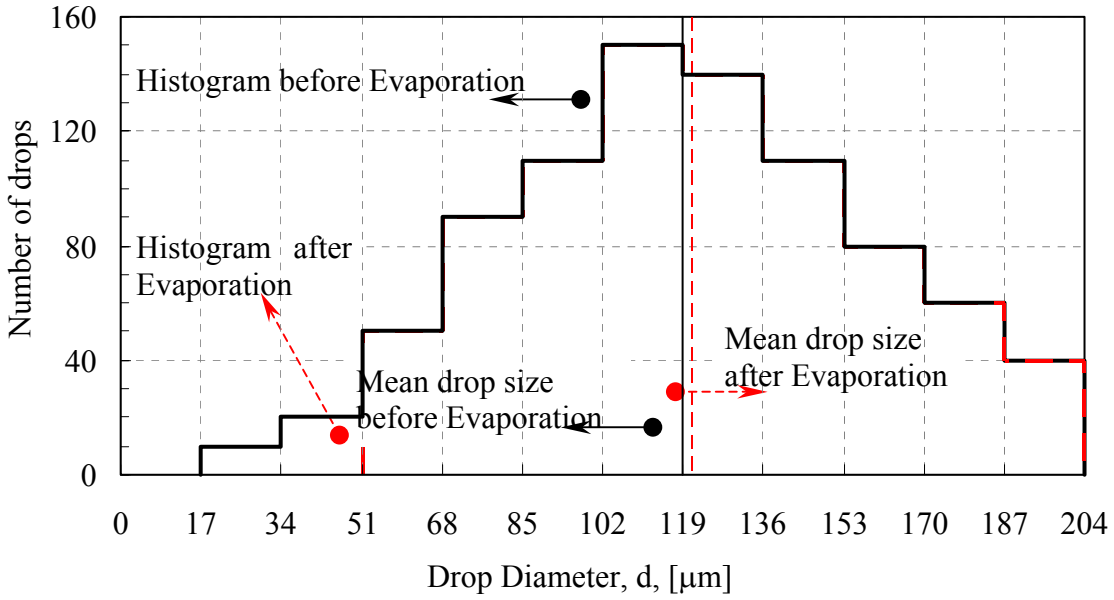

Figure 4-5 Drop size histogram showing the effect of evaporation

Lefebvre [2] reported that in order to achieve a reasonably accurate estimate of spray quality it is necessary to measure about 5500 drops. Lewis et al. [7] pointed out that one large drop in a sample of 1000 drops may affect the average diameter of the sample by as much as 100%. Figure 4-6 depicts the accuracy of the mean diameter obtained for various sample sizes for 95% confidence limits [8]. The larger the number of droplets in a sample, the higher the accuracy of the drop size measurement.

The discussion presented in Sections 4.2 and 4.3 shows that high-speed photography when compared to other sizing methods appears to be the most suitable measuring technique for the current research application. Photography is a non-intrusive, accurate [2] technique that is capable of providing detailed spatial and temporal information for dense fast-moving sprays. This information includes spray structure, spray cone angle, and average diameter.

Moreover, photography has a wide size range capability down to 5 μm [2]. Owing to the high speed at which the imaging process takes place errors due to droplet evaporation are completely eliminated. On the other hand, non-imaging methods such PDA and Malvern are constrained by the spray density and the droplet size. Also, non-imaging and electric methods provide local information about the spray and none of them is capable of providing information about the entire spray and the spray cone angle.

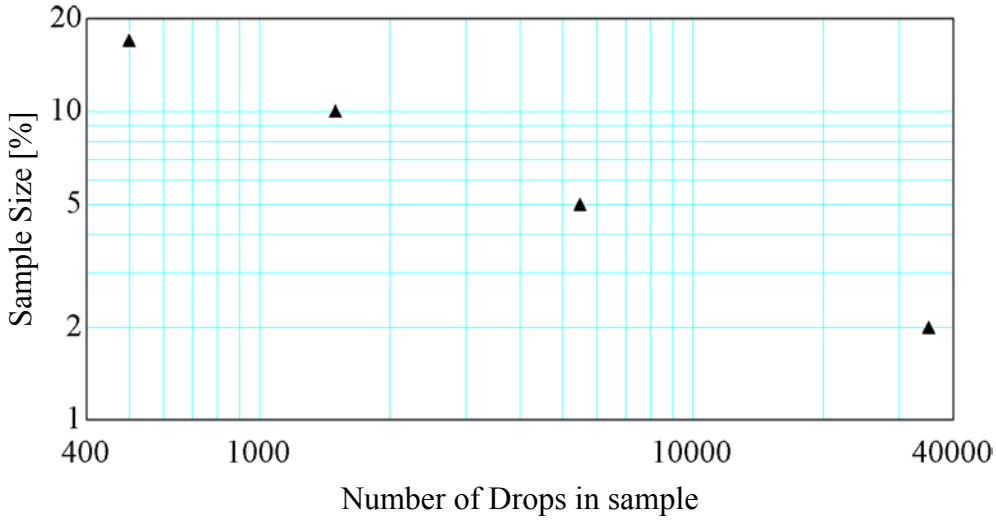

Figure 4-6 Influence of sample size on Accuracy of drop size measurements [8]

4.4 Experimental Apparatus

An experimental apparatus has been constructed to measure the macroscopic and microscopic structure of water sprays from a full-cone spray nozzle. The apparatus is designed to incorporate the ability to spray water vertically and horizontally in quiescent air at ambient conditions. The apparatus consists of a water supply system, a light source, a digital imaging system and necessary transducers for measuring water temperature, water

injection pressure, and water volume flow rate. The transducers used are identical to the ones used in the heat and mass transfer experiments discussed in Chapter 3. A schematic of the apparatus is shown in Figure 4-7. A description of individual components of the apparatus will be discussed next.

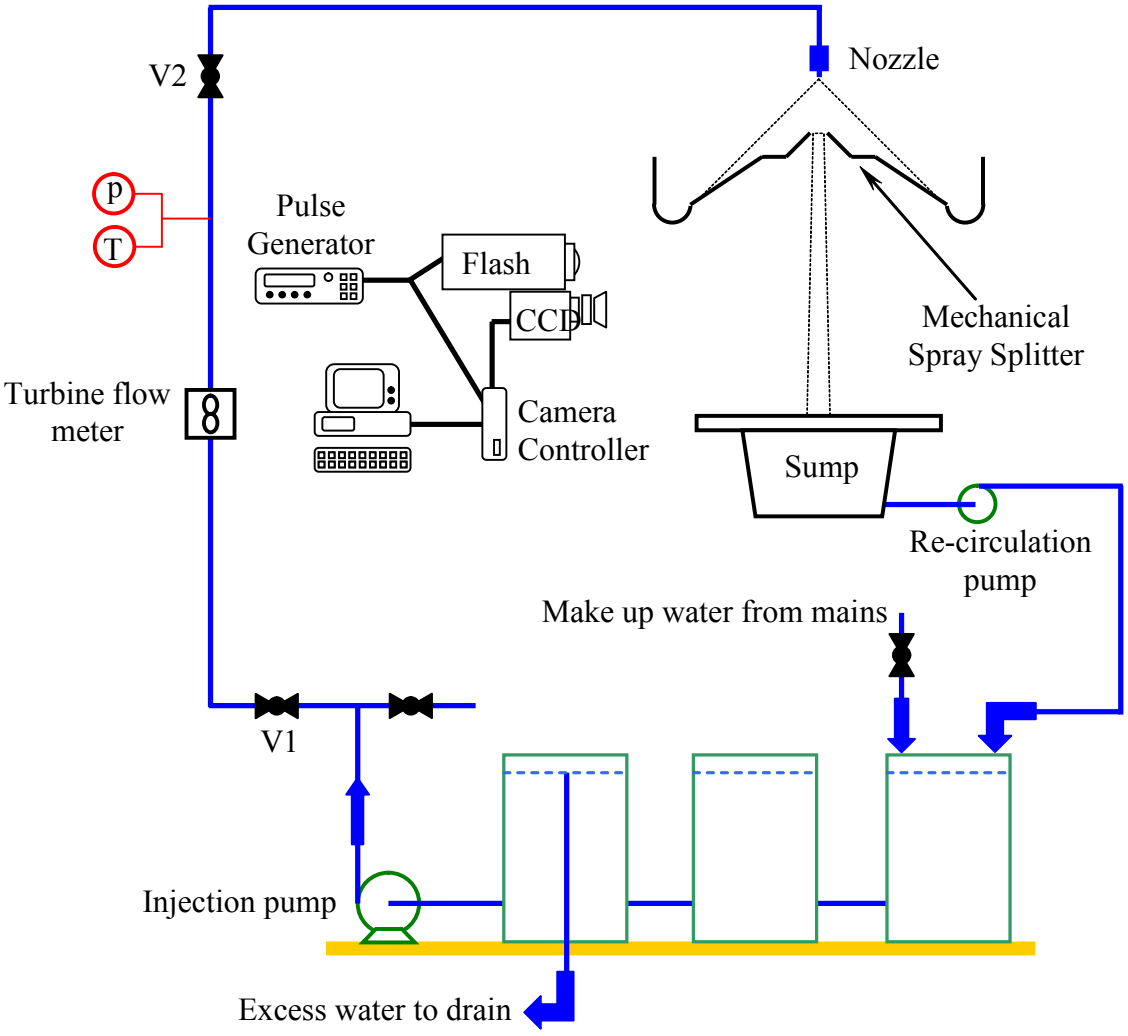

Figure 4-7 Schematic for the test rig used for measuring the spray characteristics

4.4.1 Water Supply System

The water supply system is similar to that used for the heat and mass transfer experiments, described in Chapter 3. It consists of three interconnected reservoirs, 20 gallons each, water pumps, filter, necessary piping, fittings and valves, turbine flow meter, pressure transducer and a nozzle. The three reservoirs function to dampen pressure fluctuations between the mains and the suction pump. These reservoirs reduce irregularities in the water supply flow. Water is added from the mains to the containers to compensate for water loss due to spilling of the water spray. An overflow pipe is used to maintain a constant head of water height in the reservoir feeding the supply pump. The aforementioned design (reservoir, makeup water and overflow pipe) helps to create a constant head imposed on the supply water pump thereby stabilizing the water flow rate delivered during its operation.

Water is injected via a circular pattern spray nozzle, model QLH-SS-25 [9], with a nominal orifice diameter of 4.75 mm (3/16"). Most of the injected water is collected in the sump tank, and pumped back via the circulation pump. Varying the position of the two ball valves, V1 and V2, connected in the water supply line serves to modulate the mass flow rate of water. The function of the first valve, V1, is to control both the flow rate of water and pressure supplied to the nozzle. The second valve, V2, is used for fine-tuning to achieve the required pressure. The positions of both valves are adjusted at the start of an experimental run to maintain a desired pressure at the nozzle inlet. The nozzle pressure is held constant during all the experiments. Keeping the pressure constant during an experiment is necessary since the nozzle capacity, the spray drop sizes, and spray cone angle are greatly affected by the

supply water pressure to the nozzle inlet. The nozzle inlet pressure is continuously monitored via a pressure transducer [10].

4.4.2 Light Source

Successful images of droplets in photography techniques require high quality light sources. The light source must have sufficient intensity and sufficiently short duration to allow for suitable image exposure. Preliminary experiments were conducted utilizing a standard overhead projector as a light source and an analog camera with a shutter speed of 1/4000 sec. These experiments were not successful because the light intensity was not sufficient to produce a sharp image as higher shutter speeds require higher light intensity. Manipulations involving the use of fast emulsion film, such as ASA 400 and ASA 800, were not been able to solve this problem. To overcome these limitations, a high intensity illuminace pulse flash (model 501/4/6/9 [11]) was used as a light source. The flash features a 90 mm diameter-collimating lens, and an array of four spark gaps. Each spark consists of an upper electrode (positive potential) lower electrode (negative potential) fed by a bank of electrical capacitors. Air or Argon gas flow through the upper electrode and is dispersed across the gap. The four flash pulses are 6 joules each and have a duration 750 ns. Light from each spark gap is focused by a lens to the next gap in front, as shown in Figure 4-8, to maximize the light output from the flash unit. The flash pulses can be fired simultaneously or individually in a sequential manner.

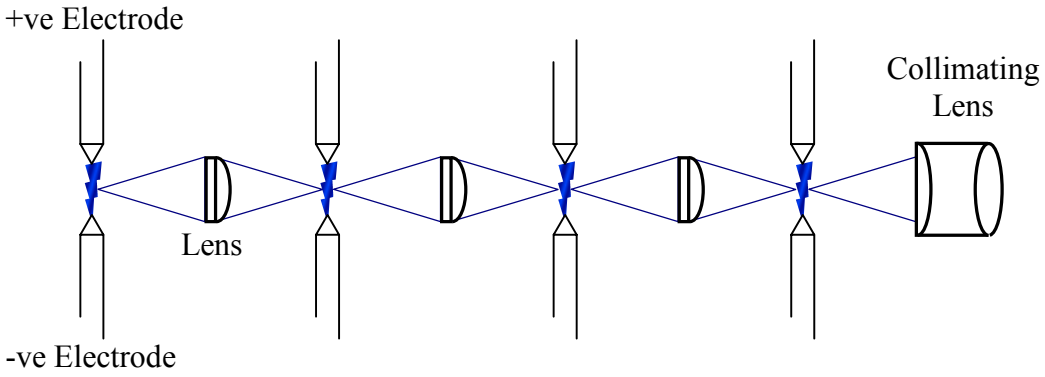

Figure 4-8 Schematic showing the optical path in the 4-flash system [11]

4.4.3 Digital Imaging System

The digital imaging a system [12], shown in Figure 4-9, consists of a high speed camera, controller, digital interface card, a computer, cables and application software. Data acquired by the camera are transferred to the computer via the controller. The software is used to control both the system configuration and data acquisition.

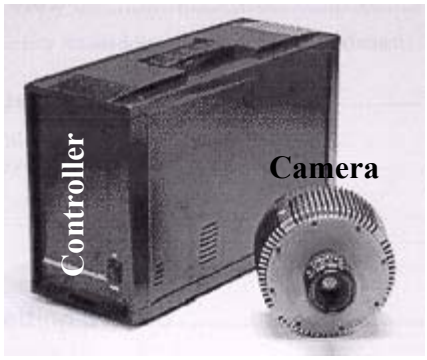

Figure 4-9 A 5Mhz MicroMAX controller and camera

As shown in Figure 4-10, the camera collects light from the object and converts the energy into a quantitative electronic signal. The controller (comprising the power supply, analog-to-digital converter, scan control and exposure timing hardware, and system I/O connectors)

receives the analog signal from the camera and converts it to a digital signal using a scientific grade 12-bit analog-to-digital converter.

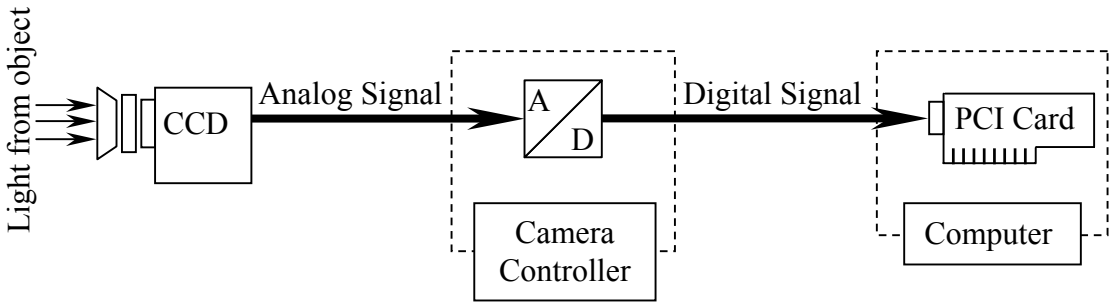

Figure 4-10 Schematic showing flow of image information

The digital signal is transferred directly to the host computer memory via a high-speed serial link to the PCI interface card. The image acquisition program then handles these data. The camera and the flash are synchronized together by a pulse generator, Model 555 [13], according to the timing profile shown in Figure 4-11.

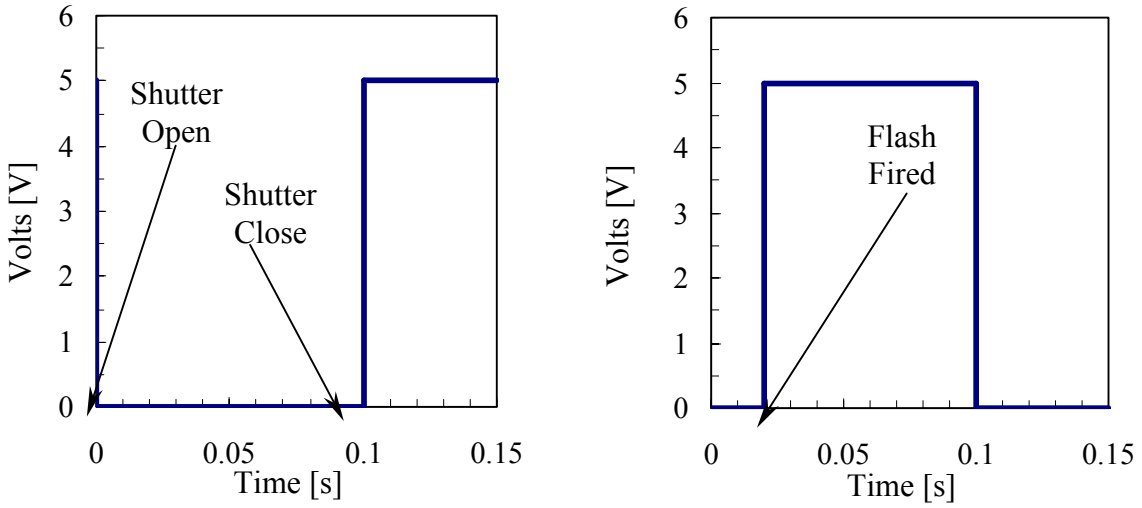

a- Triggering signal for the CCD

b- Triggering signal for the flash

Figure 4-11 Shutter and flash triggering schedule, using pulse generator

During the preliminary experimental phases, a Visual Basic code, listed in Appendix-III, was developed and used to synchronize the camera and the flash. The camera and the flash are controlled by the code via the computer parallel port according to a timing sequence similar to that shown in Figure 4-11. The only differences are in the flash delay which is set to 125 ms, and the exposure time which is set to 375 ms. The flash delay is defined as the time lag between the triggering signal to open the shutter and the triggering signal to fire the flash. These differences in timing were chosen because the clock accuracy is in the order of 125 ms.

A picture of the front end of this code is shown in Figure 4-12. An add-on library, NTPORT [14], is used to enable Visual Basic to access the computer parallel port. NTPORT is a 32-bit ActiveX/OCX control designed to be used with Visual Basic 5.0 or 6.0. It provides 8-bit or 16-bit READ and WRITE capability to any port within the computer I/O address space.

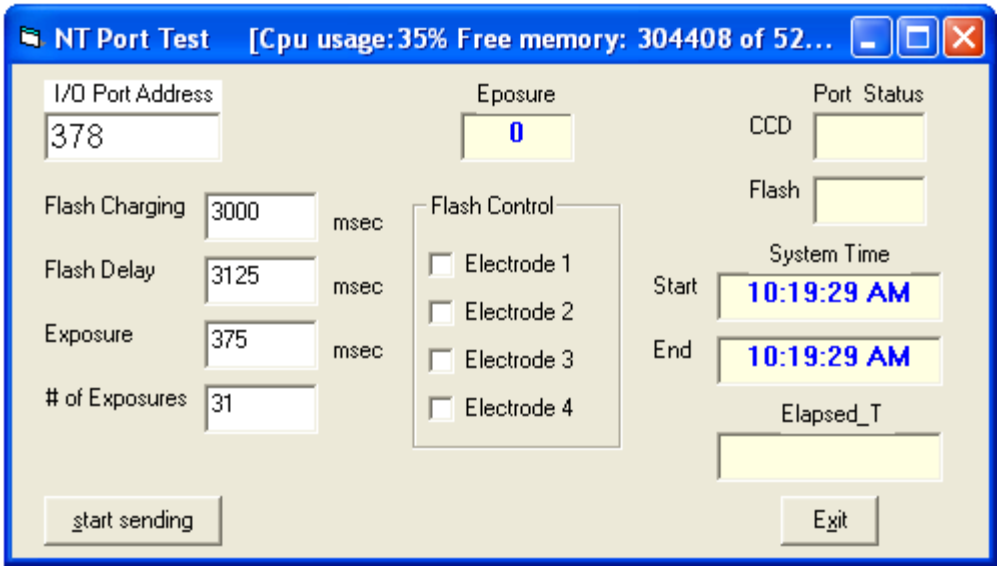

Figure 4-12 Front end for the visual basic code

Inputs to the code include the parallel port address, flash charging time, the flash delay, exposure time, number of exposures and the flash electrodes that are triggered. The code displays the starting and ending times the time elapsed after the initial triggering signal, the current exposure, and the status of the flash and camera ports (Hi or Low).

4.5 Experimental Methods and Procedure

The experiment starts by turning on the measuring and controlling equipment an hour prior to measurements for warm up. During the warm up period, the relative positions between the camera, flash and the nozzle are adjusted. After the warm up period, a chronological procedure is followed for each experimental run:

1. The injection pump is turned on to inject water from the containers to the nozzle, water temperature, pressure and flow rate at nozzle inlet are measured and recorded.
2. The circulation pump is turned on to pump water back from the sump tank to the containers.
3. Valves V1 and V2 are adjusted and tuned to achieve the required water injection pressure.
4. The pulse generator and the image acquisition program are launched to open the shutter, fire the flash, close the shutter and transfer the data to the computer as follows:
    i. The CCD cam shutter is triggered to open. After 10 ms, the shutter is fully opened and the camera is ready for the flash to be fired.

ii. The flash is fired 20 ms after triggering the shutter. The 20 ms delay is greater than the time needed for the shutter to open in order to ensure that the shutter is fully opened.

iii. The CCD cam shutter is closed after 80 ms from firing the flash. The information is transferred from the camera to the computer via the camera controller and the PCI interface card. The shutter closure is followed by a 2.9 seconds of delay to allow a suitable time for charging the flash capacitors.

iv. Steps 4 to 6 are sequentially repeated 31 times, producing 31 frames.

The collected data for each run is analyzed using ImageJ [15], an image analysis software package. The relative position between the camera and the flash is altered to get the optimum position for the light source relative to the camera that produces images easy to analyze using ImageJ. In what follows, a detailed description of the two methods, namely light sheet illumination and spray splitters, adopted to reach the optimum position are discussed.

4.5.1 Light Sheet Illumination

In this method, a sheet of light is first produced in a plane perpendicular to the camera with the aid of the optical setup shown in Figure 4-13. The setup consists of a flash, a camera, a set of two convex lenses, an iris, and a pair of cylindrical lenses. The 95 mm and the 50 mm outer diameter convex lenses reduces the 90 mm collimated light beam from the flash to a 25 mm beam.

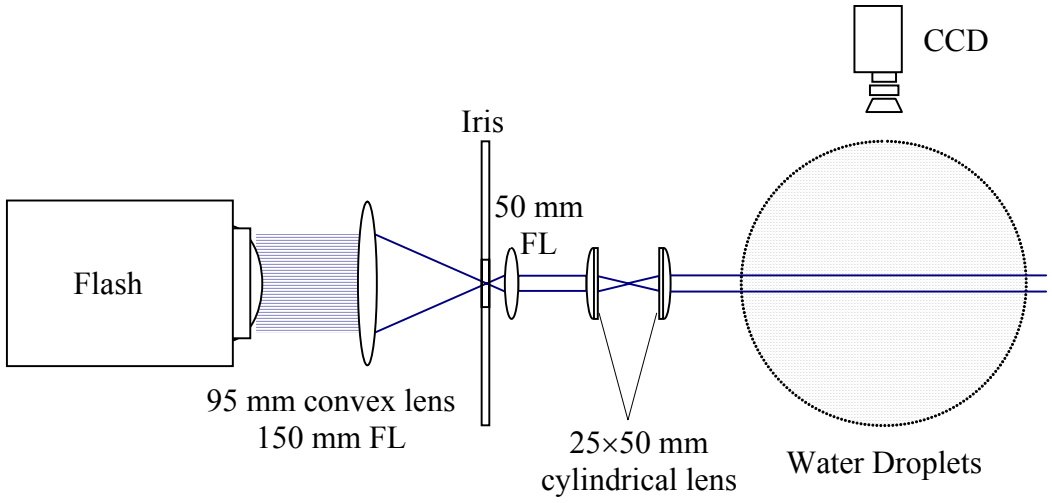

Figure 4-13 Light Sheet illumination technique

The pair of 25x50mm cylindrical lenses are used to change the light from a circular beam shape to a flat sheet, as shown in Figure 4-14. Based on this configuration, the camera lens focuses only on droplets that are illuminated by the light sheet. Consequently, no corrections are required during the image analysis phase to adjust for droplets that are out focus and in the lens depth of field. The problem with the light sheet illumination configuration is the potential for multiple scattering resulting from a combination of spray outside the light sheet and reflections from the droplets inside the light sheet. In the image analysis phase, reflections from droplets shows high illuminance or pixel values compared to the reset of the droplets. If uncorrected, the reflections lead to errors in the analysis because the results are biased towards smaller droplet sizes. In an attempt to reduce these reflections, the following methods are investigated

1. Decreasing the flash power to less than a ¼ of its full power.

2. Adding a fluorescent die to the water and using filters on the camera lens that will pass only light emitted by the fluorescent die.
3. Using spray splitters

The use of spray splitters was found to be more effective as compared to those achieved by decreasing the flash power and use of filters. In the following section the spray splitters technique will be discussed.

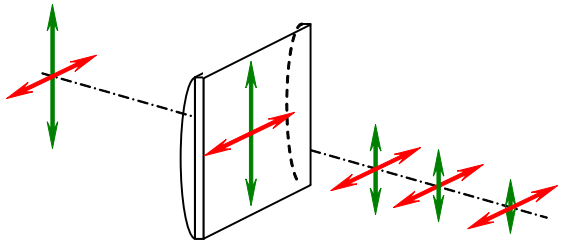

Figure 4-14 Schematic showing light passing through a cylindrical lens

4.5.2 Spray Splitters

In this method, the outer sections of the spray are physically separated to reveal an unimpeded view of a cross section of the spray core, as shown in Figure 4-15. Compared to the light sheet illumination, this method relies upon producing a sheet of spray rather than using a sheet of light. A review of the literature shows that Hung et al [16], and Omer et al [17] utilized this method in their analysis for diesel spray structure.

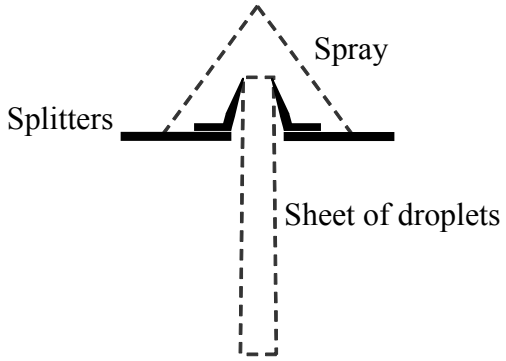

Figure 4-15 Spray Splitter configuration

The spray splitter, shown in Figure 4-16, is built from two pairs of aluminum sheets, a pair of knife edged blades, and a pair of gutters. The first pair of aluminum sheets has a roof shape which channels the outer sections of the spray towards the gutters where the water is collected and is drained back to the reservoirs mentioned in §4.4.1. The knife edged blades are used for slicing the spray. These blades are bent towards the inside at an angle of 60° to the horizontal to help cut the spray and reduce back splash. The aforementioned use of blades inclined at 60° have failed to entirely eliminate splash, which dictated the need to modify the design by adding a pair of aluminum sheets below the blades, as shown in Figure 4-16. This pair of sheets eliminates the splashed droplets by collecting them and directing them away from the measuring field. The flash and the CCD camera are placed at zero degrees to one another, as shown in Figure 4-16. This arrangement is known as forward light illumination. A photograph for the spray splitters is given in Appendix-IV.

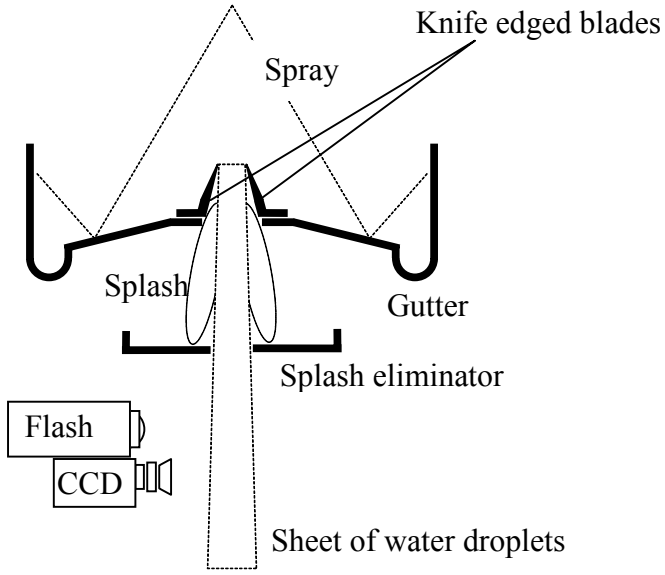

Figure 4-16 Schematic for the spray splitters

Previous trials have investigated the effect of placing the flash and the CCD camera on the same axis at 180° to one another, as shown in Figure 4-17. This arrangement is known as backward light illumination. The high light intensity from the flash resulted in a complete wash out of the picture and it was impossible to get any useful information from these photographs.

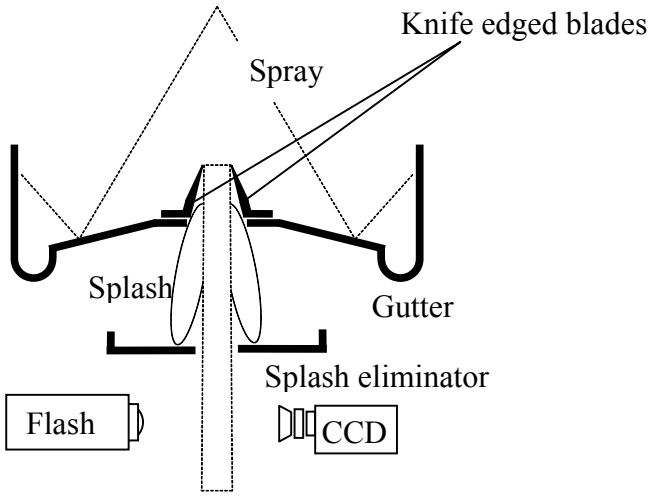

Figure 4-17 Flash and Camera at 180º (backwards light illumination)

The spray splitters are inserted at 100 mm downstream the nozzle. The spacing between the splitters is set to 10 mm. In order to alleviate doubts about the physical aberrations introduced by the spray splitters, tests were conducted by varying the spacing between the blades is increased to 3 times and 5 times the nominal nozzle diameter at the same down stream location. Figure 4-18 shows the effect of changing the spacing between the skimmer blades on the length median diameter D_{10} measured in mm at different pressures. There is no significant effect observed on the average diameter while increasing the spacing between the blades. This supports the conclusion that introducing the splitters does not affect the results. It is also observed that as the spacing between the blades increases, more out of focus droplets show up in the images.

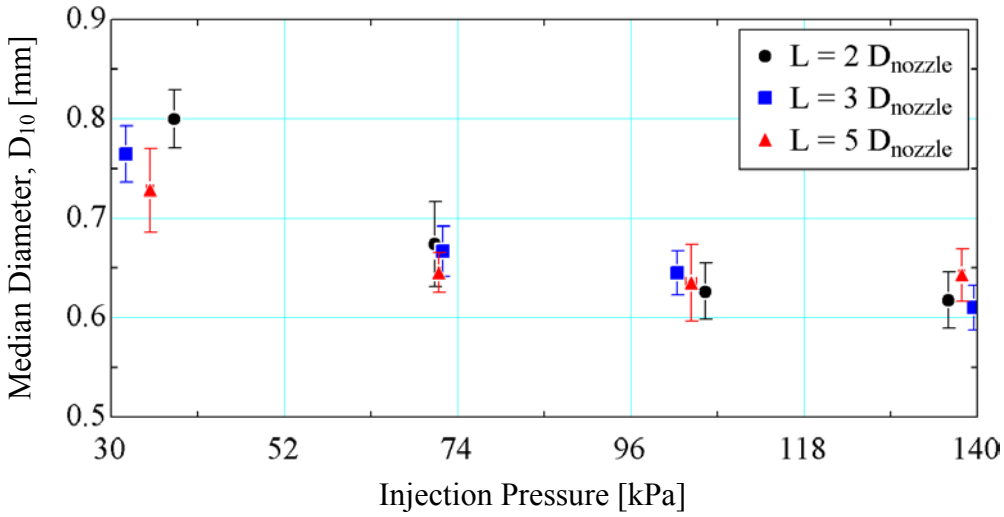

Figure 4-18 Effect of changing the distance between the skimmer blades on D_{10}

4.6 Image Analysis

The data collected for each run are analyzed using an image analysis software package, ImageJ [15], to determine the droplet median diameter. ImageJ is a public domain Java image processing program inspired by the National Institute of Health, NIH. The software is user-interactive with the capability of editing, analyzing, processing, saving and printing 8-bit, 16-bit and 32-bit images. The software counts and measures objects in binary or thresholded images by scanning an image until it detects the edge of an object. It then outlines the object, measures it, and then resumes scanning until it reaches the end of the entire image or selected area. In addition to its ability to display measurements such as area and perimeter, the software provides up to 256 bins for a particle size distribution histogram, from which the median diameter can be calculated as shown in §4.1. Similarly, ImageJ can create density histograms. It also provides standard image processing functions such as contrast manipulation, sharpening, smoothing, edge detection and median filtering.

Geometric transformations such as scaling, rotation and inversions can be also done, since ImageJ is designed with an open architecture and custom acquisition. Thus, analysis and processing plugins can be developed using ImageJ's built in editor and Java compiler. User-written plugins make it possible to process and analyze images of wide variety of applications. The analysis of the images depends on the parameter to be measured. Accordingly, the post processing of an image to measure the droplet size is different than that for measuring the spray cone angle.

4.6.1 Droplet-Size-Measurements

The image analysis process for droplet size measurement requires three preliminary stages; calibration, image processing and enhancement, and sample size selection. The first stage, calibration, is focused on testing the ImageJ software package to accurately reproduce known droplet sizes. This is followed by exploring image enhancement techniques that are essential to improve the image quality. The last phase is focused on estimating the required number frames required to statistically represent a measurement sample. Each of these phases is discussed in what follows.

4.6.1.1 Calibration

The objective of the first step of the image analysis process is to examine ImageJ's ability to provide correct particle measurements, and consequently perform the necessary calibration. Software developed by Prof. S. A. Klein, is used to randomly generate images for a known number of particles with a known size and distribution. A picture of the front end of the code, shown in Figure 4-19, shows that the software can produce three sets of particles in

each image. The generated images are divided into subsets; each subset consists of eleven images for randomly distributed particles having the same size, number, and approximately the same void fraction, as defined by equation (4.3). A sample of one of these sets is shown in Figure 4-20. These images are then analyzed using ImageJ to check its reproducibility. Table 4-3 summarizes the sets used in the calibration process.

$$\text{Void Fraction} = 1 - \frac{A_d}{A_T} \tag{4.3}$$

where A_d is the total area of the projected droplets $\sum A_i$, where A_i is the area of a single droplet, and A_T is the area of the inscribing rectangle.

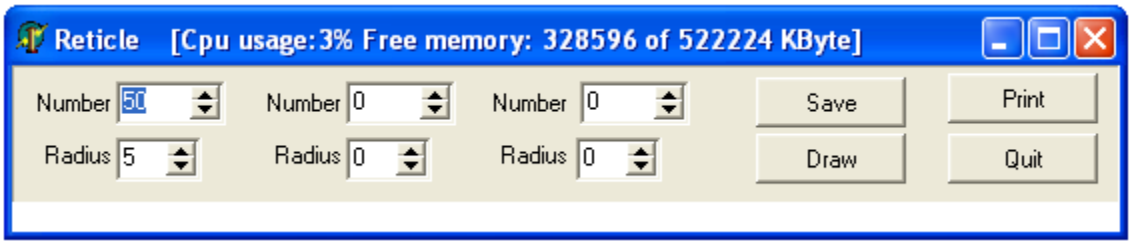

Figure 4-19 Front end of the software used to generate images for particles

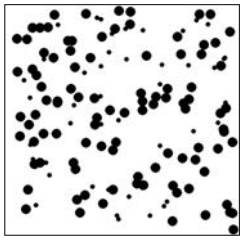
Void Fraction= 0.853

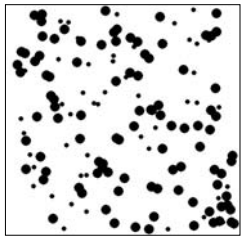
Void Fraction= 0.856

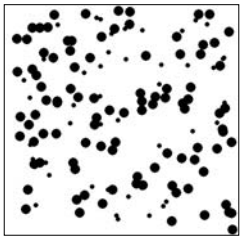
Void Fraction= 0.853

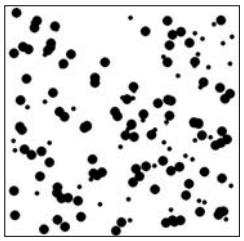
Void Fraction= 0.859

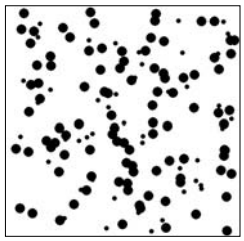
Void Fraction= 0.853

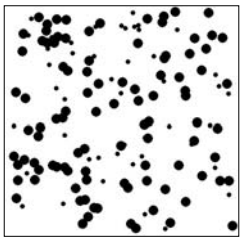
Void Fraction= 0.854

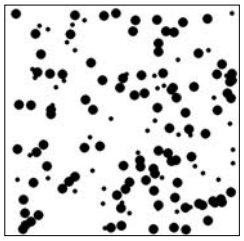
Void Fraction= 0.851

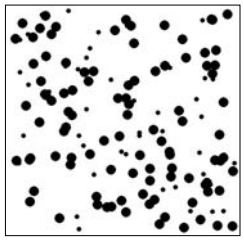
Void Fraction= 0.853

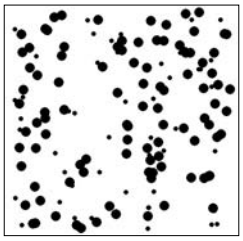
Void Fraction= 0.852

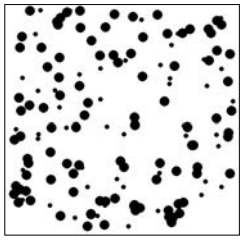
Void Fraction= 0.856

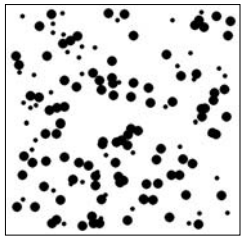
Void Fraction= 0.847

Figure 4-20 Sample of Reticle output for an average void fraction 0.85

Table 4-3 Droplet sizes used for ImageJ calibration

Void Fraction	Number of Droplets	Droplet Diameter (Size#1) [mm]	Number of Droplets	Droplet Diameter (Size#2) [mm]	Number of Droplets	Droplet Diameter (Size#3) [mm]
0.288±0.28	700	5.29	300	2.65	0	
0.355±0.019	200	7.94	80	10.58	10	2.65
0.361±0.033	1000	4.23	0		0	
0.395±0.022	600	5.29	200	2.65	0	
0.437±0.012	200	7.94	40	10.58	80	2.65
0.518±0.005	450	5.29	100	2.65		
0.532±0.012	150	7.94	30	10.58	20	2.65
0.623±0.005	500	4.23	0		0	
0.651±0.009	100	7.94	20	10.58	40	2.65
0.699±0.003	150	5.29	450	2.65		
0.787±0.003	250	4.23	0		0	
0.798±0.009	100	5.29	300	2.65		
0.798±0.009	50	7.94	10	10.58	20	2.65
0.853±0.003	100	5.29	50	2.65		
0.888±0.006	25	7.94	5	10.58	10	2.65
0.913±0.002	50	5.29	50	2.65		

Figure 4-21 depicts the effect of changing the void fraction on the ability of ImageJ to accurately estimate the particle diameter expressed as the ratio of the estimated droplet diameter using ImageJ, D_m, to the actual diameter, D_a. Figure 4-21 shows that the D_m/D_a ratio approaches unity as the void fraction increases. This is due to the decrease in the particles overlap as the void fraction increases. In conclusion, the calibration of ImageJ

shows that it can be used as a tool for estimating the droplet diameter as a function of the void fraction.

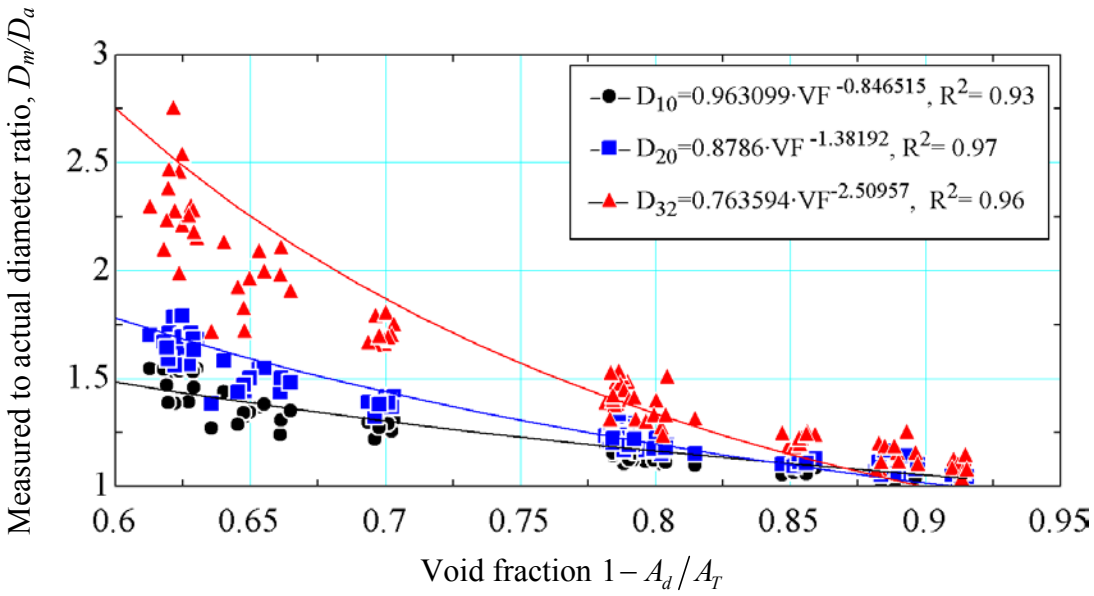

Figure 4-21 Effect of changing the void fraction on the accuracy

4.6.1.2 Image Processing and Enhancement

The first step in any image analysis process to provide real world dimensional measurements is spatial calibration. The spatial calibration is followed by a set of image enhancement operations to improve the image quality. The 31 frames for each run is subjected to the following chronological image enhancement operations; histogram equalization, background-subtraction, despeckle, histogram equalization, and sharpening. Appendix-V illustrates the effect of each of these processes on the experimental images through a sample of processed images in a sequential order. Details of each of these operations are discussed next.

4.6.1.2.1 Spatial Calibration

Spatial calibration defines the spatial scale of the active image so that the measurement results can be presented in calibrated units, such as millimeters. This calibration is achieved by taking a picture of a known scale. The ***straight line*** selection tool in ImageJ is then used to make a line selection that corresponds to a known distance and unit of measurement on the picture. Then, in the ***Set Scale*** dialog from the ***Analyze*** menu, the known distance and unit of measurement are entered.

4.6.1.2.2 Histogram Equalization

Histogram equalization is an image enhancement operation that enhances the image contrast. Equalization redistributes the brightness values of the pixels in an image by reassigning the brightness values of pixels based on the image histogram so that they more evenly represent the entire range of brightness levels (brightness histogram). The histogram shows the number of pixels in the image having each of the 2^8 or 256 possible values of stored brightness or shades of gray. Figure 4-22 shows an example of image with its histogram before and after applying the histogram equalization. The commonly used method is to change each brightness level j in the original image with a new assigned value k that is calculated as

$$k = 256\sum_{i=0}^{j}\frac{x_i}{\mathrm{X}} \tag{4.4}$$

where the summation counts the number of pixels in the image with brightness equal to or less than j and X is the total number of pixels. The result is a linear cumulative histogram.

ImageJ uses a modified algorithm that takes the square root of the histogram values. Consequently, pixels with a brightness value in the middle of the brightness range are more redistributed than those at the ends with brightness values close to zero or 256, as shown in Figure 4-22f.

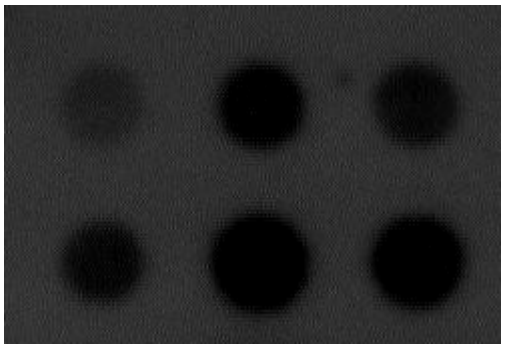

a- Image before histogram equalization

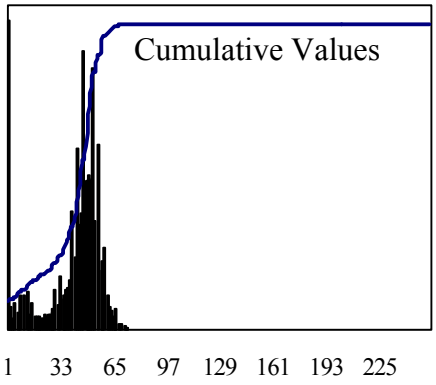

b- Brightness before histogram equalization

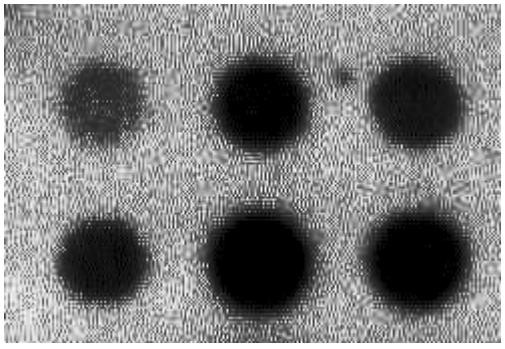

c- Image after histogram equalization

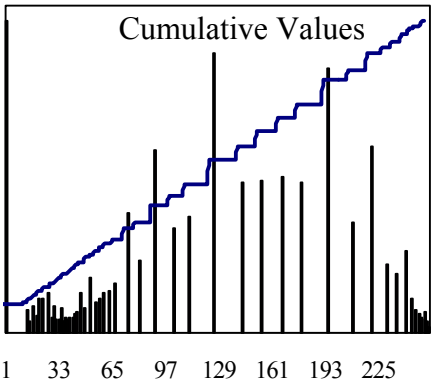

d- Brightness after histogram equalization

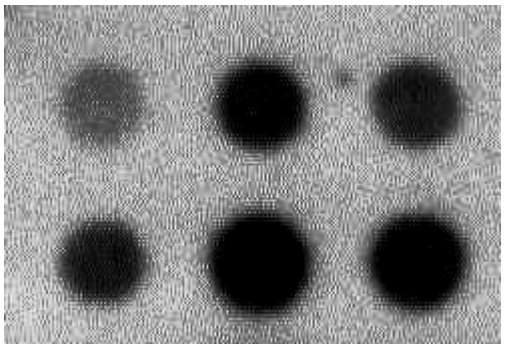

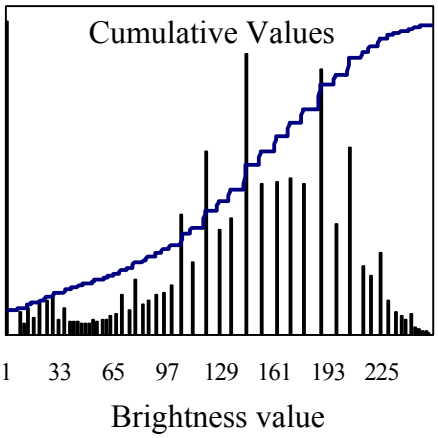

e- Image after equalization using ImageJ f- Brightness after equalization using ImageJ

Figure 4-22 Image for dots before and after applying histogram equalization

4.6.1.2.3 Background-Subtraction

Background-subtraction removes smooth continuous backgrounds from images. It uses a rolling ball algorithm inspired by Stanley Sternberg [18]. The Rolling Ball Radius has to be at least as large as the radius of the largest object in the image that is not part of the background. Figure 4-23 shows an image for water spray before and after applying background-subtraction.

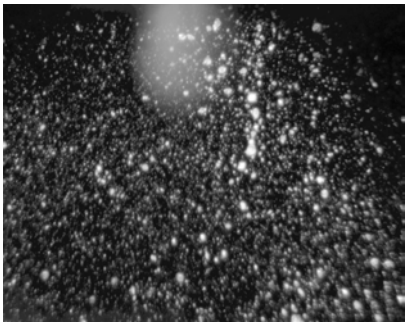

a- Before background-subtraction

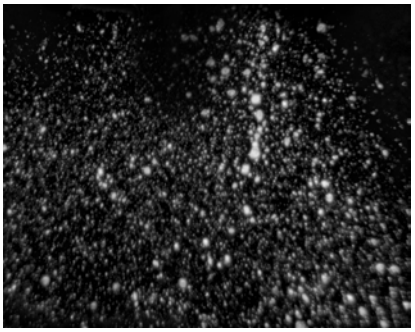

b- After background-subtraction

Figure 4-23 An image for water spray before and after applying background-subtraction

4.6.1.2.4 Despeckle

Despeckle is a neighborhood-averaging operation that is performed on every pixel in the field to reduce noise. The simplest form of spatial averaging is to add the pixel brightness values in a 3×3 neighborhood and divide the sum by the number of pixels in the neighborhood. The resulting value is used to construct a new image. This is often described as a "kernel" operation. Various approaches are used to deal with edge and corner pixels such as

i. Designing asymmetric kernels.
ii. Assuming the image edges are mirrors.
iii. Assuming the image wraps around, i.e. the left and right edges are continuous and the top and bottom are continuous.

The implementation of the kernel operation can be generalized as the sum of the pixel values in the region multiplied by a set of integer weights. The neighborhood sizes range from 3×3, upwards to 5×5, 7×7, etc. A simple 3×3 median filter uses the unity weighting factors and is represented as

$$\begin{matrix} 1 & 1 & 1 \\ 1 & 1 & 1 \\ 1 & 1 & 1 \end{matrix}$$

These coefficients are to be multiplied by pixels surrounding the central pixel. The total is then normalized by dividing it by the sum of the weights and the value is written to the location of the central pixel to form a new image. Figure 4.23 shows the brightness values along the same line for an image, before and after applying 3×3 and 5×5 median filters. This

figure shows the presence of noise and its removal by the two different filters. It should be noted that increasing the neighborhood size results in noise reduction. However this noise reduction is accompanied by a significant blurring of the feature edges. The amount of blurring can be reduced by using weighting factors other than one as shown in the following example [19]

1	2	1
2	4	2
1	2	1

In this example the brightness value of the central pixel is multiplied by 4 causing the central pixel to dominate the average thus reducing blurring. The use of 2 for the orthogonally touching pixels and 1 for the diagonally touching neighbors acknowledges the fact that the diagonal pixels are in fact farther away from the center of the neighborhood.

Thus, the goal of median filters is to reduce noise while preserving all details of the image. Choosing the values for weighting factors is in itself an art that depends on the nature of the image. ImageJ uses a simple 3×3 median filter with unity weighting factors.

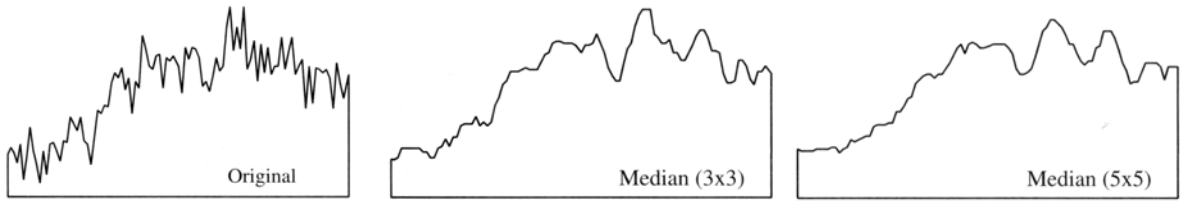

Figure 4-24 Brightness values, before and after applying different median filters [19]

4.6.1.2.5 Sharpening

Sharpening is a filter that increases contrast and accentuates detail in the image or selection to make an image appear more distinct. This filter uses the following weighting factors to replace each pixel with a weighted average of the 3x3 neighborhood.

$$\begin{matrix} -1 & -1 & -1 \\ -1 & 12 & -1 \\ -1 & -1 & -1 \end{matrix}$$

The central pixel is multiplied by 12 and the orthogonal and diagonal touching neighboring pixels are inverted while their magnitudes are unaltered. This causes the central pixel to dominate and make it distinct compared to the 8 neighboring pixels.

4.6.1.3 Sample Size Selection

The atomization process is heterogeneous in nature; droplets may collide with each other or break up into smaller droplets. Consequently, the number of imaging frames significantly affects the ability to achieve a representative average diameter. Therefore, an investigation has been conducted to study the effect of changing the sample size, number of frames, on the accuracy of the estimated spray quality.

In the preliminary experimental phase of the research, an analog camera was used. This limited the number of frames per run to thirty-six, the number of exposures available on a roll of film. As mentioned earlier, the final phases have been conducted using the digital camera. For the purpose of this investigation 10, 20, and 30 frames per run were considered. Figure 4-25 summarizes the results of this investigation. The maximum divergence observed

among the three cases was 12.3%. In conclusion, reducing the number of frames from 30 to 10 reduces the processing time and cost by 66% without sacrificing the accuracy.

It's worth mentioning that the minimum number of frames is also constrained by the total number of measured droplets, as explained earlier in §4.3. The total number of measured droplets is the product of the number of frames and the average number of droplets per frame. Since the minimum number of droplets recorded was 850 droplets per frame, and based on the aforementioned discussion, the number of frames utilized to estimate the average droplet diameter was limited to 10 frames per run.

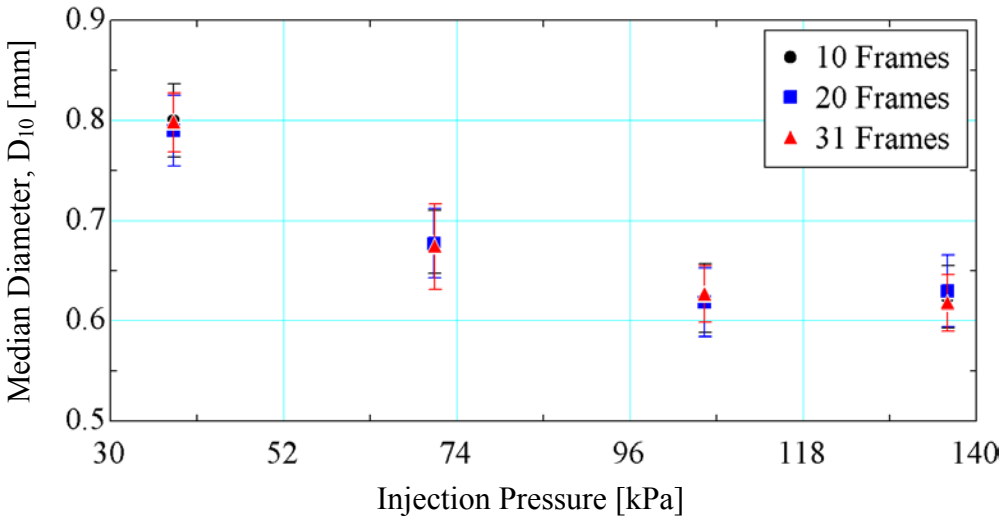

Figure 4-25 Effect of changing the sample size on D_{10}

4.6.2 Spray Cone Angle Measurement

An experimental set up similar to that illustrated in Figure 4-7, without the spray splitters, is used to measure the spray cone angle. A 2.1 MPixel digital still camera; model MVC-FD95 [20] is used to take images for the spray at different volume flow rates. These images are

then analyzed using ImageJ. The image analysis phase is composed of three processes or steps. These are summarized in Figure 4-26. First the original image is inverted, as shown in Figure 4-26a. This process creates a reversed image similar to a photographic negative, as shown in Figure 4-26b. Then comes the second step where the brightness value of the inverted image is multiplied by itself, as shown in Figure 4-26c. The resulting image of the spray is of sharp, identifiable boundaries, hence, the spray cone angle can be easily measured. The spray cone angle is measured by drawing two lines tangential to the cone periphery as shown in Figure 4-26c. ImageJ [15] provides the line inclination, to the horizontal. The spray cone angle is the difference between these two angles.

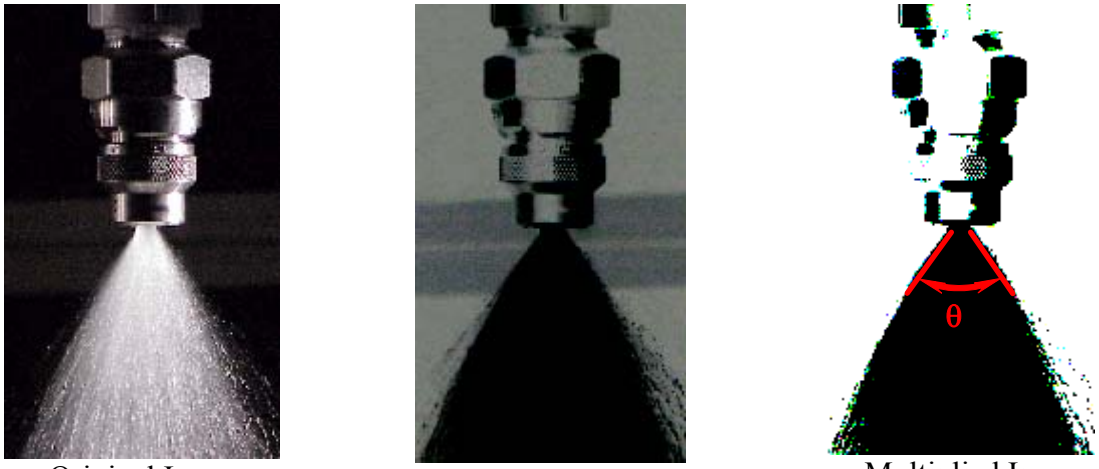

a- Original Immage b- Inverted Image c- Multiplied Image

Figure 4-26 Spray cone angle measurement

4.7 Experimental Results

This section presents the results of the experimental investigation conducted to identify the median diameter, and spray cone angle measurements. Table 4-4 summarizes the results of the experiments conducted to identify the median droplet diameter at different volume flow

rates. Figure 4-27 shows the effect of changing the volume flow rate on the median droplet diameter. The figure shows that as the volume flow rate increases the median diameter decreases. Under equilibrium conditions, the external aerodynamic pressure, represented by $p_a = 0.5\rho_{\text{air}}\left(\left|\underline{U}_\infty - \underline{\text{V}}\right|\right)^2$, and the surface tension pressure, $p_\sigma = {}^{4\sigma}\!/_{D}$, are in balance. Increasing the mass flow rate of water increases the spray velocity and consequently the aerodynamic pressure exerted on the droplet. This increase in aerodynamic pressure results in a breakup of the droplet into smaller droplets until the surface tension pressure is large enough to accommodate for the increase in aerodynamic pressure [2].

Table 4-4 Summary of experimental results

Volume flow rate	**Injection Pressure**	**Void Fraction**	D_{10}	D_{20}	D_{32}
[lit/s]	[kPa]		[mm]	[mm]	[mm]
0.1008	38±0.289	0.961	0.8±0.029	1.413±0.052	3.567±0.439
0.1401	71.12±0.049	0.946	0.6741±0.043	0.9959±0.061	2.797±0.272
0.1723	105.5±0.536	0.931	0.6268±0.028	0.8898±0.048	2.374±0.213
0.1958	136.3±0.243	0.931	0.6178±0.028	0.877±0.040	2.33±0.235

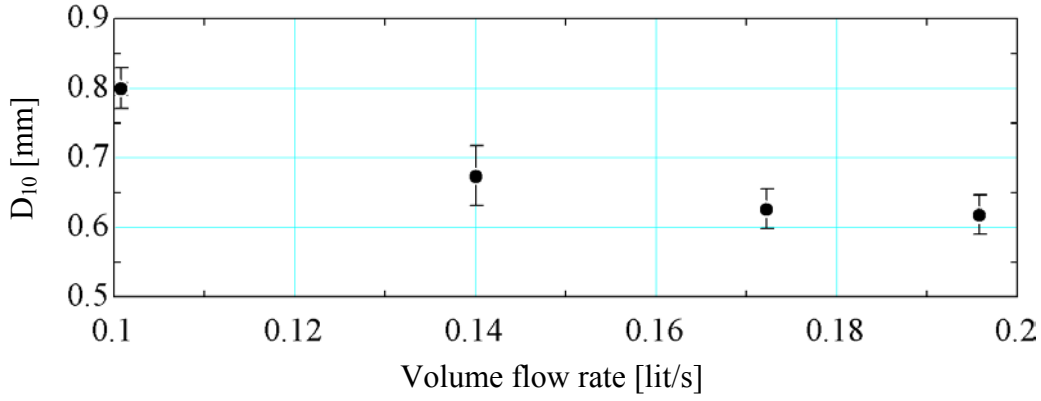

a- Median diameter D_{10}

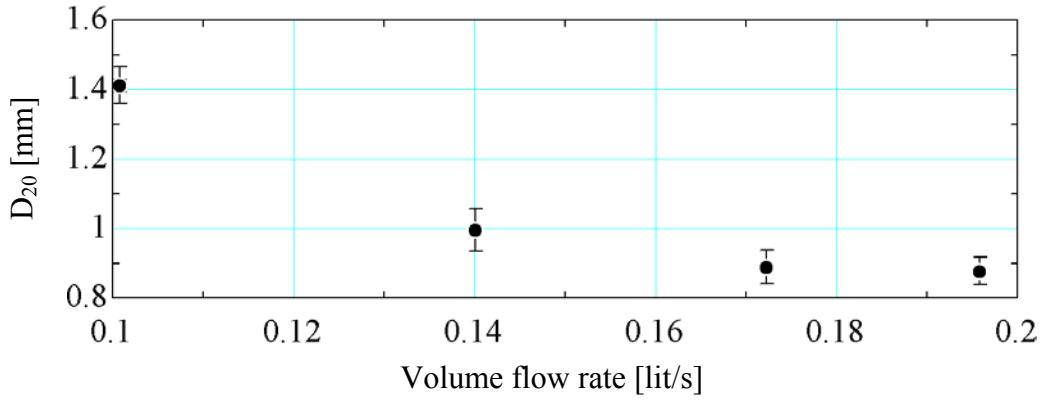

b- Median diameter D_{20}

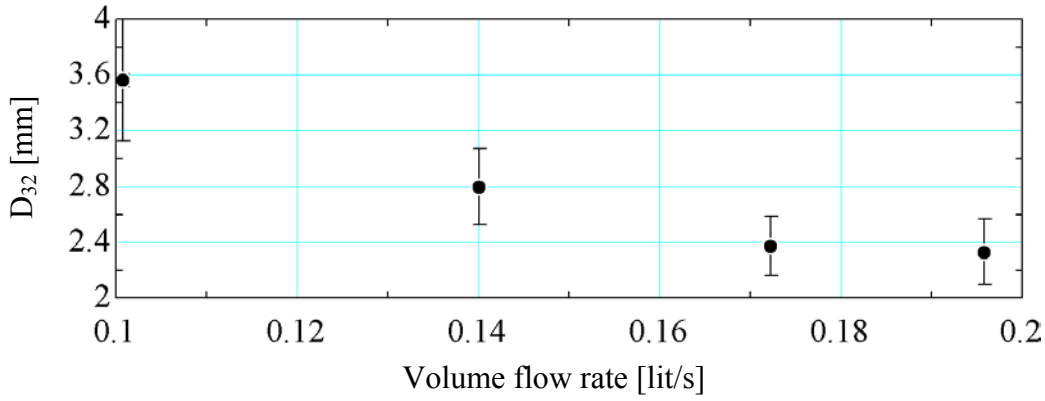

c- Median diameter D_{32}

Figure 4-27 Effect of changing water flow rate on droplet diameter and injection pressure

Figure 4-28 plots the results of the experiment on the chart developed by Reitz [21] to classify the modes of disintegration. The figure shows that the first data point lies is in the second wind-induced breakup regime, while the rest lie in the atomization regime. The common characteristic for both regimes is that the average drop diameter is less than the jet diameter, 4.75 mm, as shown in Table 4-4.

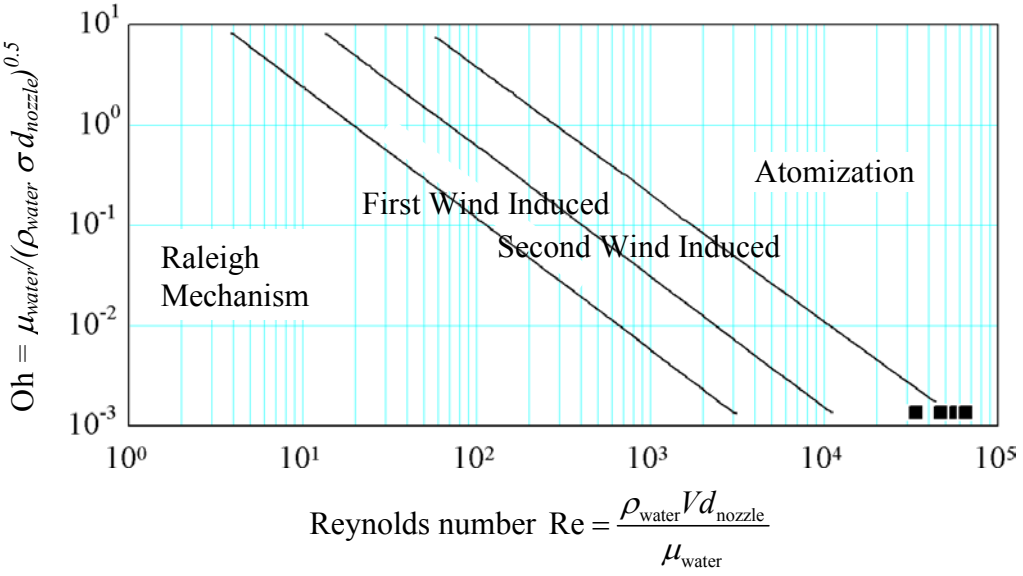

Figure 4-28 Classification of modes of integration [21]

Finally, Figure 4-29 illustrates the effect of changing the injection pressure on the spray cone angle. The figure shows that there is no obvious trend for the effect of varying the injection pressure on the spray cone angle, suggesting that pressure variations do not have a major effect on the spray cone angle.

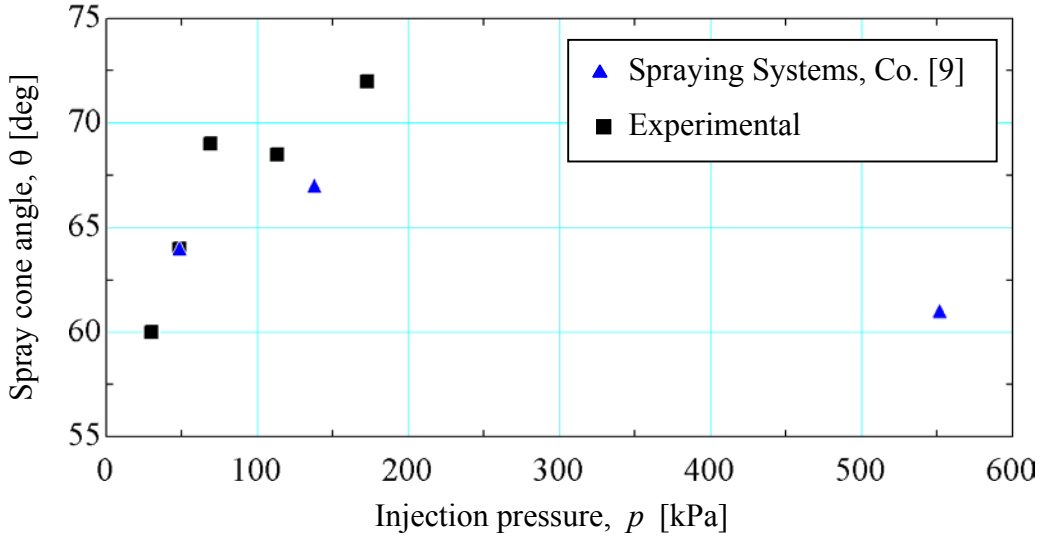

Figure 4-29 Effect of changing nozzle injection pressure on spray cone angle

4.8 Summary

Numerical simulations designed to investigate the performance of spray coolers require information about the macroscopic and microscopic spray structure. In particular, droplet diameter and spray cone angle. This chapter presented the methods used in the current research to experimentally measure both droplet size and spray cone angle for water flowing through a full cone nozzle. The chapter started with defining the most commonly used median droplet diameters, followed by an overview of the most commonly used spray structure measuring techniques available in the literature. A brief description of each method was presented, along with the drawbacks and merits of each technique as well as sources of errors that affect the results. Thereafter, a detailed description of the test facility constructed for sizing the water droplets and measuring the spray cone angle was presented. This is then followed by presenting the image analysis procedures followed to analyze the images and estimate the median diameter and spray cone angle. The chapter ended by giving the median

diameter and spray cone angle at different injection pressures. The results showed that increasing the injection pressure decreases the median diameter. However, there was no concluding trend for the effect of varying the injection pressure on the spray cone angle. This suggests that the pressure variations do not have a major effect on the spray cone angle.

4.9 Nomenclature

A_d	Total projected area of the droplets	mm^2
A_T	Area of the inscribing rectangle	mm^2
D_{ab}	Generalized median diameter	mm
D_a	Actual diameter	mm
D_m	Estimated droplet diameter using ImageJ	mm
D_i	Middle diameter of size range i	mm
D_{10}	Linear average of all drops in the spray	
D_{20}	Surface area average median diameter	
D_{32}	Sauter median diameter	
i	Size range	
j	Brightness level of the original image	
k	Brightness level of the new image	
N_i	Number of drops in the size range i	
p	Injection pressure	kPa
p_a	Aerodynamic pressure	Pa
p_σ	Surface tension pressure	
$\underline{U}_\infty$	Velocity vector of air	m/s
$\underline{V}$	Velocity vector of water	m/s
V	Velocity of water	
x_i	Number of pixels in an image with a certain brightness value	
X	Total number of pixels	

4.9.1 Greek Symbols

θ	Spray cone angle	deg
ρ_{air}	Density of air	Kg/m^3
σ	Surface tension of water	

4.10 References

1 Mugele, R. and Evans, H. D., "Droplet-Size Distribution in Sprays", Ind. Eng. Chem., Vol. 43, No. 6, 1951, pp. 1317-1324.

2 Lefebvre, A. J., "Atomization and Sprays", Hemisphere Publishing Corporation, 1989, ISBN 0-89116-603-3.

3 Wicks, M. and Dukler, A. E., Proceedings of ASME Heat Transfer Conference, Vol. V, Chicago, 1966, pp. 39.

4 Gardiner, J. A. Instrum. Pract., Vol.18, 1964, pp. 353.

5 Tate, R. W., "Some Problems Associated with the Accurate Representation Droplet Size Distributions", Proceedings of the 2nd International Conference on Liquid Atomization and Spray Systems, Madison, WI, June 1982, pp. 341-351.

6 Chin, J. S., Durrette, R., and Lefebvre, A. H., "The Interdependence of Spray Characteristics and Evaporation History of Fuel Sprays", ASME J. Eng. Gas Turbines Power, Vol. 106, 1984, pp. 639-644.

7 Lewis, H. C., Edwards, D. G., Goglia, M. J., Rice, R. I., and Smith, L. W., "Atomization of Liquids in High Velocity Gas Streams", Ind. Eng. Chem., Vol. 40, No. 1, 1948, pp. 67-74.

8 Bowen, I. G., and Davis, G. P., Report ICT 28, Shell Research Ltd., London, 1951.

9 Spraying Systems, Co., North Ave. at Schmale Rd., P.O. Box 7900, Wheaton, IL60189-7900.

10 Omega Engineering, Inc., One Omega drv., P.O. Box4047, Stamford, CT 06907-0047, www.omega.com.

11 The Cooke Corporation, 1091 Central Road, Suite 100, Auburn Hills, MI 48326-2670, www.cookecorp.com.

12 Roper Scientific, 3660 Quakerbridge Road, Trenton, NJ 08619, www.photomet.com.

13 Berkeley Nucleonics Corp., 3060 Kerner Blvd., #2. San Rafael, CA 94901, www.berkeleynucleonics.com.

14 Upper Canada Technologies, www.uct.on.ca.

15 ImageJ 1.27z, National Institute of Health, rsb.info.nih.gov/ij

16 Hung, C. C., "Insights into Droplet Behavior within High Pressure Diesel Sprays", PhD thesis, UW-Madison, 1998.

17 Omer, L. G., Gregory J. S., and David R. S., "Diesel Spray Structure Investigation by Laser Diffraction and Sheet Illumination", SAE Paper No. 920577, 1992.

18 Biomedical Image Processing", IEEE Computer, January 1983.

19 John C. Russ, "The image processing Handbook", 3rd ed., CRC Press, 1999, ISBN 0-8493-2532-3.

20 Sony Corporation of America, www.sony.com.

21 Reitz, R. D., “Atomization and Other Breakup Regimes of a Liquid Jet”, Ph.D. thesis, Princeton University, 1978.

Chapter 5 Numerical Simulations

Numerical simulations provide a tool for examining the performance of new spray coolers designs. Even though experimentation remains the best tool to obtain definitive results, numerical simulations offer several advantages. First, numerical simulations are relatively inexpensive and fast. Second, accurate simulation models make it possible to examine a given design before setting up experiments to test it. Hence, minimizing the number of prototypes that need to be tested. Third, numerical simulations offer an easy way for executing parametric studies. Finally, results from numerical simulations help in selecting which experiments need to be performed.

In the current research work, studying the effect of changing one parameter, e.g. droplet diameter, water mass flow rate, and/or injection velocity, on the performance of the spray chamber while keeping all other parameters unaltered is experimentally difficult to achieve. The difficulty arises because different nozzle sizes are required for each set of experiments and each experiment requires an imaging procedure to estimate the size of the water droplets. As a result, experimental tests are expensive and time consuming. To overcome this difficulty and to study the spray chamber performance in detail, numerical simulations are conducted. This chapter discusses the numerical analysis conducted to study the effect of changing the droplet diameter, water-mass flow rate, and air mass-flow rate on the performance of the spray chambers.

Figure 5-1 summarizes the work scheme of the for the numerical analysis documented in this chapter. The figure shows that the work scheme incorporates two phases: i) model validation and ii) parametric study. In the first phase, the numerical model, developed using the commercial software package FLUENT [1], is validated. Validation of the model is an essential step to confirm that the results obtained from the numerical simulations are consistent with those obtained from the experiments. To validate the model, FLUENT [1] requires two types of inputs. The first is the inlet temperatures and mass flow rates for both the air-side and the water-side. The second is the mean droplet diameter. Consequently, the model is validated by running the numerical experiments under the same inlet conditions of the experiment, discussed in Chapter 3, and using the mean droplet diameter measured by droplet image processing, as discussed in Chapter 4. In the second phase, a parametric study is conducted to investigate the effect of the droplet diameter and the initial speed-ratio on the performance of the spray cooler. This is done by providing FLUENT [1] the mean droplet diameter and initial speed-ratio, performing the numerical simulations and finally analyzing the results of the parametric study.

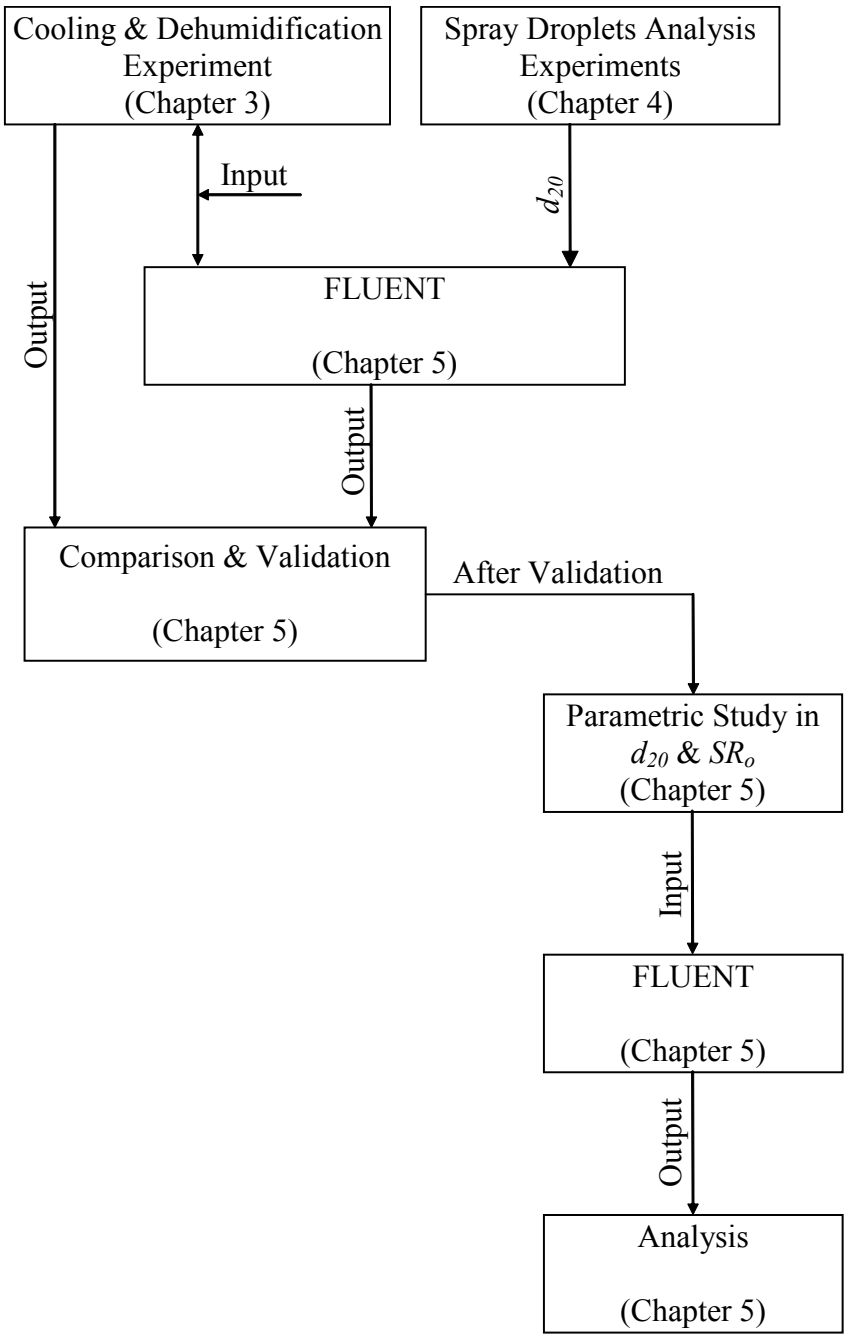

Figure 5-1 Summary for work scheme

The chapter begins by describing the problem under investigation. Next, the equations that govern the heat and mass transfer processes in the spray chamber are presented and discussed, including a summary of assumptions used to simplify the analysis. The physical properties used in the analysis are then presented, and the chapter closes by discussing the results of the numerical simulations.

5.1 Problem Description

This section provides a brief description of the spray cooler under investigation. The spray cooler is a 1 × 0.2 × 1 m chamber with a spray nozzle located at its center. Air enters the cooler, from one end, at a constant volumetric flow rate, while chilled water is sprayed in a counter flow direction, as shown in Figure 5-2. The spray cooler is simulated as a 2-D insulated duct with a dummy extra length to the left of the nozzle. This extra length is added to the chamber to satisfy FLUENT [1] outlet boundary conditions, as discussed in §5.2.2.

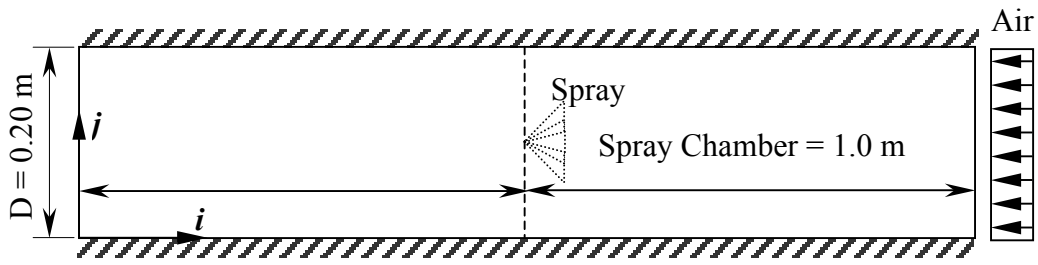

Figure 5-2 Schematic for the spray cooler

The spray cooler is numerically simulated using a uniform grid of 898 cells in the horizontal direction, i, and 70 cells in the vertical direction, j, i.e. 63,000 cells. The grid size is selected based on the desired accuracy of the solution and the droplet diameter, as shown in Figure

5-3. The governing equations are solved for different values of grid size until the offset in energy balance, $\Delta\dot{Q}_{\text{offset}}$, between the air-side and water-side is no greater than 3.5%. Beyond this value, the variation of the offset experience very slight variation with decreasing the grid size, i.e., increasing the number of cells as shown in Figure 5-2. This comes in a reasonable agreement with the experimental offset which is in the range of -1.94%-6.55%. The offset in energy balance is defined as:

$$\Delta\dot{Q}_{\text{offset}} = \frac{\text{MAX}\left(\left|\dot{Q}_{\text{air}}\right|,\left|\dot{Q}_{\text{water}}\right|\right) - \text{MIN}\left(\left|\dot{Q}_{\text{air}}\right|,\left|\dot{Q}_{\text{water}}\right|\right)}{\text{MIN}\left(\left|\dot{Q}_{\text{air}}\right|,\left|\dot{Q}_{\text{water}}\right|\right)} \tag{5.1}$$

where $\dot{Q}_{\text{air}}$ and $\dot{Q}_{\text{water}}$ are the rates of energy transferred from the air and to the water respectively. A value of $\Delta\dot{Q}_{\text{offset}}$ of 0.035 corresponds to an error in reporting the air-side exit temperature, $\Delta T_{\text{air}_{\text{error}}}$, of 0.2ºC, and 0.05ºC for the water-side exit temperature, $\Delta T_{\text{water}_{\text{error}}}$, where the error is defined as:

$$\Delta T_{\text{air}_{\text{error}}} = \text{MAX}\left(T_{\text{air}}\big|_{\text{actual}}, T_{\text{air}}\big|_{\Delta\dot{Q}_{\text{offset}}=0}\right) - \text{MIN}\left(T_{\text{air}}\big|_{\text{actual}}, T_{\text{air}}\big|_{\Delta\dot{Q}_{\text{offset}}=0}\right) \tag{5.2}$$

$$\Delta T_{\text{water}_{\text{error}}} = \text{MAX}\left(T_{\text{water}}\big|_{\text{actual}}, T_{\text{water}}\big|_{\Delta\dot{Q}_{\text{offset}}=0}\right) - \text{MIN}\left(T_{\text{water}}\big|_{\text{actual}}, T_{\text{water}}\big|_{\Delta\dot{Q}_{\text{offset}}=0}\right) \tag{5.3}$$

where $T_{\text{air}}\big|_{\Delta\dot{Q}_{\text{offset}}=0}$, and $T_{\text{water}}\big|_{\Delta\dot{Q}_{\text{offset}}=0}$ are the temperatures of air and water at $\Delta\dot{Q}_{\text{offset}} = 0$, respectively.

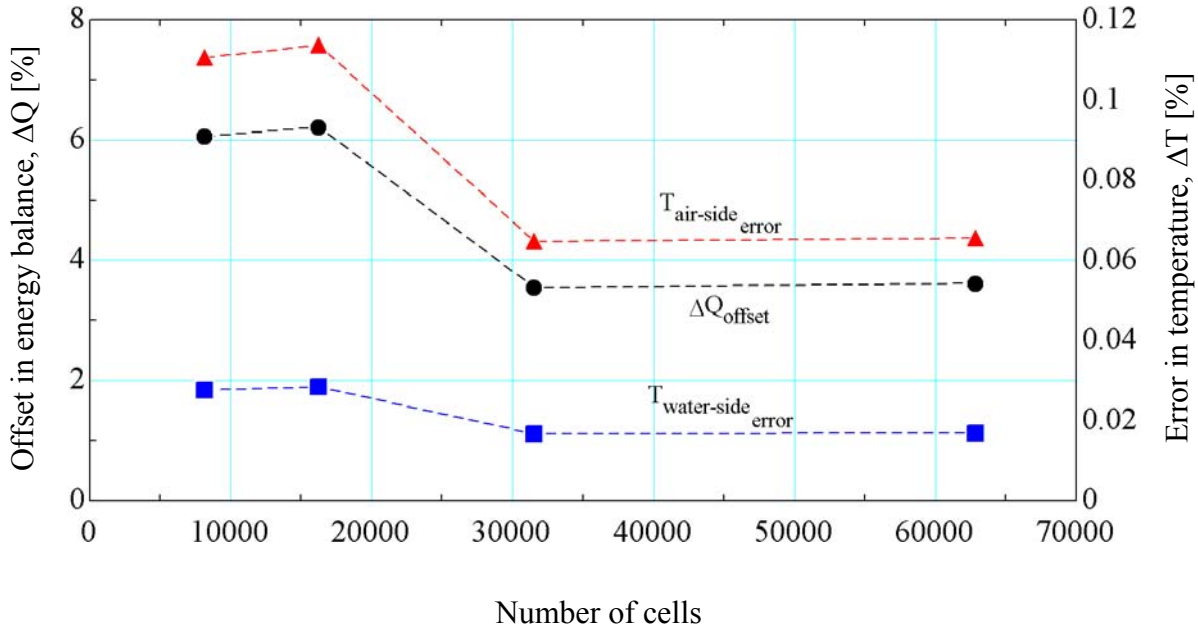

Figure 5-3 Effect of changing the grid spacing on the overall energy balance between the water-side and air-side

5.2 Physical Models and Boundary Conditions

The physical models used in the analysis and the spray chamber boundary conditions are discussed in this section. The equation set includes solution of turbulent flow with heat transfer and species transport. A turbulence model is required to solve these transport equations, since the air flows in the chamber at a Reynolds number of 61,200 which is greater than the critical value of 2,300 for internal flows [2]. The $k-\varepsilon$ turbulent model has been chosen to model the problem. However, it should be mentioned that the re-normalization group (RNG) $k-\varepsilon$ has been consulted for some randomly selected cases and the results were in good agreement with the chosen model.

Inputs to the numerical model include the inlet conditions for both the continuous phase, air, and the dispersed phase, water. Air-inlet conditions include temperature and velocity. The inlet conditions for the water-side are the initial temperature, velocity, droplet diameter, mass flow rate and number of injections. Also, the wall boundary conditions of the spray chamber are specified.

Air enters the spray cooler at an initial temperature of 303 K while water is sprayed at a temperature of 275 K. The water injection rate, water velocity and droplet diameter are varied, as shown in Table 5-1, to study their effect on the spray cooler performance. Details of the boundary conditions are discussed next.

Table 5-1 Test matrix

Air-side inlet							***Water-side inlet***	
Temperature [K]		Velocity [m/s]					Temperature [K]	Mass flow rate [kg/s]
303		-5					275	0.5
Droplet Diameter [mm]								
0.75	1		1.2		1.4	1.6		1.8
Initial speed- ratio								
0.25	0.5	-0.75		1		2	3	4

5.2.1 Air-Side Inlet

The "velocity inlet" boundary condition is used to define the air-side inlet of the spray chamber. This, "velocity inlet" boundary condition requires knowledge of the Cartesian velocity components, the velocity profile, the turbulence intensity, the length scale, and the air inlet temperature. Air enters the computational domain, i.e., the spray cooler, axially at a

temperature of 303 K with a uniform velocity profile. Since the velocity vector points in the negative coordinate direction, the velocity vector is negative. The turbulence intensity, defined as the ratio of the root-mean-square turbulent velocity fluctuations to the mean velocity, u'/u_∞, is set to 10%. The turbulence intensity at the inlet, I, is used to calculate the turbulent kinetic energy, k, [1] using

$$k = \frac{3}{2}\left(u_\infty I\right)^2 \tag{5.4}$$

The turbulence integral length scale at inlet, ℓ, is restricted by the size of the duct, since this is the largest scale in the problem that can affect the turbulent eddies. The maximum value for the mixing length in fully developed turbulent flow in a pipe is $0.07D$ [1], where D is the duct width. Consequently, ℓ, is defined as

$$\ell = 0.07D \tag{5.5}$$

5.2.2 Air-Side Outlet

The "outlet" boundary condition in FLUENT is used to model the flow outlet. Since the details of the flow velocity and pressure are not known prior to the solution of the problem, the built in boundary condition used by FLUENT assumes

1. Zero diffusion flux for all flow variables except pressure
2. Overall mass balance correction.

The zero diffusion flux condition means that the conditions at the outlet plane are extrapolated from within the computational domain and have no impact on the upstream flow. This is also commonly referred to as a “natural” boundary condition. The

extrapolation procedure used by FLUENT updates the outlet velocity and pressure in a manner that is consistent with a fully-developed flow assumption where there is no area change at the outlet [1]. The outlet section extends for 1 m behind the nozzle to give the flow a chance to approach a fully-developed flow at the outlet to satisfy FLUENT outlet boundary condition. The overall mass balance correction applied at outlet cells accelerates convergence, but has no other impact on the final solution. This mass balance correction is zero when flow solution is converged and a mass balance is obeyed locally in each control volume [1].

5.2.3 Water Inlet

Water, at a temperature of 275 K, is sprayed into the air stream. The primary inputs for the dispersed phase calculations are the initial conditions such as the initial positions and initial velocities for each droplet. These initial conditions provide the starting values for the variables that describe the instantaneous conditions of an individual droplet including its position, x, y, z, velocity components, $\underline{u}_o, \underline{v}_o, \underline{w}_o$, diameter, temperature and mass flow rate of the droplet stream following the trajectory of the individual droplet. These dependent variables are updated according to the equation of motion, equation (5.24), and according to the heat and mass transfer between the air and an individual droplet as it moves along its trajectory.

Initial conditions for the dispersed phase are referred to in FLUENT as "Injections", with each set of initial conditions represented by an injection number. The injection number label is an integer between 1 and the upper limit of the number of injections specified. A group of

multiple injections is used to define a range of initial velocities for a stream of droplets such that a spray of droplets is represented, as shown in Figure 5-4. Each injection that is part of the group has initial conditions based on the inputs in the initial conditions table. In the initial conditions table the initial condition, ϕ_1, for the first injection and the initial condition, ϕ_2, for the last N$^{\underline{th}}$ injection are defined. FLUENT assigns a value of ϕ_1 to the $I^{\underline{th}}$ injection in the group using a linear variation between the first and last values for ϕ

$$\phi_I = \phi_1 + \frac{\phi_2 - \phi_1}{N-1}(I-1) \tag{5.6}$$

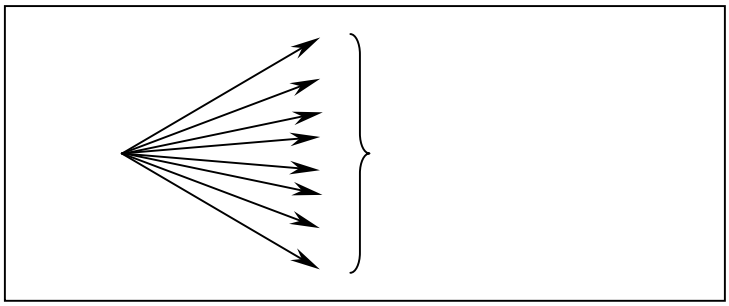

Figure 5-4 Droplet injection defining an initial spray distribution of the droplet velocity

The spray under investigation is represented by 100 injections. The solid 2-D spray angle is defined by setting the initial $\underline{u}_o$ and $\underline{v}_o$ velocity of the first and last injections, where $\underline{u}_o$ and $\underline{v}_o$ are the horizontal and vertical velocity components, respectively. The mass flow rate for each injection is the total water mass flow rate divided by the number of injections. Table 5-2 summarizes the initial conditions for this investigation.

The dispersed phase boundary conditions are applied on each droplet as soon as it reaches a physical boundary, inlet boundary, outlet boundary, or walls, to determine the fate of the trajectory. At the inlet and outlet boundaries, the droplets escape the computational domain. However, at the walls two different scenarios are investigated. The first scenario assumes a unity coefficient of restitution, e, i.e. all droplets perfectly reflect back from the walls to participate again in the heat and mass transfer process. This case is referred to as the "reflect" wall boundary condition. The second scenario assumes that the droplets escape the computational domain as soon as they reach the walls. This case is referred to as the "escape" wall boundary condition. These two scenarios bracket the range of possibilities for all wall conditions. The coefficient of restitution, e, is defined as

$$e = \frac{v_{2n}}{v_{1n}} \tag{5.7}$$

where v_{in} is the droplet velocity component normal to the wall and the subscripts 1 and 2 refer to before and after collision, respectively. A unity coefficient of restitution implies that the droplet retains all of its normal momentum after colliding with the wall.

Table 5-2 Spray initial conditions

1st X-location [m]	1
1st Y-location [m]	0.1
2nd X-location [m]	1
2nd Y-location [m]	0.1
1st U-velocity [m/s]	Refer to test matrix Table 5-1
1st V-velocity [m/s]	Refer to test matrix Table 5-1

Table 5-2 continued	
1st W-velocity [m/s]	0
2nd U-velocity [m/s]	Refer to test matrix Table 5-1
2nd V-velocity [m/s]	Refer to test matrix Table 5-1
2nd W-velocity [m/s]	0
1st Temperature [K]	275
2nd Temperature [K]	275
Minimum diameter [m]	Refer to test matrix Table 5-1
Maximum diameter [m]	Refer to test matrix Table 5-1
1st Mass flow rate [kg/s]	Refer to test matrix Table 5-1
2nd Mass flow rate [kg/s]	Refer to test matrix Table 5-1

5.3 Governing Equations

This section presents the basic equations, solved by FLUENT, that govern the process of heat and mass transfer from/to the air-side to the water-side. The governing equations, mass, momentum, and energy, are written for the spray chamber taken as the control volume of interest. Although these equations are derived and simplified based on a set of assumptions, summarized in §5.5, they are still complex. This complexity is mainly due to the fact that the equations are linked together in a way that makes the closed form solution intractable. Consequently, the numerical approach offers a tractable alternative to solve the necessary governing equations. The governing equations are solved numerically using the by dividing the domain of interest into a finite number of computational cells, finite difference techniques, and the gas phase and liquid phase equations are solved using FLUENT.

5.3.1 Heat and mass transfer calculations

Consider the water droplet shown in Figure 5-5 which is at a temperature T_w less than the moist air dew point temperature. The dry bulb temperature and humidity ratio of the moist air are T and ω, respectively. This difference in temperature and concentration between the air-side and the water-side creates a potential for heat and mass transfer. The mechanisms by which heat and mass transfer occur are outlined in Figure 5-6. The heat transfer to the water droplet is composed of two components: sensible (conduction, convection, and radiation) due to the temperature difference, and latent due to concentration gradient. The energy balance for the water droplet in a differential volume, dV_ℓ in m^3 is

$$\frac{dE_{\text{water}}}{d\text{t}} = \delta\dot{Q}_{\text{water}} = m_{\text{water}}\, c_{\text{water}} \frac{dt_{\text{water}}}{d\text{t}} + t_{\text{water}}\, c_{\text{water}} \frac{dm_{\text{water}}}{d\text{t}} + t_{\text{cond}}\, c_{\text{water}} \frac{dm_{\text{cond}}}{d\text{t}} \qquad (5.8)$$

where, m_{water} is the mass of the water droplets in kg, c_{water} is the specific heat in J/kg-ºC of pure water at the water temperature t_{water} in ºC, and m_{cond} is the air moisture condensing on the water droplet. The energy balance for the air-side for the same differential volume is

$$\frac{dE_{\text{air}}}{d\text{t}} = \delta\dot{Q}_{\text{air}} = -m_{\text{air}} \frac{dh_{\text{air}}}{d\text{t}} - h_{\text{air}} \frac{dm_{\text{air}}}{d\text{t}} - t_{\text{cond}}\, c_{\text{water}} \frac{dm_{\text{cond}}}{d\text{t}} \qquad (5.9)$$

where m_{air} is the mass of dry air in kg, h_{air} is the specific enthalpy of moist air in J/kg of dry air.

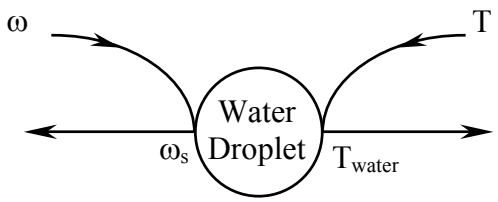

Figure 5-5 Variation of temperature and humidity ratio of air as it approaches the water droplet

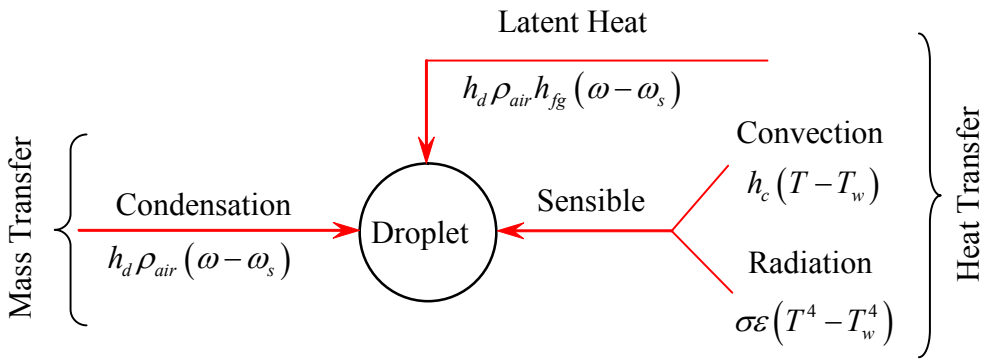

Figure 5-6 Heat and mass transfer to a water droplet [3]

The spray cooler is well insulated and assumed to be adiabatic.

$$\frac{dE_{\text{water}}}{d\text{t}} = \frac{dE_{\text{air}}}{d\text{t}} = \delta\dot{Q} \tag{5.10}$$

Substituting equation (5.8) and equation (5.9) at steady state into equation (5.10) gives

$$\delta\dot{Q} = \dot{m}_{\text{water}} dh_{\text{water}} + h_{\text{water}} d\dot{m}_{\text{water}} + t_{\text{cond}}\, c_{\text{water}} d\dot{m}_{\text{cond}} = -\dot{m}_{\text{air}} dh_{\text{air}} - t_{\text{cond}}\, c_{\text{water}} d\dot{m}_{\text{cond}} \tag{5.11}$$

The change in the energy of the water droplets in the control volume is due to sensible heat transfer and latent heat. The sensible heat transfer can be expressed as

$$\delta\dot{Q}_{\text{sensible}} = A_{\text{v}}\, dV_{\ell}\, h_c (T - T_{\text{w}}) + A_{\text{v}}\, dV_{\ell}\, h_{\text{r}} (T - T_{\text{w}}) \tag{5.12}$$

where A_v is the total interfacial area in m^2 for water droplets contained in the control volume, h_c and h_r are the convection and radiation heat transfer coefficients, respectively, in W/m^2-K. The radiation heat transfer coefficient is defined as

$$h_r = \sigma \varepsilon \left(T^2 + T_w^2 \right) \left(T + T_w \right) \tag{5.13}$$

The change in the water droplet mass, $d\dot{m}_{water}$, in the differential volume dV_ℓ due to the condensation of the water vapor from the air-side is controlled by the mass transfer coefficient, h_d, and the concentration difference expressed in terms of the humidity ratio, ω, as follows

$$d\dot{m}_{water} = d\dot{m}_{cond} = -\dot{m}_{air} d\omega = A_v \, dV_\ell \, h_d \, \rho_{air} \left(\omega - \omega_s \right) \tag{5.14}$$

where, h_d is the mass transfer coefficient in m/s, ω is the humidity ratio of the main air stream, ω_s is the humidity ratio at the water droplet surface calculated using the water droplet temperature and 100% relative humidity, and ρ_{air} is the density of moist air in kg/m^3 calculated at the local temperature and humidity ratio. This mass transfer invokes a latent heat transfer expressed as

$$\delta \dot{Q}_{latent} = A_v \, dV_\ell \, h_d \, \rho_{air} \, h_{fg} \left(\omega - \omega_s \right) \tag{5.15}$$

where, h_{fg} is the latent heat of condensation in J/kg calculated at the dew point temperature. Combining equation (5.12) and equation (5.15), the heat transfer from the air-side to the water-side can be expressed as

$$\delta\dot{Q} = A_{\mathrm{v}} dV_{\ell} \left[h_c \left(T - T_{\mathrm{w}} \right) + h_{\mathrm{r}} \left(T - T_{\mathrm{w}} \right) + h_d \, \rho_{\mathrm{air}} \, h_{fg} \left(\omega - \omega_{\mathrm{s}} \right) \right] \tag{5.16}$$

Equation (5.16) can not be used without defining the local heat and mass transfer coefficients h_c and h_d for the droplets. Ranz and Marshall [4] suggested the following two correlations for single droplets

$$\mathrm{Nu} = \frac{h_c d}{k} = 2 + 0.6 \, \mathrm{Pr}^{1/3} \, \mathrm{Re}^{1/2} \tag{5.17}$$

$$\mathrm{Sh} = \frac{h_d d}{D_{AB}} = 2 + 0.6 \mathrm{Sc}^{1/3} \, \mathrm{Re}^{1/2} \tag{5.18}$$

where Nu is the Nusselt number, Sh is the Sherwood number, and Re is the relative Reynolds number based on the relative speed between the droplet and the carrier gas.

$$\mathrm{Re} = \frac{\rho_{\mathrm{air}} \left| \underline{U}_{\infty} - \underline{\mathrm{V}} \right| d}{\mu_{\mathrm{air}}} \tag{5.19}$$

where d is the droplet diameter in m, and $\underline{U}_{\infty}$ and $\underline{\mathrm{V}}$ are the velocity vectors of the continuous phase, air, and the dispersed phase, water droplet, in m/s, respectively. Pr is the Prandtl number defined by

$$\mathrm{Pr} = \frac{\mu_{\mathrm{air}} c_{p_{\mathrm{air}}}}{k_{\mathrm{air}}} \tag{5.20}$$

where μ_{air}, $c_{p_{\mathrm{air}}}$ and k_{air} are the viscosity, specific heat and thermal conductivity of air at the in kg/m-s , J/kg-K and W/m-K, respectively. Sc is the Schmidt number, defined by

$$Sc = \frac{\nu_{\text{air}}}{D_{\text{AB}}} \tag{5.21}$$

where ν and D_{AB} are the kinematic viscosity and mass diffusivity or diffusion coefficient in m^2/s, respectively.

In this section the equations necessary to calculate the heat and mass transfer between the air-side and the water-side are presented. Examining the terms in equation (5.14) it can be shown that the change in the water droplet mass, $d\dot{m}_{\text{water}}$ can be neglected. This is due to the fact that the term $(\omega - \omega_{\text{s}})$ is in the order of 10^{-3} and h_d is in the order of 10^{-1}. Accordingly, condensation and the associated latent load can be neglected. This reduces equations (5.11) and (5.16) to:

$$\delta\dot{Q} = \dot{m}_{\text{water}} dh_{\text{water}} = -\dot{m}_{\text{air}} dh_{\text{air}} \tag{5.22}$$

$$\delta\dot{Q} = A_{\text{v}} dV_{\ell} \left[h_c \left(T - T_{\text{w}} \right) + h_{\text{r}} \left(T - T_{\text{w}} \right) \right] \tag{5.23}$$

The above assumption is supported by the experimental results. The experimental results show that the latent load comprises only 7.5% of the total load. Accordingly, if the latent load were to be neglected the spray cooler would behave principally as a sensible cooler. For this assumption, the effectiveness will be 10% higher and the exit dry-bulb temperature would be 1.29 ºC lower (7%). For a sensible cooler, one of the main parameters that control the cooler performance is the interfacial area of the spray, which is the sum of the surface areas of all droplets. For a surface area controlling application, the surface area median diameter, d_{20}, should be used [5]. Therefore, hereinafter the d_{20} will be referred to as d

At this point the only piece of information missing is the particles instantaneous velocity. The following section presents the equations necessary to calculate the instantaneous droplet velocity and position.

5.3.2 Trajectory calculations

The last piece of information necessary to model the spraying process is the particle trajectory expressed in terms of droplet velocity and position. The trajectories of the dispersed phase, water droplets, obey the Newtonian dynamics laws and are calculated by applying a force balance written in the Lagrangian reference frame. The force balance equates the droplet inertia with forces acting on it, as shown in the following equation [6]:

$$m_d \underline{V} \frac{d\underline{V}}{dx} = \underline{F}_{ss} + m_d \underline{g} + \underline{F}_{\Delta p} + \underline{F}_{\text{us}} + \underline{F}_{\text{L}} \tag{5.24}$$

where, m_d, is the droplet mass in kg and $\underline{V}$ is the velocity vector of the water droplet in m/s. The right hand side of equation (5.24) represents all the force vectors acting on the droplet. The first term $\underline{F}_{ss}$ is the steady state viscous drag, the second term in the gravity force. $\underline{F}_{\Delta p}$ is the force exerted on the droplet as result of static pressure gradient in the gas. $\underline{F}_{\text{us}}$ is the unsteady force due to the acceleration of the droplet, and $\underline{F}_{\text{L}}$ is the lift force due to droplet rotation. Each of aforementioned terms will be discussed below.

5.3.2.1 Steady state drag

The steady-state drag is the aerodynamic force that opposes the motion of the particles through the continuous phase. The drag force is generated due to the interaction between the

particles and the continuous phase and acts in a direction opposite to the velocity of the particles. The steady-state drag arises from two sources, skin friction and form drag. The skin friction is associated with the development of the boundary layer due to the fluid viscosity, shear stress, and it scales with Reynolds number. The form drag is associated with the pressure distribution, normal stress, over the entire body and is proportional to the square of the particle velocity. The drag force is quantified by the drag coefficient, C_d, as

$$\underline{\mathrm{F}}_{ss} = C_d \frac{1}{2} \rho_{air} A_d \left(\underline{U}_\infty - \underline{\mathrm{V}}\right)\left|\underline{U}_\infty - \underline{\mathrm{V}}\right| \tag{5.25}$$

where A_d is the frontal area of the droplet m^2, ρ_{air} is the density of moist air in $\mathrm{kg/m}^3$, $\underline{U}_\infty$ and $\underline{\mathrm{V}}$ are the velocity vectors of the continuous phase, air, and the dispersed phase, water droplet, in m/s, respectively. The drag coefficient, C_d, depends on the particle shape and Reynolds number. The variation of drag coefficient with Reynolds number for a non-rotating sphere is shown in Figure 5-7. At very small Reynolds numbers, $\mathrm{Re} \le 0.1$, the viscous forces dominate and the inertial forces becomes negligible [6] the flow is regarded as a creeping flow. This regime is known as Stokes flow and the coefficient of drag in this region is defined as

$$C_d = \frac{24}{\mathrm{Re}} \tag{5.26}$$

As the Reynolds number increases the inertial forces becomes significant and can't be neglected. At a Reynolds number ~ 100 the flow begins to separate and vortices are formed behind the sphere giving rise to form drag. With the Reynolds number increasing the form-

drag dominates, and the drag coefficient approaches a constant value of approximately 0.4, owing to the proportionality of the drag force with the square of the velocity. This regime of constant drag coefficient is referred to as the inertia range or the Newton's law [6], and it extends in the Reynolds number range of $750 < \mathrm{Re} < 3.5\times10^5$. At the critical Reynolds, $\mathrm{Re} \sim 0.5\times10^5$, the boundary layer becomes turbulent and the separation point is moved backward. This causes a significant decrease in the form-drag causing a sudden decrease in the drag coefficient.

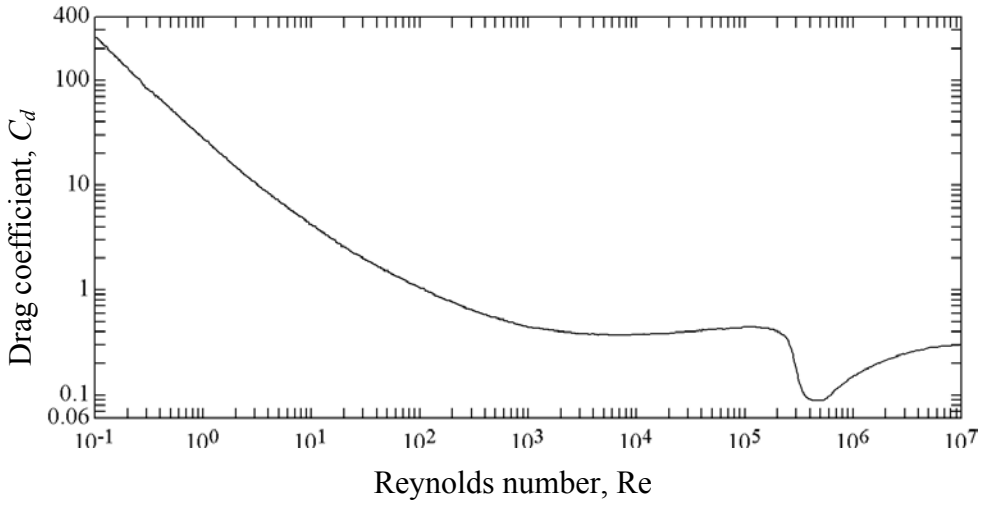

Figure 5-7 Variation of the drag coefficient of a sphere with Reynolds Number [7]

In the intermediate range $0.1 < \mathrm{Re} < 750$ the drag coefficient varies with Reynolds in a complicated manner. Many empirical formulae have been suggested in the literature to describe the Reynolds number-drag coefficient relation in that range. For example while according to Prandtl [8]

$$C_d = \frac{24}{\mathrm{Re}} + 1 \qquad (\mathrm{Re} < 1000) \tag{5.27}$$

Langmuir and Blodgett [9] suggested the following equation

$$C_d = \frac{24}{\mathrm{Re}}\left(1 + 0.197\,\mathrm{Re}^{0.63} + 2.6\times10^{-4}\,\mathrm{Re}^{1.38}\right) \tag{5.28}$$

Mellor [10] employed the following equation for low values of Reynolds number for his predictions of drop trajectories

$$C_d = \frac{1}{\mathrm{Re}}\left(23 + \sqrt{1 + 16\,\mathrm{Re}^{0.33}}\right) \tag{5.29}$$

Morsi and Alexandar [11] calculated the drag coefficient and approximated it by the following equation which is within 1-2% of the experimental value

$$C_d = a_1 + \frac{a_2}{\mathrm{Re}} + \frac{a_3}{\mathrm{Re}^2} \tag{5.30}$$

where a_1, a_2, and a_3 are constants that apply over ranges given in Table 5-3. Equation (5.30) is used in the numerical study through FLUENT to calculate the drag coefficient.

Table 5-3 Coefficients for the drag coefficient equation by Morsi and Alexander [11]

Reynolds Number Re	**Coefficients**		
	a₁	***a₂***	***a₃***
Re<0.1	0	24	0
0.1<Re<1.0	3.69	22.73	0.0903
1.0<Re<10.0	1.222	29.1667	-3.8889
10.0<Re<100.0	0.6167	46.5	-116.67

Table 5-3 continued			
Reynolds Number Re	**Coefficients**		
	a_1	a_2	a_3
100.0<Re<1000.0	0.3644	98.33	-2778
1000.0<Re<5000.0	0.357	148.62	-4.75
5000.0<Re<10000.0	0.46	-490.546	57.87
10,000.0<Re<50,000.0	0.5191	-1662.5	5.4167

The above drag coefficients approach Stokes' law as Reynolds number tends to zero. Some of these equations are not easy for the integration that is necessary for trajectory predictions. Equations (5.27) and (5.29) are both suitable for integration; the former is simple but it over predicts the drag coefficient, as shown in Figure 5-8. The latter is too complicated. In an effort to find an expression for the drag coefficient that is suitable for integration, necessary for predicting the particles trajectory, and also accurate Putnam [12] obtained the following empirical equation

$$C_d = \frac{24}{\mathrm{Re}}\left(1+\frac{1}{6}\mathrm{Re}^{2/3}\right) \tag{5.31}$$

The above equation is easy to integrate to obtain the drop velocities and trajectories and is recommended for Reynolds numbers less than 1000 [13]

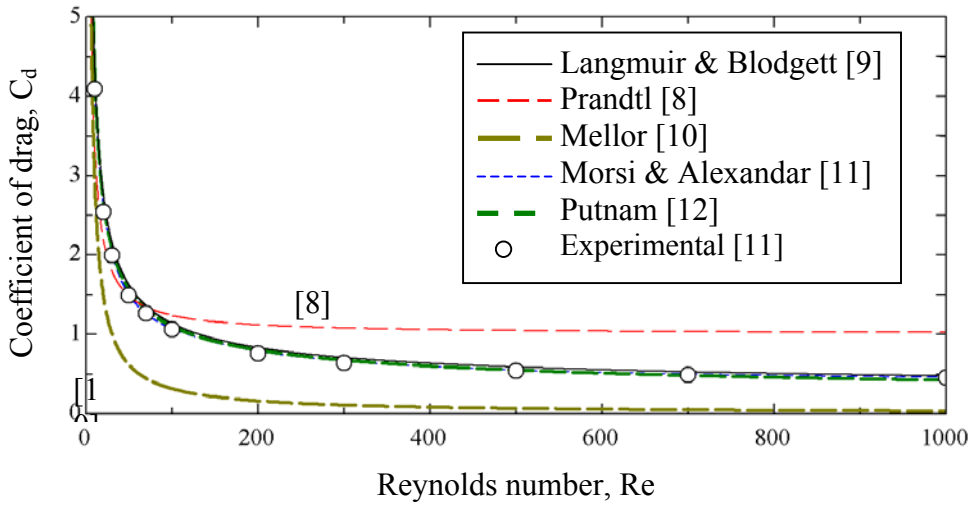

Figure 5-8 Variation of empirically determined drag coefficient of a sphere with Reynolds number

5.3.2.2 Pressure Gradient Drag

Pressure drag comes from the eddy motions that are set up in the fluid by the passage of the body. This drag is associated with the formation of a wake and it is usually less sensitive to Reynolds number than the frictional drag. The direction of this force is in the direction of the pressure gradient. The net force acting on a particle is given by

$$\underline{F}_{\Delta p} = -\int_{\text{surf}} p\,\underline{n}\,dA$$

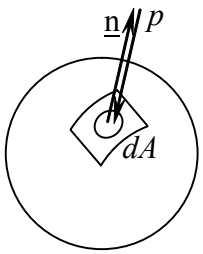

Figure 5-9 Pressure-force on a particle

Applying the divergence theorem

$$\underline{F}_{\Delta p} = -\int_{V_d} \underline{\nabla}\, p\, dV_d$$

Assuming the pressure gradient constant over the particle volume

$$\underline{\mathrm{F}}_{\Delta p} = -p \int_{V_d} \underline{\nabla}\, dV_d$$

$$\underline{\mathrm{F}}_{\Delta p} = \left(-\underline{\nabla}\, p\right) V_d \tag{5.32}$$

where p is the pressure in N/m^2 acting on an elemental area dA, $\underline{n}$ is the unit vector normal to dA in the outwards direction, and V_d is the particle volume. Crow et. al. [6] presented an estimate for the ratio of the force due to the pressure gradient to the force due to particle acceleration,

$$\frac{\underline{\mathrm{F}}_{\Delta p}}{\underline{\mathrm{F}}_{\mathrm{acc}}} = \frac{V_d \frac{\partial p}{\partial x}}{m_d \frac{du}{d\mathrm{t}}} \tag{5.33}$$

The magnitude of the pressure gradient in the continuous phase is of the order of the flow acceleration

$$\frac{\partial p}{\partial x} \sim \rho_{\mathrm{air}} \frac{Du_\infty}{D\mathrm{t}} \tag{5.34}$$

Thus, the ratio of the pressure force to the accelerating force is

$$\frac{V_d \frac{\partial p}{\partial x}}{m_d \frac{du}{d\mathrm{t}}} \sim \frac{\rho_{\mathrm{air}}}{\rho_{\mathrm{water}}} \frac{Du_\infty / D\mathrm{t}}{du/d\mathrm{t}} \tag{5.35}$$

If the acceleration of the two phases is of the same order, then the ratio of the pressure force to the acceleration force is

$$\frac{V_d \frac{\partial p}{\partial x}}{m_d \frac{du}{d\mathrm{t}}} \sim \frac{\rho_{\mathrm{air}}}{\rho_{\mathrm{water}}} \cong 0.001 \tag{5.36}$$

5.3.2.3 Unsteady Forces

The unsteady forces, namely the virtual mass and the Basset force, come from the acceleration of the particles in the air, and are in the order of the air/particle density ratio. The former, virtual mass, relates to the force required to accelerate the surrounding fluid. The later, the Basset force, is a history effect due to past acceleration of the drop. In other words the virtual mass accounts for the form drag due to acceleration, while the Basset term accounts for viscous effects. These two forces are discussed in what follows.

5.3.2.3.1 Virtual mass (added mass)

The injection of water particles into the continuous phase, air, displaces a volume of air equal to that of the water particles. Thus, the displaced volume of the air accelerates along with the water particles. This acceleration of the displaced volume induces a force, $\underline{F}_{vm}$. For inviscid flow the virtual mass force is [6]

$$\underline{F}_{vm} = \frac{\pi}{12}\rho_{air} d^3 \frac{d\underline{V}_r}{dt} \tag{5.37}$$

$$\underline{F}_{vm} = \frac{\rho_{air}}{\rho_{water}} \frac{\frac{1}{6}\pi\rho_{water} d^3}{2} \frac{d\underline{V}_r}{dt} \tag{5.38}$$

$$\underline{F}_{vm} = \frac{\rho_{air}}{\rho_{water}} \frac{m_d}{2} \frac{d\underline{V}_r}{dt} \cong 0.001 \tag{5.39}$$

5.3.2.3.2 Basset drag

The Basset term describes the force due to the lagging of the boundary layer around the particle. This term address the temporal delay in the boundary layer development as the

relative velocity changes with time. Applying the approach of flow past an impulsively accelerated flat plate to the impulsive flow over a sphere at low Reynolds number, Basset found that the drag [6].

$$\underline{F}_B = \frac{3}{2} d^2 \sqrt{\pi \rho_{air} \mu_{air}} \int_0^t \frac{d\underline{V}_r / dt}{\sqrt{t - t'}} dt' \tag{5.40}$$

$$\underline{F}_B = \frac{3}{2} \sqrt{6 \frac{\pi}{6} d^3 \rho_{water} d \frac{\rho_{air}}{\rho_{water}} \mu_{air}} \int_0^t \frac{d\underline{V}_r / dt}{\sqrt{t - t'}} dt' \tag{5.41}$$

$$\underline{F}_B = \frac{3}{2} \sqrt{\mu_{air} \frac{\rho_{air}}{\rho_{water}}} \sqrt{6 m_{drop} d} \int_0^t \frac{d\underline{V}_r / dt}{\sqrt{t - t'}} dt' \tag{5.42}$$

5.3.2.4 Lift Forces

Lift forces on a particle are due to the particle rotation. This rotation may be caused by velocity gradients, in a high shear flow region. This force consists of two components, namely Magnus and Saffman effects.

5.3.2.4.1 Magnus Effect

Rotating particles traveling in a medium experience a lift force, named Magnus force, due to its rotation. The lift force, $\underline{F}_L$, acts in a direction perpendicular to both the velocity and the angular velocity of the spinning particle, as shown in Figure 5-10.

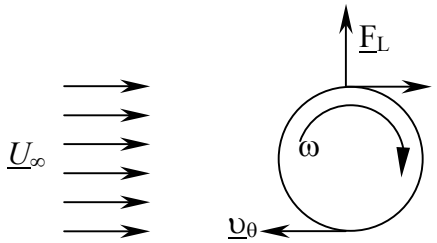

Figure 5-10 Particle rotating in a velocity field

The particle tangential velocity, $\underline{\upsilon}_\theta$, at the top is in the direction of the main flow, and against the main flow at the bottom. The higher velocity on the top of the particle gives rise to a low pressure, while the low velocity side gives rise to a high pressure. This pressure differential between the top and bottom sides of the particle induces a lift force acting upwards. For a particle in an inviscid rotational field the Magnus lift is [6]

$$\underline{F}_{mag} = \frac{\pi}{8} d^3 \rho_{air} \left[\left(\left(\frac{1}{2} \nabla \times \underline{U}_\infty \right) - \underline{\omega} \right) \times \left(\underline{U}_\infty - \underline{V} \right) \right] \tag{5.43}$$

where d is the particle diameter, $\frac{1}{2} \nabla \times \underline{U}_\infty$ is the local fluid rotation, $\underline{\omega}$ is the particle rotation, $\underline{U}_\infty$ is the main stream velocity and $\underline{V}$ is the particle velocity.

5.3.2.4.2 Saffman Effect

The Saffman force, $\underline{F}_{Saff}$, is induced by shear flow gradients, as shown in Figure 5-11. The higher velocity on the top of the particle gives rise to a low pressure at the top, and the high pressure on the low velocity side gives rise to a lift force, Saffman lift. This velocity gradient

also induces particle rotation. Saffman analyzed this force for low Reynolds number and found the magnitude of the force to be

$$\underline{F}_{\text{Saff}} = 1.61\mu_{\text{air}} d \left|\underline{U}_{\infty} - \underline{V}\right| \sqrt{\text{Re}_G} \tag{5.44}$$

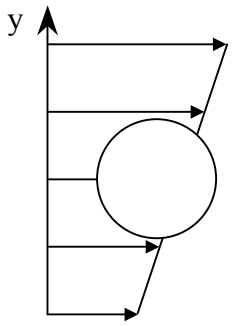

Figure 5-11 Particle in a shear flow

where Re_G is the shear Reynolds number based on the velocity difference between the top and the bottom of the particle and is defined as

$$\text{Re}_G = \frac{d^2}{\gamma_{\text{air}}} \left|\frac{du_{\infty}}{dy}\right| \tag{5.45}$$

Saffman's analysis is based on the conditions that the Reynolds number based on the relative velocity between the particle and the main stream, $\underline{U}_{\infty} - \underline{V}$, is much less than the shear Reynolds number, Re_G.

In this section the equation of motion (5.24) of the dispersed phase is presented. The trajectory of the dispersed phase, droplets, can be calculated by integrating the equation of motion, written in the Lagrangian reference frame. Examining each term of the equation it

can be shown that the pressure force, unsteady forces and the lift forces can be neglected. The pressure force and the unsteady forces, virtual mass and Basset term, can be neglected because they are in the order of the air/droplet density which is approximately 10^{-3}. On the other hand, the Saffman lift and Magnus force are neglected because the droplets are not in a high-shear region of the continuous phase flow. This reduces the equation of motion to two terms; the steady-state viscous drag term and the gravity force term.

$$m_d \underline{V} \frac{d\underline{V}}{dx} = \underline{F}_{ss} + m_d \underline{g} \tag{5.46}$$

5.4 Physical Properties

This section presents the physical properties of both the dispersed and continuous phases required by the physical models described in §5.3. The thermo-physical properties of water are summarized in Table 5-4 and Table 5-5. On the other hand, Table 5-6, summarizes the thermo-physical properties of air. A number of assumptions have been used to compute the fluids thermo-physical properties

1. The water vapor pressure is approximated by a piecewise linear function using the data pairs as shown in Table 5-5.
2. The air density is calculated using the gas law.
3. The specific heat, thermal conductivity and viscosity, for air, are assumed constant and assigned average values as shown in Table 5-6.

Table 5-4 Thermo-physical properties of water

Property	Value	Unit
Density, ρ_{water}	1000	Kg/m^3
Latent heat of vaporization, h_{fg}	2.25×10^6	J/kg
Specific heat, c_{water}	4180	J/kg-K
Diffusion coefficient, D_{AB}	2.6×10^6	m^2/s

Table 5-5 Variation of water vapor pressure with temperature

Temperature [K]	Pressure [Pa]
256	133
275	664
285	1329
296	2658
307	5316
315	7974
325	13289
340	26579
356	53158
373	101000

Table 5-6 Average thermo-physical properties of air

	Average	Standard Deviation	Unit	Air-exit Temperature [K]
Specific heat, $c_{p_{\text{air}}}$	1006.511	±5.098E-05	J/kg-K	291.776+0.006
Thermal Conductivity, k_{air}	0.0245	±2.183E-04	W/m-K	291.776±0.03
Viscosity, μ_{air}	1.7825E-05	±1.393E-07	Kg/m-s	291.776±0.03

Figure 5-12 illustrates the temperature dependence of the air specific heat [14], thermal conductivity [15] and viscosity [16]. In addition, Figure 5-12 shows that these properties can be assumed constant within the temperature range of the numerical simulations. This is also evident by visiting the standard deviations summarized in Table 5-6. Also, Table 5-6 shows that using a constant value for the specific heat, thermal conductivity and viscosity affects the results of the temperature of air leaving the spray chamber by a maximum error of 0.03ºC.

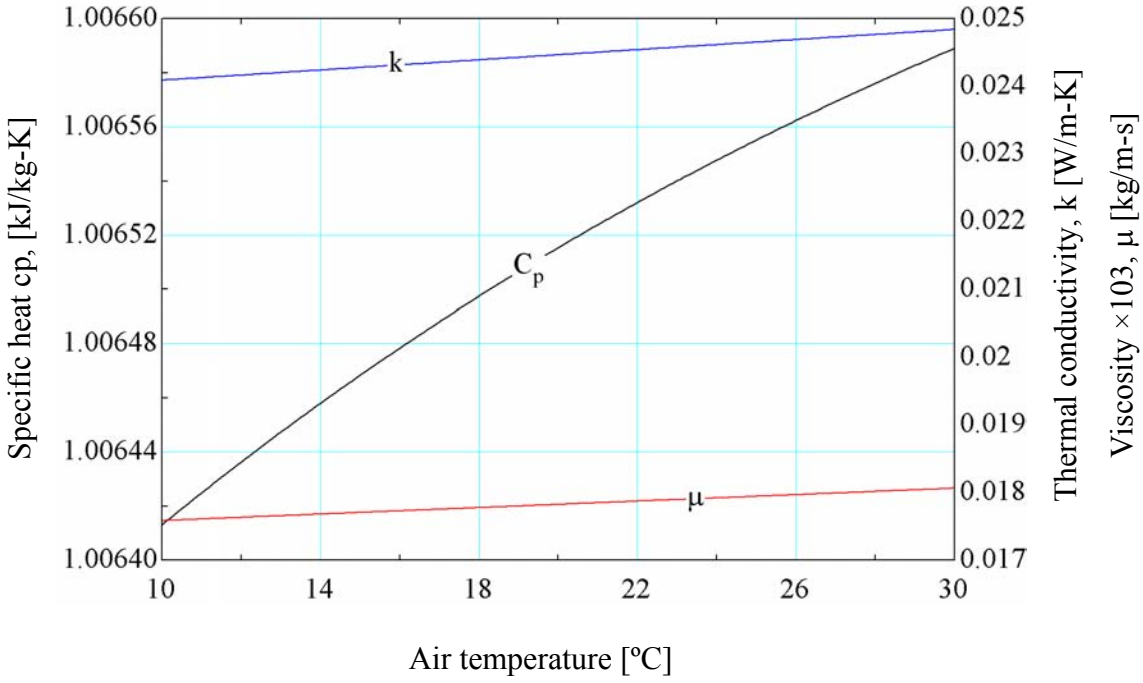

Figure 5-12 Variation of air physical properties with temperature

5.5 Assumptions and Limitations

This section summarizes the assumptions adopted to simplify and numerically solve the governing equations, discussed earlier in §5.3. The equations are simplified according to the following assumptions

1. Heat transfer with the surrounding is neglected, since the spray cooler is insulated.

2. Uniform inlet conditions for air and water.
3. Both fluids, air and water, are considered incompressible. This assumption is reasonable for water. For air, Mach number is evaluated assuming ideal gas behavior and is found to be $7.3\text{x}10^{-03}$ which is less than 0.3 at which compressibility effects become important.
4. Quasi-steady-flow conditions in accordance with the criteria identified in section 4.1.
5. Radiation exchange effects are neglected, since $h_c \approx 53 h_r$. The radiation heat transfer, h_r, coefficient is in the order of 5.5 W/m^2-K and the minimum convective heat transfer coefficient, h_c, is in the order of 293 W/m^2-K.
6. The mass flow rate of dry air is constant. Consequently, $\frac{d\dot{m}_{\text{air}}}{d\text{t}} = 0$.
7. Well mixed water droplets, i.e., the temperature inside the droplet is uniform. This assumption is assessed by evaluating the Biot number for most of the studied cases and it is found to be in the vicinity of 0.1.
8. Water droplets are spherical.
9. Forces due to pressure gradient, $\underline{F}_{\Delta p}$, virtual mass, $\underline{F}_{\text{vm}}$, and Basset, $\underline{F}_{\text{B}}$, terms are neglected because they are of the order of the air/water density ratio, which is 10^{-3}.
10. The Saffman, $\underline{F}_{\text{Saff}}$, and Magnus, $\underline{F}_{\text{mag}}$, forces are neglected because the droplets are not in a high shear region of gas flow.

5.6 Results and Discussion

The results of the numerical simulations carried out to study the performance of the spray cooler are presented in this section. The section starts by depicting the results of the numerical experiments performed to validate the numerical model. This is then followed by introducing the results of the parametric study conducted to investigate the effect of the droplet diameter and the initial speed-ratio on the performance of the spray cooler.

5.6.1 Model Validation

Validation of the numerical model is necessary to check its ability to predict the spray cooler performance. The model is verified by running numerical simulations at exactly the same inlet conditions of the experiment. It should be mentioned, however, that the numerical model allows for one of two wall boundary conditions, namely, “reflect” wall boundary condition or “escape” wall boundary condition. These are chosen to confirm that the results obtained from the numerical simulations bracket those obtained from the experimental study. In reality neither of these idealized wall boundary conditions is ever met. Therefore, a deviation between the numerical and experimental results is expected. However, the numerical results should bracket the experimental data for the numerical model to be realistic. Table 5-7 summarizes the results of the numerical simulations and experiment performed under the same conditions for the same droplet diameter.

Table 5-7 Summary of the model validation experiment

		Experiment	"Reflect" Wall	"Escape" Wall
	Droplet diameter, [mm]	1.168		
Air Side	Inlet dry-bulb [ºC]	30.52		
	Exit dry-bulb [ºC]	18.56	10.26	25.96
Water Side	Inlet Temperatures [ºC]	0.58		
	Exit Temperatures [ºC]	3.37	5.10	1.88
Effectiveness		0.4	0.68	0.15

It can be noted from the comparison that the air side exit dry bulb temperature, the water side exit temperature, and the effectiveness of the experimental data nearly represents the arithmetic mean value of the corresponding quantities of "reflect" and "escape" wall boundary conditions. Several conclusions can be drawn from these results. First the numerical model is realistic because it succeeds in bracketing the experiment. Second, the real physical wall boundary condition is nearly 50% reflect and 50% escape.

5.6.2 Parametric Study

This section presents the results of the numerical simulations conducted to study the effect of changing the spray cooler initial-speed ratio, SR_o, and the surface area droplet median diameter, d, on the performance of the chilled water spray cooler. This analysis is carried out for two wall boundary conditions, "reflect" and "escape", with and without the effect of gravity. The section starts by presenting the effects of the initial speed-ratio and droplet diameter on the spray-tip-penetration-length, $S_{\max}$. This is then followed by studying their

effects on the spray cooler effectiveness, ε. The initial-speed ratio is varied in the range of $0.25 \le SR_o \le 4$, and the droplet diameter, d, is varied in the range of $0.76 \le d \le 1.8$.

The spray cooler initial speed-ratio, is defined as the ratio of the magnitude of the initial spray horizontal velocity component, u_o, to the that of the initial velocity of air, u_∞, as shown in equation (5.47)

$$SR_o = \frac{u_o}{u_\infty} \tag{5.47}$$

5.6.2.1 Spray-tip-penetration-length

The spray-tip-penetration-length, $S_{\max}$, is defined as the maximum distance traveled by the water droplets in the horizontal direction inside the spray chamber, as shown in Figure 5-13 The spray tip-penetration-length depends on the ratio of the momentum of water to that of air. This behavior is supported with the analytical investigation presented in Chapter 6, which indicates that:

$$S_{\max} \propto \frac{\rho_{\text{water}}}{\rho_{\text{air}}} \frac{u_o}{u_\infty} d \tag{5.48}$$

$$S_{\max} \propto \frac{\rho_{\text{water}}}{\rho_{\text{air}}} \left(SR_o\right) d \tag{5.49}$$

The above equation suggests that the spray-tip-penetration-length increases by increasing either the initial speed-ratio, SR_o, or the droplet diameter. The following section illustrates

this relation in detail. It also investigates the effect of gravity forces for the two wall boundary conditions.

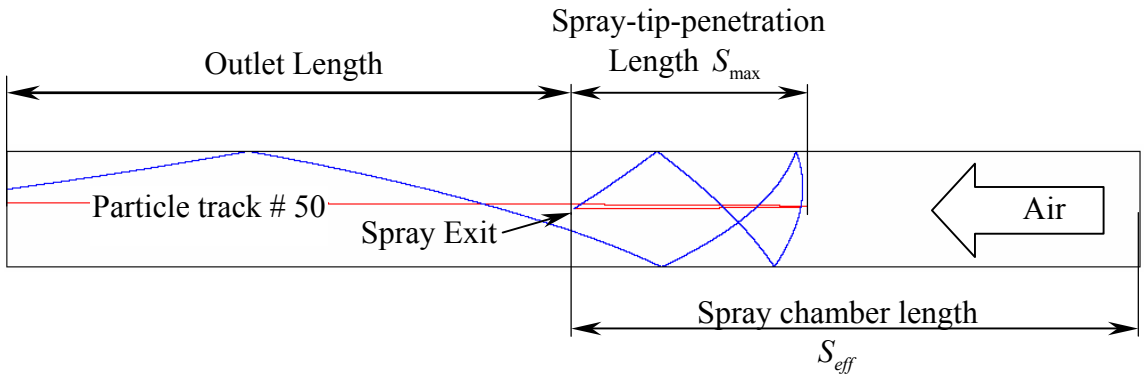

Figure 5-13 Schematic showing particle tracks 1 and 50, and the spray-tip-penetration-length for a spray cooler with "reflect" wall boundary condition.

5.6.2.1.1 Effect of the initial speed-ratio on the spray-tip-penetration-length

Figure 5-14 and Figure 5-15 show the effect of changing the initial-speed ratio, SR_o, on the spray-tip-penetration-length, S_{max}, for different droplet diameters, d. The figures show that increasing the initial speed-ratio, SR_o, increases the spray-tip-penetration-length until the spray-tip reaches the end of the spray cooler. This increase in spray-tip-penetration-length is a result of the increase in the droplet momentum, by increasing its initial velocity, with respect to that of air as illustrated by equation (5.48). The momentum of air is held constant by keeping the velocity and mass flow rate of air unaltered.

Figure 5-14 and Figure 5-15 also show that there is a critical initial speed-ratio, SR_C, at which the spray-tip-penetration-length is equal to the spray cooler length. The spray-tip-penetration-length at the critical initial-speed ratio will be referred to as the effective spray-

tip-penetration-length, S_{eff}. Where S_{eff} is the length at which the spray-tip-penetration-length equals the spray chamber length.

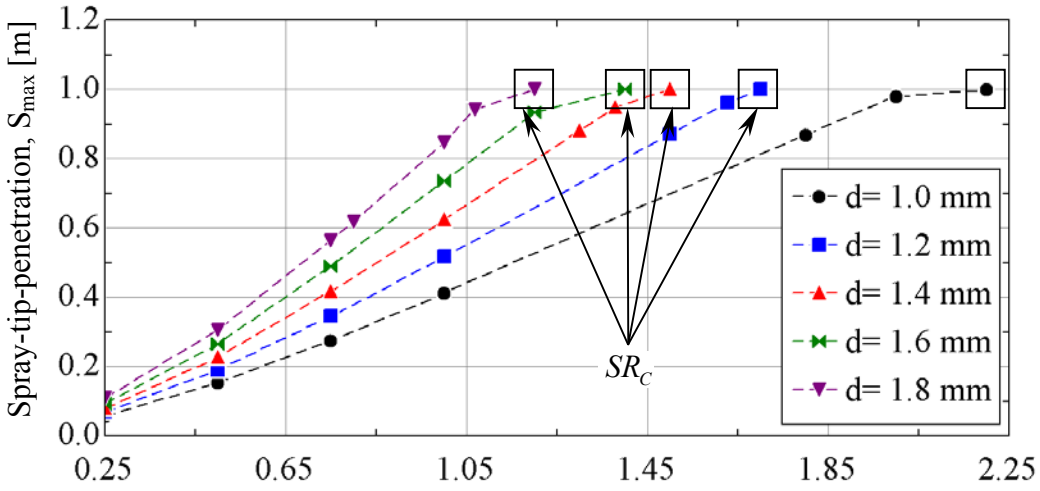

a- Gravity = 0 m/s^2

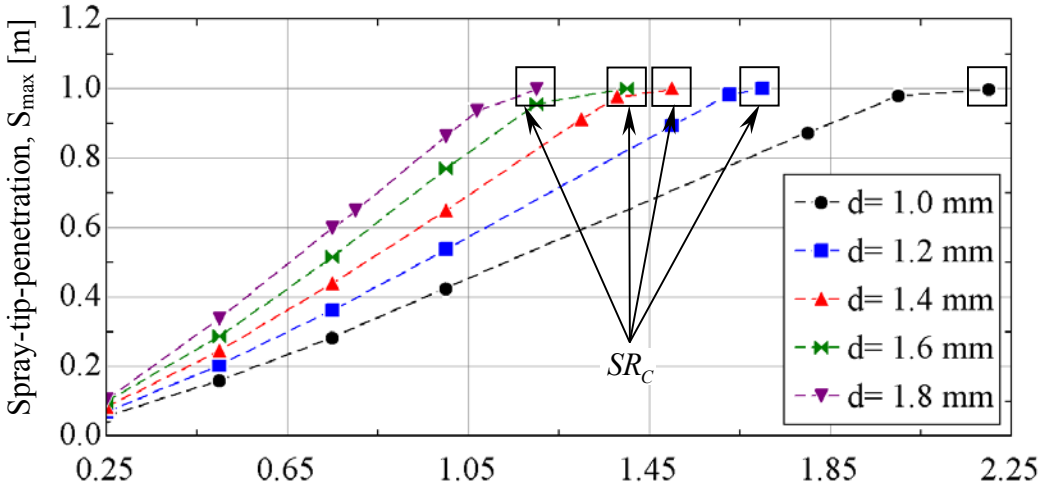

b- Gravity = -9.81 m/s^2

Figure 5-14 Effect of the spray cooler initial speed-ratio on the spray-tip-penetration-length for a "reflect" wall boundary condition, $\underline{u}_\infty = -5\,\text{m/s}$ and $\text{MR}=\frac{\dot{m}_{\text{water}}}{\dot{m}_{\text{air}}}=0.5$

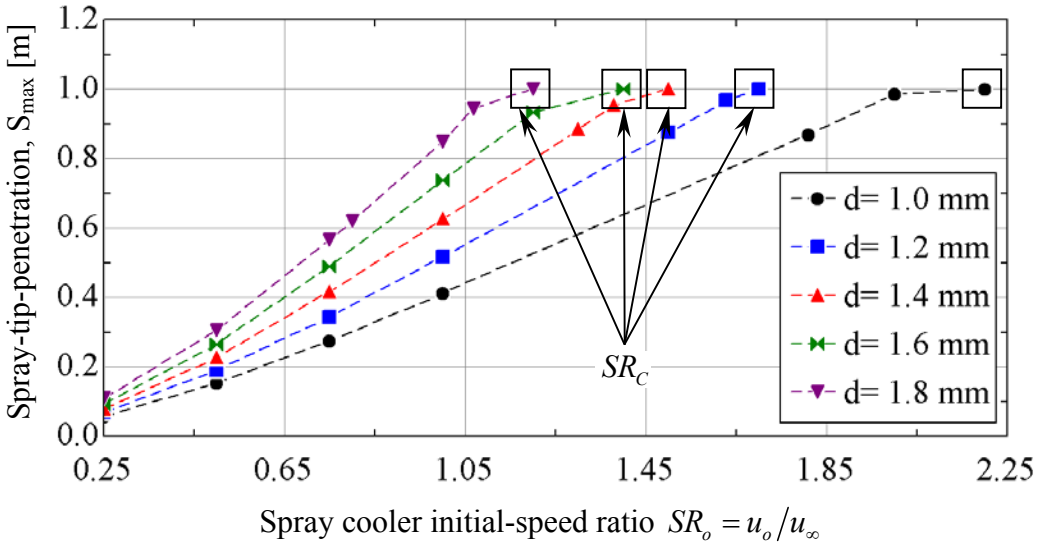

a- Gravity = 0 m/s^2

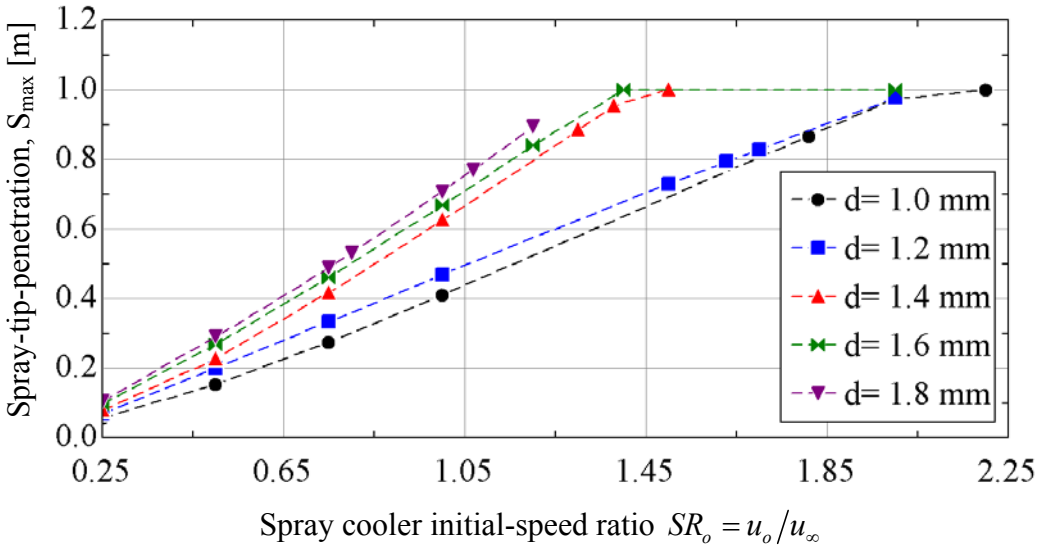

b- Gravity = -9.81 m/s^2

Figure 5-15 Effect of the spray cooler initial speed-ratio on the spray-tip-penetration-length for a "escape" wall boundary condition, $\underline{u}_\infty = -5\,\text{m/s}$ and $\text{MR} = \frac{\dot{m}_{\text{water}}}{\dot{m}_{\text{air}}} = 0.5$

For initial spray speed-ratios greater than SR_C, the spray-tip will penetrate to the outside the spray cooler. On the other hand for initial spray speed-ratios less than the critical value SR_C, the droplet velocity reaches zero at the position of maximum penetration, and comes to an instantaneous rest, shown in Figure 5-16. At this point in the droplet trajectory, the droplet momentum goes to zero and the droplets will begin to move backwards, and subsequently accelerate in the opposite direction, as they get carried by air, as shown in Figure 5-17 to Figure 5-20.

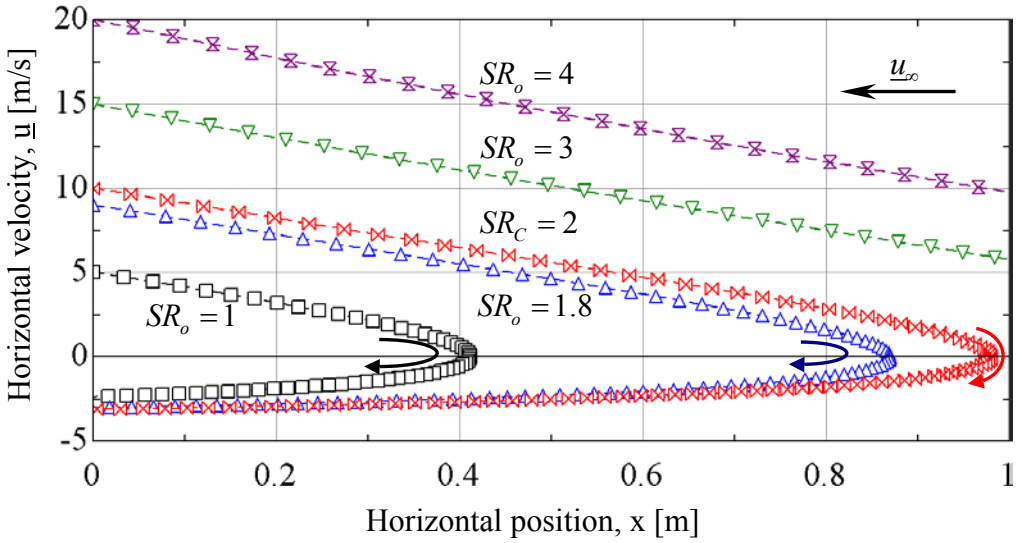

Figure 5-16 Variation of the spray horizontal velocity component, u, along the spray chamber length, for particle track # 50, d=1mm, gravity = 0 m/s^2, reflecting walls,

$$u_\infty = -5\,\text{m/s} \text{ and } \text{MR}=\frac{\dot{m}_{\text{water}}}{\dot{m}_{\text{air}}}=0.5$$

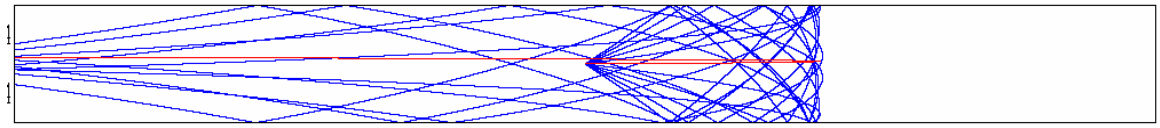

a- Initial speed-ratio $SR_o = 1.0$

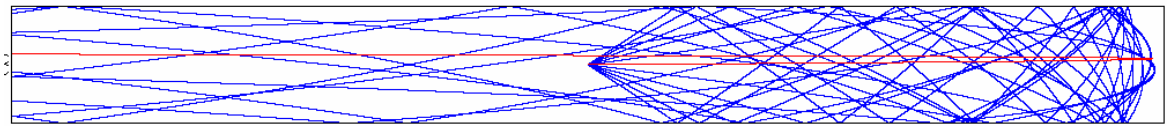

b- Initial speed-ratio $SR_o = 2.0$

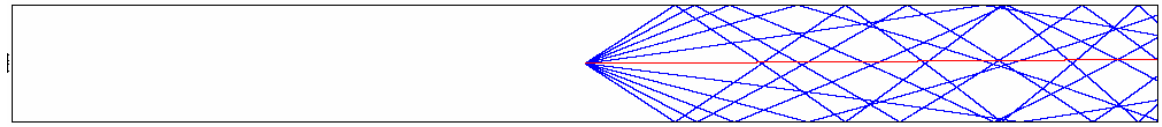

c- Initial speed-ratio $SR_o = 3.0$

Figure 5-17 Particle tracks for spray cooler with "reflect" wall boundary condition, gravity = 0 m/s^2, $\underline{u}_\infty = -5$ m/s , $d = 1$mm , and MR$=\frac{\dot{m}_{\text{water}}}{\dot{m}_{\text{air}}} = 0.5$

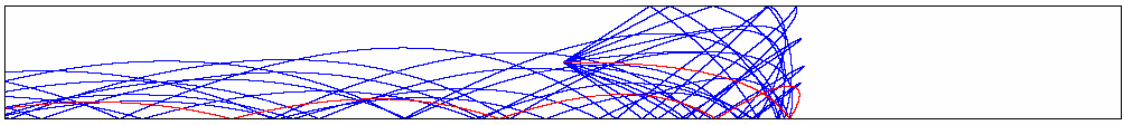

a- Initial speed-ratio $SR_o = 1.0$

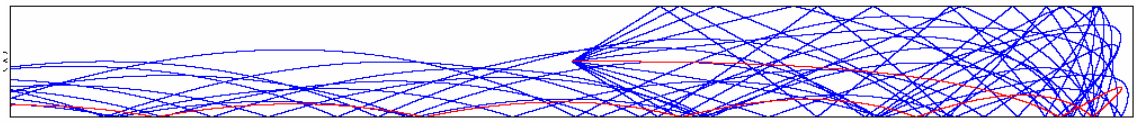

b- Initial speed-ratio $SR_o = 2.0$

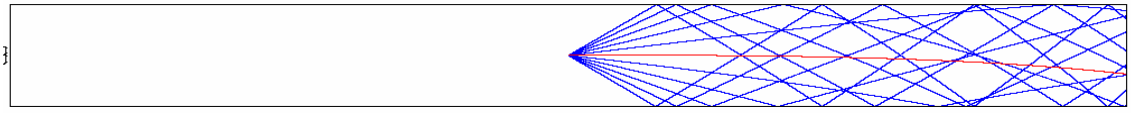

c- Initial speed-ratio $SR_o = 3.0$

Figure 5-18 Particle tracks for spray cooler with "reflect" wall boundary condition, gravity = -9.81 m/s^2, $\underline{u}_\infty = -5$ m/s , $d = 1$mm , and MR$=\frac{\dot{m}_{\text{water}}}{\dot{m}_{\text{air}}} = 0.5$

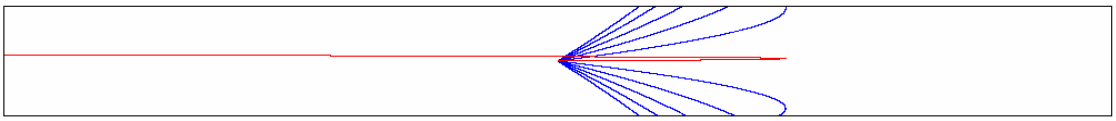

a- Initial speed-ratio $SR_o = 1.0$

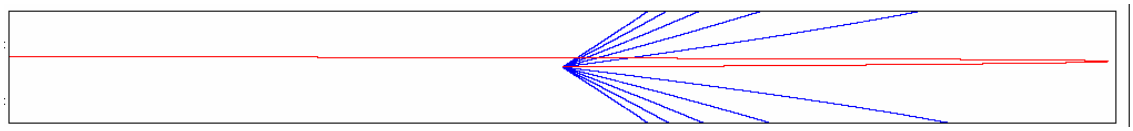

b- Initial speed-ratio $SR_o = 2.0$

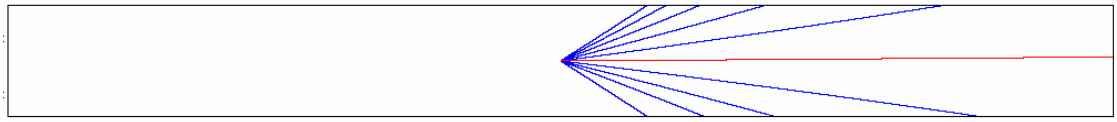

c- Initial speed-ratio $SR_o = 3.0$

Figure 5-19 Particle tracks for spray cooler with "escape" wall boundary condition, gravity = 0 m/s^2, $\underline{u}_\infty = -5\,\text{m/s}$, $d = 1\text{mm}$, and $\text{MR} = \frac{\dot{m}_{\text{water}}}{\dot{m}_{\text{air}}} = 0.5$

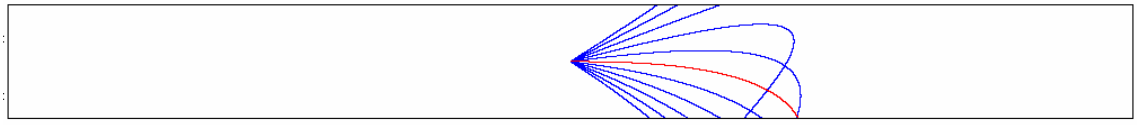

a- Initial speed-ratio $SR_o = 1.0$

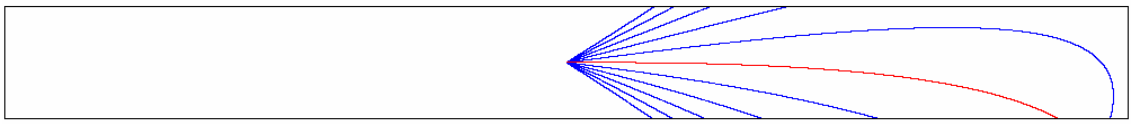

b- Initial speed-ratio $SR_o = 2.0$

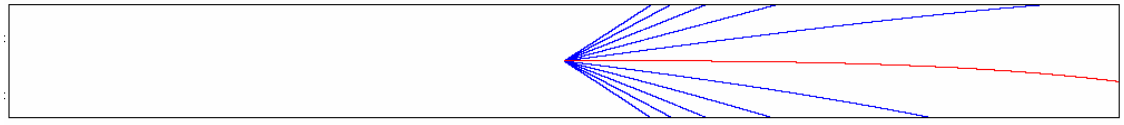

c- Initial speed-ratio $SR_o = 3.0$

Figure 5-20 Particle tracks for spray cooler with "escape" wall boundary condition, gravity = -9.81 m/s^2, $\underline{u}_\infty = -5\,\text{m/s}$, $d = 1\text{mm}$, and $\text{MR} = \frac{\dot{m}_{\text{water}}}{\dot{m}_{\text{air}}} = 0.5$

5.6.2.1.2 *Effect of droplet diameter on the spray-tip-penetration-length*

Figure 5-14 and Figure 5-15 also illustrate the effect of changing the droplet diameter on the spray-tip-penetration-length. The figures show that, for the same initial speed-ratio, droplets with large diameters penetrate the spray chamber more than those with smaller diameter. Also, the effective spray-tip-penetration-length, S_{eff}, occurs at lower initial speed-ratios for large diameter droplets. In other words, a lower initial speed-ratio, SR_C, is required by larger droplets to achieve the same penetration length, as shown in Figure 5-21. This can be attributed to the fact that large diameter droplets have higher momentum compared to smaller ones, having the same velocity.

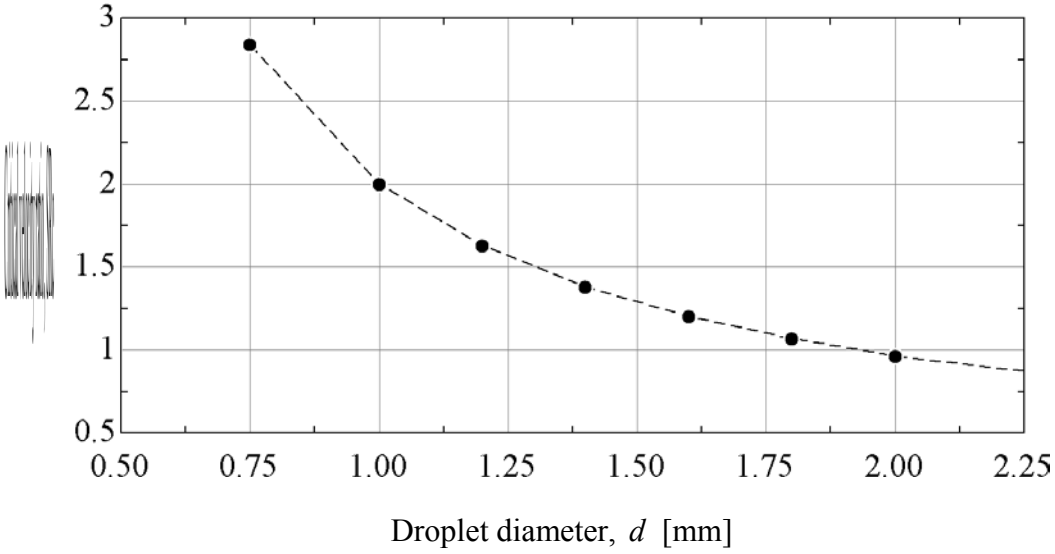

Figure 5-21 Effect of droplet diameter on the critical velocity ratio, "reflect" wall boundary condition, gravity = 0 m/s^2, $\underline{u}_\infty = -5$ m/s, and MR$=\frac{\dot{m}_{\text{water}}}{\dot{m}_{\text{air}}}=0.5$

5.6.2.1.3 Effect of gravitational force and wall boundary condition

Figure 5-17 and Figure 5-20 depict the particle tracks for a spray chamber with "reflect" wall boundary condition for the two cases; $g = 0$ m/s^2, and $g = -9.81$ m/s^2. It can be seen from these figures that as soon as the particles reach the walls they reflect from the walls and continue their penetration. Consequently for a spray chamber with "reflect" wall boundary condition, the spray-tip-penetration-length is identical for both cases $g = 0$ m/s^2 and $g = -9.81$ m/s^2, as shown in Figure 5-22a. This is owed to the assumption of perfect reflection, which assumes that the droplet will retain all its momentum after colliding with the spray chamber wall. On the other hand, for a spray chamber with "escape" wall boundary condition the particles stick to the wall as soon as they reach the spray chamber walls, and loose all their momentum.

Figure 5-22b shows that the zero gravity case over-predicts the spray-tip-penetration-length. This is due to the fact that, for the zero gravity case, the vertical component of the drag force is the only force that acts on the droplet in the vertical direction. When gravity is included, the gravitational force and the vertical component of the drag act together on the droplet, moving it downwards. Consequently, and in accordance with Newton's second law of motion, the droplets will accelerate faster towards the lower wall in the vertical direction due to the gravitational forces. Thus, the droplets can not penetrate any further since they lose all their momentum once they collide with the wall. The deviation from the zero gravity case is more pronounced for larger diameter droplets, due to their faster acceleration towards the walls owing to their larger mass.

Finally, Figure 5-23 shows the effect of changing the spray chamber wall boundary condition on the penetration length. It can be noticed that for the zero gravity case the predictions for the spray-tip-penetration-length are identical, while the "reflect" wall boundary condition over predicts the spray-tip-penetration-length.

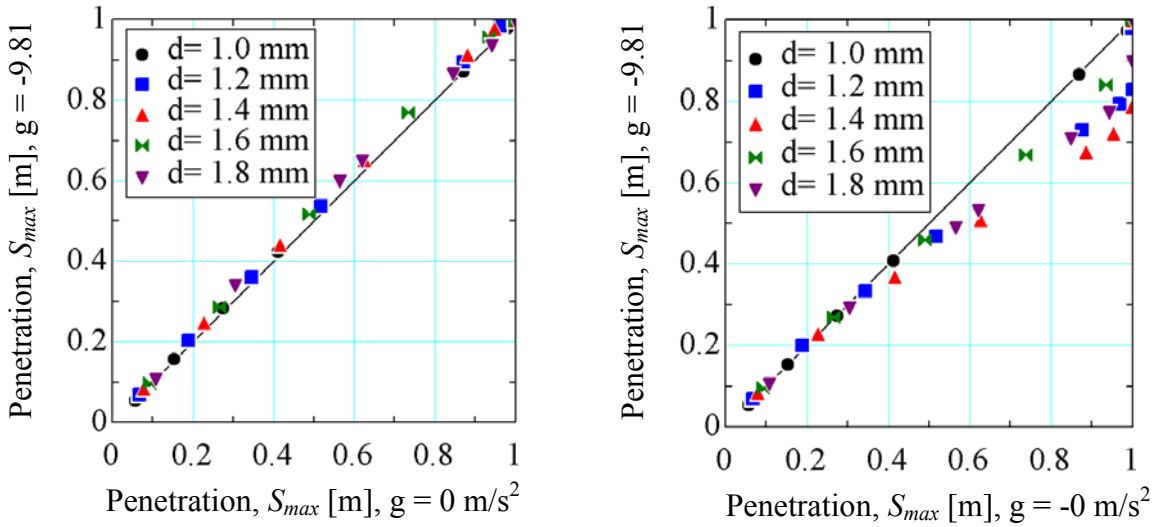

a- "Reflect" wall

b- "Escape" wall

Figure 5-22 Effect of gravity on the spray-tip-penetration-length, for different spray chamber wall boundary conditions $\underline{u}_{\infty} = -5\,\text{m/s}$, and $\text{MR}=\frac{\dot{m}_{\text{water}}}{\dot{m}_{\text{air}}}=0.5$

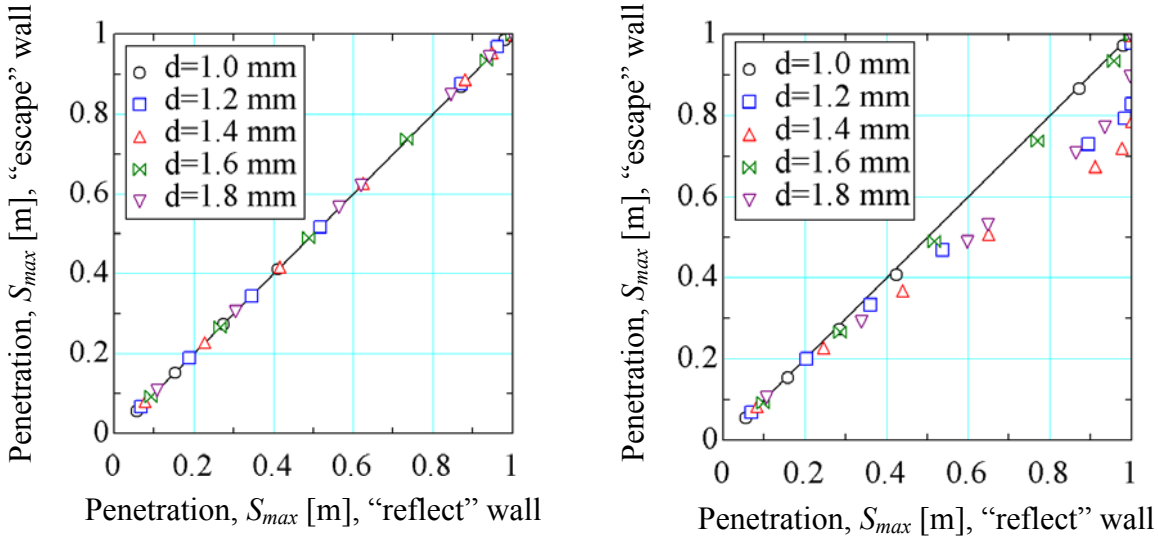

a- Gravity = 0 m/s^2 b- Gravity = -9.81 m/s^2

Figure 5-23 Effect of spray chamber wall boundary condition on the spray-tip-penetration-length $\underline{u}_\infty = -5\,\text{m/s}$, and $\text{MR}=\frac{\dot{m}_{\text{water}}}{\dot{m}_{\text{air}}}=0.5$

The aforementioned discussion shows that the spray-tip-penetration-length increases with increasing the initial speed-ratio or increasing the droplet diameter due to the increase in initial momentum of water droplets. The discussion also illustrates the effect of gravity force and spray chamber wall boundary condition on the spray-tip-penetration-length. For the "reflect" wall boundary condition, the spray penetration is insensitive to gravity effects because of the complete momentum recovery. On the other hand, for "escape" wall boundary condition the zero gravity case over predicts the gravity case. This is owed to the gravitational force that accelerates the droplets faster towards the spray chamber walls. At the walls, the droplets they lose their momentum and come to rest.

In the following section the effects of initial speed-ratio, droplet diameter and the gravitational force on the spray chamber effectiveness are discussed for the two wall boundary conditions.

5.6.2.2 Spray chamber effectiveness

The effectiveness, ε, is the ratio of the actual heat transfer rate to the maximum possible heat transfer rate. The maximum possible heat transfer rate occurs when the minimum capacitance rate fluid experiences the maximum temperature change. In the case of the spray chamber, the minimum capacitance rate fluid is the air. The spray chamber effectiveness is defined as follows [17]

$$\varepsilon = \frac{\dot{Q}}{C_{\min}\Delta T_{\max}} \tag{5.50}$$

$$\varepsilon = \frac{\left(\dot{m}_{\text{air}} C_{\text{p}}\right)\left(T_{\text{in}} - T_{\text{out}}\right)\Big|_{\text{air}}}{\left(\dot{m}_{\text{air}} C_{\text{p}}\right)\left(T_{\text{in}}\Big|_{\text{air}} - T_{\text{in}}\Big|_{\text{water}}\right)} \tag{5.51}$$

$$\varepsilon = \frac{T_{\text{in}}\Big|_{\text{air}} - T_{\text{out}}\Big|_{\text{air}}}{T_{\text{in}}\Big|_{\text{air}} - T_{\text{in}}\Big|_{\text{water}}} \tag{5.52}$$

where $\dot{Q}$ is the actual heat transfer, $C_{\min}$ is the minimum thermal capacitance rate and $\Delta T_{\max}$ is the maximum temperature difference across the spray cooler. The effectiveness of the spray cooler can be also expressed as

$$\varepsilon = \frac{(UA)\Delta T_{\text{mean}}}{C_{\min}\Delta T_{\max}} \tag{5.53}$$

where U is the overall heat transfer coefficient, A is the total surface area of the spray available for heat and mass transfer. ΔT_{mean} is the mean temperature difference defined as $F\,\Delta T_{\text{LM}}$, where F is a correction factor that depends on the air and water temperatures and the spray cooler geometry, and ΔT_{LM} is the logarithmic mean temperature difference defined as

$$\Delta T_{\text{LM}} = \frac{\left(T_{\text{in}}\big|_{\text{air}} - T_{\text{out}}\big|_{\text{water}}\right) - \left(T_{\text{out}}\big|_{\text{air}} - T_{\text{in}}\big|_{\text{water}}\right)}{\ln\left(\left(T_{\text{in}}\big|_{\text{air}} - T_{\text{out}}\big|_{\text{water}}\right)\Big/\left(T_{\text{out}}\big|_{\text{air}} - T_{\text{in}}\big|_{\text{water}}\right)\right)} \tag{5.54}$$

Equation (5.53) shows that the spray cooler effectiveness is proportional to the spray cooler conductance, UA product. The surface area of the spray, A, is proportional to the total number of droplets, N_{droplets}, and the square of the droplet diameter, d, as shown below

$$A \propto N_{\text{droplets}} d^2 \tag{5.55}$$

The total number of droplets depends on the mass flow rate of water:

$$\dot{m}_{\text{water}} \propto \dot{N}_{\text{droplets}} d^3 \tag{5.56}$$

where $\dot{N}_{\text{droplets}} = \dfrac{N_{\text{droplets}}}{\mathrm{t}_{\text{res}}}$, where t_{res} is the residence time defined as $\mathrm{t}_{\text{res}} \propto \dfrac{S_{\max}}{u_o}$

$$\mathrm{t}_{\text{res}} \propto \frac{S_{\max}}{u_\infty \left(SR_o\right)} \tag{5.57}$$

where the residence time is the average time the droplets spend in the spray chamber. Substituting the above expressions into equation (5.55) gives

$$A \propto \frac{\dot{m}_{\text{water}}}{u_\infty}\frac{1}{SR_o}\frac{S_{\max}}{d} \propto \frac{\dot{m}_{\text{water}}}{u_\infty}\frac{1}{SR_o}\zeta_A \tag{5.58}$$

where $\zeta_A = S_{\max}/d$. Equation (5.17) shows that the Nusselt number and thus the overall heat transfer coefficient, U , is proportional to the square root of Reynolds number

$$U \propto \frac{\sqrt{\text{Re}}}{d} \tag{5.59}$$

where $\text{Re} \propto \left|\underline{u}_\infty - \underline{u}\right| d$, as shown by equation (5.19). Combining this expression into equation (5.59) gives

$$U \propto \sqrt{\frac{u_\infty \left|1 - SR_o\right|}{d}} \tag{5.60}$$

Consequently, the spray chamber conductance, UA product, depends on the mass flow rate of water, $\dot{m}_{\text{water}}$, spray-tip-penetration-length, $S_{\max}$, the air velocity, u_∞ , droplet diameter, d , and the spray initial-speed-ratio, SR_o , as shown below

$$UA \propto \sqrt{\frac{u_\infty \left|1 - SR_o\right|}{d}}\ \frac{\dot{m}_{\text{water}}}{u_\infty\left(SR_o\right)}\frac{S_{\max}}{d} \tag{5.61}$$

$$UA \propto \frac{\dot{m}_{\text{water}}}{\sqrt{u_\infty}}\frac{S_{\max}}{\sqrt{d^3}}\sqrt{\frac{\left|1 - SR_o\right|}{SR_o^2}} \propto \frac{\dot{m}_{\text{water}}}{\sqrt{u_\infty}}\zeta_{UA}\sqrt{\frac{\left|1 - SR_o\right|}{SR_o^2}} \tag{5.62}$$

5.6.2.2.1 *Effect of spray initial speed-ratio on spray chamber effectiveness*

Figure 5-24 illustrates the effect of changing the initial speed-ratio, SR_o , on the spray chamber effectiveness, ε , for "reflect" wall boundary condition. The figure shows that for

initial speed-ratios less than SR_C, the effectiveness increases as the initial speed-ratio increases. However, this trend is reversed at initial speed-ratios greater than SR_C. This phenomenon is discussed in more detail below

The effectiveness of the spray cooler increases as the initial speed-ratio increases until the maximum effectiveness, $\varepsilon_{\max}$, is reached at an initial speed-ratio, SR_ε. This increase in effectiveness is owed to the increase in the spray cooler conductance, UA product, as shown in Figure 5-25. The overall heat transfer coefficient increases with the increase in the initial speed-ratio due to the increase of the Reynolds number, as illustrated by equation (5.59). Also, increasing the initial speed-ratio increases the total surface area, as long as the initial speed-ratios are less than the critical value SR_C. This increase in total surface area can be attributed to the following two reasons:

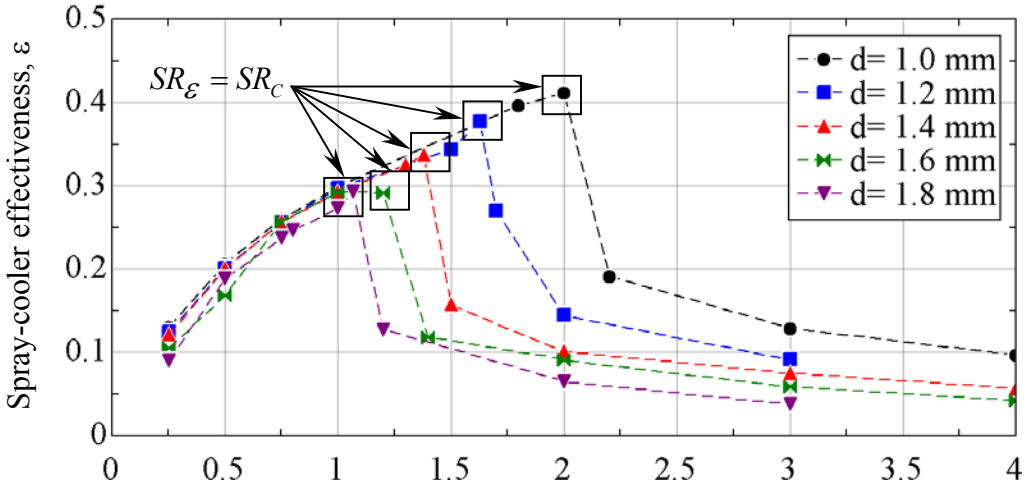

a- Gravity = 0 m/s^2

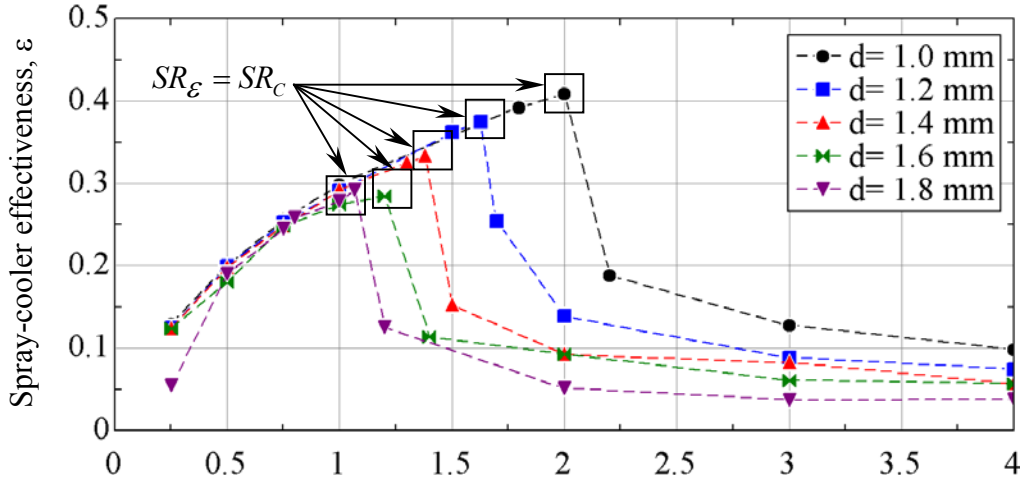

b- Gravity = -9.81 m/s^2

Figure 5-24 Effect of the spray cooler initial speed-ratio on the spray cooler effectiveness for "reflect" wall boundary condition $\underline{u}_\infty = -5\,\text{m/s}$ and MR=$\dfrac{\dot{m}_{\text{water}}}{\dot{m}_{\text{air}}} = 0.5$

1. The increase in penetration length, as shown in Figure 5-14 and equation (5.58)
2. The doubling effect of the surface area due to the retraction of water droplets inside the spray chamber, as seen in Figure 5-17 and Figure 5-18. However, the surface area doubling effect vanishes for initial speed-ratios greater than the critical value SR_C since the water droplets retract outside the spray chamber.

Therefore, both initial speed-ratios SR_ε and SR_C are the same for "reflect" wall boundary condition, as shown in Figure 5-14 and Figure 5-24. Increasing the initial speed-ratio above the critical value SR_C decreases the spray chamber effectiveness, due to the decrease in the UA product, as shown in Figure 5-25. As mentioned earlier, increasing the initial speed-ratio increases the heat transfer coefficient. However, increasing the initial speed-ratio beyond the critical value SR_C results in

1. The elimination of the surface area doubling effect.
2. The decrease of the droplets residence time, as shown by equation (5.57). This is because $S_{\max}$ has reached its maximum value, S_{eff}, which is equal to the spray chamber length.

This reduction in residence time causes a reduction in the total available surface area, as demonstrated by equations (5.57) and (5.58). At initial speed-ratios greater than the critical value, SR_C, the effect of residence time and surface area reduction overcomes the effect of heat transfer coefficient increase. Thus, the net effect is a decrease in the conductance of the spray cooler, as shown in Figure 5-26.

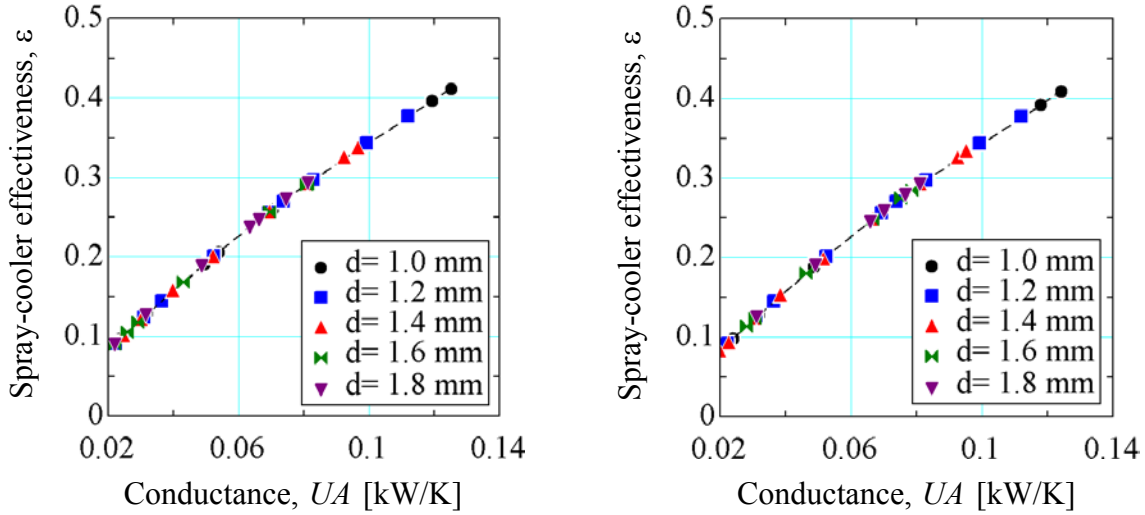

a- Gravity = 0 m/s^2 b- Gravity = -9.81 m/s^2

Figure 5-25 Effect of spray cooler conductance on the spray cooler effectiveness, for "reflect" wall boundary condition $\underline{u}_\infty = -5\,\text{m/s}$ and $\text{MR}=\frac{\dot{m}_{\text{water}}}{\dot{m}_{\text{air}}}=0.5$

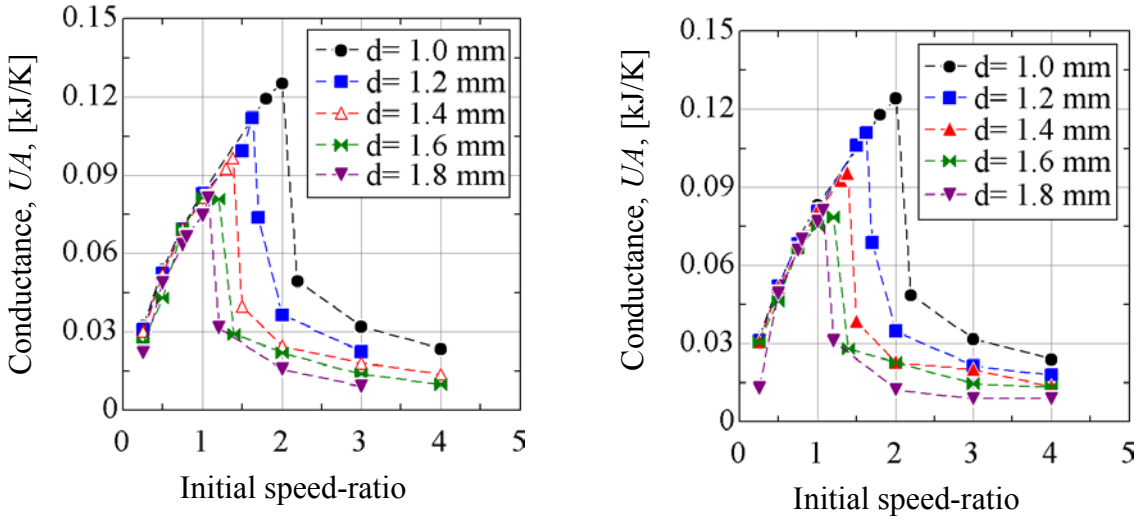

a- Gravity = 0 m/s^2 b- Gravity = -9.81 m/s^2

Figure 5-26 Effect of the spray cooler initial speed-ratio on the spray cooler conductance for "reflect" wall boundary condition $\underline{u}_\infty = -5\,\text{m/s}$ and $\text{MR}=\frac{\dot{m}_{\text{water}}}{\dot{m}_{\text{air}}}=0.5$

Figure 5-27 depicts the effect of changing the initial-speed-ratio, SR_o, on the spray chamber effectiveness, ε, for "escape" wall boundary condition. It can be seen from this figure that there are two critical values for the initial speed-ratio. The first critical speed-ratio, SR_ε, corresponds to the point of maximum effectiveness. The second critical speed-ratio, SR_C, corresponds to the effective spray-tip-penetration-length, S_{eff}. Figure 5-27 shows that SR_ε is in the vicinity of 0.5. This suggests that the effectiveness not only depends on the initial speed-ratio, but also on the spray cone angle, and the spray chamber geometry. This is discussed in details in section 6.2.3.2.

Figure 5-27 also shows that the effectiveness increases as the initial speed-ratio increases until the maximum effectiveness, $\varepsilon_{\max}$, is reached at SR_ε. However, this trend is reversed at initial speed-ratios greater than SR_ε. The effectiveness of the spray chamber deteriorates monotonously as the initial speed-ratio increases beyond SR_ε until SR_C is reached. At the second critical speed-ratio, SR_C, the effectiveness suddenly drops. Following this sharp drop at SR_C the effectiveness continues to deteriorate with further increase in the initial speed-ratio. This response of effectiveness to variation in initial speed-ratio may be explained as follows.

Increasing the initial speed-ratio, while keeping the mass flow rates and droplet diameter constant, increases the heat transfer coefficient and the total surface area available for heat transfer. The increase in surface area is due to the increase in the spray-tip-penetration-length and the doubling effect of the surface area by the retracting droplets. However, as the

spray-tip-penetration-length increases more droplets reach the walls, as shown in Figure 5-19 and Figure 5-20. Consequently, owing to the "escape" wall boundary condition, these droplets are lost at the walls. The lost droplets don't participate any further in the heat and mass transfer process. For initial speed-ratios less than SR_{ε} the increase in surface area, due to the increase in spray-tip-penetration-length, overcomes the effect of water droplets loss. The net effect is an increase in the UA product, as shown in Figure 5-28, which increases the spray cooler effectiveness, as shown in Figure 5-29. However, the effect of loosing water droplets becomes very pronounced at initial speed-ratios greater than SR_{ε} resulting in a drop in the conductance, UA product, and consequently, the effectiveness. Moreover, at initial speed-ratios greater than SR_C the surface area doubling effect vanishes resulting in a further drop in the spray chamber effectiveness. This reduction in surface area, is also accompanied by a reduction in the residence time. Consequently, the net effect is a reduction in effectiveness due to the decrease in the conductance, as shown in Figure 5-28 and Figure 5-29

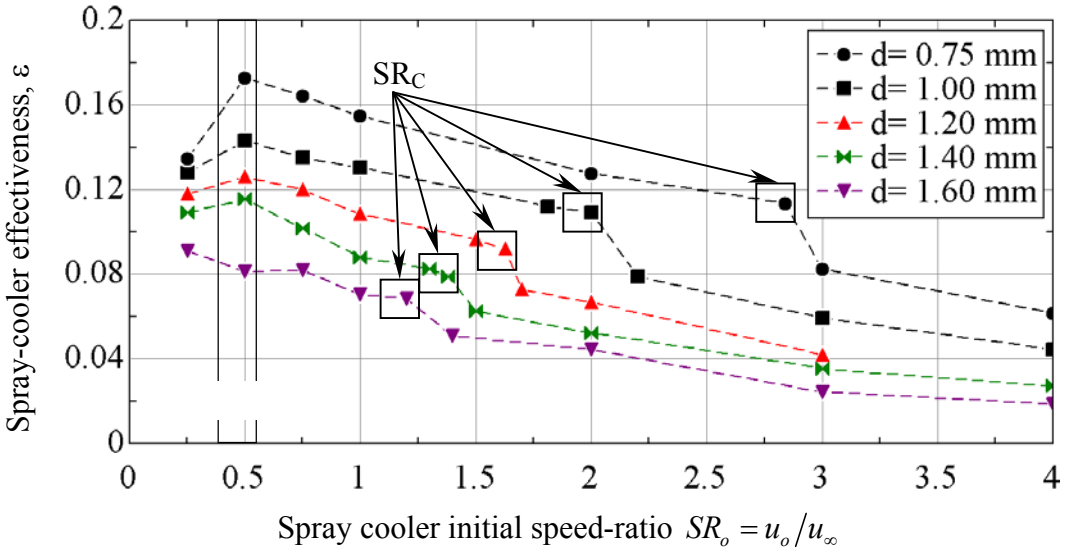

a- Gravity = 0 m/s^2

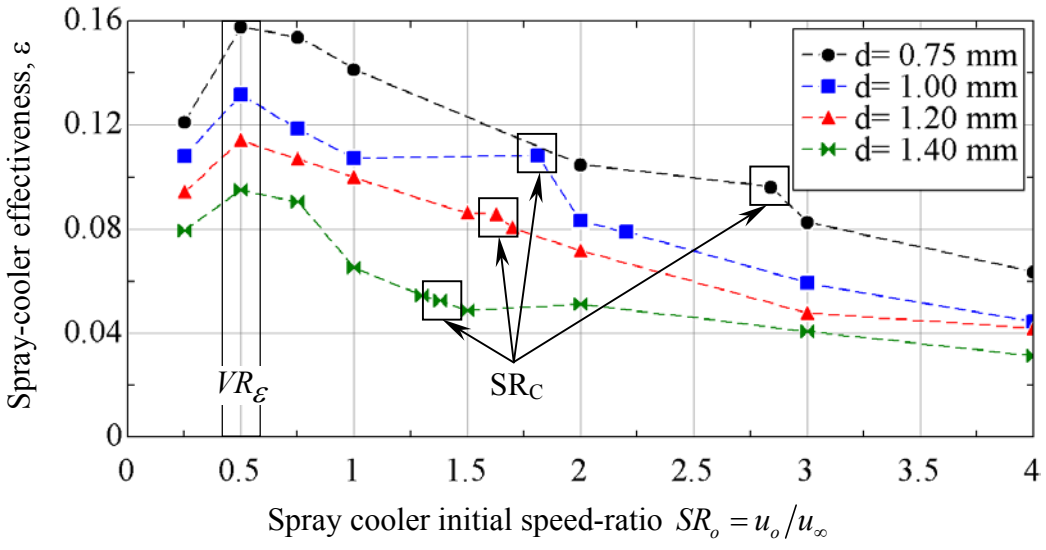

b- Gravity = -9.81 m/s^2

Figure 5-27 Effect of the spray cooler initial speed-ratio, SR_o, on the spray cooler effectiveness for "escape" wall boundary condition $\underline{u}_\infty = -5\,\text{m/s}$ and $\text{MR} = \frac{\dot{m}_{\text{water}}}{\dot{m}_{\text{air}}} = 0.5$

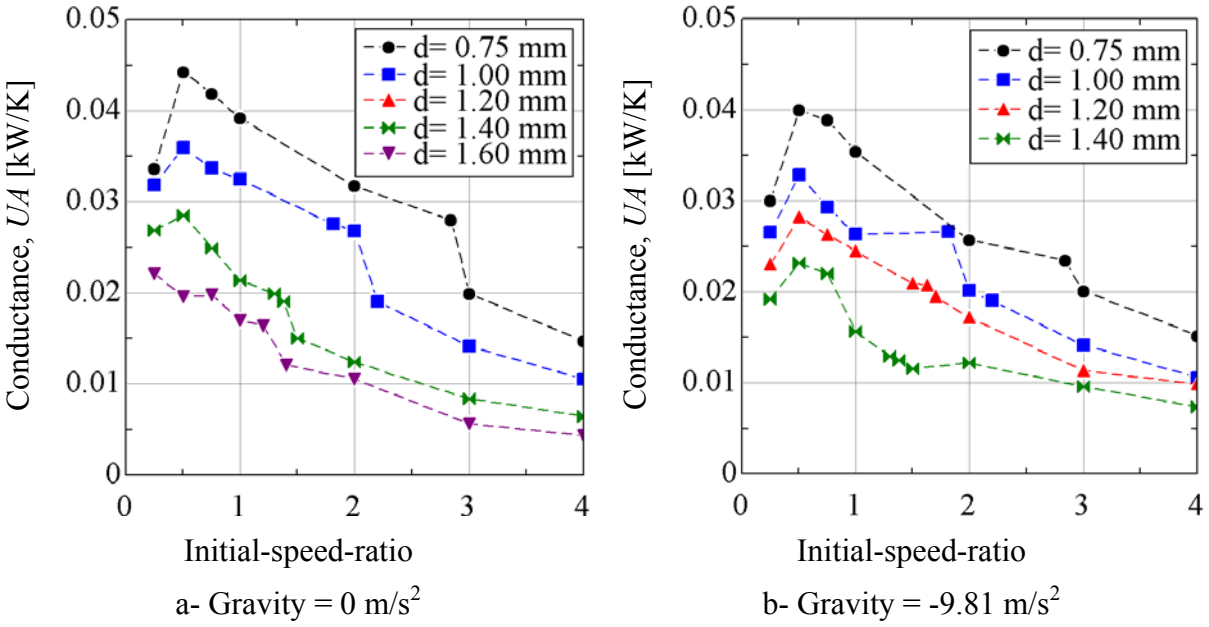

Figure 5-28 Effect of the spray cooler initial speed-ratio on the spray cooler conductance for "escape" wall boundary condition $\underline{u}_{\infty} = -5\,\text{m/s}$ and $\text{MR}=\frac{\dot{m}_{\text{water}}}{\dot{m}_{\text{air}}}=0.5$

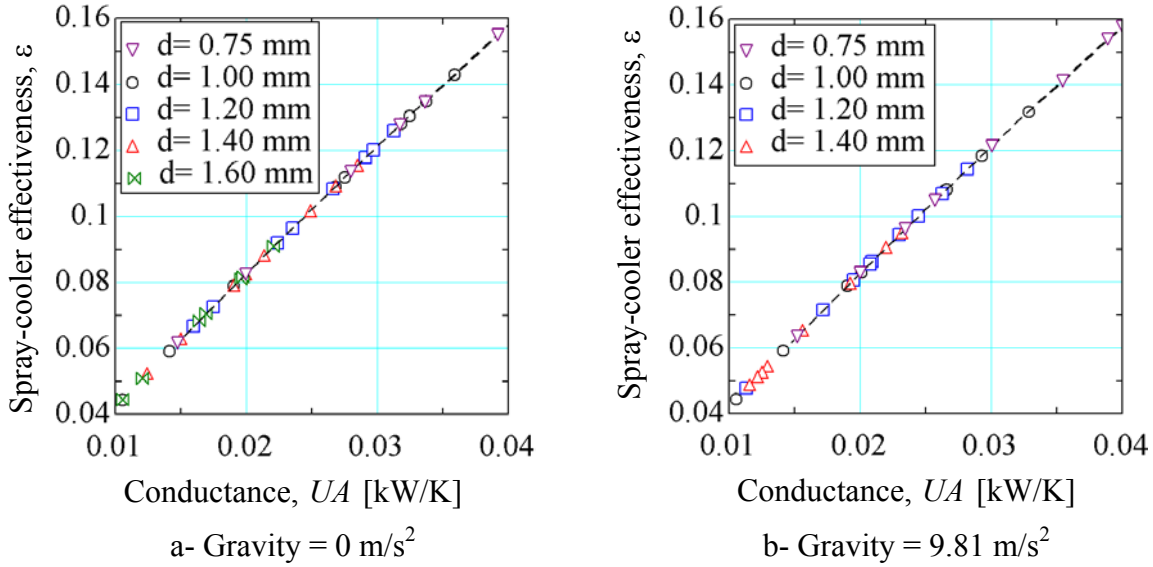

Figure 5-29 Effect of spray cooler conductance, UA product, on the spray cooler effectiveness, ε, for "escape" wall boundary condition $\underline{u}_{\infty} = -5\,\text{m/s}$ and $\text{MR}=\frac{\dot{m}_{\text{water}}}{\dot{m}_{\text{air}}}=0.5$

5.6.2.2.2 Effect of droplet diameter on spray chamber effectiveness

Figure 5-24 and Figure 5-27 show that the response of the spray cooler effectiveness to the change in droplet diameter is the same for both wall boundary conditions, for all initial speed-ratios, with and without gravity. Increasing the droplet diameter decreases the effectiveness. The effectiveness-droplet-diameter relation is controlled by the conductance of the spray chamber, where the spray-tip-penetration-length to diameter ratio, $\zeta_A = S_{\max} / d$ and $\zeta_{UA} = S_{\max} / \sqrt{d^3}$ plays a pivotal role, as shown by equations (5.58) and (5.62), respectively.

For both wall boundary conditions at initial speed-ratios greater than SR_C, the spray-tip-penetration-length is at its maximum value S_{eff}. Therefore, increasing the droplet diameter decreases the spray-tip-penetration-length to diameter ratio, ζ_A, and, hence, the total surface area decreases, for the same mass flow rate, as illustrated by equation (5.58). Also, increasing the droplet diameter decreases the overall heat transfer coefficient, as shown by equation (5.60). Thus, the net effect is a reduction in the conductance, UA product, and, consequently, the spray cooler effectiveness.

The same trend is true at initial speed-ratios less than SR_C. Increasing the droplet diameter decreases the spray cooler effectiveness, due to the reduction of the conductance of the spray cooler, UA product. Equation (5.58) shows that the spray-tip-penetration-length and the droplet diameter counter act one another. Increasing the droplet diameter increases the spray-tip-penetration-length, as shown in Figure 5-14. For initial speed-ratios less than SR_C,

the effect of the spray-tip-penetration-length overcomes the effect of droplet diameter. Consequently, the spray-tip-penetration-length to droplet diameter ratio, $\zeta_A = S_{\max} / d$, increases as the droplet diameter increases, as shown in Figure 5-30. Accordingly, the surface area increases, as illustrated by equation (5.58). On the other hand, equation (5.60) shows that increasing the droplet diameter decreases the overall heat transfer coefficient. Nevertheless, as the droplet diameter increases the ratio $\zeta_{UA} = S_{\max} / \sqrt{d^3}$ decreases, as illustrated in Figure 5-31. Thus, the net effect is a reduction in the conductance, as shown in Figure 5-32, and in accordance the effectiveness of the spray cooler, as shown in Figure 5-33. This suggests that the reduction in the overall heat transfer coefficient overcomes the increase in surface area.

For the "escape" wall boundary condition, for initial speed-ratios greater than SR_C, Figure 5-27 shows that increasing the droplet diameter decreases the spray cooler effectiveness. Increasing the droplet diameter increases the penetration-length, as shown in Figure 5-15. As a result, the surface area tends to increase and, one would expect the effectiveness to increase. However, as the penetration length increases more droplets reach the walls, as shown in Figure 5-19 and Figure 5-20. Consequently, these droplets are lost at the walls, with the imposition of the "escape" wall boundary condition; therefore, the effectiveness decreases. The effect of water loss at the walls dominates the effect of the penetration-length increase. This implies that the droplet diameter is the principal factor that controls the effectiveness. Consequently, as the droplet diameter increases, the effectiveness decreases due to the reduction in surface area, as illustrated by equation (5.58).

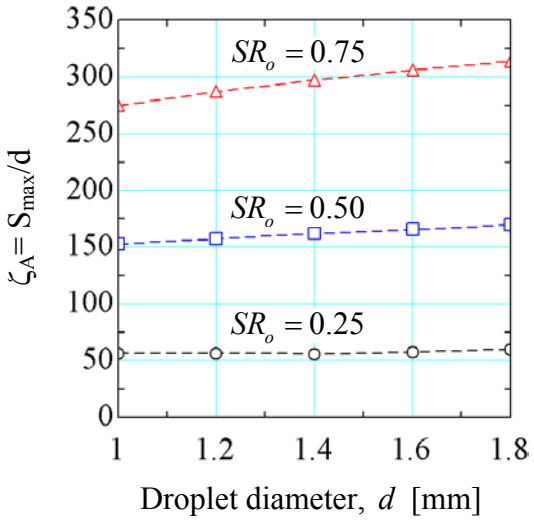

Figure 5-30 Effect of droplet diameter on the spray-tip-penetration-length to droplet-diameter ratio, $\zeta_A = S_{\max}/d$ for "reflect" wall boundary condition, gravity = 0 m/s^2.

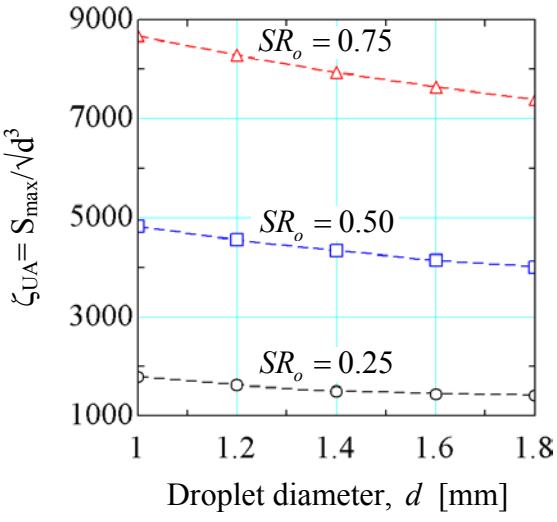

Figure 5-31 Effect of droplet diameter on the spray-tip-penetration-length to droplet-diameter ratio, $\zeta_{UA} = S_{\max}/\sqrt{d^3}$ for "reflect" wall boundary condition, gravity = 0 m/s^2

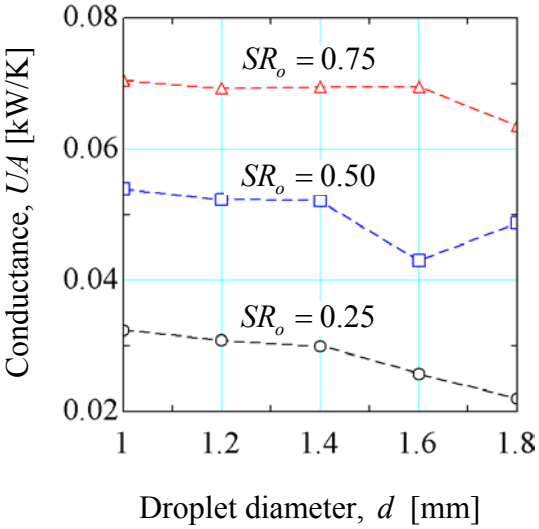

Figure 5-32 Effect of droplet diameter on the spray cooler conductance, UA for "reflect" wall boundary condition, gravity = 0 m/s^2

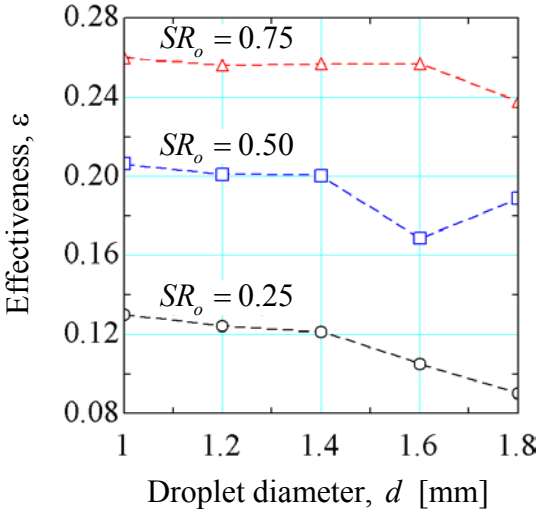

Figure 5-33 Effect of droplet diameter on the spray cooler effectiveness, ε for "reflect" wall boundary condition, gravity = 0 m/s^2

5.6.2.2.3 *Effect of gravity force*

The discussion presented in sections 5.6.2.2.1, and 5.6.2.2.2, shows that the conductance, *UA* product, of the spray-chamber is the main controlling factor that affects the spray chamber heat transfer effectiveness. The spray-chamber conductance depends on a number of parameters, as illustrated by equation (5.62). Consequently, the parameters that are affected by gravity are the ones that will dictate the effect of gravity on the spray cooler effectiveness.

Figure 5-22 a shows that for "reflect" wall boundary condition, the spray-tip-penetration-length is similar for both cases $g = 0$ m/s^2 and $g = -9.81$ m/s^2. Consequently, the conductance, *UA* product, is the same for both cases as illustrated by equation (5.62) and Figure 5-34a. Hence, the effectiveness of the spray cooler with "reflect" wall boundary condition is not sensitive to gravitational forces, as shown in Figure 5-35a.

On the other hand, for "escape" wall boundary condition the spray-tip-penetration-length differs for the two cases $g = 0\,\text{m/s}^2$ and $g = -9.81\,\text{m/s}^2$. Figure 5-22b shows that the zero gravity case over predicts the spray-tip-penetration-length. Thus, the conductance and accordingly the effectiveness for the zero gravity case are higher, as shown in Figure 5-34b and Figure 5-35b.

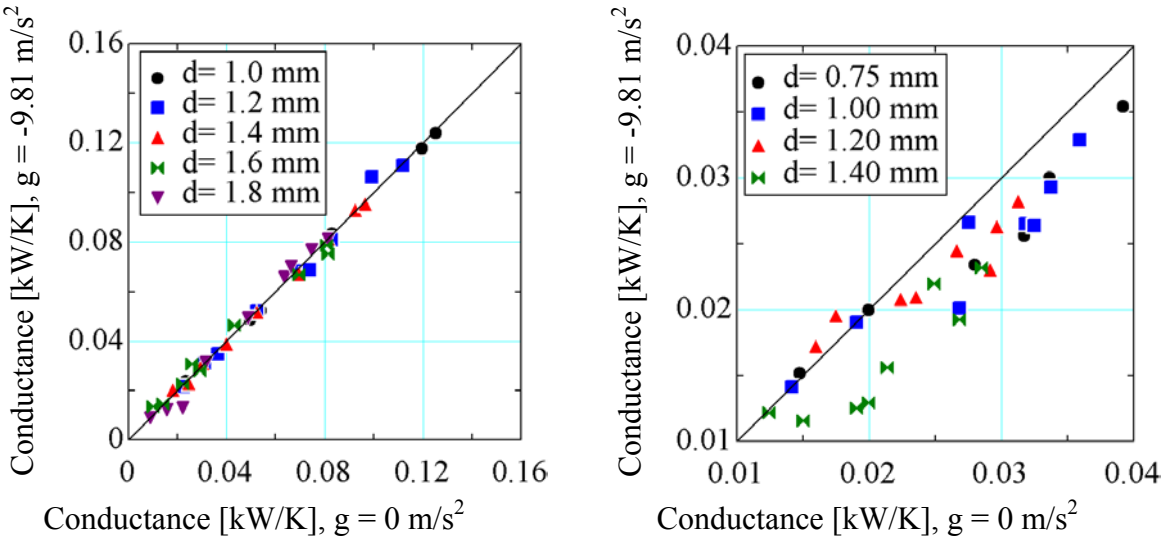

Figure 5-34 Effect of gravity on the spray cooler conductance, UA, for different spray chamber wall boundary conditions $\underline{u}_\infty = -5\,\text{m/s}$, and $\text{MR}=\frac{\dot{m}_{\text{water}}}{\dot{m}_{\text{air}}}=0.5$

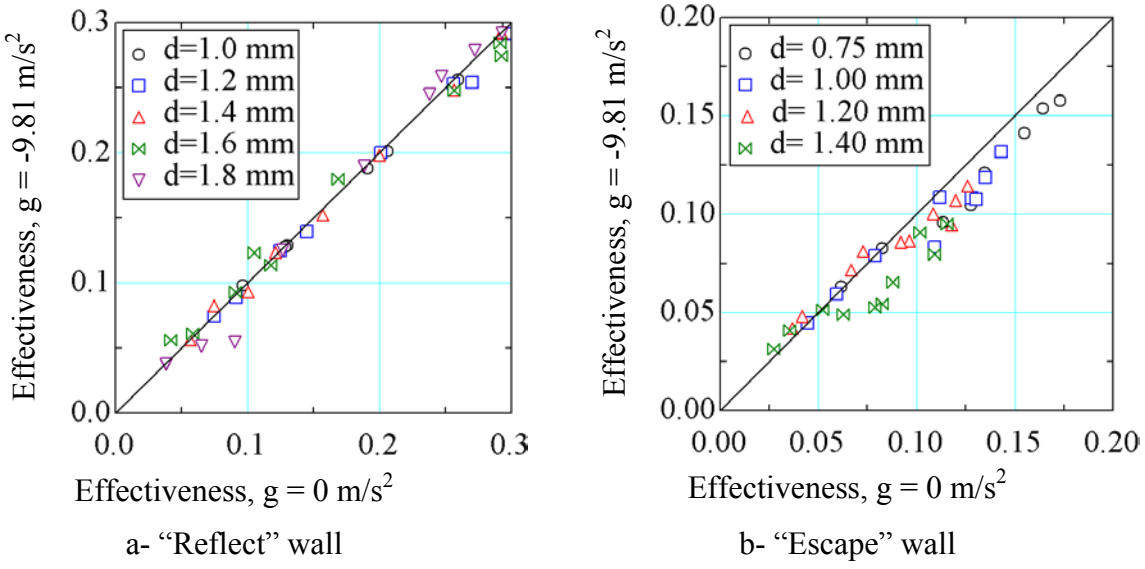

Figure 5-35 Effect of gravity on the spray cooler effectiveness, ε, for different spray chamber wall boundary conditions $\underline{u}_\infty = -5\,\text{m/s}$, and $\text{MR}=\frac{\dot{m}_{\text{water}}}{\dot{m}_{\text{air}}}=0.5$

Figure 5-36 to Figure 5-39 depict the temperature contours for the two cases: $g = 0\,\mathrm{m/s^2}$ and $g = -9.81\,\mathrm{m/s^2}$ for "reflect" and "escape" wall boundary condition, respectively. These figures show that the gravitational force causes the profiles to be skewed towards the bottom, resulting in a non uniform temperature distribution along the vertical direction.

However, this non uniformity decreases as the initial speed-ratio decreases due to the fact that as the initial speed-ratio increases the droplets initial velocity increases. Consequently, the droplets gain more initial momentum that helps to overcome the effect of the gravitational force, and the droplets are lifted upwards away from the lower wall, as shown in Figure 5-18 and Figure 5-20.

The abovementioned discussion shows that, the spray cooler effectiveness depends on several parameters. These parameters include the droplet diameter, the spray-tip-penetration-length, and the spray cooler initial speed-ratio. Also, the effectiveness of the spray cooler is dependent on the type of wall boundary condition. The effectiveness for "reflect" wall spray chamber doesn't depend on the geometry of the spray chamber. It only depends on the hydrodynamics of the air and water droplets, expressed as the speed-ratio SR_o. On the other hand, the effectiveness for "escape" wall chamber depends on the geometry as well as the hydrodynamics. In general, the effectiveness tends to increase as the spray cooler initial speed-ratio increases until the maximum effectiveness is reached. The trend is then reversed beyond this point. Furthermore, increasing the droplet diameter decreases the effectiveness. The results show that for "reflect" wall boundary condition the spray cooler effectiveness is insensitive to gravity effects, owing to the complete momentum recovery of the water

droplets. However, for “escape” wall boundary condition the zero gravity case over predicts the gravity case. This is owed to the gravitational force that accelerates the droplets faster towards the spray chamber walls. At the walls, the droplets lose their momentum and come to rest.

It is should be mentioned that the effect of the droplet diameter, ranging from 1 mm to 1.8 mm, on the performance of the spray cooler chamber was studied under the reflective wall boundary conditions. For the escape wall boundary condition however, the droplet diameter was in the range of 0.75 mm and up to 1.4 mm. The reason for not using the same diameter range in both cases is that under the escape wall boundary condition, a droplet diameter greater than 1.4 mm leads to a very poor heat transfer characteristics so that the air exit temperature was almost the same as the air inlet temperature. Therefore, a droplet diameter greater than 1.4 mm is not of interest for any spray cooler of practical use under the escape wall boundary condition. The noticed poor heat transfer performance of the spray cooler under the escape wall boundary conditions can be attributed to two effects, namely, loosing droplets, by the definition of the escape wall boundary condition, leads to lower heat transfer area and consequently lower heat transfer performance. The second effect is that as the droplet diameter increases, its weight increases and it has higher gravity effect and its tendency to fall down and hit the wall increases. Once the droplet hits the wall, it is considered out of the domain. These two effects lead to the same result of reducing the heat transfer area and deteriorate the heat transfer performance of the spray cooler.

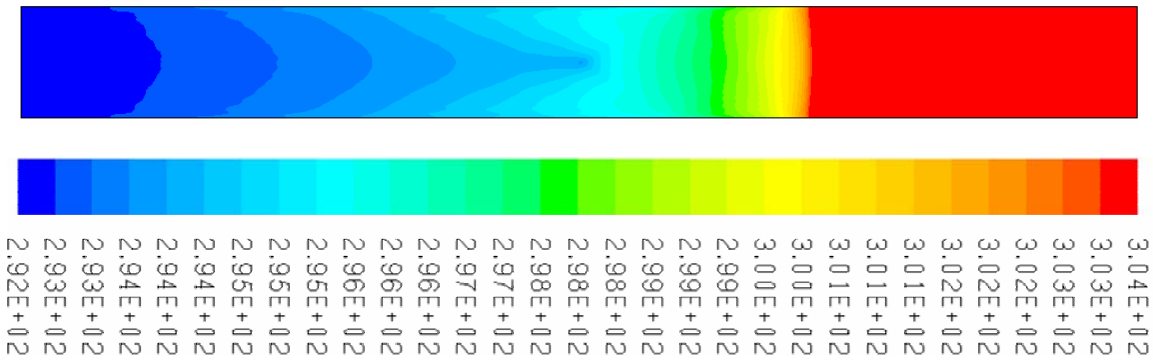

a- Velocity ratio $SR_o = 1.0$

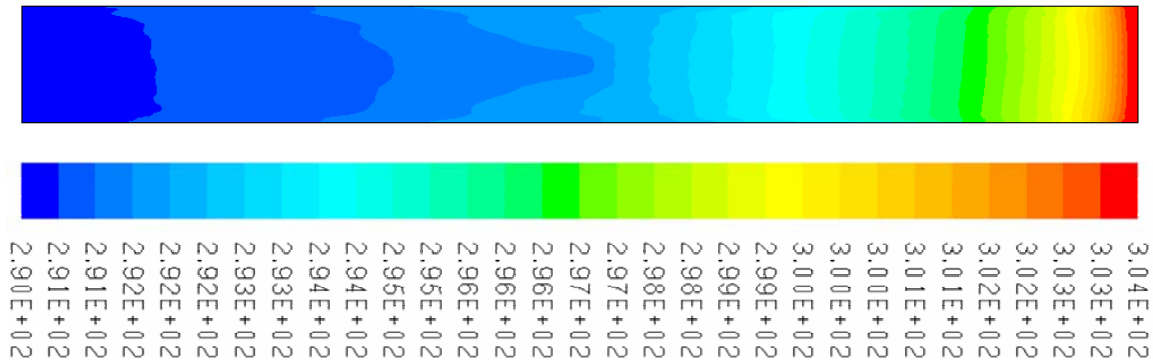

b- Velocity ratio $SR_o = 2.0$

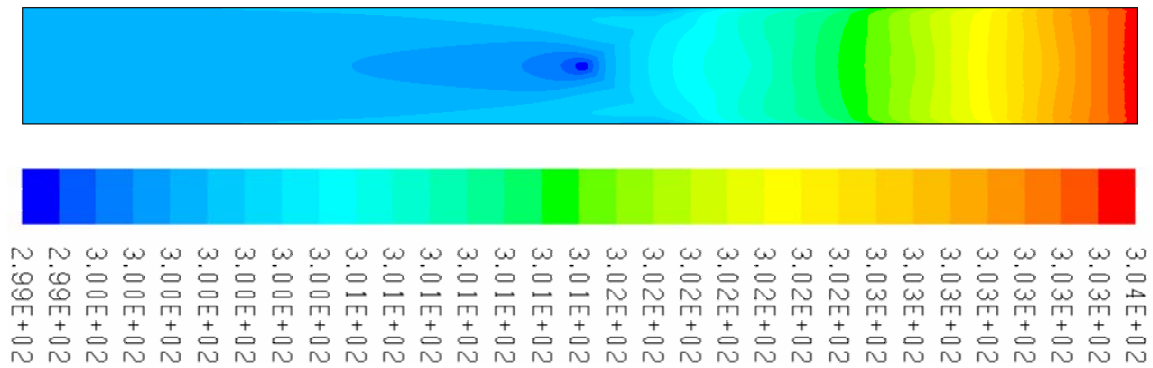

c- Velocity ratio $SR_o = 3.0$

Figure 5-36 Temperature contours for spray cooler with "reflect" wall boundary condition, gravity = 0 m/s^2, $\underline{u}_\infty = -5$ m/s, $d = 1$mm, and MR$=\dfrac{\dot{m}_{\text{water}}}{\dot{m}_{\text{air}}} = 0.5$

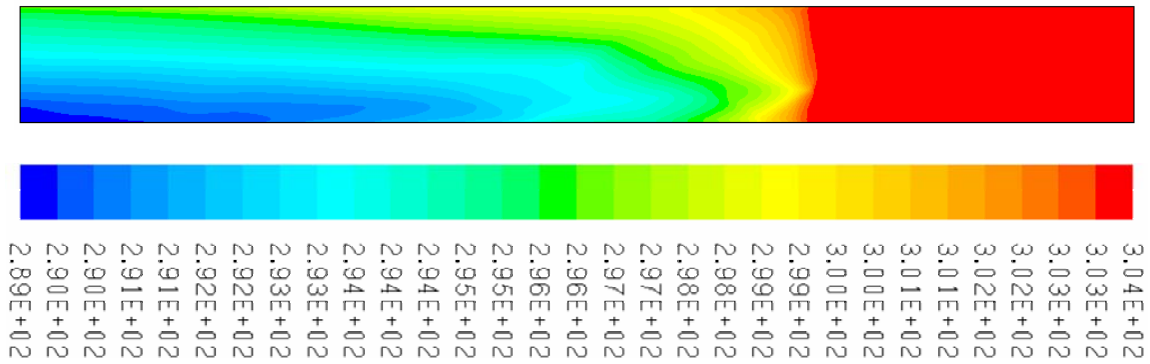

a- Velocity ratio $SR_o = 1.0$

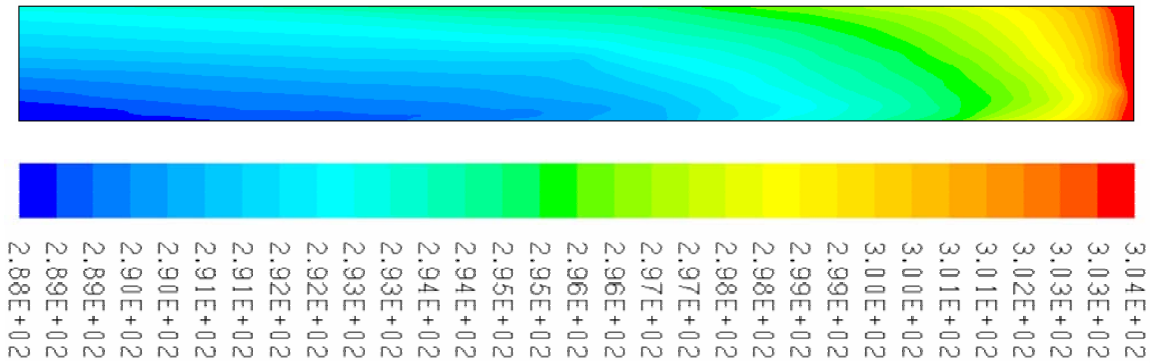

b- Velocity ratio $SR_o = 2.0$

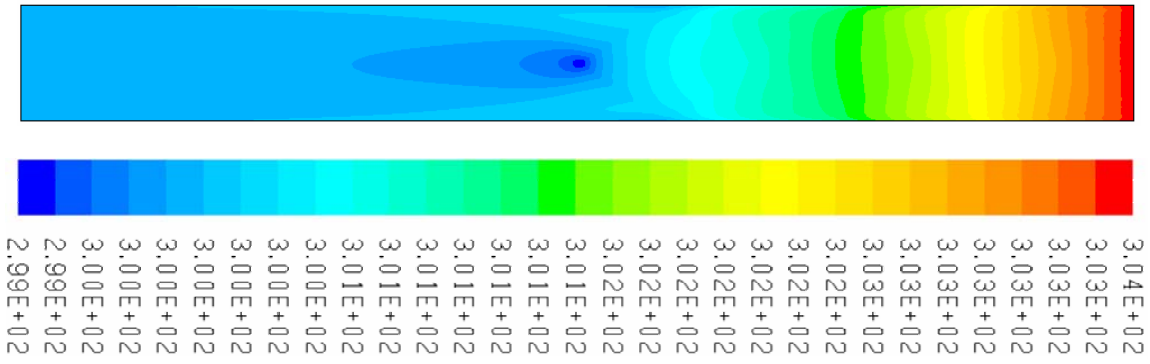

c- Velocity ratio $SR_o = 3.0$

Figure 5-37 Temperature contours for spray cooler with "reflect" wall boundary condition,

gravity = -9.81 m/s^2, $\underline{u}_\infty = -5\,\text{m/s}$, $d = 1\text{mm}$, and $\text{MR} = \dfrac{\dot{m}_{\text{water}}}{\dot{m}_{\text{air}}} = 0.5$

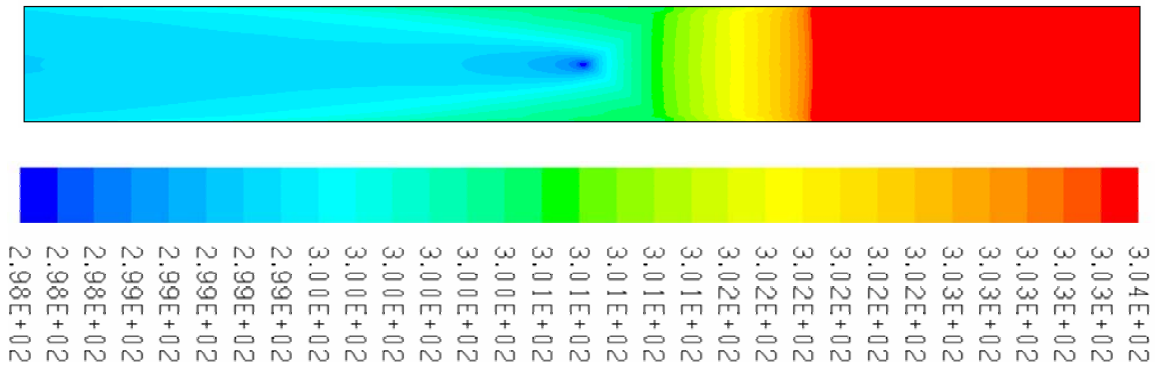

a- Velocity ratio $SR_o = 1.0$

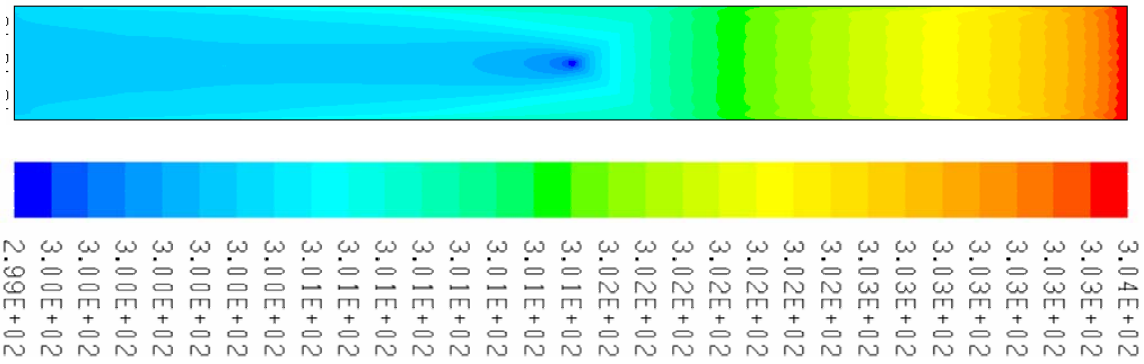

b- Velocity ratio $SR_o = 2.0$

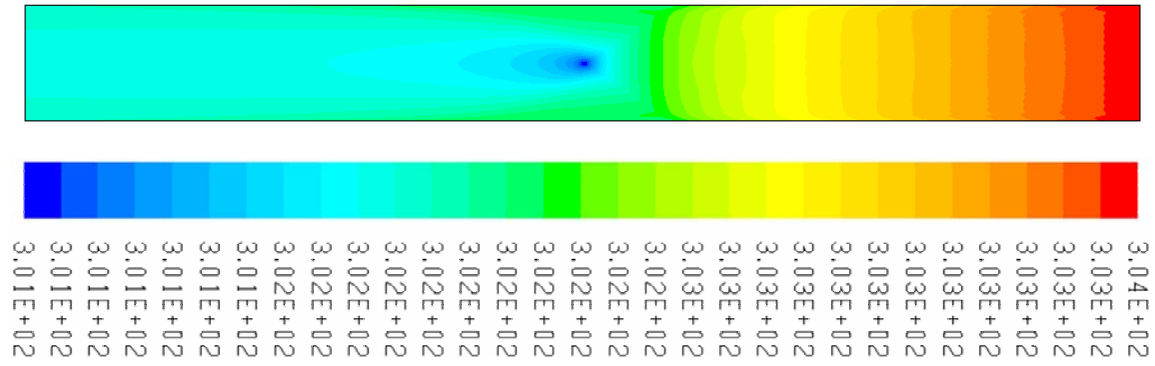

c- Velocity ratio $SR_o = 3.0$

Figure 5-38 Temperature contours for spray cooler with "escape" wall boundary condition,

gravity = 0 m/s^2, $\underline{u}_\infty = -5$ m/s , $d = 1$mm , and MR$= \dfrac{\dot{m}_{\text{water}}}{\dot{m}_{\text{air}}} = 0.5$

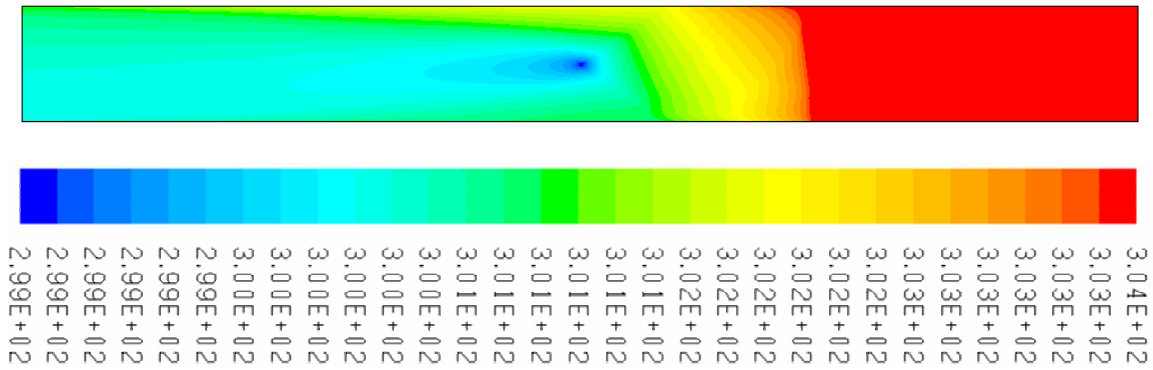

a- Velocity ratio $SR_o = 1.0$

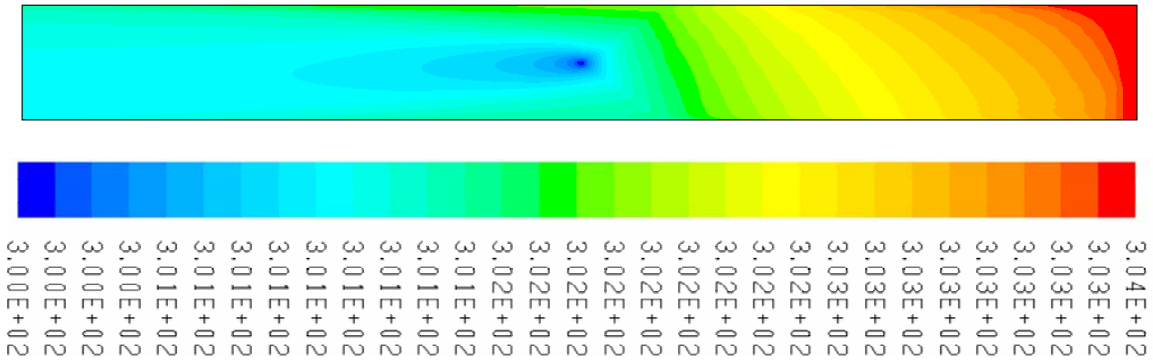

b- Velocity ratio $SR_o = 2.0$

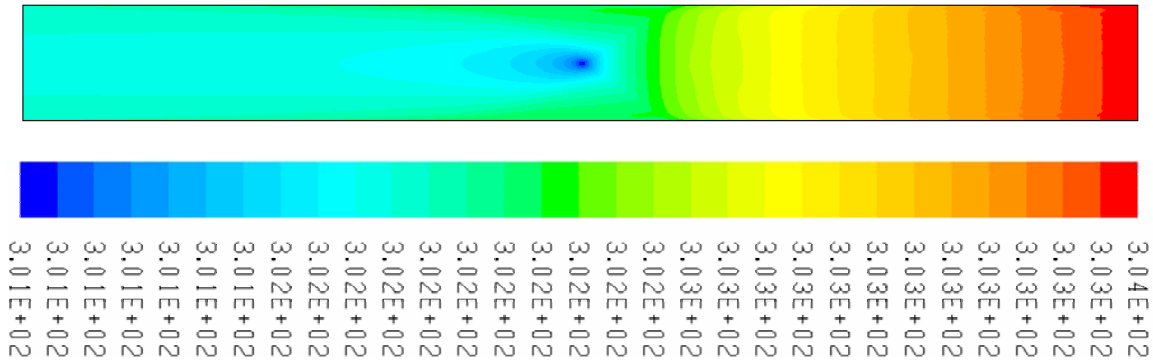

c- Velocity ratio $SR_o = 3.0$

Figure 5-39 Temperature contours for spray cooler with "escape" wall boundary condition, gravity = -9.81 m/s^2, $\underline{u}_\infty = -5\,\text{m/s}$, $d = 1\text{mm}$, and $\text{MR} = \dfrac{\dot{m}_{\text{water}}}{\dot{m}_{\text{air}}} = 0.5$

5.7 Summary

Numerical simulations provide a tool for examining the performance of new spray coolers designs. Even though experimentation remains the best tool to obtain definitive results, numerical simulations have some major advantages. In particular, they are relatively inexpensive and fast. Also, numerical simulations offer an easy way for making parametric studies. Morover, results from numerical simulations help in selecting which experiments need to be performed.

In the current research work, a software package, FLUENT 4, is used to numerically simulate the spray cooler. The model is used to assess the impacts of changing the spray cooler initial speed-ratio and droplet diameter on the performance of the spray cooler. Two types of spray chamber wall boundary conditions "reflect" and escape" are investigated for two cases $g = 0\,\text{m/s}^2$ and $g = -9.81\,\text{m/s}^2$. These two scenarios bracket the range of possibilities for all wall conditions. The results show that the thermal performance of the spray chamber, expressed in the form of effectiveness, is highly dependent on the hydrodynamics of the air and water in the spray chamber.

For "reflect" wall boundary condition, the effectiveness of the spray cooler increases as the initial speed-ratio increases until the maximum effectiveness is reached at an initial speed-ratio where the spray-tip-penetration-length equals the spray chamber length. This increase in effectiveness is owed to the increase in the spray cooler conductance due to increasing Reynolds number and the total surface area.

For “escape” wall boundary condition, the maximum effectiveness is at an initial speed-ratio where the increase in surface area, due to the increase in spray-tip-penetration-length, is counter balanced by the adverse effect of water droplets loss at the walls.

In real life spray chamber walls are neither “reflect” or “escape” the are a mix between both scenarios. Consequently, the optimum initial speed-ratio would be an intermediate value between that for these two deal cases.

5.8 Nomenclature

A	Total interfacial area for water droplets contained in the spray chamber	m^2
A_d	Frontal area of the droplet	m^2
A_v	Total interfacial area for water droplets contained in the control volume dV_ℓ	
C_d	Drag-coefficient for spheres	
C_{min}	Minimum capacitance rate	J/K
$c_{p_{air}}$	Specific heat of air at constant pressure	J/kg-K
c_{water}	Specific heat of water	J/kg-K
D	Duct diameter	m
D_{AB}	Mass diffusivity, or diffusion coefficient	m^2/s
d	Droplet diameter	m
dA	Elemental area	m^2
dV_ℓ	Differential volume	m^3
E_{air}	Energy transferred from the air	J
E_{water}	Energy transferred to water droplet	J
e	Coefficient of restitution	
F	Correction factor for mean temperature difference	
$\underline{F}_{acc}$	Acceleration force	N
$\underline{F}_B$	Basset drag force	N
$\underline{F}_L$	Lift force	N
$\underline{F}_{mag}$	Magnus lift force	N
$\underline{F}_{us}$	Unsteady force	N

$\underline{F}_{vm}$	Force of virtual mass	N
$\underline{F}_{\Delta p}$	Pressure gradient force	N
$\underline{F}_{ss}$	Steady-state force	N
$\underline{g}$	Gravitational acceleration	m^2/s
h_{air}	Specific enthalpy of moist air	J/kg
h_c	Convection heat transfer coefficient	W/m^2-K
h_{fg}	Latent heat of condensation	J/kg-K
h_r	Radiation heat transfer coefficient	W/m^2-K
h_{water}	Specific enthalpy of water	J/kg
I	Turbulence intensity	
k	Turbulent kinetic energy	
k_{air}	Thermal conductivity of air	W/m-K
ℓ	Integral length scale	m
MR	Mass ratio	
m_{air}	Mass of air	kg
$\dot{m}_{air}$	Mass flow rate of air	kg/s
m_{cond}	Mass of condensate	kg
m_d	Droplet mass	kg
$\dot{m}_{cond}$	Mass flow rate of condensate	kg/s
m_{water}	Mass of water droplet	kg
$\dot{m}_{water}$	Mass flow rate of water	kg/s
$N_{droplets}$	Total number of droplets in the spray chamber	
$\dot{N}_{droplets}$	Droplets rate	s^{-1}
$\underline{n}$	Unit vector	
p	Pressure on the water droplet	N/m^2

$\dot{Q}$	Rate of energy exchange between the air-side and water-side	W
$\dot{Q}_{\text{air}}$	Rate of energy transfer from the air-side to the water-side	kW
$\dot{Q}_{\text{sensible}}$	Sensible heat transfer	W
$\dot{Q}_{\text{latent}}$	Latent heat transfer	W
$\dot{Q}_{\text{water}}$	Rate of energy transfer from the water-side to the air-side	kW
S_{eff}	Effective spray-tip penetration length	m
S_{max}	Spray-tip penetration length	m
SR_o	Spray chamber initial speed-ratio	
SR_C	Critical initial speed-ratio that corresponds to maximum spray penetration length	
$SR_{\mathcal{E}}$	Critical initial speed-ratio that corresponds to maximum spray cooler effectiveness	
T	Air dry bulb temperature	K
$T_{\text{air}}\big\vert_{\text{actual}}$	Actual air-side exit temperature	ºC
$T_{\text{air}}\big\vert_{\Delta\dot{Q}_{\text{offset}}=0}$	Air-side exit temperature at zero energy balance offset	ºC
$T_{\text{in}}\big\vert_{\text{air}}$	Spray chamber air-side inlet temperature	ºC
$T_{\text{in}}\big\vert_{\text{water}}$	Spray chamber water-side inlet temperature	ºC
$T_{\text{out}}\big\vert_{\text{air}}$	Spray chamber air-side outlet temperature	ºC
$T_{\text{water}}\big\vert_{\text{actual}}$	Actual water-side exit temperature	ºC
$T_{\text{water}}\big\vert_{\Delta\dot{Q}_{\text{offset}}=0}$	Water-side exit temperature at zero energy balance offset	ºC
T_{w}	Water droplet temperature	K
t	Time	s
t_{cond}	Condensate temperature	ºC
t_{water}	Water temperature	ºC

t_{res}	Particle residence time	s
UA	Conductance	W/K
U	Overall heat transfer coefficient	W/m^2-K
$\underline{U}_\infty$	Continuous phase, air, velocity vector	m/s
u	Magnitude of the horizontal velocity component of the water droplet	m/s
u'	Root-mean-square of the turbulent velocity fluctuation	m/s
u_o	Magnitude of the initial horizontal velocity component of the spray.	m/s
$\underline{u}_o$	Horizontal initial velocity vector of the spray	m/s
u_∞	Magnitude of the horizontal velocity component of air	m/s
$\underline{u}_\infty$	Horizontal velocity vector of air	m/s
$\underline{V}$	Water droplet velocity vector	m/s
V_d	Droplet volume	m^3
$\underline{V}_r$	Relative velocity vector	m/s
$\underline{v}_o$	Vertical initial velocity vector of the spray	m/s
v_{1n}	droplet velocity component normal to the wall before collision	m/s
v_{2n}	droplet velocity component normal to the wall after collision	m/s
$\underline{w}_o$	Initial velocity vector of the spray in the z direction	m/s
x, y, z	Position Cartesian coordinates	
$\Delta\dot{Q}_{\text{offset}}$	Offset in energy balance between the air side and water side	%
$\Delta T_{\text{air}_{\text{error}}}$	Error in reporting the air-side exit temperature	ºC
ΔT_{LM}	Logarithmic mean temperature difference	ºC
ΔT_{max}	Maximum temperature difference across the spray cooler	ºC
ΔT_{mean}	Mean temperature difference	ºC
$\Delta T_{\text{water}_{\text{error}}}$	Error in reporting the water-side exit temperature	ºC

5.8.1 Dimensionless numbers

Nu	Nusselt number
Pr	Prandtl number
Re	Reynolds number
Re_G	
Sc	Schmidt number
Sh	Sherwood number

5.8.2 Greek symbols

ω	Air humidity ratio	kg/kg
ω_s	Air humidity ratio at the water droplet temperature	kg/kg
$\underline{\omega}$	Particle rotation	Rad/s
σ	Steffan Boltzman constant	W/ m^2-K^4
ε	Effectiveness	
ε_{max}	Maximum effectiveness	
$\boldsymbol{\varepsilon}$	Emissivity	
ζ_A	S_{max}/d	
ζ_{UA}	$\frac{S_{max}}{\sqrt{d^3}}$	
ρ_{air}	Density of moist air	kg/m^3
ρ_{water}	Density of water	kg/m^3
μ_{air}	Viscosity of air	kg/m-s
ν	Kinematic viscosity	m^2/s

5.9 References

1 Fluent Incorporated Network Services, 10 Cavendish Court, Lebanon, NH 03766-1442, www.fluent.com.

2 Frank M White, "Fluid Mechanics", McGraw-Hill, 4th ed., 1999, ISBN 0-07-069716-7.

3 Zarling, J, "Heat and mass transfer from freely falling drops at low temperature", CRREL-Rep. n 80-18 Aug 1980, 20 p

4 Ranz, W. E. and W.R. Marshall, "Evaporation from drops", Chemical Engineering Progress, vol. 48, no.3 & 4, 1952, pp 141-146, 173-180.

5 Mugele, R. and Evans, H. D., Droplet Distribution in Sprays, Ind. Eng. Chem., Vol. 43, No. 43 No. 6, 1951, pp. 1317-1324.

6 Clayton Crowe, Martin Sommerfeld, Yutaka Tsuji, "Multiphase flows with droplets and particles", CRC Press, 1st ed., 1998, ISBN-0849394694.

7 Munson, B.R., Okisshi, T.H., Young, D.F., "Fundamentals of fluid mechanics", John Willey & Sons, 1990, ISBN 0-471-85526-X.

8 Prandtl, L., "Guide to the theory of flow", 2nd ed. Braunschweig, 1944, pp173.

9 Langmuir, I., and Blodgett, K., "A mathematical investigation of water droplet trajectories", A.A.F. Tech. Rep. 5418, Air Material Command, Wright Patterson Air Force Base, 1946.

10 Mellor, R., Ph.D. thesis, University of Sheffield, 1969.

11 Morsi, S.A, and Alexander, A.J., “An investigation of particle trajectories in two-phase flow systems”, Journal of Fluid Mechanics, vol. 55 (part 2), Sep 1972, pp 193-208.

11 Putnam, A. “Integratable form of droplet drag coefficient”, J. Am. Rocket Soc., Vol.31, 1961, pp. 1467-1468.

12 Putnam, A. “Integratable form of droplet drag coefficient”, J. Am. Rocket Soc., Vol.31, 1961, pp. 1467-1468.

13 Lefebvre, A.H., “Atomization and sprays”, Hemisphere publishing corporation, 1989, ISBN 0-89116-603-3.

14 Keenan, Chao, Keyes, Gas Tables, Wiley, 1985.

15 Y.S. Touloukian, P.E. Liley, S.C. Saxena, “Thermophysical Properties of Matter”, FI/Plenun, NY, Vol.3, 1970, ISBN 0-306067020-8.

16 Y.S. Touloukian, P.E. Liley, S.C. Saxena, “Thermophysical Properties of Matter”, FI/Plenun, NY, Vol.11, 1970, ISBN 0-306067020-8.

17 White, F.M., “Heat and mass transfer”, Addison-Wesley publishing company, 1988, ISBN 0-201-17099-X

Chapter 6 Design and Performance

To study the performance of spray coolers, a model that describes the hydrodynamics and thermal performance is required. After the model is chosen, constructed and parameterized, the next step is to find an appropriate method for solving the model. There are two solution techniques by which the model can be solved. These may be broadly classified as numerical simulation and analytical solution techniques.

Section 5.3 shows that the equations used to model the spray-cooler are complex. This complexity is mainly due to the fact that the equations are linked together in a way that makes the closed form analytical solution intractable. Consequently, a numerical approach offers a better alternative to solve the necessary governing equations. Several simulation runs are required to generate a sample of adequate size to allow for a parametric study to be carried out. Therefore, the problem of the theoretical modeling of direct contact spray cooling devices is computationally involved. The model should be simple and clear in revealing the essentials of the physical processes and at the same time reliable in predicting the performance of direct contact spray cooling devices. This chapter presents semi-analytical models that predict spray-tip-penetration length, overall heat transfer coefficient, interfacial area, and effectiveness for direct contact spray cooling devices. The models are composed of a set of formulae and/or computational algorithms that provide the desired performance measures as functions of the performance parameters.

6.1 Trajectory calculations

The previous chapter showed that the thermal performance of the spray-cooler is highly dependent on the hydrodynamics of the spray chamber, namely the initial velocity-ratio and the spray-tip-penetration-length. This section illustrates the equations, derivations, and assumptions necessary to calculate the velocity ratio and the spray-tip-penetration-length. The section begins by presenting the equation of motion and is followed by its solution to calculate the velocity ratio and the spray-tip-penetration-length.

6.1.1 Velocity

The trajectories of the dispersed phase, water droplets, obey Newtonian dynamics and are calculated by applying a force balance written in the Lagrangian reference frame. The force balance equates the droplet inertia with all the forces acting on it, as illustrated by the following equation

$$m_d \frac{d\underline{V}}{d\mathrm{t}} = \underline{\mathrm{F}}_{ss} + m_d \underline{g} \tag{6.1}$$

where $\underline{\mathrm{F}}_{ss} = C_d \frac{1}{2} \rho_{air} A_d \left(\underline{U}_\infty - \underline{\mathrm{V}}\right)\left|\underline{U}_\infty - \underline{\mathrm{V}}\right|$ is the steady state viscous drag.

6.1.1.1 Horizontal velocity component

The droplet acceleration in the horizontal direction obtained from the equation of motion, (6.1) is as follows

$$m_d \frac{d\underline{u}}{d\mathrm{t}} = C_d \frac{1}{2} \rho_{air} \underline{u}_{rel}^2 A_d \tag{6.2}$$

where, $m_d = \rho_{\text{water}} \pi d^3/6$, is the droplet mass, $A_d = \pi d^2/4$ is the droplet projected area, ρ_{water} and ρ_{air} are the water and air densities, respectively, $\underline{u}_{rel} = \underline{u}_\infty - \underline{u}$ is the relative velocity, where $\underline{u}_\infty$ and $\underline{u}$ are the air and droplet velocities, respectively. C_d is the drag coefficient for a sphere. Since Reynolds number is less than 1000, Putnam's [1] expression of the drag coefficient for spheres is used, $C_d = \frac{24}{\text{Re}}\left(1+\frac{1}{6}\text{Re}^{2/3}\right)$. Moreover, this expression is continuous, and can be easily integrated. Assuming that the air velocity and the droplet diameter are constant, and substituting for the drag coefficient, equation (6.2) becomes

$$\frac{d\underline{u}}{d\text{t}} = \frac{24}{\text{Re}}\left(1+\frac{1}{6}\text{Re}^{2/3}\right)\left(\underline{u}_\infty - \underline{u}\right)\left|\underline{u}_\infty - \underline{u}\right|\frac{3}{4}\frac{\rho_{\text{air}}}{\rho_{\text{water}}}\frac{1}{d} \tag{6.3}$$

Defining the Reynolds number for the dispersed phase as

$$\text{Re} = \frac{\rho_{\text{air}}\left|\underline{u}_\infty - \underline{u}\right| d}{\mu_{\text{air}}} \tag{6.4}$$

Equation (6.3) can be rewritten as

$$\frac{d\underline{u}}{d\text{t}} = \frac{24\mu_{\text{air}}}{\rho_{\text{air}}\left|\underline{u}_\infty - \underline{u}\right| d}\left(1+\frac{1}{6}\left(\frac{\rho_{\text{air}}\left|\underline{u}_\infty - \underline{u}\right| d}{\mu_{\text{air}}}\right)^{2/3}\right)\left(\underline{u}_\infty - \underline{u}\right)\left|\underline{u}_\infty - \underline{u}\right|\frac{3}{4}\frac{\rho_{\text{air}}}{\rho_{\text{water}}}\frac{1}{d} \tag{6.5}$$

Rearranging the terms gives

$$\frac{d\underline{u}}{d\text{t}} = \frac{1}{6\mu_{\text{air}}^{2/3}}\frac{18\mu_{\text{air}}}{\rho_{\text{water}} d^2}\left(6\mu_{\text{air}}^{2/3}\left(\underline{u}_\infty - \underline{u}\right) + \left(\rho_{\text{air}} d\right)^{2/3}\left(\underline{u}_\infty - \underline{u}\right)^{5/3}\right) \tag{6.6}$$

The momentum response time or relaxation time, which is the time required for a droplet to respond to a change in velocity, is defined as $\tau_m = \frac{\rho_{\text{water}} d^2}{18\mu_{\text{air}}}$ [2]. Incorporating the expression for momentum response time allows equation (6.6) to be rewritten as

$$\frac{d\underline{u}}{d\text{t}} = \frac{1}{6\mu_{\text{air}}^{2/3}\tau_m}\left(6\mu_{\text{air}}^{2/3}\left(\underline{u}_\infty - \underline{u}\right) + \left(\rho_{\text{air}} d\right)^{2/3}\left(\underline{u}_\infty - \underline{u}\right)^{5/3}\right) \tag{6.7}$$

If the air velocity and water droplet diameter are constant, then integration of equation (6.7) gives

$$\ln\left(\frac{\left(6\mu_{\text{air}}^{2/3} + \left(\rho_{\text{air}} d\right)^{2/3}\left(\underline{u}_\infty - \underline{u}\right)^{2/3}\right)^3}{\left(\underline{u}_\infty - \underline{u}\right)^2}\right)\Bigg|_{\underline{u}_o}^{\underline{u}} = \frac{2}{\tau_m}\text{t}\Bigg|_0^{\text{t}} \tag{6.8}$$

Applying the integration limits gives

$$\ln\left(\frac{\left(6\mu_{\text{air}}^{2/3} + \left(\rho_{\text{air}} d\right)^{2/3}\left(\underline{u} - \underline{u}_\infty\right)^{2/3}\right)^3}{\left(\underline{u} - \underline{u}_\infty\right)^2}\frac{\left(\underline{u}_{\text{o}} - \underline{u}_\infty\right)^2}{\left(6\mu_{\text{air}}^{2/3} + \left(\rho_{\text{air}} d\right)^{2/3}\left(\underline{u}_{\text{o}} - \underline{u}_\infty\right)^{2/3}\right)^3}\right) = \frac{2}{\tau_m}\text{t} \tag{6.9}$$

Rearranging the terms gives the following solution for equation (6.7) for constant air velocity, $\underline{u}_\infty$, and an initial droplet velocity $\underline{u}_o$

$$\frac{\left(6\mu_{\text{air}}^{2/3} + \left(\rho_{\text{air}} d\right)^{2/3}\left(\underline{u} - \underline{u}_\infty\right)^{2/3}\right)^3}{\left(\underline{u} - \underline{u}_\infty\right)^2} = \frac{\left(6\mu_{\text{air}}^{2/3} + \left(\rho_{\text{air}} d\right)^{2/3}\left(\underline{u}_o - \underline{u}_\infty\right)^{2/3}\right)^3}{\left(\underline{u}_o - \underline{u}_\infty\right)^2} e^{\frac{2}{\tau_m}\text{t}} \tag{6.10}$$

Taking the cube root of both roots sides of the equation gives:

$$6\mu_{\text{air}}^{2/3}+\left(\rho_{\text{air}}d\right)^{2/3}\left(\underline{u}-\underline{u}_{\infty}\right)^{2/3}= \frac{\left(\underline{u}-\underline{u}_{\infty}\right)^{2/3}}{\left(\underline{u}_{o}-\underline{u}_{\infty}\right)^{2/3}}\left(6\mu_{\text{air}}^{2/3}+\left(\rho_{\text{air}}d\right)^{2/3}\left(\underline{u}_{o}-\underline{u}_{\infty}\right)^{2/3}\right)e^{\frac{2}{3\tau_m}\text{t}} \tag{6.11}$$

Rearranging the terms

$$\left(\underline{u}-\underline{u}_{\infty}\right)^{2/3}=\frac{6\mu_{\text{air}}^{2/3}}{\frac{\left(6\mu_{\text{air}}^{2/3}+\left(\rho_{\text{air}}d\right)^{2/3}\left(\underline{u}_{o}-\underline{u}_{\infty}\right)^{2/3}\right)e^{\frac{2}{3\tau_m}\text{t}}}{\left(\underline{u}_{o}-\underline{u}_{\infty}\right)^{2/3}}-\left(\rho_{\text{air}}d\right)^{2/3}} \tag{6.12}$$

Raising both sides of the equation to the $3/2$ power and rearranging the terms yields

$$\underline{u}=\frac{6^{3/2}\mu_{\text{air}}\left(\underline{u}_{o}-\underline{u}_{\infty}\right)}{\left(\left(6\mu_{\text{air}}^{2/3}+\left(\rho_{\text{air}}d\right)^{2/3}\left(\underline{u}_{o}-\underline{u}_{\infty}\right)^{2/3}\right)e^{\frac{2}{3\tau_m}\text{t}}-\left(\rho_{\text{air}}d\right)^{2/3}\left(\underline{u}_{o}-\underline{u}_{\infty}\right)^{2/3}\right)^{3/2}}+\underline{u}_{\infty} \tag{6.13}$$

Dividing the numerator and the denominator of the first term of the right-hand side of Equation (6.13) by the viscosity of air, gives

$$\underline{u}=\frac{6\sqrt{6}\left(\underline{u}_{o}-\underline{u}_{\infty}\right)}{\left(\left(6+\frac{\left(\rho_{\text{air}}d\right)^{2/3}\left(\underline{u}_{o}-\underline{u}_{\infty}\right)^{2/3}}{\mu_{\text{air}}^{2/3}}\right)e^{\frac{2}{3\tau_m}t}-\frac{\left(\rho_{\text{air}}d\right)^{2/3}\left(\underline{u}_{o}-\underline{u}_{\infty}\right)^{2/3}}{\mu_{\text{air}}^{2/3}}\right)^{3/2}}+\underline{u}_{\infty} \tag{6.14}$$

Equation (6.14) gives the instantaneous horizontal velocity component of a droplet in m/s. Figure 6-1 compares the horizontal velocity component of a droplet calculated by equation (6.14) with the results of the numerical simulations. The figure shows that the numerical and the analytical solutions are in good agreement. The difference $\Delta u_{\%}=\frac{u_{\text{Analytical}}-u_{\text{Numerical}}}{u_{\text{Numerical}}}$ is in

the range of 0-6%. This difference originates from the assumption of a constant air velocity, $\underline{u}_\infty$. Also, this difference can be attributed to the difference between the drag coefficient used for the analytical predictions and the one used for the numerical predictions. The Putnam [1] definition was used in the analytical analysis, while, the definition of Morsi et. al. [3] is used in the numerical analysis.

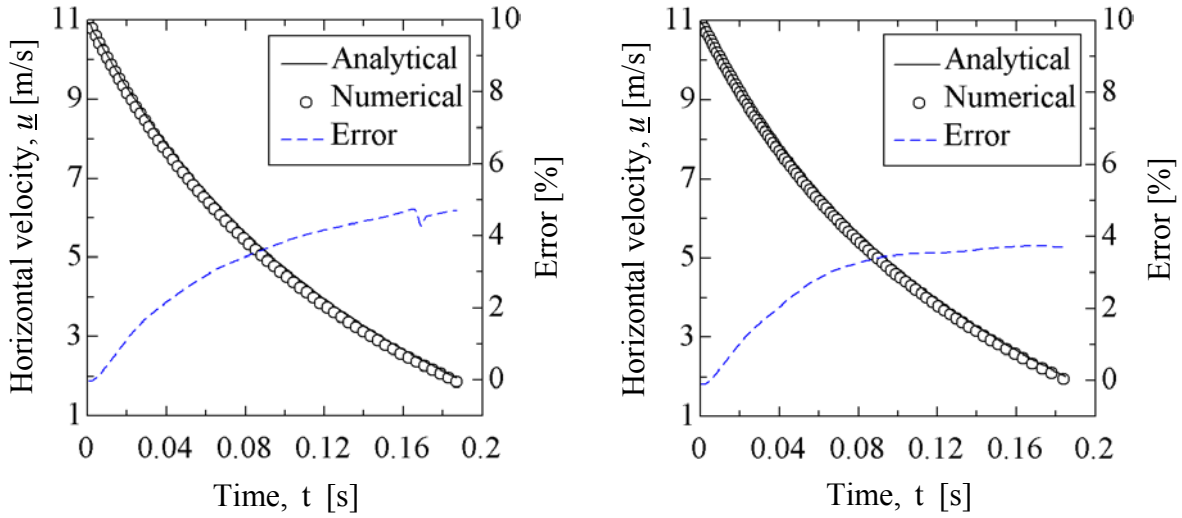

a- Gravity = -9.81 m/s^2 b- Gravity = 0 m/s^2

Figure 6-1 Comparison of the theoretical droplet horizontal velocity component with the numerical results, for "reflect" wall boundary condition, initial speed-ratio $SR_o = 2.2$, droplet diameter $d = 1$ mm, $\underline{u}_\infty = -5$ m/s, and MR$=\dfrac{\dot{m}_{\text{water}}}{\dot{m}_{\text{air}}} = 0.5$

The instantaneous velocity-ratio is defined as $VR = \underline{u} \cdot \underline{U}^*$, and $\alpha = VR - 1$, where $\underline{U}^*$ is a velocity vector with a magnitude that is equal to the reciprocal of the continuous phase velocity, $1/u_\infty$, and in the same direction.

Multiplying both sides of equation (6.14) by $\underline{U}^*$, and substituting by the following definitions $\alpha_o = VR_o - 1$, $VR_o = -\frac{u_o}{u_\infty}$, gives the velocity-ratio, $VR = -\frac{u}{u_\infty}$, at any time t

$$VR = \frac{\sqrt{216}}{\left(\left(6 + \left(\alpha_o \,\mathrm{Re}_\infty\right)^{2/3}\right) e^{(2/3\tau_m)\mathrm{t}} - \left(\alpha_o \,\mathrm{Re}_\infty\right)^{2/3}\right)^{3/2}} \alpha_o + 1 \tag{6.15}$$

where Re_∞ is the Reynolds number defined as follows

$$\mathrm{Re}_\infty = \frac{\rho_{\mathrm{air}} u_\infty d}{\mu_{\mathrm{air}}} \tag{6.16}$$

Rearranging the terms in equation (6.15) gives the time, t, required for the droplet to reach a velocity $\underline{u}$.

$$\mathrm{t} = \frac{\tau_m}{2} \ln\left(\frac{\left(6\mu_{\mathrm{air}}^{2/3} + \left(\rho_{\mathrm{air}} d\right)^{2/3} \left(\underline{u} - \underline{u}_\infty\right)^{2/3}\right)^3 \left(\underline{u}_o - \underline{u}_\infty\right)^2}{\left(6\mu_{\mathrm{air}}^{2/3} + \left(\rho_{\mathrm{air}} d\right)^{2/3} \left(\underline{u}_o - \underline{u}_\infty\right)^{2/3}\right)^3 \left(\underline{u} - \underline{u}_\infty\right)^2} \right) \tag{6.17}$$

Multiplying the numerator and the denominator of the natural log term by $\frac{1}{\mu_{\mathrm{air}}^2}$ gives

$$\mathrm{t} = \frac{\tau_m}{2} \ln\left(\frac{\left(6 + \frac{\left(\rho_{\mathrm{air}} d\right)^{2/3}}{\mu_{\mathrm{air}}^{2/3}} \left(\underline{u}_\infty \left(VR - 1\right)\right)^{2/3}\right)^3 \left(\underline{u}_\infty \left(VR_o - 1\right)\right)^2}{\left(6 + \frac{\left(\rho_{\mathrm{air}} d\right)^{2/3}}{\mu_{\mathrm{air}}^{2/3}} \left(\underline{u}_\infty \left(VR_o - 1\right)\right)^{2/3}\right)^3 \left(\underline{u}_\infty \left(VR - 1\right)\right)^2} \right) \tag{6.18}$$

Rearranging the terms gives and using the definitions for Re_∞, α_o, and α

$$\frac{\mathrm{t}}{\tau_m} = \frac{1}{2}\ln\left(\frac{\left(6+\left(\alpha\,\mathrm{Re}_\infty\right)^{2/3}\right)^3 \alpha_o^2}{\left(6+\left(\alpha_o\,\mathrm{Re}_\infty\right)^{2/3}\right)^3 \alpha^2}\right) \tag{6.19}$$

6.1.2 Spray tip penetration

The droplet displacement in the horizontal direction, $\underline{S}$, can be calculated by integrating the horizontal velocity component of a droplet, $\underline{u}$, with respect to time as follows

$$\underline{S} = \int_0^{\mathrm{t}} \underline{u}\, d\mathrm{t} \tag{6.20}$$

$$\underline{S} = \left(\frac{-2(6)^{3/2}\,\mu_{\mathrm{air}}\tau_m}{2/3\left(\rho_{\mathrm{air}}d\right)^{2/3}}\right)\frac{\tan^{-1}\sqrt{\dfrac{\left(6\mu_{\mathrm{air}}^{2/3}+\left(\rho_{\mathrm{air}}d\right)^{2/3}\left(\underline{u}_o-\underline{u}_\infty\right)^{2/3}\right)e^{(2/3\tau_m)\mathrm{t}}}{\left(\rho_{\mathrm{air}}d\right)^{2/3}\left(\underline{u}_o-\underline{u}_\infty\right)^{2/3}}-1}}{\sqrt{\left(\rho_{\mathrm{air}}d\right)^{2/3}}}\Bigg|_0^{\mathrm{t}}$$

$$+\left(\frac{-2(6)^{3/2}\,\mu_{\mathrm{air}}\tau_m}{2/3\left(\rho_{\mathrm{air}}d\right)^{2/3}}\right)\frac{1}{\sqrt{\dfrac{\left(6\mu_{\mathrm{air}}^{2/3}+\left(\rho_{\mathrm{air}}d\right)^{2/3}\left(\underline{u}_o-\underline{u}_\infty\right)^{2/3}\right)e^{(2/3\tau_m)\mathrm{t}}}{\left(\underline{u}_o-\underline{u}_\infty\right)^{2/3}}-\left(\rho_{\mathrm{air}}d\right)^{2/3}}}\Bigg|_0^{\mathrm{t}} \tag{6.21}$$

$$+\,\underline{u}_\infty \mathrm{t}\Big|_0^{\mathrm{t}}$$

Dividing the numerator and the denominator of the square root terms by the viscosity of air, $\mu_{\mathrm{air}}^{2/3}$, and using the definition for α_o and Re_∞, gives

$$\underline{S} = \left(\frac{-2(6)^{3/2}\,\mu_{\text{air}}\tau_m}{2/3(\rho_{\text{air}}d)^{2/3}} \right) \frac{\tan^{-1}\sqrt{\frac{\left(6+(\alpha_o\,\text{Re}_\infty)^{2/3}\right)e^{(2/3\tau_m)\text{t}}}{(\alpha_o\,\text{Re}_\infty)^{2/3}}-1}}{\sqrt{(\rho_{\text{air}}d)^{2/3}}}\Bigg|_0^{\text{t}}$$

$$+\left(\frac{-2(6)^{3/2}\,\mu_{\text{air}}\tau_m}{2/3(\rho_{\text{air}}d)^{2/3}} \right) \frac{1}{\sqrt{(\rho_{\text{air}}d)^{2/3}}\sqrt{\frac{\left(6+(\alpha_o\,\text{Re}_\infty)^{2/3}\right)e^{(2/3\tau_m)\text{t}}}{(\alpha_o\,\text{Re}_\infty)^{2/3}}-1}}\Bigg|_0^{\text{t}} \qquad (6.22)$$

$$+\,\underline{u}_\infty \text{t}\Big|_0^{\text{t}}$$

Using the expression for t defined in equation (6.19) and $\tau_m = \frac{\rho_{\text{water}}d^2}{18\mu_{\text{air}}}$

$$\underline{S} = \left(\sqrt{6}\,\frac{\rho_{\text{water}}}{\rho_{\text{air}}}d \right) \tan^{-1}\sqrt{\frac{\left(6+(\alpha_o\,\text{Re}_\infty)^{2/3}\right)\frac{\left(6+(\alpha\,\text{Re}_\infty)^{2/3}\right)\alpha_o^{2/3}}{\left(6+(\alpha_o\,\text{Re}_\infty)^{2/3}\right)\alpha^{2/3}}}{(\alpha_o\,\text{Re}_\infty)^{2/3}}-1}\Bigg|_0^{\text{t}}$$

$$+\left(\sqrt{6}\,\frac{\rho_{\text{water}}}{\rho_{\text{air}}}d \right) \frac{1}{\sqrt{\frac{\left(6+(\alpha_o\,\text{Re}_\infty)^{2/3}\right)\frac{\left(6+\text{Re}^{2/3}\right)\alpha_o^{2/3}}{\left(6+(\alpha_o\,\text{Re}_\infty)^{2/3}\right)\alpha^{2/3}}}{(\alpha_o\,\text{Re}_\infty)^{2/3}}-1}}\Bigg|_0^{\text{t}} \qquad (6.23)$$

$$+\,\underline{u}_\infty \text{t}\Big|_0^{\text{t}}$$

Rearranging the terms of the above equation yields:

$$\underline{S} = \sqrt{6}\,\frac{\rho_{\text{water}}}{\rho_{\text{air}}}\,d\left(\tan^{-1}\left(\sqrt{\frac{6}{\left(\alpha\,\text{Re}_{\infty}\right)^{2/3}}} \right) + \sqrt{\frac{\left(\alpha\,\text{Re}_{\infty}\right)^{2/3}}{6}} \right)\Bigg|_{0}^{\text{t}} + \underline{u}_{\infty}\text{t}\Big|_{0}^{\text{t}} \tag{6.24}$$

Applying the limits of the integration yields

$$\begin{aligned} \underline{S} &= \sqrt{6}\,\frac{\rho_{\text{water}}}{\rho_{\text{air}}}\,d\left(\tan^{-1}\left(\sqrt{\frac{6}{\left(\alpha_o\,\text{Re}_{\infty}\right)^{2/3}}} \right) - \tan^{-1}\left(\sqrt{\frac{6}{\left(\alpha\,\text{Re}_{\infty}\right)^{2/3}}} \right) \right) \\ &+ \sqrt{6}\,\frac{\rho_{\text{water}}}{\rho_{\text{air}}}\,d\left(\sqrt{\frac{\left(\alpha_o\,\text{Re}_{\infty}\right)^{2/3}}{6}} - \sqrt{\frac{\left(\alpha\,\text{Re}_{\infty}\right)^{2/3}}{6}} \right) + \underline{u}_{\infty}\text{t} \end{aligned} \tag{6.25}$$

Using the trigonometric conversion [4],

$$\tan^{-1}\left(a\right) - \tan^{-1}\left(b\right) = \tan^{-1}\left(\frac{a-b}{1+ab}\right)$$

$$\begin{aligned} \frac{\underline{S}}{d} &= \sqrt{6}\,\frac{\rho_{\text{water}}}{\rho_{\text{air}}}\left(\tan^{-1}\left(\sqrt{6\,\text{Re}_{\infty}^{2/3}}\,\frac{\sqrt{\alpha^{2/3}} - \sqrt{\alpha_o^{2/3}}}{6 + \text{Re}_{\infty}^{2/3}\sqrt{\alpha_o^{2/3}\alpha^{2/3}}} \right) \right) \\ &- \frac{1}{\sqrt{6}}\,\frac{\rho_{\text{water}}}{\rho_{\text{air}}}\sqrt{6\,\text{Re}_{\infty}^{2/3}}\left(\sqrt{\alpha^{2/3}} - \sqrt{\alpha_o^{2/3}} \right) \\ &+ \underline{u}_{\infty}\,\frac{\text{t}}{d} \end{aligned} \tag{6.26}$$

Substituting by equation (6.19) into equation (6.26)

$$\frac{\underline{S}}{d} = \sqrt{6}\,\frac{\rho_{\text{water}}}{\rho_{\text{air}}}\left(\tan^{-1}\left(\sqrt{6\,\text{Re}_{\infty}^{2/3}}\,\frac{\sqrt{\alpha^{2/3}}-\sqrt{\alpha_o^{2/3}}}{6+\text{Re}_{\infty}^{2/3}\sqrt{\alpha_o^{2/3}\alpha^{2/3}}}\right)\right)$$
$$-\frac{1}{\sqrt{6}}\frac{\rho_{\text{water}}}{\rho_{\text{air}}}\sqrt{6\,\text{Re}_{\infty}^{2/3}}\left(\sqrt{\alpha^{2/3}}-\sqrt{\alpha_o^{2/3}}\right) \qquad (6.27)$$
$$+\,\underline{u}_{\infty}\frac{\tau_m}{2d}\ln\left(\frac{\left(6+\left(\alpha\,\text{Re}_{\infty}\right)^{2/3}\right)^3\alpha_o^2}{\left(6+\left(\alpha_o\,\text{Re}_{\infty}\right)^{2/3}\right)^3\alpha^2}\right)$$

Equation (6.27) gives the displacement $\underline{S}$, in the horizontal direction at any time t. Figure 6-2 compares the horizontal velocity component of a droplet calculated by equation (6.27) to the results of the numerical simulations. The figure shows that the numerical and the analytical solutions are in good agreement. The difference $\Delta S_{\%} = \frac{S_{\text{Analytical}} - S_{\text{Numerical}}}{S_{\text{Numerical}}}$ is in the range of 0-3%. This difference is due to the assumption of constant air velocity and the difference in the drag coefficient as discussed earlier.

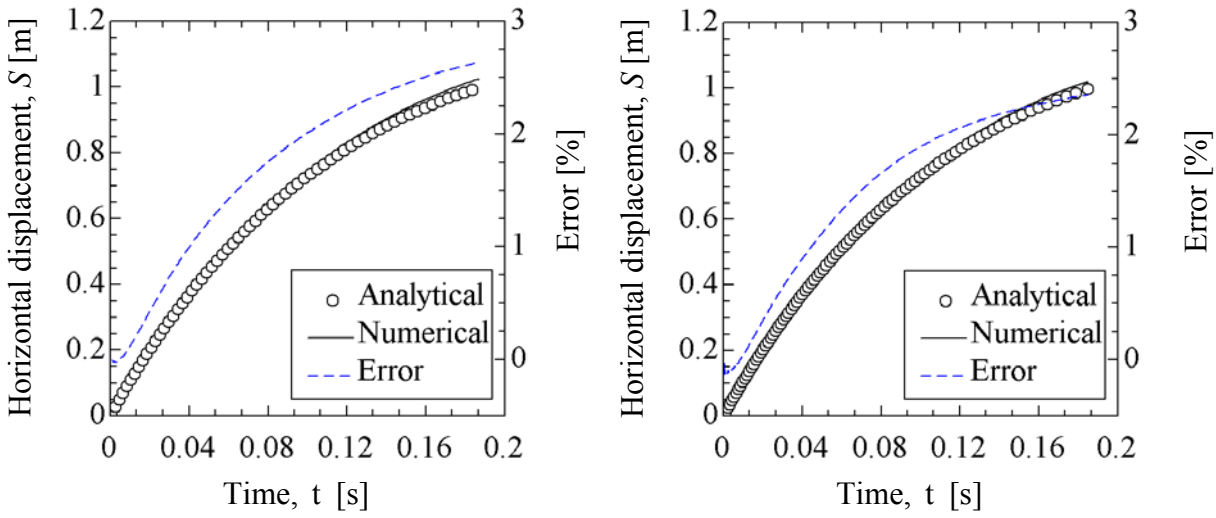

Figure 6-2 Comparison of the theoretical droplet horizontal displacement, $\underline{S}$ with the numerical results, for $\alpha_o = 1.2$, droplet diameter $d = 1$ mm, $\underline{u}_\infty = -5$ m/s, and

$$\text{MR} = \frac{\dot{m}_{\text{water}}}{\dot{m}_{\text{air}}} = 0.5$$

The time required to reach the maximum penetration $t_{S_{\max}}$ is calculated from equation (6.19) by setting $\alpha = -1$

$$t_{S_{\max}} = \frac{\tau_m}{2} \ln\left(\frac{\left(6 + \left(\text{Re}_\infty\right)^{2/3}\right)^3}{\left(6 + \left(\alpha_o \, \text{Re}_\infty\right)^{2/3}\right)^3} \alpha_o^2 \right) \qquad (6.28)$$

Substituting equation (6.28) in equation (6.26) gives the maximum spray-tip-penetration $S_{\max}$.

$$\frac{S_{\max}}{d} = \sqrt{6}\,\frac{\rho_{\text{water}}}{\rho_{\text{air}}}\left(\tan^{-1}\left(\sqrt{6\,\text{Re}_{\infty}^{\,2/3}}\,\frac{1-\sqrt{\alpha_o^{\,2/3}}}{6+\text{Re}_{\infty}^{2/3}\sqrt{\alpha_o^{2/3}}}\right)\right)$$
$$-\frac{\rho_{\text{water}}}{\rho_{\text{air}}}\sqrt{\text{Re}_{\infty}^{\,2/3}}\left(1-\sqrt{\alpha_o^{\,2/3}}\right) \qquad (6.29)$$
$$+\underline{u}_{\infty}\frac{\tau_m}{2d}\ln\left(\frac{\left(6+\text{Re}_{\infty}^{\,2/3}\right)^3}{\left(6+\left(\alpha_o\,\text{Re}_{\infty}\right)^{2/3}\right)^3}\alpha_o^2\right)$$

The above equation shows that the spray-tip-penetration-length, $S_{\max}$, depends on Reynolds number, Re_{∞}, the droplet diameter, d, and the spray cooler initial velocity-ratio $\alpha_o = VR_o - 1$. Figure 6-3 shows the effect of changing the spray-cooler initial speed-ratio, $SR_o = |VR_o|$ and Reynolds number, Re_{∞}, on the spray-tip-penetration length to diameter ratio, $\zeta_A = S_{\max}/d$.

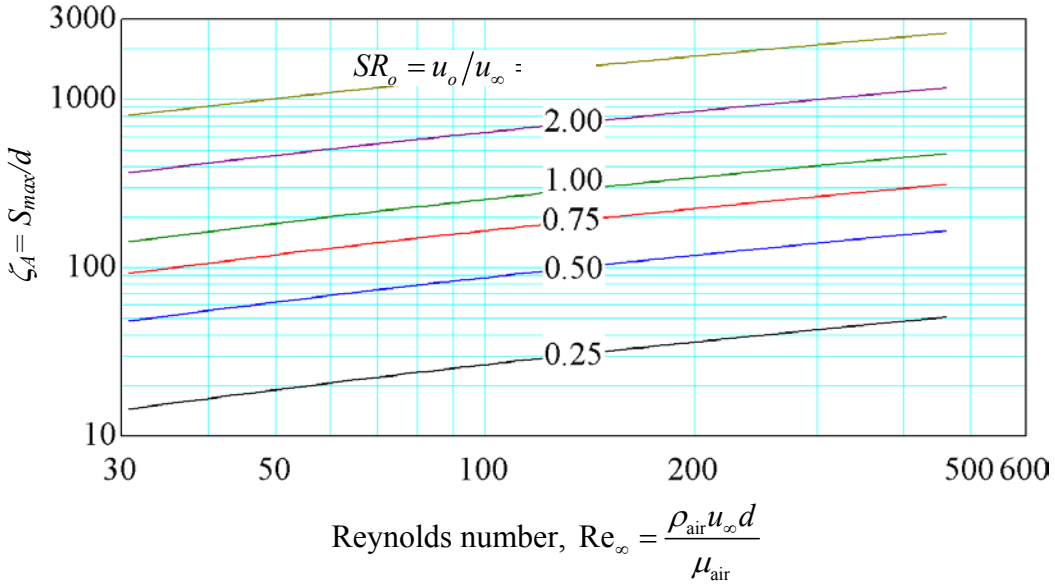

Figure 6-3 Effect of Reynolds number, Re_{∞}, on the spray-tip-penetration length to diameter ratio $\zeta_A = S_{\max}/d$ for different initial speed-ratios, $SR_o = u_o/u_{\infty}$, assuming constant diameter

The figure shows that, for the same SR_o, increasing Reynolds number, Re_∞, increases ζ_A. The Reynolds number increases by increasing either the droplet diameter, d, or the continuous phase velocity, $\underline{u}_\infty$. Large diameter droplets can penetrate deeper than small diameter ones owing to their high momentum. Consequently, the spray-tip-penetration-length to diameter ratio, ζ_A, increases. Also, for the same initial speed-ratio, the increase in the continuous phase velocity goes together with an increase in the spray initial velocity $\underline{u}_o$. Consequently, the droplet initial momentum increases as its initial velocity increases, and so does the spray-tip-penetration-length.

Figure 6-3 also shows that for the same Reynolds number, increasing the initial speed-ratio increases the spray-tip-penetration-length. This is due to the fact that as the initial speed-ratio increases, for fixed $\underline{u}_\infty$, the spray initial velocity, $\underline{u}_o$, increases. Consequently, the droplet initial momentum increases, with respect to the momentum of air. Finally, Figure 6-3 shows that the same penetration length can be achieved at higher initial speed-ratios by decreasing the air velocity, $\underline{u}_\infty$, i.e. Reynolds number, Re_∞.

Equation (6.29) can be used to predict the initial velocity-ratio, necessary to achieve a spray-tip-penetration-length that is equal to the spray chamber length, S_{eff}. This is the critical initial velocity-ratio, $|VR_C|$, beyond which the spray extends to the outside of the spray chamber. Figure 6-4 shows the effect of changing the droplet diameter on the critical initial speed-ratio, $SR_C = |VR_C|$, necessary to achieve a given spray-tip-penetration-length.

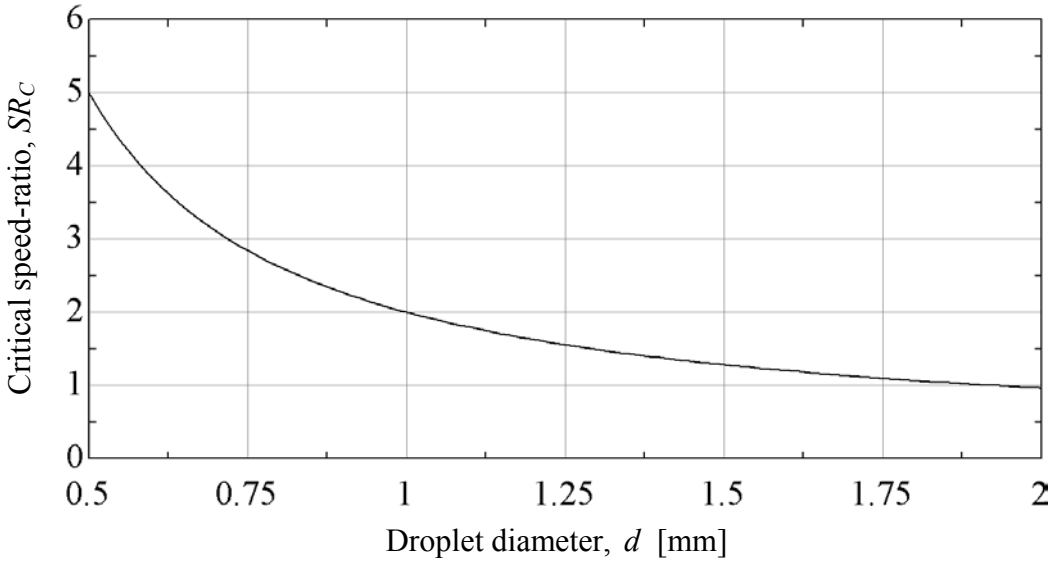

Figure 6-4 Effect of changing the droplet diameter on the critical speed-ratio, for $\underline{u}_\infty = -5$ m/s, $S_{\max} = S_{eff} = 1$ m

The figure shows that the initial speed-ratio, SR_C, required to reach a given spray-tip-penetration-length decreases with increasing the droplet diameter due to the higher momentum of the large diameter droplets. Consequently, a lower initial spray velocity is required to achieve the same penetration.

In this section, the equation of motion has been presented and solved to predict the droplet velocity, $\underline{u}$, and its displacement, $\underline{S}$, at any time t. Also, the equation necessary to predict the spray-tip-penetration-length, $S_{\max}$, has been presented. The aforementioned discussion shows that the spray-tip-penetration-length depends on Reynolds number, Re_∞, the droplet diameter, d, and the spray cooler initial speed-ratio, $SR_o = |VR_o|$. The spray-tip-penetration-length, $S_{\max}$ increases by increasing Reynolds number, Re_∞, the droplet diameter, d, and

increasing the initial speed-ratio SR_o. In the following section the equations necessary to predict the thermal performance of the spray chamber are presented. The influence of the hydrodynamics of the air and water droplets on the spray chamber thermal performance is also discussed.

6.2 Heat transfer

Prediction of the thermal performance of the spray cooler requires knowledge of the interfacial area of the droplets, A, the overall heat transfer coefficient, U, and the inlet fluid temperatures. A simplified model of the spray-cooler assumes its thermal behavior is analogous to a shell-and-tube heat exchanger. For initial speed-ratios $SR_o \leq SR_C$, the particles retract, i.e. change direction, inside the spray chamber, as shown in Figure 6-5a and Figure 6-5b. Hence, the spray chamber is modeled as a double-pass single shell heat exchanger. The critical initial speed-ratio, SR_C, is defined as the initial speed-ratio at which the spray-tip-penetration-length is equal to the spray cooler length, S_{eff}. For initial speed-ratios greater than SR_C, the retraction takes place outside the spray chamber, as shown in Figure 6-5c. Therefore, the spray cooler is modeled as a single-pass counter flow heat exchanger for this condition. This section presents the semi-analytical equations necessary to predict the performance of the spray-cooler using the effectiveness-NTU method. The section starts by presenting the equations necessary to predict the interfacial area and overall heat transfer coefficient. This is then followed by calculating the conductance, UA product, of the spray chamber and the effectiveness.

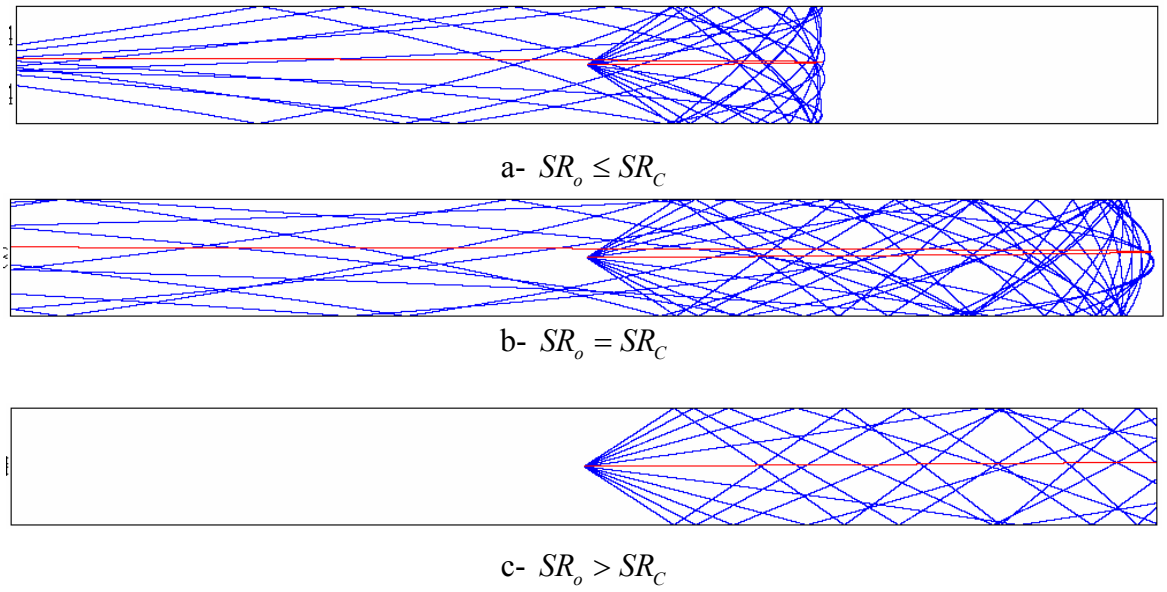

a- $SR_o \leq SR_C$

b- $SR_o = SR_C$

c- $SR_o > SR_C$

Figure 6-5 Particle tracks for spray cooler with "reflect" wall boundary condition

6.2.1 Surface area

The interfacial area of the spray cooler is the sum of the surface areas of all droplets in the spray chamber as given below

$$A_i = N_{i_{droplets}} A_s \tag{6.30}$$

where A_i is the total interfacial area of the spray. Subscript i is unity for initial speed-ratios, SR_o, greater than the critical initial speed-ratio, SR_C, and 2 for initial speed-ratios less than or equal to SR_C. $A_s = \pi d^2$ is the droplet surface area in m^2, and $N_{i_{droplets}}$ is the total number of droplets. The total number of droplets, $N_{i_{droplets}}$, is defined as

$$N_{i_{droplets}} = i \; \dot{N}_{droplets} \; \mathrm{t}_{res_i} \tag{6.31}$$

where i is a factor that accounts for the effect of the particle retraction inside the spray chamber and, in accordance, the surface area doubling effect.

$$i = \begin{cases} 1 & SR_o > SR_C \\ 2 & SR_o \leq SR_C \end{cases}$$

For initial speed-ratios greater than SR_C the retraction takes place outside the spray chamber, therefore $i = 1$. On the other hand, for $SR_o \leq SR_C$ the particles retract inside the spray chamber, therefore $i = 2$ to account for the surface area doubling effect. $\dot{N}_{droplets}$ is the droplet number flow rate, in s^{-1}, and is defined as follows

$$\dot{N}_{droplets} = \dot{m}_{\text{water}} / \rho_{\text{water}} V_d \tag{6.32}$$

where $\dot{m}_{\text{water}}$ is the water mass flow rate in kg/s, ρ_{water} is the water density in kg/m^3, and $V_d = \frac{\pi d^3}{6}$ is the droplet volume in m^3. Substituting by the aforementioned definitions into equation (6.30)

$$A_i = i \left(\frac{\dot{m}_{\text{water}}}{\rho_{\text{water}} \left(\frac{\pi d^3}{6} \right)} \mathrm{t}_{res_i} \right) \pi d^2 \tag{6.33}$$

$$A_i = i \frac{6 \dot{m}_{\text{water}}}{\rho_{\text{water}} d} \mathrm{t}_{res_i} \tag{6.34}$$

t_{res_i} is the particle residence time, in seconds. The particle residence time is the dwell time that the particles need to travel from the spray nozzle exit to either the penetration depth for $SR_o \le SR_C$, or the end of the spray chamber for $SR_o > SR_C$. The particle residence time can be calculated from equation (6.26) as follows

$$t_{res_i} = \sqrt{6}\,\frac{d}{u_\infty}\frac{\rho_{\text{water}}}{\rho_{\text{air}}}\left(\tan^{-1}\left(\sqrt{6\,\text{Re}_\infty^{2/3}}\,\frac{\sqrt{\alpha_i^{2/3}}-\sqrt{\alpha_o^{2/3}}}{6+\text{Re}_\infty^{2/3}\sqrt{\alpha_o^{2/3}\alpha_i^{2/3}}}\right)\right) + \frac{d}{u_\infty}\frac{1}{\sqrt{6}}\frac{\rho_{\text{water}}}{\rho_{\text{air}}}\sqrt{6\,\text{Re}_\infty^{2/3}}\left(\sqrt{\alpha_i^{2/3}}-\sqrt{\alpha_o^{2/3}}\right)-\frac{S_i}{u_\infty} \tag{6.35}$$

For $SR_o > SR_C$, $S_i = S_1 = S_{eff}$ and α_1 is calculated at $S_1 = S_{eff}$. On the other hand, for $SR_o \le SR_C$, $S_i = S_2 = S_{\max}$ and $\alpha_i = \alpha_2 = -1$. Consequently, the surface area A_i is

$$A_i = 6i\left(\frac{\sqrt{6}\dot{m}_{\text{water}}}{u_\infty\rho_{\text{air}}}\tan^{-1}(\beta_i)+\frac{\dot{m}_{\text{water}}\Gamma_i}{\sqrt{6}u_\infty\rho_{\text{air}}}-\frac{\dot{m}_{\text{water}}}{u_\infty\rho_{\text{water}}}\frac{S_i}{d}\right) \tag{6.36}$$

where $\beta_i = \dfrac{\Gamma_i}{6+\text{Re}_\infty^{2/3}\sqrt{\alpha_o^{2/3}\alpha_i^{2/3}}}$ and $\Gamma_i = \sqrt{6\,\text{Re}_\infty^{2/3}}\left(\sqrt{\alpha_i^{2/3}}-\sqrt{\alpha_o^{2/3}}\right)$. Dividing equation (6.36) through by $\dfrac{\dot{m}_{\text{water}}}{u_\infty\rho_{\text{air}}}$ gives

$$\frac{A_i}{\dfrac{\dot{m}_{\text{water}}}{u_\infty\rho_{\text{air}}}} = 6i\left(\sqrt{6}\tan^{-1}(\beta_i)+\frac{\Gamma_i}{\sqrt{6}}-\frac{\rho_{\text{air}}}{\rho_{\text{water}}}\frac{S_i}{d}\right) \tag{6.37}$$

Since β_i and Γ_i depend on α_i which is $(VR-1)$, equation (6.37) provides the interfacial area of the water droplets at different velocity ratios.

6.2.2 Overall heat transfer coefficient

The overall heat transfer coefficient accounts for all thermal resistances between the air-side and the water-side. The discussion in section 5.3.1, shows that the convection resistance is the dominating resistance; consequently, the overall heat transfer coefficient is approximately equal to the average convective heat transfer coefficient.

$$U = \frac{1}{1/\bar{h}_{c_i}} \tag{6.38}$$

Since the heat transfer coefficient varies with position in the spray chamber, the average heat transfer coefficient is calculated by integrating the local heat transfer coefficient along the penetration length for $SR_o \le SR_C$, $S_{\max}$, or the spray chamber length for $SR_o > SR_C$, S_{eff}, as follows

$$\bar{h}_{c_i} = \frac{1}{S_i}\int_0^{S_i} h_{c_i}\, dS \tag{6.39}$$

where $\bar{h}_{c_i}$ is the average heat transfer coefficient in W/m^2-K. The local heat transfer coefficient, h_{c_i}, in W/m^2-K, calculated using the Ranz and Marshall [5] correlation:

$$\mathrm{Nu}_{S_i} = \frac{h_{c_i} d}{k_{\mathrm{air}}} = 2 + 0.6\,\mathrm{Pr}^{1/3}\,\mathrm{Re}_{S_i}^{1/2} \tag{6.40}$$

where Nu_{S_i} is the local Nusselt number, k_{air} is the conductivity of air in W/m-K, and d is the droplet diameter in m. Pr is the Prandtl number, $\mathrm{Re}_{S_i} = \dfrac{\rho_{\mathrm{air}} \left|\underline{U}_\infty - \underline{V}\right|_{S_i} d}{\mu_{\mathrm{air}}}$ is the local

Reynolds number, $\left|\underline{U}_{\infty}\text{-}\underline{V}\right|_{S_i}$ is the local relative velocity in m/s, and μ_{air} is the viscosity of air in kg/m-s. Substituting by equation (6.40) into equation (6.39)

$$\overline{h}_{c_i} = \left(\frac{1}{S_i} \int_0^{S_i} \left(2 + 0.6 \,\text{Pr}^{1/3} \,\text{Re}_{S_i}^{1/2} \right) dS \right) \frac{k_{\text{air}}}{d} \tag{6.41}$$

$$\overline{h}_{c_i} = \left(2 + 0.6 \,\text{Pr}^{1/3} \left(\frac{1}{S_i} \int_0^{S_i} \left(\text{Re}_{S_i}^{1/2} \right) dS \right) \right) \frac{k_{\text{air}}}{d} \tag{6.42}$$

$$U_i = \overline{h}_{c_i} = \left(2 + 0.6 \,\text{Pr}^{1/3} \,\overline{\text{Re}_i}^{1/2} \right) \frac{k_{\text{air}}}{d} \tag{6.43}$$

The square root of the average Reynolds number, $\overline{\text{Re}_i}^{1/2}$, is defined

$$\overline{\text{Re}_i}^{1/2} = \frac{1}{S_i} \int_0^{S_i} \left(\text{Re}_{S_i}^{1/2} \right) dS = \frac{1}{S_i} \int_0^{S_i} \left(\frac{\rho_{\text{air}} \left|\underline{U}_{\infty}\text{-}\underline{V}\right|_{S_i} d}{\mu_{\text{air}}} \right)^{1/2} dS \tag{6.44}$$

Equation (6.43) shows that the average overall heat transfer coefficient, U_i, depends on the average Reynolds number, $\overline{\text{Re}_i}$. This requires the knowledge of the function that relates the relative velocity vector, $\left|\underline{U}_{\infty}\text{-}\underline{V}\right|_{S_i}$, to the spray chamber length S, as illustrated by equation (6.44). Due to the complex nature of this function, an approximate Reynolds number based on the horizontal velocity component (the dominant velocity component) is used.

$$\overline{\text{Re}_1} = \text{Re}_o = \frac{\rho_{\text{air}} \left| u_{\infty} - u_o \right| d}{\mu_{\text{air}}} \tag{6.45}$$

$$\overline{\text{Re}_2} = \text{Re}_{\infty} = \frac{\rho_{\text{air}} u_{\infty} d}{\mu_{\text{air}}} \tag{6.46}$$

Correction factors are thus used to adjust, the conductance of the spray chamber to compensate for this approximation. These correction factors are produced by comparing the results of the analytical predictions to the corresponding numerical simulations. The correction factors depend on the spray-chamber wall boundary condition and the initial speed-ratio.

6.2.3 Spray chamber conductance

The conductance of the spray chamber is the product of the interfacial area, A, and overall heat transfer coefficient, U. However, further modifications are still required to account for the effect of spray chamber wall boundary conditions.

6.2.3.1 Reflect wall boundary condition

The discussion presented in section 5.6.2 shows that the conductance of the spray chamber depends on the initial speed-ratio. The initial speed-ratio can be $SR_o \le SR_{\varepsilon}$, or $SR_o > SR_C$, or $SR_o \ge SR_{cutoff}$, where SR_{ε} is the initial speed-ratio that corresponds to maximum effectiveness and consequently, maximum conductance, and SR_{cutoff} is the initial speed-ratio above which all the spray retracts outside the spray chamber. For each of the aforementioned initial speed-ratios, the conductance is predicted using a different approach as shown in what follows.

6.2.3.1.1 High initial-velocity-ratios

For initial speed-ratios greater than or equal to SR_{cutoff}, no retraction takes place inside the spray chamber. Consequently, the conductance is at its lowest value. Increasing the initial

speed-ratio above the critical value SR_{cutoff} decreases the particle residence time and consequently the conductance of the spray chamber. The conductance within this range is calculated as $UA = F_i\left(U_i A_i\right)$, where $i = 1$. The factor F_i is a correction factor, developed from the results of the numerical simulations, that accounts for the approximation of Reynolds number, where $F_1 = 0.95 \pm 0.077$

6.2.3.1.2 Low initial speed-ratios

For initial speed-ratios smaller than or equal to SR_{ε}, the particles retract inside the spray chamber, as shown in Figure 6-5a. Consequently, the conductance, UA product, is at its highest value. As the initial speed-ratio increases, below the critical value SR_{ε}, some of the droplets retract inside the spray chamber, while others escape the spray chamber and retract outside, as shown in Figure 6-6. The escaping particles decrease the doubling effect of the surface area and hence the conductance. Further increase in the initial speed-ratio, leads to the escape of all particles outside the spray chamber through its outlet, as shown in Figure 6-5b. This drastically decreases the conductance of the spray chamber. For "reflect" wall boundary condition, the initial speed-ratio corresponding to the maximum effectiveness, SR_{ε}, coincides with that for maximum spray-tip-penetration-length, SR_C. The conductance within this range is calculated as $UA = F_i\left(U_i A_i\right)$, where $i = 2$ and $F_2 = 1.127 \pm 0.084$

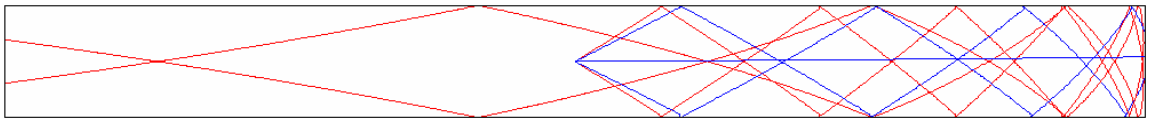

Figure 6-6 Particle tracks for spray-cooler with "reflect" wall boundary condition, $SR_{\varepsilon} < SR_o < SR_{cutoff}$

6.2.3.1.3 Intermediate initial speed-ratios

For initial speed-ratios in the range $SR_{\varepsilon} < SR_o < SR_{cutoff}$, the conductance has an intermediate value between the corresponding values $UA|_{cutoff}$ and $UA|_{\varepsilon}$, where $UA|_{cutoff}$ and $UA|_{\varepsilon}$ are the conductance of the spray chamber that corresponds to $SR_o = SR_{cutoff}$ and $SR_o = SR_{\varepsilon}$, respectively. The intermediate conductance is calculated assuming an elliptic distribution between the two values $UA|_{cutoff}$ and $UA|_{\varepsilon}$, as shown in Figure 6-7. For, $SR_{\varepsilon} < SR_o < SR_{cutoff}$, the conductance is calculated based on an elliptic distribution. Linear and parabolic distributions were also evaluated, but the elliptic distribution provides the best fit to the results of the numerical simulations. The elliptic distribution is given by

$$\frac{\left(S_{\max} - S_{eff}\right)^2}{\left(S_{EC}\right)^2} + \frac{\left(UA - UA|_{cutoff}\right)^2}{\left(UA|_{EC}\right)^2} - 1 = 0 \qquad (6.47)$$

where $S_{EC} = S_{Cutoff} - S_{eff}$, and $UA|_{EC} = UA|_{cutoff} - UA|_{\varepsilon}$. Defining $X = \frac{\left(S_{\max} - S_{eff}\right)^2}{\left(S_{EC}\right)^2}$ and substituting in equation (6.47)

$$UA = \sqrt{(1 - X)\left(UA|_{EC}\right)^2} + UA|_{cutoff} \qquad (6.48)$$

Equation (6.48) gives the conductance of the spray chamber for $SR_{\varepsilon} < SR_o < SR_{cutoff}$.

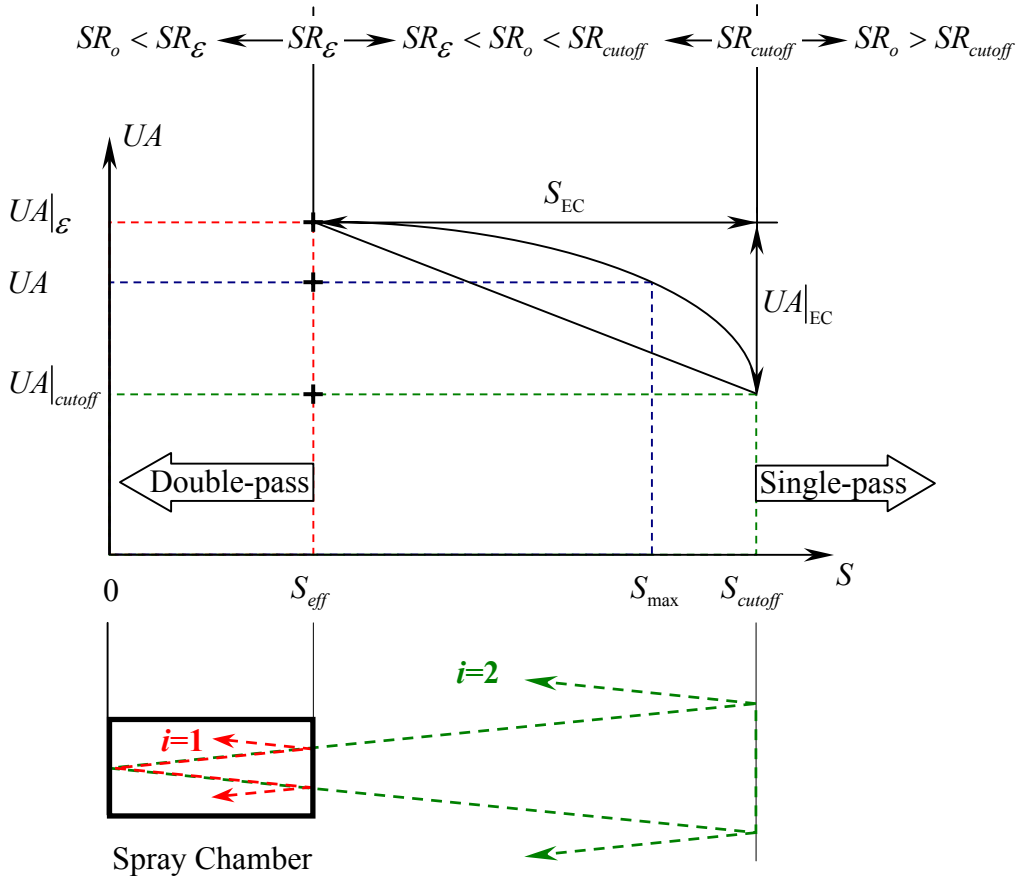

Figure 6-7 Elliptic conductance distribution for $SR_{\varepsilon} < SR_o < SR_{cutoff}$

Figure 6-8 depicts a comparison between the conductance of the spray chamber with "reflect" wall boundary condition, calculated using the semi-analytical model and that of the numerical results. The figure shows that the semi-analytical results are in good agreement with the numerical results, with an average deviation of 5.9%.

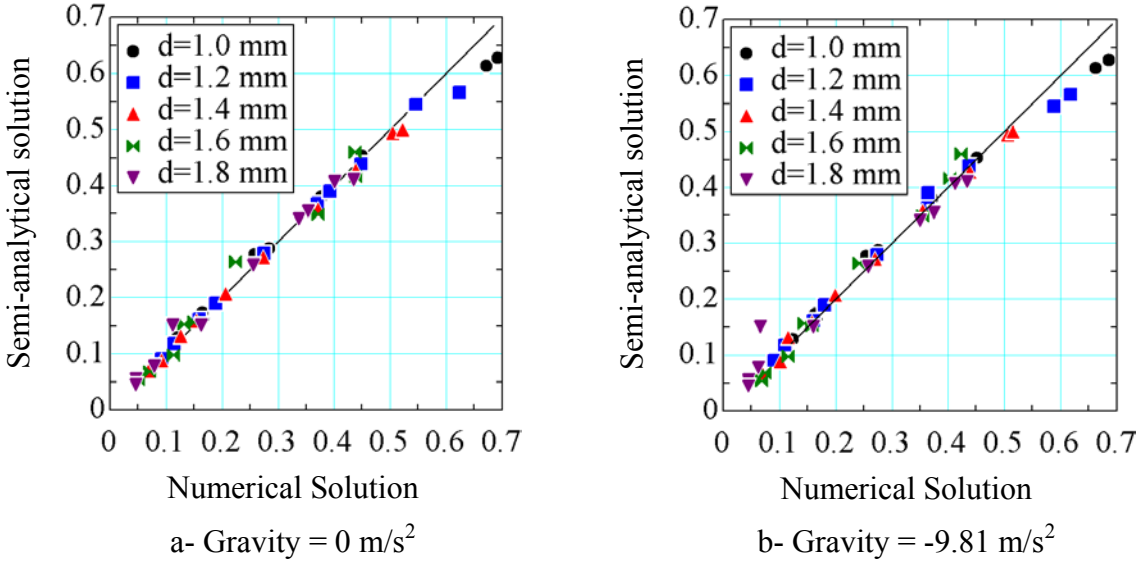

Figure 6-8 Comparison of the semi-analytical and numerical results for the conductance for "reflect" wall boundary condition, $\underline{u}_\infty = -5\,\text{m/s}$, and $\text{MR}=\frac{\dot{m}_{\text{water}}}{\dot{m}_{\text{air}}}=0.5$

In the above discussion the semi-analytical models necessary to predict the spray chamber conductance with "reflect" wall boundary condition are presented. The discussion shows that the main controlling factor for the conductance is the initial speed-ratio. As the initial speed-ratio increases, the conductance increases until a maximum is reached at $SR_o = SR_{\mathcal{E}} = SR_C$. Decreasing the initial speed-ratio beyond this value will result in a reduction of the conductance due to the retraction of the particles outside the spray chamber. Comparing the results of the semi-analytical models to the corresponding numerical simulations shows that these models well predict the conductance of the spray chamber. Table 6-1 summarizes these models.

Table 6-1 Summary of spray chamber conductance semi-analytical correlations for "reflect" wall boundary condition

Correlation	Restrictions	Assumptions
$0.95\ U_1 A_1$	$SR_o \geq SR_{cutoff}$	$\overline{\mathrm{Re}_1} = \mathrm{Re}_o = \frac{\rho_{\mathrm{air}} u_o d}{\mu_{\mathrm{air}}}$ $\underline{U}_\infty = \text{constant}$
$1.127\ U_2 A_2$	$SR_o \leq SR_{\varepsilon}$	$\overline{\mathrm{Re}_2} = \mathrm{Re}_\infty = \frac{\rho_{\mathrm{air}} u_\infty d}{\mu_{\mathrm{air}}}$ $\underline{U}_\infty = \text{constant}$
$\sqrt{(1-\mathrm{X})\left(UA\big\|_{\mathrm{EC}}\right)^2 + UA\big\|_{\mathrm{C}}}$	$SR_{\varepsilon} < SR_o < SR_{cutoff}$	

6.2.3.2 Escape wall boundary condition

The "escape" nature of the wall plays a pivotal role in dictating the thermal performance of the spray chamber. As the initial speed-ratio increases, some droplets retract inside the spray chamber, while others depart from further participation in the heat transfer process once they impact the spray chamber at its walls, as shown in Figure 6-9. As a result, the conductance of the spray chamber not only depends on the initial speed-ratio, but also on the spray cone angle, and the spray chamber geometry. The initial speed-ratio can fall into one of the following ranges

1. High initial speed-ratio, $SR_o > SR_C$
2. Low initial speed-ratio, $SR_o \leq SR_{\varepsilon}$
3. Intermediate initial speed-ratio, $SR_{\varepsilon} < SR_o < SR_C$

For each of these cases a different approach is used to predict the conductance of the spray chamber. A detailed description of each of these approaches is presented in what follows.

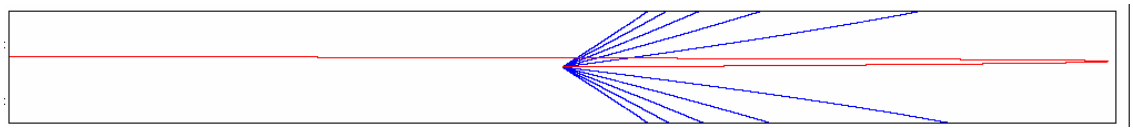

Figure 6-9 Particle tracks for spray-cooler with "escape" wall boundary condition $SR_o \le SR_C$

6.2.3.2.1 High initial speed-ratios

At initial speed-ratios $SR_o > SR_C$ or $SR_o \approx SR_C$, the particle tracks are as shown in Figure 6-9. To model these cases, the spray chamber is divided into two zones, a periphery and a core, as shown in Figure 6-10, with conductance $AU\big|_P$ and $AU\big|_C$, respectively.

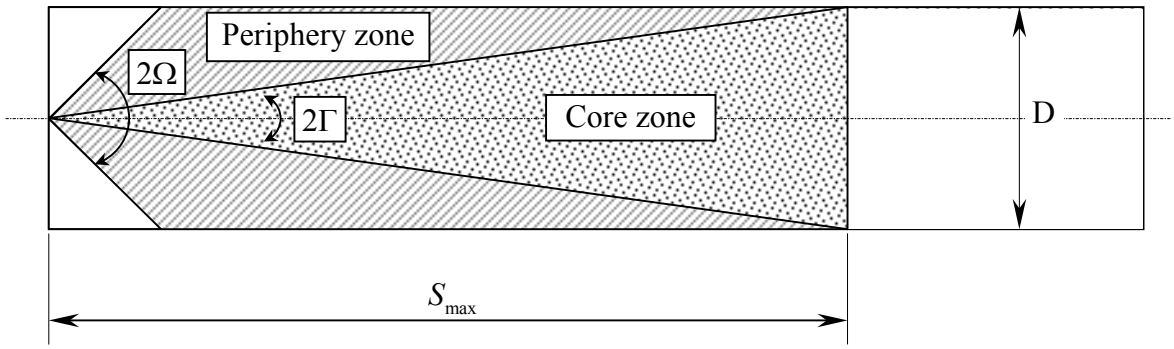

Figure 6-10 Schematic showing a spray chamber with "escape" wall boundary

The periphery zone contains droplets that follow single pass trajectories, and escape the spray chamber once they reach the walls. Consequently, the conductance for this zone is proportional to A_1U_1 as follows

$$AU\big|_{\mathrm{P}} = \left(A_1U_2\right)\mathrm{F}_{\theta_{\mathrm{P}}}\,\mathrm{F}_{S_{\mathrm{P}}} \tag{6.49}$$

The proportionality constant is composed of two factors $\mathrm{F}_{\theta_\mathrm{P}}$ and $\mathrm{F}_{S_\mathrm{P}}$. $\mathrm{F}_{\theta_\mathrm{P}} = 1 - \frac{2\Gamma}{2\Omega}$ is the fraction of the spray in the periphery zone, where 2Ω is the spray cone angle and $\Gamma = \tan^{-1}\left(\frac{D/2}{S_{\max}}\right)$. $\mathrm{F}_{S_\mathrm{P}} = \frac{S_{eq}}{S_{\max}}$ accounts for the fact that the trajectories are not equal in length, where $S_{eq} = \frac{1}{2}\left(S_{\max} - \frac{D/2}{\tan(\Omega)}\right)$ is calculated by representing the peripheral zone by an equivalent duct with the same width D and an equivalent length, S_{eq}. The equivalent length is calculated such that the area of the peripheral zone, as shaded in Figure 6-10, is equal to that of the equivalent duct.

On the other hand, the droplets in the core zone follow either double pass or single pass trajectories, depending on the initial speed-ratio. The conductance for this zone is calculated as follows.

$$AU\big|_{\mathrm{C}_i} = \left(A_i U_i\right)\mathrm{F}_{\theta_\mathrm{C}}\,\mathrm{F}_{S_\mathrm{C}} \tag{6.50}$$

where $i = 1$ for single pass trajectories, i.e. for $SR_o > SR_C$, and $i = 2$ for double pass trajectories, i.e. for $SR_o < SR_C$. $\mathrm{F}_{\theta_\mathrm{C}} = \frac{2\Gamma}{2\Omega}$ and $\mathrm{F}_{S_\mathrm{C}} = 0.5$ are the proportionality constants.

The overall conductance of the spray chamber, $AU\big|_{\mathrm{low}}$, is the equivalent conductance for both zones. The equivalent conductance is calculated by equating the total rate of energy exchange between the air-side and the water in the spray chamber to the sum of the exchange in the periphery and the core zones. This can be expressed as follows

$$\dot{Q}_p + \dot{Q}_C = \dot{Q} \tag{6.51}$$

$$\dot{Q}_p = AU\big|_P \left(t_\infty - t_{\mathrm{w_p}}\right) = \dot{m}_p c_{\mathrm{w}} \left(t_{\mathrm{w_p}} - t_{\mathrm{w}}\right) \tag{6.52}$$

$$\dot{Q}_{C_i} = AU\big|_{\mathrm{C}_i} \left(t_\infty - t_{\mathrm{w_C}}\right) = \dot{m}_C c_{\mathrm{w}} \left(t_{\mathrm{w_C}} - t_{\mathrm{w}}\right) \tag{6.53}$$

$$\dot{Q} = AU\big|_{\mathrm{high}} \left(t_\infty - t_{\mathrm{w_o}}\right) = \dot{m}_{\mathrm{w}} c_{\mathrm{w}} \left(t_{\mathrm{w_o}} - t_{\mathrm{w}}\right) \tag{6.54}$$

where $\dot{Q}_p$ is the energy exchange between the air-side and the water in the periphery zone, $\dot{Q}_{C_i}$ is the energy exchange between the air-side and the water in the core zone, and $\dot{Q}$ is the overall energy exchange in the spray chamber. t_∞ is the air average temperature in ºC, $t_{\mathrm{w_p}}$ is the water exit temperature from the periphery zone in ºC, $t_{\mathrm{w_C}}$ is the water exit temperature from the core zone in ºC, and $t_{\mathrm{w_o}}$ is the water exit temperature from the spray chamber in ºC. c_{w} is the specific heat of water and t_{w} is the water inlet temperature in ºC. $\dot{m}_C$, $\dot{m}_p$ are the mass flow rates of water in the core zone and periphery zone in kg/s, respectively. In the above definitions for the rate of energy exchange, the mathematical mean temperature difference is used rather than the logarithmic mean temperature difference for simplification. It is also assumed that the air average temperature in both zones is the same and it is equal to the air inlet temperature. Furthermore, the average water temperature is assumed to be equal to the exit temperature. The validity of these assumptions and simplifications will be evaluated. Substituting by equations (6.52), (6.53), and (6.54) in equation (6.51) gives

$$\dot{m}_p c_{\mathrm{w}} \left(t_{\mathrm{w_p}} - t_{\mathrm{w}}\right) + \dot{m}_C c_{\mathrm{w}} \left(t_{\mathrm{w_C}} - t_{\mathrm{w}}\right) = \dot{m}_{\mathrm{w}} c_{\mathrm{w}} \left(t_{\mathrm{w_o}} - t_{\mathrm{w}}\right) \tag{6.55}$$

Also, the aforementioned equations are used to give the following expressions for t_{w_p}, t_{w_C}, and t_{w_o}

$$t_{w_p} = \frac{\dot{m}_p c_w t_w + AU\big|_P \, t_\infty}{\dot{m}_p c_w + AU\big|_P} \tag{6.56}$$

Dividing the numerator and denominator by $\dot{m}_w c_w$ and using the expression for $AU\big|_P$, equation (6.49), gives:

$$t_{w_p} = \frac{F_{\theta_P} t_w + \dfrac{(A_1 U_2) F_{\theta_P} F_{S_P}}{\dot{m}_w c_w} t_\infty}{F_{\theta_P} + \dfrac{(A_1 U_2) F_{\theta_P} F_{S_P}}{\dot{m}_w c_w}} \tag{6.57}$$

Rearranging the terms

$$t_{w_p} = \frac{\dot{m}_w c_w t_w + (A_1 U_2) F_{S_P} t_\infty}{\dot{m}_w c_w + (A_1 U_2) F_{S_P}} \tag{6.58}$$

$$t_{w_{C_i}} = \frac{\dot{m}_C c_w t_w + AU\big|_{C_i} \, t_\infty}{\dot{m}_C c_w + AU\big|_{C_i}} \tag{6.59}$$

Dividing the numerator and denominator by $\dot{m}_w c_w$, using the expression for $AU\big|_{C_i}$, equation (6.50), and applying the same algebra as above gives

$$t_{w_{C_i}} = \frac{\dot{m}_w c_w t_w + (A_i U_i) F_{S_C} t_\infty}{\dot{m}_w c_w + (A_i U_i) F_{S_C}} \tag{6.60}$$

$$t_{w_o} = \frac{\dot{m}_w c_w t_w + AU\big|_{high}\, t_\infty}{\dot{m}_w c_w + AU\big|_{high}} \tag{6.61}$$

Substituting by the above definitions for t_{w_p}, $t_{w_{C_i}}$, and t_{w_o} into equation (6.55) gives

$$F_{\theta_P}\Delta T_p + F_{\theta_C}\Delta T_{C_i} = \left(\frac{\dot{m}_w c_w t_w + AU\big|_{high}\, t_\infty}{\dot{m}_w c_w + AU\big|_{high}} - t_w \right) \tag{6.62}$$

where $F_{\theta_C} = \frac{2\Gamma}{2\Omega} = \frac{\dot{m}_C}{\dot{m}}$, $F_{\theta_P} = 1 - F_{\theta_C} = \frac{\dot{m}_P}{\dot{m}}$, $\Delta T_p = \frac{\dot{m}_w c_w t_w + \left(A_l U_2\right) F_{S_P} t_\infty}{\dot{m}_w c_w + \left(A_l U_2\right) F_{S_P}} - t_w$,

and $\Delta T_{C_i} = \frac{\dot{m}_w c_w t_w + \left(A_i U_i\right) F_{S_C} t_\infty}{\dot{m}_w c_w + \left(A_i U_i\right) F_{S_C}} - t_w$. Rearranging the terms of equation (6.62) and introducing a correction factor F_{high_i} gives the conductance of the spray chamber as follows:

$$AU\big|_{high_i} = F_{high_i} \frac{\dot{m}_w c_w \left(F_{\theta_P}\Delta T_p + F_{\theta_C}\Delta T_{C_i}\right)}{\left(t_\infty - t_w - F_{\theta_P}\Delta T_p - F_{\theta_C}\Delta T_{C_i}\right)} \tag{6.63}$$

where
$$\begin{cases} i = 1 & SR_o > SR_C & F_{high_1} = 0.953 \pm 0.174 \\ i = 2 & SR_o \approx SR_C & F_{high_2} = 0.834 \pm 0.135 \end{cases}$$

F_{high_i} is a correction factor developed from the results of the numerical simulations that accounts for the approximation of Reynolds number, and the assumption adopted in calculating the air and water average temperatures.

6.2.3.2.2 Low initial speed-ratios

At initial speed-ratios $SR_o \ll SR_C$, the particle tracks are as shown in Figure 6-11. For "escape" wall boundary condition this case is in the vicinity of $SR_o \approx SR_{\mathcal{E}}$. To model this case, two limiting scenarios are considered. The first of these scenarios assumes the trajectories shown in Figure 6-12a. It can be seen from this figure that the particles retract at an angle $2\Omega = 2\sin^{-1}\left(y/S_{\max}\right)$. In this case, the droplets never reach the walls of the spray chamber. Consequently, the "reflect" wall boundary condition perfectly depicts this assumed behavior. Hence, the conductance is given by:

$$UA\big|_{\mathrm{low_a}} = \mathrm{F}_{\mathrm{low_a}}\left(U_2 A_2\right) \tag{6.64}$$

The factor $\mathrm{F}_{\mathrm{low_a}}$ is a correction factor, developed from the results of the numerical simulations, that accounts for the approximation of Reynolds number $\overline{\mathrm{Re}_{\mathrm{l}}} = \mathrm{Re}_o$, where $\mathrm{F}_{\mathrm{low_a}} = 0.938 \pm 0.14$. This scenario best fits cases with initial speed-ratios that corresponds to $S_{\max} \le \dfrac{y}{\sin\Omega}$, where $y = D/4$.

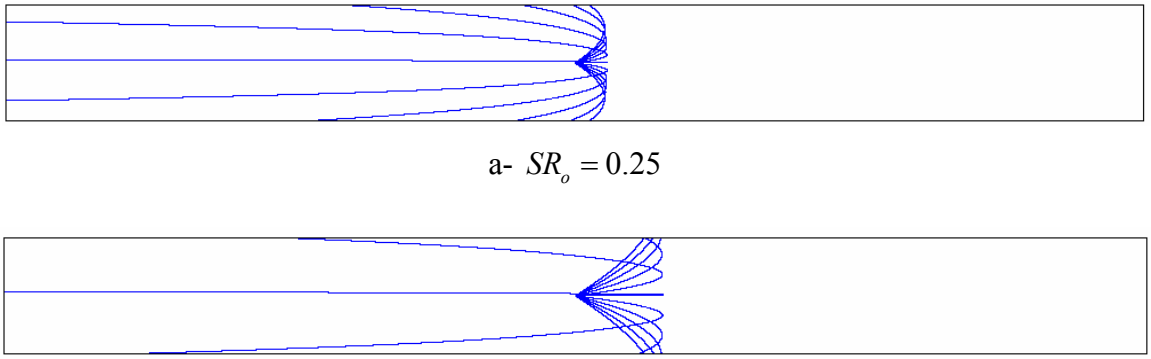

a- $SR_o = 0.25$

b- $SR_o = 0.5$

Figure 6-11 Particle tracks for spray-cooler with "escape" wall boundary condition

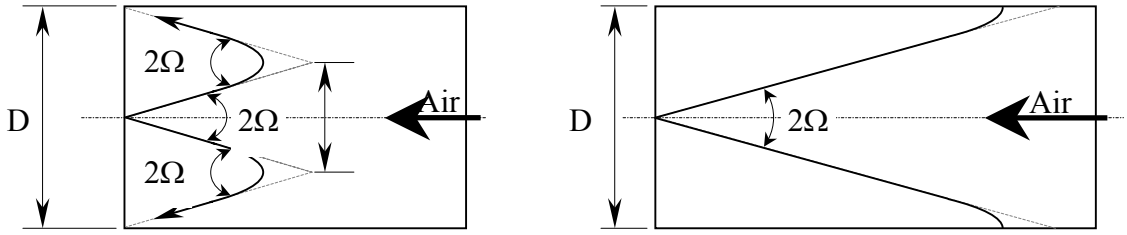

a- $2y = D/2$ b- $2y = 1.25D$

Figure 6-12 Schematic showing the particle tracks for for spray-cooler with "escape" wall boundary condition, for initial speed-ratio $SR_o \ll SR_C$

On the other hand, the other scenario best fits cases with initial speed-ratios that correspond to $\frac{D/4}{\sin\Omega} < S_{\max} \leq \frac{5/8\,D}{\sin\Omega}$. The trajectories for this scenario are as shown in Figure 6-12b. As shown in this figure the assumption of "reflect" wall is no longer valid because some water droplets reach the walls and consequently, escape the spray chamber. The "reflect" wall model over predicts the conductance of the spray chamber, while the periphery-core model under predicts it. Therefore, an average value is used to represent the conductance of the

spray chamber, $UA\big|_{\text{low}_b}$, for the range $\frac{D/4}{\sin\Omega} < S_{\max} \le \frac{5/8\,D}{\sin\Omega}$. Consequently, the conductance of the spray chamber is given by:

$$UA\big|_{\text{low}_b} = \text{F}_{\text{low}_b}\left(\frac{U_2 A_2 + UA\big|_{\text{high}}}{2}\right) \tag{6.65}$$

where $\text{F}_{\text{low}_b} = 0.855 \pm 0.069$ is a correction factor, developed from the results of the numerical simulations, that accounts for the assumptions needed to derive the expression of $UA\big|_{\text{low}_b}$.

6.2.3.2.3 Intermediate initial speed-ratios

At initial speed-ratios that corresponds to $\frac{5D}{8\sin\Omega} < S_{\max} < 0.8S_{eff}$ the periphery-core model under predicts the conductance. At the same time, assuming a linear relationship between the conductance of the two cases $S_{\max} = \frac{5D}{8\sin\Omega}$ and $S_{\max} = 0.8S_{eff}$ over predicts the conductance of the spray chamber. Consequently, the conductance of the spray chamber, UA_{int}, is approximated by taking the mean value of the conductance of these two cases. Consequently, the conductance of the spray chamber is given by:

$$UA_{\text{int}} = \text{F}_{\text{int}}\left(\frac{AU\big|_{\text{high}} + UA\big|_{\text{linear}}}{2}\right) \tag{6.66}$$

where F_{int} is a correction factor, developed from the results of the numerical simulations, that accounts for the assumptions needed to derive the expression of UA_{int}. $UA\big|_{\text{linear}} = \left(UA\big|_{S_A} - UA\big|_{S_B}\right)\left(\frac{S_B - S_{\max}}{S_B - S_A}\right) + UA\big|_{S_B}$, is the linear relationship for the conductance

between the two cases $S_A = \dfrac{5D}{8\sin\Omega}$, and $S_B = 0.8S_{eff}$. The corresponding conductance are $UA\big|_{S_A} = UA\big|_{\text{low}_b}$ and $UA\big|_{S_B} = AU\big|_{\text{high}_2}$.

Figure 6-13 depicts a comparison between the conductance, of the spray chamber with "escape" wall boundary condition, calculated using the semi-analytical model and that of the numerical results. The semi-analytical results agrees with the numerical results with an average offset of 9.2% for the case where $g = 0\,\text{m/s}^2$ and 14.5% for $g = -9.81\,\text{m/s}^2$.

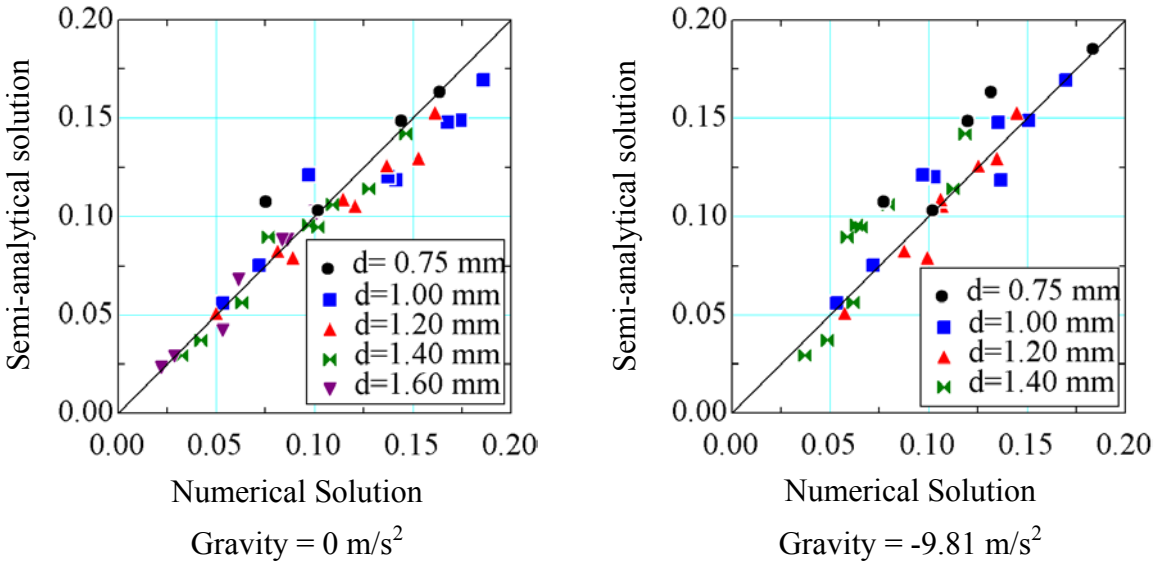

Figure 6-13 Comparison of the semi-analytical and numerical results for the conductance for "escape" wall boundary condition, initial speed-ratio $SR_o = 2.2$, droplet diameter $d = 1$ mm, $\underline{u}_\infty = -5\,\text{m/s}$, and $\text{MR} = \dfrac{\dot{m}_{\text{water}}}{\dot{m}_{\text{air}}} = 0.5$

The above discussion presented the semi-analytical models necessary to predict the conductance of the spray chamber with "escape" wall boundary condition. The discussion

shows that the conductance of the spray chamber not only depends on the initial speed-ratio, but also on the spray cone angle, and the spray chamber geometry. Comparing the results of the semi-analytical models to the corresponding numerical simulations shows that these models well predict the conductance of the spray chamber. These models are summarized in Table 6-2.

Table 6-2 Summary of spray chamber conductance semi-analytical correlations for "escape" wall boundary condition

Correlation	**Restrictions**	
$0.938\left(U_2 A_2\right)$	$S_{\max} \le \dfrac{D/4}{\sin\Omega}$	*Low initial speed-ratio* $SR_o \le SR_{\mathcal{E}}$
$0.855\left(\dfrac{U_2 A_2 + UA\big\|_{\text{low}}}{2}\right)$	$\dfrac{D/4}{\sin\Omega} < S_{\max} \le \dfrac{5/8\,D}{\sin\Omega}$	
$0.878\left(\dfrac{AU\big\|_{\text{low}} + UA\big\|_{\text{linear}}}{2}\right)$	$\dfrac{5/8\,D}{\sin\Omega} < S_{\max} < 0.8 S_{eff}$	*Intermediate initial speed-ratio* $SR_{\mathcal{E}} < SR_o < SR_C$
$0.834\dfrac{\dot{m}c_{\text{w}}\left(\text{F}_{\theta_{\text{P}}}\Delta T_p + \text{F}_{\theta_{\text{C}}}\Delta T_{C_2}\right)}{\left(t_\infty - t_{\text{w}} - \text{F}_{\theta_{\text{P}}}\Delta T_p - \text{F}_{\theta_{\text{C}}}\Delta T_{C_2}\right)}$	$0.8 S_{eff} \le S_{\max} < 1.1 S_{eff}$	*High initial speed-ratio* *a-* $SR_o \approx SR_C$
$0.953\dfrac{\dot{m}c_{\text{w}}\left(\text{F}_{\theta_{\text{P}}}\Delta T_p + \text{F}_{\theta_{\text{C}}}\Delta T_{C_1}\right)}{\left(t_\infty - t_{\text{w}} - \text{F}_{\theta_{\text{P}}}\Delta T_p - \text{F}_{\theta_{\text{C}}}\Delta T_{C_1}\right)}$	$S_{\max} \ge 1.1 S_{eff}$	*b-* $SR_o > SR_C$

6.2.4 Spray Chamber Non-Dimensional Conduction

Figure 6-14 shows the effect of changing the spray-cooler initial speed-ratio, SR_o and Reynolds number, Re_∞, on the non-dimensional conductance, β_{UA}. The non-dimensional conductance is defined as

$$\kappa_{UA} = \frac{\frac{U}{\frac{k_{\text{air}}}{d}}}{\frac{\dot{m}_{\text{water}}}{u_\infty \rho_{\text{air}}}} = \frac{Ud}{k_{\text{air}}} \frac{A}{\frac{A_c}{\dot{m}_{\text{air}}} \dot{m}_{\text{water}}} \tag{6.67}$$

Rearranging the terms gives

$$\kappa_{UA} = \frac{A}{A_c} \frac{\dot{m}_{\text{air}}}{\dot{m}_{\text{water}}} \frac{Ud}{k_{\text{air}}} = \frac{A}{A_c} \left(\frac{\rho_{\text{air}} D^2}{\rho_{\text{water}} d_{\text{nozzle}}^2} \frac{U_\infty}{V} \right) \frac{Ud}{k_{\text{air}}} \tag{6.68}$$

$$\kappa_{UA} = \frac{A}{A_c} \left(\frac{\rho_{\text{air}} D^2}{\rho_{\text{water}} d_{\text{nozzle}}^2} \frac{u_\infty}{V} \right) \frac{Ud}{k_{\text{air}}} = \frac{A}{A_c} \left(\frac{\rho_{\text{air}} D^2}{\rho_{\text{water}} d_{\text{nozzle}}^2} \frac{u_\infty}{u_o \cos\Omega} \right) \frac{Ud}{k_{\text{air}}}$$

$$\kappa_{UA} = \left(\frac{\rho_{\text{air}}}{\rho_{\text{water}}} \frac{D^2}{d_{\text{nozzle}}^2} \frac{1}{\cos\Omega} \frac{A}{A_c} \right) \frac{1}{SR_o} \frac{Ud}{k_{\text{air}}} \tag{6.69}$$

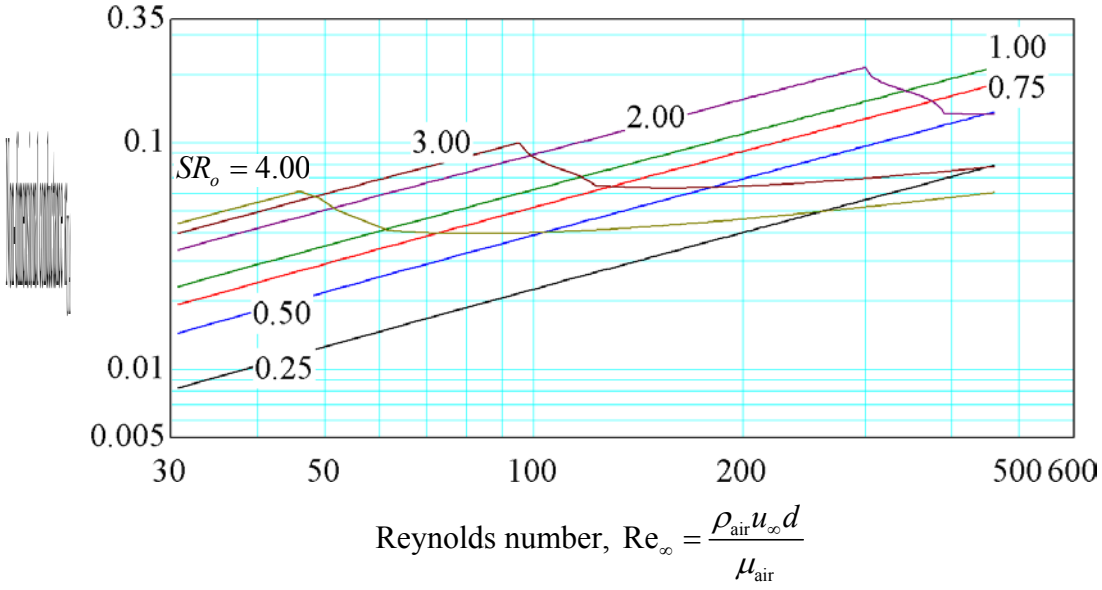

Figure 6-14 Effect of Reynolds number, Re_∞, on the non dimensional conductance for different initial speed-ratios, $SR_o = u_o / u_\infty$, assuming constant diameter

where A is the interfacial area of the spray cooler, A_c is the cross sectional area of the spray cooler, $\dot{m}_{\text{air}}$ and $\dot{m}_{\text{water}}$ are the mass flow rates of air and water, respectively. U is the overall heat transfer coefficient d is the droplet diameter and k_{air} is the conductivity of air. ρ_{air} ρ_{water} are the densities of air and water, respectively. D is the spray chamber width, d_{nozzle} is the nozzle diameter and 2Ω is the spray cone angle.

Figure 6-14 shows that for the same SR_o, as the Reynolds number, Re_∞, increases the non-dimensional conductance, κ_{UA}, increases. This increase in the non-dimensional conductance, κ_{UA}, is due to the increase in the surface area and the overall heat transfer coefficient Figure 6-3 shows that increasing the Reynolds number increases the spray-tip-penetration-length to diameter ratio, and consequently the total surface area increases. The increase in Reynolds number Re_∞ is achieved by increasing the air velocity and/or the droplet diameter, consequently the average Reynolds number Re_i also increases. Equation (6.43) shows that increasing the average Reynolds number Re_i increases the overall heat transfer coefficient.

Figure 6-14 also shows that for the same Reynolds number, increasing the initial speed-ratio, SR_o, increases the non-dimensional conductance. This is due to the fact that as the initial speed-ratio increases, for fixed $\underline{u}_\infty$, the spray initial velocity, $\underline{u}_o$, increases. This increases the droplet initial momentum with respect to the momentum of air and therefore the spay-tip-penetration-length increases. This leads to an increase in the total surface area of the spray cooler. Also, increasing the spray initial velocity increases the overall heat transfer

coefficient. The net effect is an increase in the conductance of the spray chamber. Figure 6-14 shows a sudden drop in conductance at initial speed-ratios $SR_o = 2$ and above. This drop in conductance occurs when spray-tip reaches the end of the spray chamber and starts to penetrate outside the spray chamber. At this point the spray chamber switches from double pass to single pass operation.

It should be noted that increasing the initial speed-ratio, SR_o, by decreasing the air velocity $\underline{u}_\infty$ and keeping the spray initial velocity $\underline{u}_o$ also increases the non-dimensional conductance of the spray chamber. As the Reynolds number increases the initial momentum of air increases. Hence, the spray-tip-penetration-length decreases and accordingly the total surface area decreases. Figure 6-15 shows that despite the increase in the overall heat transfer coefficient as the Reynolds number Re_∞ increase, the decrease in surface area has more effect on the conductance of the spray chamber.

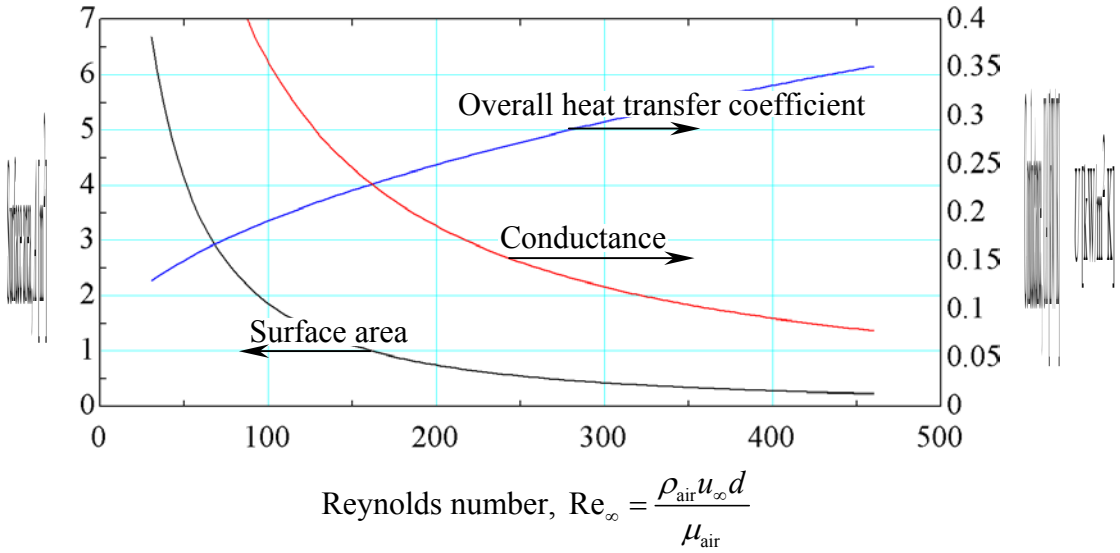

Figure 6-15 Effect of changing the Reynolds number on the surface area and overall heat transfer coefficient

6.2.5 Effectiveness

The prediction of the performance of the spray-cooler requires the knowledge of its conductance and inlet fluid temperatures. In the preceding section, the conductance of the spray-chamber is predicted. The conductance establishes the basis for predicting the thermal performance of the spray chamber for any set of given parameters using the effectiveness-NTU method. The effectiveness, ε, is the ratio of the actual heat transfer rate to the maximum possible heat transfer rate. The maximum possible heat transfer rate occurs when the minimum capacitance rate fluid experiences the maximum temperature change. In the case of the spray chamber, the minimum capacitance rate fluid is the air.

$$\varepsilon = \frac{\dot{Q}}{C_{\min} \Delta T_{\max}} \tag{6.70}$$

$$\varepsilon = \frac{(UA)\Delta T_{\text{mean}}}{C_{\min}\Delta T_{\max}} \tag{6.71}$$

$$\varepsilon = \frac{\left(\dot{m}_{\text{air}} C_{\text{p}}\right)\left(T_{\text{in}} - T_{\text{out}}\right)\Big|_{\text{air}}}{\left(\dot{m}_{\text{air}} C_{\text{p}}\right)\left(T_{\text{in}}\Big|_{\text{air}} - T_{\text{in}}\Big|_{\text{water}}\right)} \tag{6.72}$$

$$\varepsilon = \frac{\left(\dot{m}_{\text{air}} C_{\text{p}}\right)\left(T_{\text{in}} - T_{\text{out}}\right)\Big|_{\text{air}}}{\left(\dot{m}_{\text{air}} C_{\text{p}}\right)\left(T_{\text{in}}\Big|_{\text{air}} - T_{\text{in}}\Big|_{\text{water}}\right)} \tag{6.73}$$

Kays and London [6] show that for any heat exchanger geometry, the effectiveness is a function solely of the heat capacities of the fluids and the conductance, as shown by equations (6.74) and (6.75). Equation (6.74) is used to predict the effectiveness for single pass trajectories while equation (6.75) is used for double pass trajectories.

$$\varepsilon_1 = \frac{1 - e^{-(\text{NTU})(1-C)}}{1 - Ce^{-(\text{NTU})(1-C)}} \tag{6.74}$$

$$\varepsilon_2 = \frac{2}{1 + C + B\left(\dfrac{1 + e^{-(\text{NTU})B}}{1 - e^{-(\text{NTU})B}}\right)} \tag{6.75}$$

where $C = C_{\min}/C_{\max}$, $\text{NTU} = UA/C_{\min}$, and $B = \sqrt{1 + C^2}$.

Equation (6.71) shows that the spray chamber effectiveness is proportional to the spray chamber conductance, *UA* product. Hence, as shown from the discussion in §6.2.3, the effectiveness of the spray chamber with "reflect" boundary condition will depend entirely on the initial speed-ratio. On the other hand, for a spray chamber with "escape" wall boundary

condition the effectiveness will depend on the initial speed-ratio, spray cone angle, and the spray chamber geometry. This is discussed in what follows.

6.2.5.1 Reflect wall boundary condition

For initial speed-ratios greater or equal than SR_{cutoff}, no retraction takes place inside the spray chamber. Therefore, the spray-cooler is modeled as a single-pass, counter flow heat exchanger. Equation (6.74) is thus used to calculate the effectiveness, where the number of transfer units, $\text{NTU} = 0.95\, U_1 A_1 / C_{\min}$.

On the other hand, for initial speed-ratios smaller or equal than SR_{ε}, the particles retract inside the spray chamber. Therefore, the spray-cooler is modeled as a double-pass, single shell heat exchanger. For this case, equation (6.75) is used to calculate the effectiveness, with the following representation for the number of transfer units, $\text{NTU} = 1.13\, U_2 A_2 / C_{\min}$.

For initial speed-ratios in the range $SR_{\varepsilon} < SR_o < SR_{cutoff}$, the effectiveness is calculated assuming an elliptic distribution between the effectiveness $\varepsilon|_{\text{E}}$ and $\varepsilon|_{\text{C}}$ at S_{eff} and S_{cutoff}, respectively, as follows

$$\varepsilon = \sqrt{(1-\text{X})\left(\varepsilon|_{\text{EC}}\right)^2} + \varepsilon|_{\text{C}} \qquad (6.76)$$

where $\varepsilon|_{\text{EC}} = \varepsilon|_{\text{E}} - \varepsilon|_{\text{C}}$. Figure 6-16 compares the semi-analytical and numerical results for the effectiveness for “reflect” wall boundary condition. The figure shows that the semi-

analytical results are in a good agreement with the numerical results, with an average offset of 5.22%.

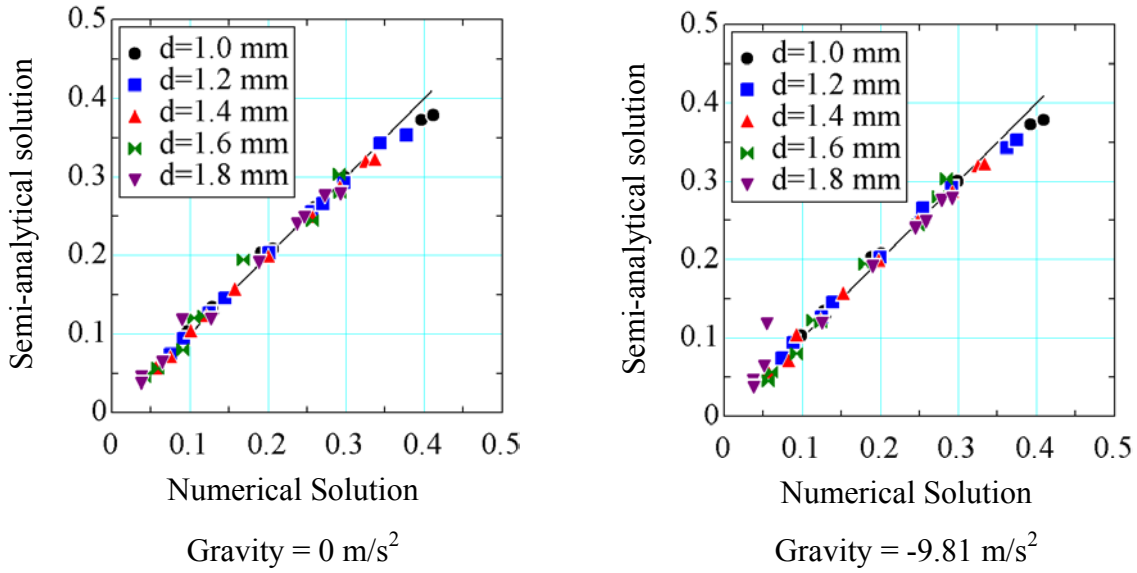

Figure 6-16 Comparison of the semi-analytical and numerical results for the effectiveness for "reflect" wall boundary condition, $\underline{u}_{\infty} = -5\,\text{m/s}$, and $\text{MR}=\frac{\dot{m}_{\text{water}}}{\dot{m}_{\text{air}}}=0.5$

6.2.5.2 Escape wall boundary condition

For initial speed-ratios greater or equal than SR_C, no retraction takes place inside the spray chamber. Therefore, the spray-cooler is modeled as a single-pass, counter flow heat exchanger. Equation (6.74) is used to calculate the effectiveness based on the following relation for the number of transfer units, $\text{NTU} = AU\big|_{\text{high}_1} \big/ C_{\min}$.

On the other hand for initial speed-ratios smaller or equal than SR_C, the particles retract inside the spray chamber. Therefore, the spray-cooler is modeled as a double-pass, single

shell heat exchanger. Consequently, equation (6.75) is used to calculate the effectiveness, where the number of transfer units, $\text{NTU} = UA/C_{\min}$. The conductance of the spray chamber depends on the initial speed-ratio as summarized in Table 6-2.

Figure 6-17 compares the semi-analytical and numerical results for the effectiveness for "escape" wall boundary condition. The figure shows that the semi-analytical results are in a good agreement with the numerical results. The semi-analytical results agrees with the numerical results with an average offset of 8.6% for the case where $g = 0\,\text{m/s}^2$ and 13.6% for $g = -9.81\,\text{m/s}^2$.

At this stage the effectiveness of the spray chamber, ε, the minimum capacitance rate, $C_{\min}$, the inlet temperatures and consequently $\Delta T_{\max}$ are known. This paves the way to predict the rate of energy transfer, $\dot{Q}$, and the exit temperatures of air and water streams, T_{out}, using equations (6.70), (6.72), and (6.73), respectively.

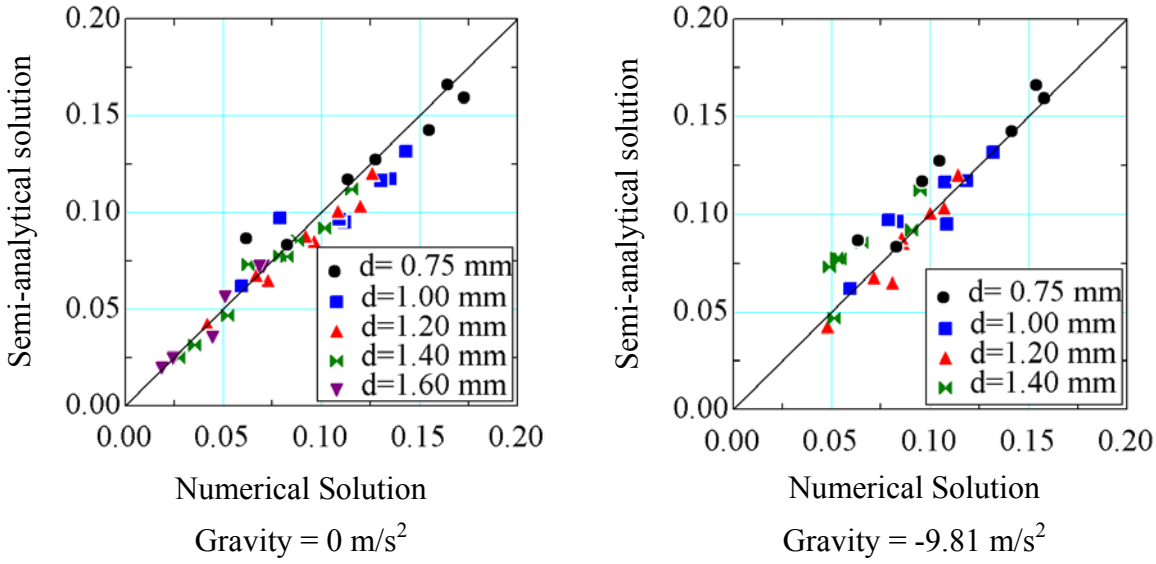

Figure 6-17 Comparison of the semi-analytical and numerical results for the effectiveness for "escape" wall boundary condition, initial speed-ratio $SR_o = 2.2$, droplet diameter $d = 1$ mm, $\underline{u}_\infty = -5\,\text{m/s}$, and $\text{MR} = \dfrac{\dot{m}_{\text{water}}}{\dot{m}_{\text{air}}} = 0.5$

Up to this point, no mention is made of a method to identify the optimum initial speed-ratio, $SR_{\mathcal{E}}$, for "escape" wall boundary condition. This optimum value is controlled by two competing effects; one tends to increase the conductance, while the other tends to decrease it. Particularly, increasing the initial speed-ratio increases the spray-tip-penetration-length. This results in an increase in the conductance of the spray chamber as shown by equation (6.64). However, as the spray-tip-penetration-length increases the number of droplets that reach the walls and eventually escape increases. This results in a reduction in the conductance of the spray chamber, as shown in equation (6.63). The intersection of both functions, equations

(6.63) and (6.64), identifies the optimum initial speed-ratio as shown in Figure 6-18. Equation (6.77) gives this optimum by equating equations (6.63) and (6.64) as follows:

$$0.938\left(U_2 A_2\right) = 0.834 \frac{\dot{m} c_{\mathrm{w}} \left(\mathrm{F}_{\theta_{\mathrm{P}}} \Delta T_p + \mathrm{F}_{\theta_{\mathrm{C}}} \Delta T_{C_2}\right)}{\left(t_\infty - t_{\mathrm{w}} - \mathrm{F}_{\theta_{\mathrm{P}}} \Delta T_p - \mathrm{F}_{\theta_{\mathrm{C}}} \Delta T_{C_2}\right)} \tag{6.77}$$

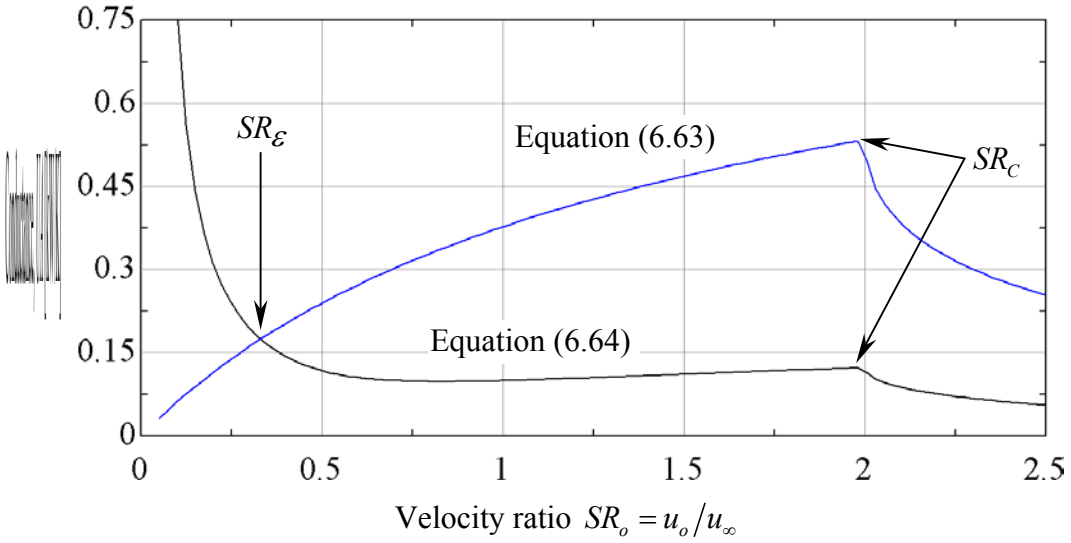

Figure 6-18 Optimum initial speed-ratio SR_ε for droplet diameter $d = 1$ mm and "escape" wall boundary condition

The optimum initial speed-ratio, SR_ε, can not be obtained explicitly from equation (6.77). Thus, an iterative method should be used in order to solve equation (6.77) for $\left|VR_\varepsilon\right|$. Figure 6-19 shows the as the droplet diameter increases SR_ε increase. Larger diameter droplets have higher initial momentum; therefore they reach the walls faster than smaller ones.

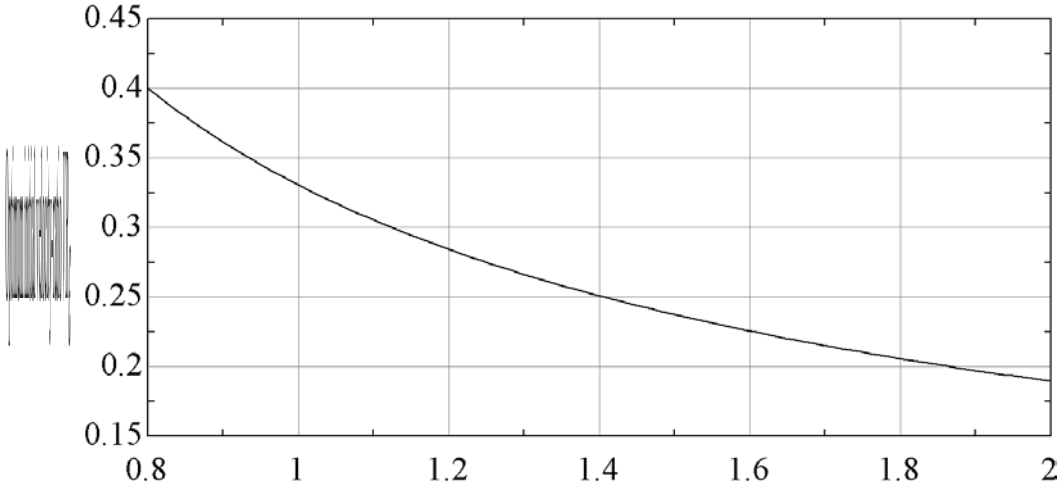

Figure 6-19 Optimum initial speed-ratio SR_{ε} for different droplet diameters and "escape" wall boundary condition

6.3 Summary

This chapter presented the semi-analytical models that predict the hydrodynamics and the thermal performance of a direct contact spray-cooler. The equations used to model the spray-cooler are complex and linked together in a way that makes the closed form analytical solution intractable. However, the numerical approach doesn't offer a better alternative since several simulation runs are required to generate a sample of adequate size to carry out a parametric study. Therefore, semi-analytical models are needed. These models predict the spray-tip-penetration-length, the overall heat transfer coefficient, the interfacial area, and the effectiveness for direct contact spray cooling devices. The chapter begins by solving the equation of motion to predict the instantaneous horizontal droplet velocity, $\underline{u}$, and droplet displacement, $\underline{S}$ and the spray-tip-penetration-length, $S_{\max}$. The spray-tip-penetration-

length depends on Reynolds number, Re_∞, the droplet diameter, d, and the spray-cooler initial speed-ratio. The spray-tip-penetration-length, $S_{\max}$ increases by increasing Reynolds number, Re_∞, the droplet diameter, d, and the initial speed-ratio, SR_o. This is then followed by presenting the equations necessary to predict the conductance of the spray chamber. The main controlling factors are the initial speed-ratio and the wall type boundary condition. For the "reflect" wall boundary condition, the conductance is only dependent on the hydrodynamics of the spray-cooler. Increasing the initial speed-ratio, SR_o, increases the conductance until the maximum is reached when the spray-tip-penetration-length equals the spray chamber length. For the "escape" wall boundary condition, the conductance depends on the hydrodynamics as well as the spray chamber geometry. Comparing the results of these models to the corresponding numerical simulations shows that these models predict the hydrodynamics and the thermal performance of the spray chamber successfully.

6.4 Nomenclature

A_c	Cross sectional area of the spray cooler	m^2
A_d	Frontal area of the droplet	m^2
A_i	Total interfacial area for water droplets contained in the spray chamber	m^2
A_s	Droplet surface area	
C_d	Drag-coefficient for spheres	
$C_{\min}$	Minimum capacitance rate	J/K
c_w	Specific heat of water	J/kg-K
D	Duct width	m
d	Surface area mean droplet diameter	m
d_{nozzle}	Nozzle diameter	m
F_i	Correction factor for the conductance	
$\underline{F}_{ss}$	Steady-state force	N
F_{S_p}	Correction factor to correct for unequal trajectory length	
F_{θ_C}	Proportionality constant	
F_{θ_p}	Fraction of spray in the periphery zone	
F_{S_C}	Proportionality constant	
$\underline{g}$	Gravitational acceleration	m/s^2
$\overline{h}_{c_i}$	Average heat transfer coefficient	W/m^2-K
h_{c_i}	Local heat transfer coefficient	W/m^2-K
i	is a factor that accounts for the effect of the particle retraction inside the spray chamber	

k_{air}	Conductivity of air	W/m-K
MR	Mass ratio	
m_d	Droplet mass	kg
$\dot{m}_{\text{air}}$	Air mass flow rate	kg/s
$\dot{m}_C$	Mass flow rate of water in the core zone	kg/s
$\dot{m}_p$	Mass flow rate of water in the periphery zone	kg/s
$\dot{m}_w$	Water mass flow rate	kg/s
$\dot{N}_{droplets}$	Droplets rate	1/s
Pr	Prandtl number	
$\dot{Q}$	Overall energy exchange in the spray chamber	W
$\dot{Q}_{c_{\text{i}}}$	Energy exchange between the air-side and the water in the core zone	W
$\dot{Q}_{p_{\text{i}}}$	Energy exchange between the air-side and the water-side in the periphery zone	W
Re	Reynolds number	
$\text{Re}_{S_{\text{i}}}$	Local Reynolds number	
$\overline{\text{Re}}_i$	Average Reynolds number	
Re_o	Reynolds number	
Re_∞	Reynolds number	
S	Horizontal displacement magnitude of the water droplet	m
$\underline{S}$	Horizontal displacement vector of the water droplet	m
$S_{\text{Analytical}}$	Analytical prediction of the droplets horizontal displacement	m
$S_{\text{Numerical}}$	Numerical prediction of the droplets horizontal displacement	m
S_A	$S_A = \frac{5D}{8\sin\Omega}$	m
S_B	$S_B = 0.8S_{eff}$	m

S_{Cutoff}	Spray-tip-penetration-length beyond which all particles retract outside the spray chamber	m
S_{EC}	$S_{\mathrm{EC}} = S_{Cutoff} - S_{eff}$	m
S_{eff}	Effective spray-tip-penetration-length	m
S_{eq}	Spray chamber equivalent length	m
$\underline{S}_{\max}$	Spray-tip-penetration-length vector	m
$S_{\max}$	Spray-tip-penetration-length	m
SR	Speed ratio	
SR_C	Initial speed ratio corresponding to the maximum spray-tip-penetration-length	
SR_{cutoff}	Initial speed-ratio above which all the spray retracts outside the spray chamber	
SR_o	Initial speed ratio	
SR_ε	Initial speed ratio corresponding to the maximum effectiveness	
$\Delta S_{\%}$	Percentage deviation between analytical and numerical predictions of the droplet horizontal displacement	%
t	Time	s
t_{res}	Particle residence time	s
$t_{S_{\max}}$	Time to reach the maximum penetration	s
t_w	Water inlet temperature	ºC
t_{wc}	Water exit temperature from the core zone	ºC
t_{wp}	Water exit temperature from the periphery zone	ºC
t_{wo}	Water exit temperature	ºC
t_∞	Air average temperature	ºC
UA_{low}		W/K
UA_{int}		W/K

UA_{high}		W/K
UA_{linear}		W/K
UA_{SA}		W/K
UA_{SB}		W/K
$UA\|_{cutoff}$	Conductance of the spray chamber that corresponds to $SR_o = SR_{cutoff}$	
$UA\|_{EC}$	$UA\|_{\mathrm{EC}} = UA\|_{cutoff} - UA\|_{\varepsilon}$	W/K
$UA\|_{C}$	Conductance in the core zone	W/K
$UA\|_{P}$	Conductance in the periphery	W/K
$UA\|_{low}$	Equivalent conductance for periphery and core zones	W/K
$UA\|_{\varepsilon}$	Conductance of the spray chamber that corresponds to $SR_o = SR_{\varepsilon}$	
U^*	$1/u_\infty$	m/s
$\underline{U}^*$	Velocity vector with a magnitude that is equal to the reciprocal of the continuous phase velocity and in the same direction.	m/s
U_i	Average overall transfer coefficient	W/m^2 K
U	Local overall heat transfer coefficient	W/m^2 K
$\underline{U}_\infty$	Continuous phase, air, velocity vector	m/s
u	Horizontal velocity magnitude of the water droplet	m/s
$\underline{u}$	Horizontal velocity vector of the water droplet	m/s
$u_{\mathrm{Analytical}}$	Analytical prediction of the velocity	m/s
$u_{\mathrm{Numerical}}$	Numerical prediction of the velocity	m/s
$\underline{u}_o$	Horizontal initial velocity vector of the spray	m/s
$\underline{u}_{rel}$	Horizontal relative velocity vector	m/s
$\underline{u}_\infty$	Horizontal velocity component of air	m/s

u_∞	Magnitude of the horizontal velocity component of air	m/s
$\Delta u_{\%}$	Percentage deviation between numerical and analytical speeds	%
$\underline{V}$	Water droplet velocity vector	m/s
VR	Velocity ratio	
VR_C	Critical initial velocity ratio	
VR_ε	Initial velocity-ratio that corresponds to maximum effectiveness	
VR_o	Initial velocity-ratio	
X	$X = \dfrac{\left(S_{\max} - S_{eff}\right)^2}{\left(S_{\mathrm{EC}}\right)^2}$	

6.4.1 Greek Symbols

α	$\alpha = VR - 1$	
α_o	$\alpha_o = VR_o - 1$	
ε	Effectiveness	
Γ_i	$\Gamma_i = \sqrt{6\,\mathrm{Re}_\infty^{2/3}}\left(\sqrt{\alpha_i^{2/3}} - \sqrt{\alpha_o^{2/3}}\right)$	
β_i	$\beta_i = \dfrac{\Gamma_i}{6 + \mathrm{Re}_\infty^{2/3}\sqrt{\alpha_o^{2/3}\alpha_i^{2/3}}}$	
ρ_{air}	Density of moist air	kg/m^3
ρ_{water}	Density of water	kg/m^3
μ_{air}	Viscosity of air	kg/m-s
θ		
τ_m	Momentum response time	s
2Ω	Spray cone angle	
ζ_A	Spray-tip-penetration-length to diameter ratio	
κ_{UA}	Non-dimensional conductance	

6.5 References

1 Putnam, A. “Integratable form of droplet drag coefficient”, J. Am. Rocket Soc., Vol.31, 1961, pp. 1467-1468.

2 Crowe, C. T., Sommerfeld, M., and Tsuji, Y., “Multiphase flows with droplets and particles”, CRC press LLC, 1998, ISBN 0-8493-9469-4.

3 Morsi, S.A, and Alexander, A.J., “An investigation of particle trajectories in two-phase flow systems”, Journal of Fluid Mechanics, vol. 55 (part 2), Sep 1972, pp 193-208.

4 K. Giek and R. Giek, “Engineering Formulas”, 7th ed, McGraw-Hill, 1997, ISBN 0-07024572-X, pp. E8

5 Ranz, W. E. and W.R. Marshall, “Evaporation from drops”, Chemical Engineering Progress, vol. 48, no.3 & 4, 1952, pp 141-146, 173-180.

6 Kays and London, “Compact Heat Exchangers” McGraw-Hill Book Company, 2nd ed.,1995,

Chapter 7 Conclusions and Recommendations

The current research work focuses on the design and control of direct-contact spray heat exchangers using chilled water to achieve optimum performance. A goal of the work has been an understanding of the physical processes involved in the operation of the direct-contact heat exchanger. This chapter summarizes the significant findings of the present work. This is then followed by presenting recommendations for directions and areas of focus for future investigations related to this topic.

7.1 Conclusions

The work includes experimental, numerical and semi-analytical investigations. The experimental portion of the research effort, presented in Chapter 3, investigates the heat and mass transfer characteristics of the direct-contact spray cooler. Two sets of experiments are performed. The first investigates the effect of changing the water flow rate on the spray chamber performance. The results of this experiment indicate that increasing the water flow rate increases the spray chamber air-side pressure drop and effectiveness. The increase in pressure drop leads to decreases in the air flow rate. The increase in the effectiveness can be attributed to the increase in $Q_{sensible}$ due to the increase in water mass flow rate and reduction in $h_{\text{air}}\big|_{\text{x}}$. The second set of experiments address the ability of the direct-contact heat exchanger to effectively cool and dehumidify a moist air stream at a given ambient condition to a desired leaving state. In the experimental conditions investigated, the latent load

comprises only 7.5% of the total load for the runs analyzed. If the latent load were to be neglected, the effectiveness of the spray chamber would be 0.44 (10% higher) and the exit dry-bulb would be 17.27 C (1.29 C lower). Hence, the cooler can be considered as a sensible cooler for the operating conditions analyzed.

Chapter 4 illustrates the method used to experimentally measure the droplet diameter and spray cone angle. The results of the experiments indicate that as the volume flow rate increases the droplet diameter decreases. This behavior can be explained as follows: increasing water flow rates increases the water velocity. As the velocity increases, the force due to the aerodynamic pressure exerted on the droplet increases. The increased force results in breakup of the droplets until the surface tension is large enough to balance the external force due to the aerodynamic pressure. The chapter also investigates the effects of changing the injection pressure on the spray chamber cone angle. The result of this investigation suggests that there is no obvious trend for the effect of varying the injection pressure on the spray cone angle.

The numerical analysis, presented in Chapter 5, is conducted to identify and characterize important parameters in spray cooling systems operation and suggest means for maximizing the effectiveness of the cooler. The results of the numerical analysis show that increasing the initial speed-ratio increases the spray-tip-penetration-length until the spray reaches the end of the spray cooler. The results also show that for the same initial speed-ratio, droplets with larger diameter penetrate the spray chamber more than those with smaller diameter. In other words, the effective spray-tip-penetration-length, S_{eff}, occurs at a lower initial speed-ratios

for larger diameter droplets. Since large diameter droplets have higher momentum compared to smaller ones, having the same initial velocity. The effect of gravitational force and wall boundary condition is also investigated. For "reflect" wall boundary condition, the spray penetration is independent of gravity because of the complete momentum recovery. On the other hand, for escape wall boundary condition, the gravitational force is a dominating factor. The droplets accelerate faster towards the lower spray chamber walls, where they lose their momentum and come to rest. This behavior is due to the fact that the droplets are subject to the vertical component of the drag force and the gravitational force. The zero gravity case, however, over-predicts the penetration length because the vertical component of the drag is the only force acting on the droplets.

The numerical simulations show that for "reflect" wall boundary condition, the spray chamber effectiveness increases by increasing the initial speed-ratio until SR_{ε} is reached, because the increase in the spray chamber conductance, UA. Increasing the initial speed-ratio increases the Reynolds number, which increases the overall heat transfer coefficient. For initial speed-ratios greater than SR_C; however, the trend is reversed and the effectiveness starts to decrease. This trend can be explained as follows: as the initial speed-ratio increases, the overall heat transfer area increases due to the increase in penetration length and the doubling effect of the surface area due to retraction of particles inside the spray chamber. This behavior is not exhibited for speed ratios greater than the critical speed-ratio, SR_C, as the particle retraction occurs outside the spray chamber. Moreover, increasing the initial speed-ratio beyond its critical value decreases the droplets residence time, which causes a

decrease in the total heat transfer area. Therefore, both initial speed-ratios SR_{ε} and SR_C are the same for "reflect" wall boundary condition. For "escape" wall boundary condition the maximum effectiveness is reached at an initial SR_{ε} which is less than SR_C. For initial speed-ratios less than SR_{ε}, the increase in surface area, due to the increase in spray-tip-penetration-length, overcomes the effect of water droplets loss at the walls. However, the effect of loosing water droplets becomes very pronounced at initial speed-ratios greater than SR_{ε} resulting in a drop in the conductance, UA product, and consequently, the effectiveness. Moreover, at initial speed-ratios greater than SR_C the surface area doubling effect vanishes resulting in a further drop in the spray chamber effectiveness. This reduction in surface area, is also accompanied by a reduction in the residence time. Consequently, the net effect is a reduction in effectiveness due to the decrease in the conductance

This chapter also addresses the effect of changing the droplet diameter on the spray chamber effectiveness for both wall boundary conditions. Increasing the droplet diameter decreases the effectiveness, for both wall boundary conditions. The effectiveness–droplet diameter relationship is governed by the spray chamber conductance, where the spray-tip-penetration-length to diameter ratio, $\zeta_A = S_{\max}/d$, plays a pivotal role. For both wall boundary conditions, increasing the droplet diameter decreases ζ_A. Accordingly, the total surface area decreases. Decreasing the droplet diameter also decreases the overall heat transfer coefficient. The net effect is, therefore, a decrease in the conductance of the spray chamber and consequently its effectiveness. For "reflect" wall boundary condition, the spray-tip-penetration-length and consequently the conductance, is the same for both cases g= 0 and g=

-9.81 m/s^2. While for "escape" wall boundary condition, however, the zero gravity case over predicts the spray-tip-penetration-length. Accordingly, the conductance and hence the effectiveness are higher for the zero gravity case.

7.2 Recommendations

The current research work focused on the design and control of direct contact spray coolers using chilled water to achieve optimum performance. Numerical and analytical models of a spray cooler have been developed to study assess the impacts of initial speed ratio and droplet diameter on the spray cooler performance. Several experiments were performed to validate these models. A limiting factor on this research work, however, is the limited amount of experimental data available. More experiments and model modifications are still needed to develop a better understanding of the system. Specifically, an in-depth study of the physical phenomena involved in cooling and dehumidification modes of operation is required. Characterizing the effects of both particle evaporation and condensation would certainly make the model more realistic. The work could also be enhanced by investigating the effect of using an array of spray nozzles. The interaction between these can greatly increase the spray chamber conductance and hence effectiveness. The work can be further developed to include the effect of inserting a packing material downstream the spray chamber. The packing material would act as a mist eliminator and simultaneously enhance the heat transfer coefficient and accordingly the spray chamber effectiveness. Other possible areas of investigation or future work could be: experimental investigation of the effect of varying the duct diameter and spray cone angle on the performance of the spray chamber.

The case where the particles retraction occurs completely inside the spray chamber is also a possible area of future experimental work.

Appendix I Pictures for Test Rig

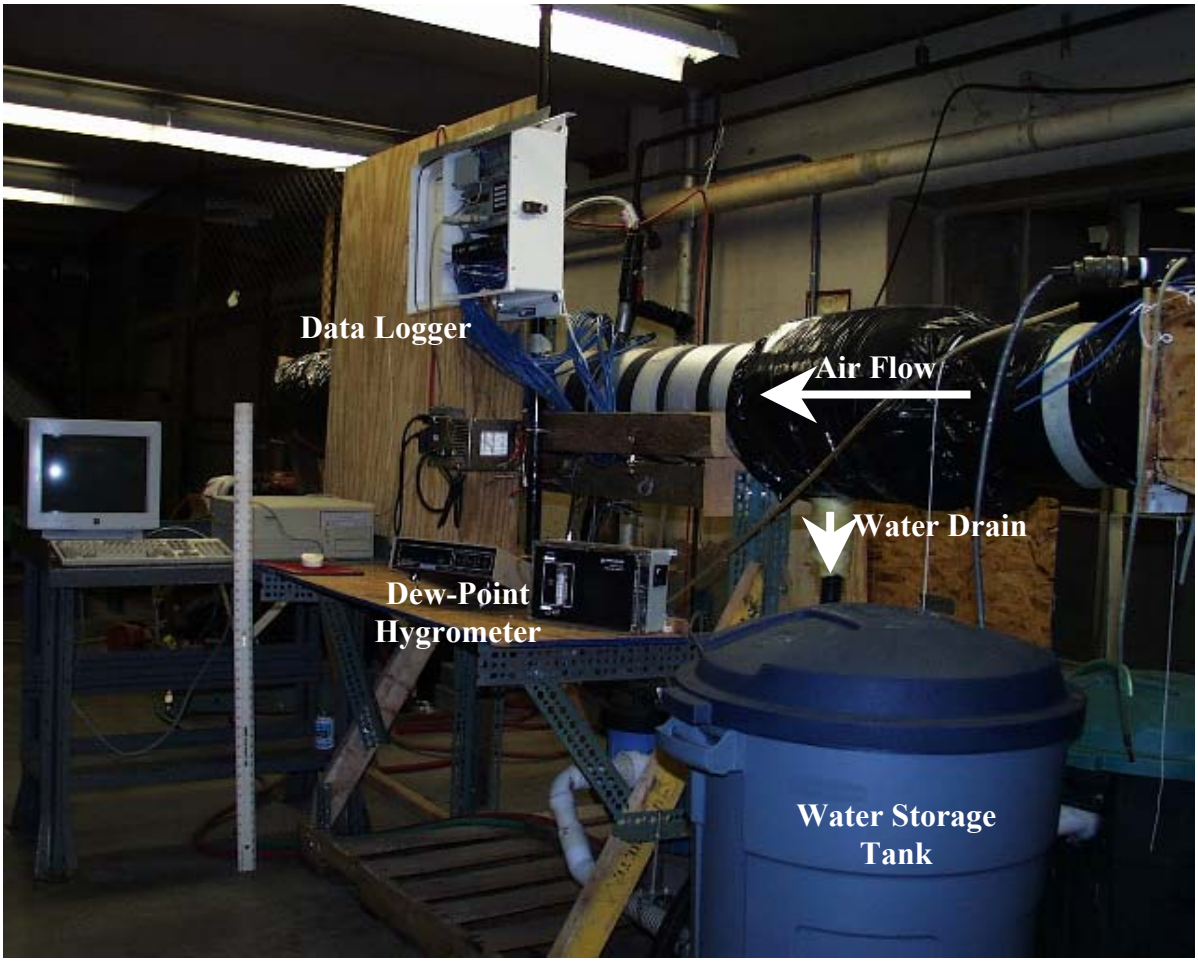

Figure I-1 Photograph for the test facility

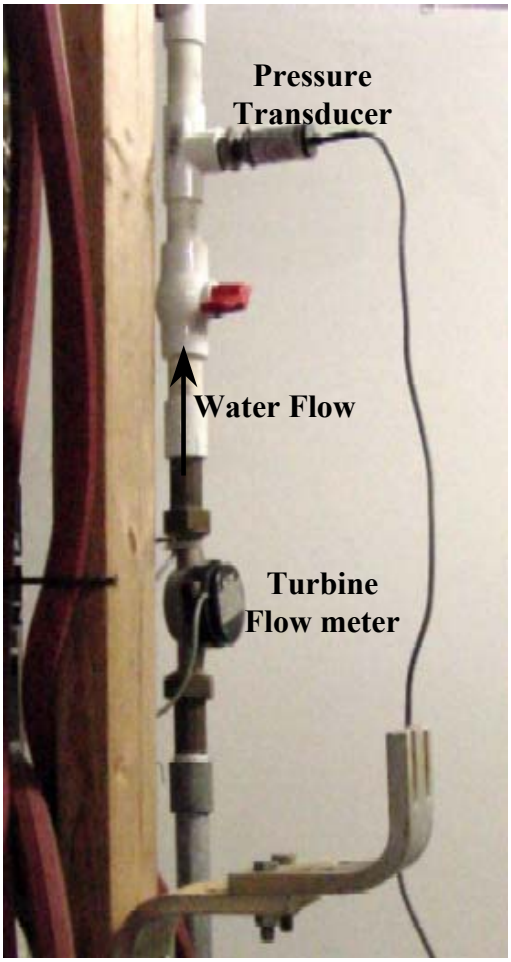

Figure I-2 Photograph for water supply system

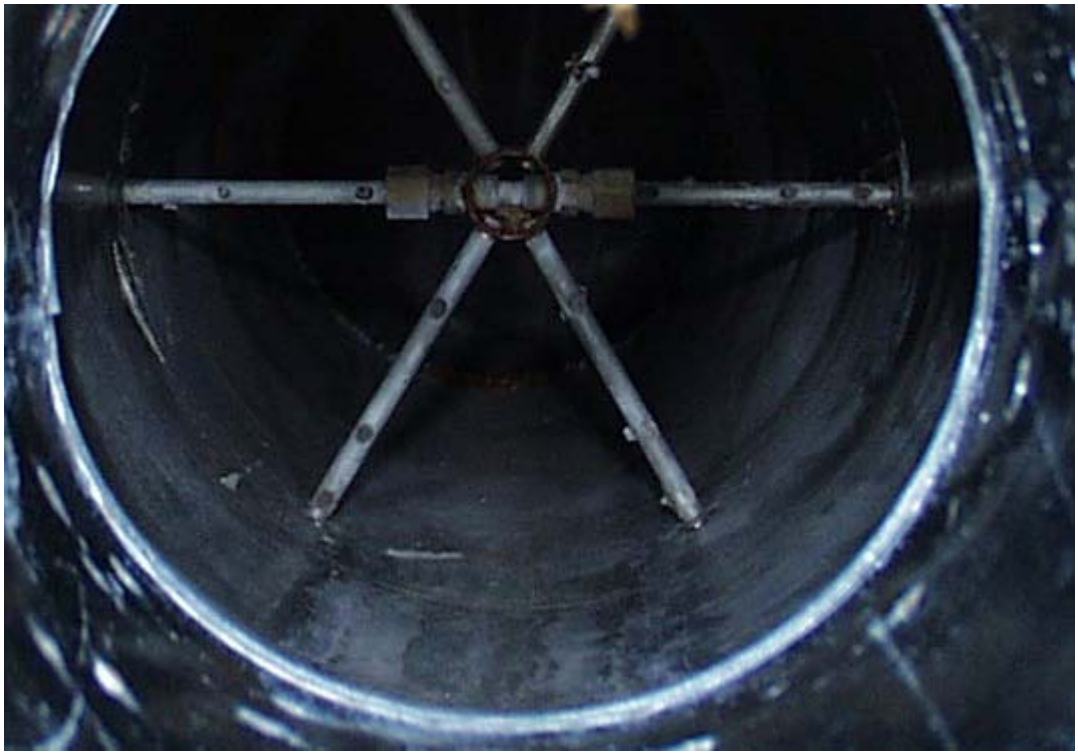

Figure I-3 Thermocouple assembly for measuring the average dry-bulb temperature at exit

Appendix II Data Logger Code

```
;{CR23X}
;
*Table 1 Program
        01:01   Execution Interval (seconds)

1:      Panel Temperature     (P17)
  1:    1         Loc [ Refrence  ]

2:      AM25T         Multiplexer     (P134)
   1:   25            Reps
   2:   21            10 mV, 60 Hz Reject, Slow Range
   3:   1             Channel
   4:   1             DIFF Channel
   5:   21            Exchan 1, 60 Hz Reject
   6:   1             Clock Control
   7:   2             Reset Control
   8:   1             Type T (Copper-Constantan)
   9:   1             Ref Temp (Deg. C) Loc [ Refrence  ]
  10:   2             Loc [ TempC     ]
  11:   1             Mult
  12:   0             Offset

3:      Volt (Diff)     (P2)
   1:   1             Reps
   2:   23            200 mV, 60 Hz Reject, Slow Range
   3:   2             DIFF Channel
   4:   27            Loc [ Pressure  ]
   5:   0.46856       Mult
   6:   -12.576       Offset

4:      Pulse   (P3)
   1:   1             Reps
   2:   5             Control Port 5
   3:   20            High Frequency, Output Hz
   4:   28            Loc [ Frequency ]
   5:   0.7926        Mult
   6:   0             Offset
```

```
5:      If time is      (P92)
   1:   0               Minutes (Seconds --) into a
   2:   1               Interval (same units as above)
   3:   10              Set Output Flag High (Flag 0)

6:      Set Active Storage Area (P80)
   1:   1               Final Storage Area 1
   2:   123             Array ID

7:      Real Time       (P77)
   1:   111             Day,Hour/Minute,Seconds (midnight = 0000)

8:      Average         (P71)
   1:   1               Reps
   2:   1               Loc [ Refrence  ]

9:      Average         (P71)
   1:   25              Reps
   2:   2               Loc [ TempC     ]

10:     Average         (P71)
   1:   1               Reps
   2:   27              Loc [ Pressure  ]

11:     Average         (P71)
   1:   1               Reps
   2:   28              Loc [ Frequency ]

12:     Z=X-Y           (P35)
   1:   3               X Loc [ TempC_2   ]
   2:   2               Y Loc [ TempC     ]
   3:   9               Z Loc [ TempC_8   ]

13:     If (X<=>Y)      (P88)
   1:   7               X Loc [ TempC_6   ]
   2:   4               <
   3:   8               Y Loc [ TempC_7   ]
   4:   30              Then Do
```

```
14:   Z=X-Y          (P35)
1:    3               X Loc [ TempC_2   ]
2:    7               Y Loc [ TempC_6   ]
3:    10              Z Loc [ TempC_9   ]

15:   Else            (P94)
      16:   Z=X-Y          (P35)
        1:  3        X Loc [ TempC_2   ]
        2:  8        Y Loc [ TempC_7   ]
        3:  10       Z Loc [ TempC_9   ]

17:   End     (P95)

18:   Z=X/Y          (P38)
1:    9               X Loc [ TempC_8   ]
2:    10              Y Loc [ TempC_9   ]
3:    11              Z Loc [ TempC_10  ]

19:   Average        (P71)
  1:  1               Reps
  2:  11              Loc [ TempC_10  ]

20:   If (X<=>F)     (P89)
  1:  11              X Loc [ TempC_10  ]
  2:  3               >=
  3:  1               F
  4:  11              Set Flag 1 High

21:   Z=F            (P30)
  1:  0.84413         F
  2:  0               Exponent of 10
  3:  29              Z Loc [ C1        ]

22:   Z=F            (P30)
  1:  0.4714          F
  2:  0               Exponent of 10
  3:  30              Z Loc [ C2        ]

23:   Z=X^Y          (P47)
  1:  27              X Loc [ Pressure  ]
  2:  30              Y Loc [ C2        ]
  3:  30              Z Loc [ C2        ]
```

```
24:     Z=X*Y          (P36)
   1:   29             X Loc [ C1      ]
   2:   30             Y Loc [ C2      ]
   3:   30             Z Loc [ C2      ]

25:     Average        (P71)
   1:   1              Reps
   2:   30             Loc [ C2      ]

*Table 2 Program
         0        02:00.0          Execution Interval (seconds)

*Table 3 Subroutines

End Program
```

Appendix III Visual Basic Code for Synchronizing the CCD Cam and the Flash

```
Dim address
Dim bitsize
Dim value
Dim Tick

Dim t_ChargCap
Dim t_FlashON
Dim t_Exposure
Dim Num_Exposures
Dim T_start
Dim T_end
Dim PortValue
Dim PortValue1
Dim PortValue2
Dim PortValue3
Dim PortValue4

Private Sub cmdwrite_Click()

    NTPORT1.bitsize = 8
    NTPORT1.value = 64
    CCD.Text = "OFF"
    Flash.Text = "OFF"
```

III-2

```
    PortValue = PortValue1 + PortValue2 + PortValue3 + PortValue4
    Print PortValue

    t_ChargCap = Val(Text1.Text)
    t_FlashDel = Val(Text2.Text)
    t_Exposure = Val(Text3.Text)
    Num_Exposures = Val(Text4.Text)

    Start.Caption = TimeValue(Now())
    T_start = TimeValue(Now())

    Tick = 1

    Timer1.Enabled = True
    Timer2.Enabled = True

    Timer1.Interval = t_ChargCap
    Timer2.Interval = t_FlashDel
    Timer3.Interval = t_Exposure

End Sub

Private Sub Check1_Click()
    If Check1.value = 1 Then
        PortValue1 = 4
    Else
        PortValue1 = 0
    End If
End Sub
```

III-3

```
Private Sub Check2_Click()
    If Check2.value = 1 Then
        PortValue2 = 8
    Else
        PortValue2 = 0
    End If
End Sub

Private Sub Check3_Click()
    If Check3.value = 1 Then
        PortValue3 = 16
    Else
        PortValue3 = 0
    End If
End Sub

Private Sub Check4_Click()
    If Check4.value = 1 Then
        PortValue4 = 32
    Else
        PortValue4 = 0
    End If
End Sub

Private Sub Timer1_Timer()

    CCD.Text = "ON"
    NTPORT1.value = 0
```

```
    Timer3.Enabled = True
    Timer1.Enabled = False

End Sub

Private Sub Timer2_Timer()

    Flash.Text = "ON"
    NTPORT1.value = PortValue
    Timer2.Enabled = False
    'dataout.Text = NTPORT1.value
End Sub

Private Sub Timer3_Timer()
    CCD.Text = "OFF"
    Flash.Text = "OFF"
    Timer3.Enabled = False
    NTPORT1.value = 64
    'dataout.Text = NTPORT1.value

    Label6.Caption = Tick
    Tick = Tick + 1
    T_n = TimeValue(Now())
    Elapsed = Format(T_n - T_start, "h:m:ss")
    Elapsed.Caption = Elapsed

    If Tick <= Num_Exposures Then
        Timer1.Enabled = True
        Timer2.Enabled = True
```

```
    Else
       Timer1.Enabled = False
       Timer2.Enabled = False
       EndT.Caption = TimeValue(Now())
       T_end = TimeValue(Now())

    End If



End Sub

Private Sub cmdexit_Click()
 End
End Sub

Private Sub Form_Load()

    txtaddress = 378
    Text1 = 5000
    Text2 = 5125
    Text3 = 1000
    Text4 = ""

    CCD.Text = ""
    Flash.Text = ""
    Label6.Caption = 0

    Start.Caption = TimeValue(Now())
    EndT.Caption = TimeValue(Now())
```

```
End Sub
'When a user enters a number in the "I/O Port Address" text box
'and then hits ENTER, (ENTER causes the variable: "KeyAscii" to be equal to 13)
Private Sub txtaddress_KeyPress(KeyAscii As Integer)
   If KeyAscii = 13 Then

      'as long as the value entered is between 0 and 65535..
      If (Val(txtaddress.Text) >= 0) And (Val(txtaddress.Text) <= 65535) Then

      'then set the ntport.address to this new value
      NTPORT1.address = Val(txtaddress.Text)

      'otherwise the value entered is out of range, send an error message
      'to the user.
      Else
      MsgBox "I/O Address must be between 0 and 65535!", vbExclamation, "Address Value
ERROR"

      End If
   End If

End Sub
```

Appendix IV Pictures for Spray Splitters

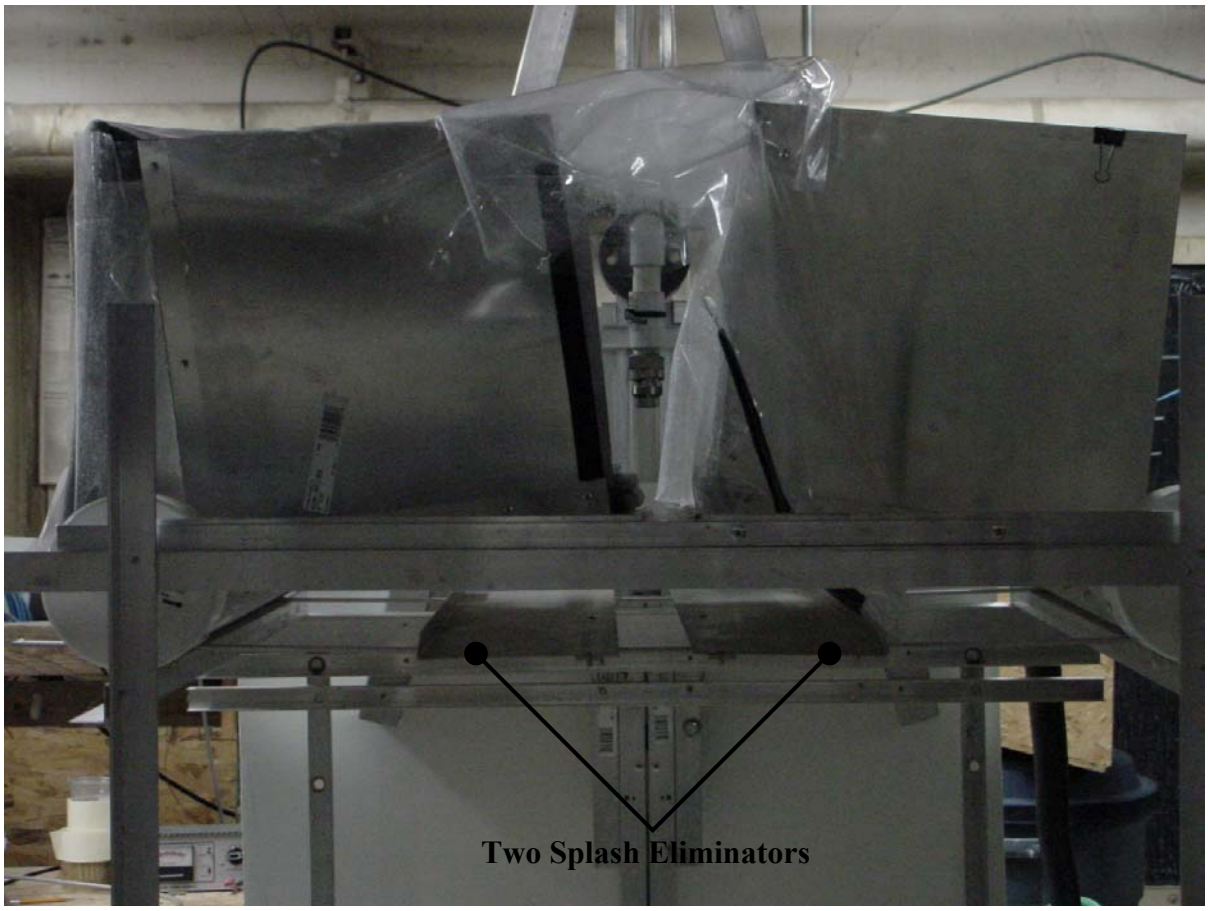
Two Splash Eliminators

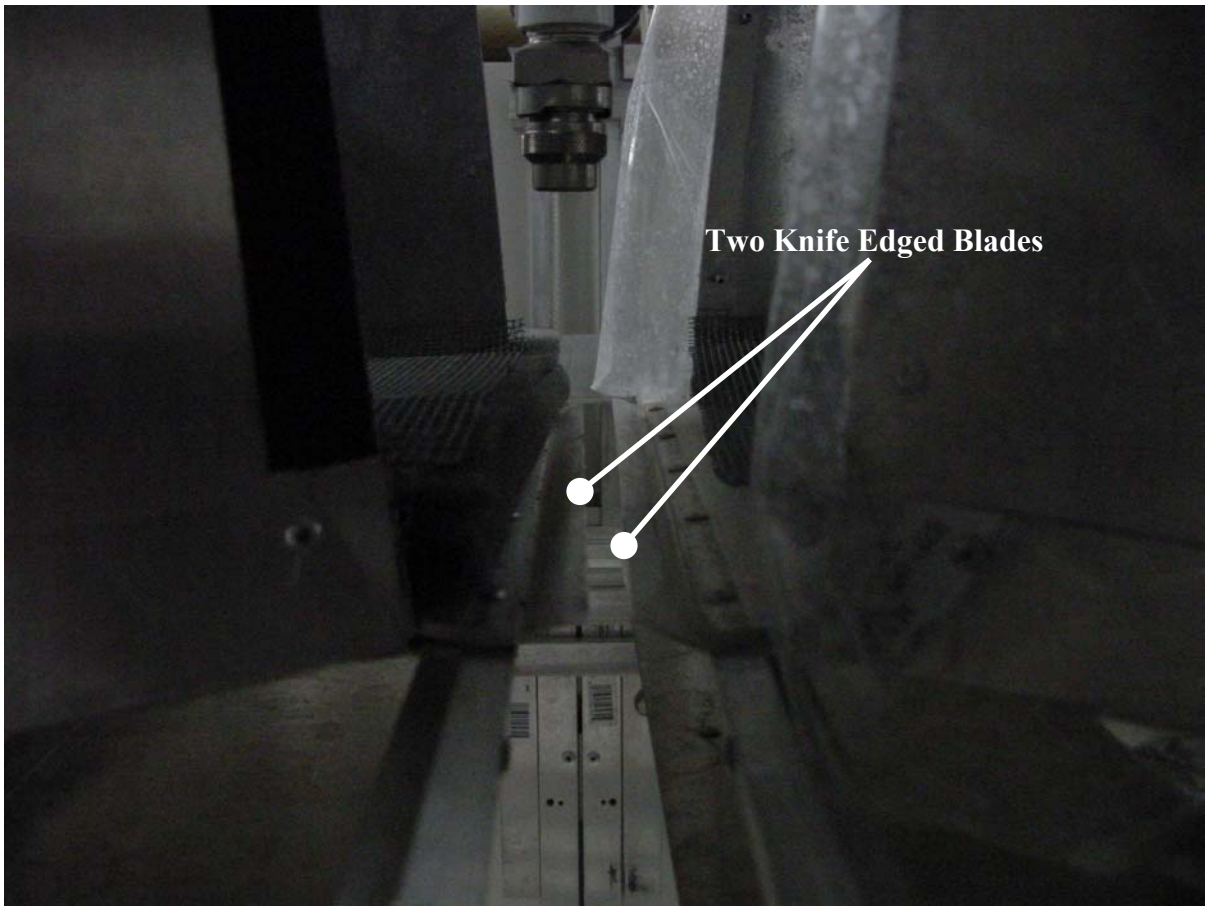
Two Knife Edged Blades

Appendix V Image Analysis Processes

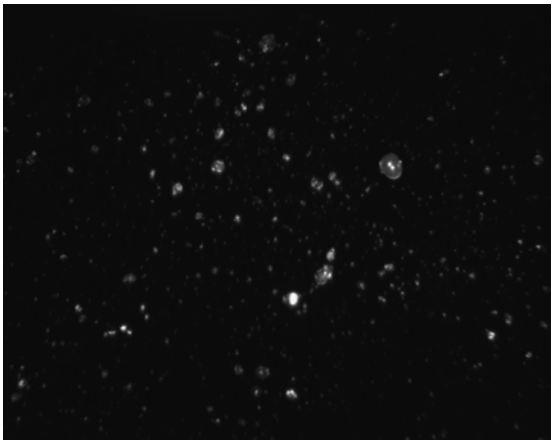

Figure V-1 Original image

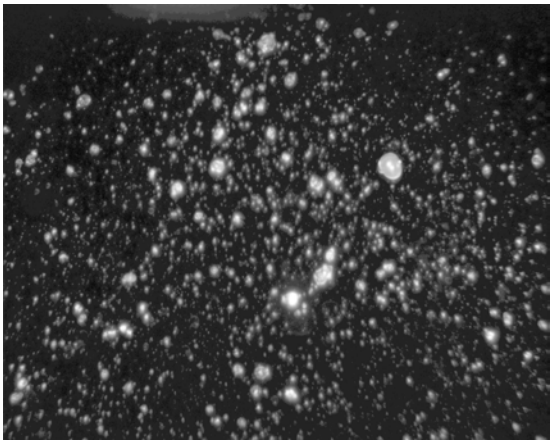

Figure V-2 Equalized image

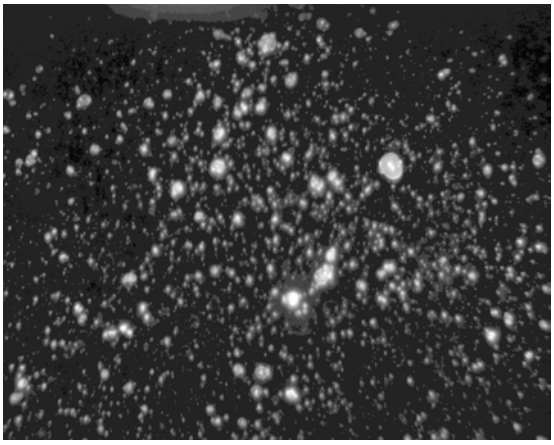

Figure V-3 Equalized image despeckled

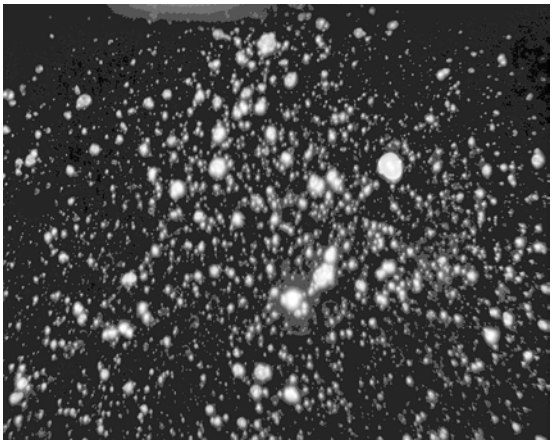

Figure V-4 Image after re-equalization

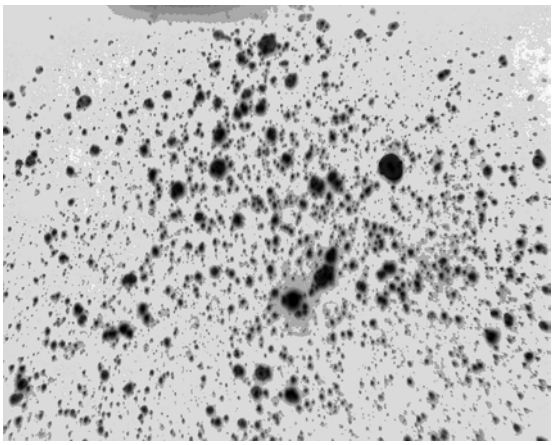

Figure V-5 Re-equalized image after inversion

Figure V-6 Low-pass filter with brightness value 80

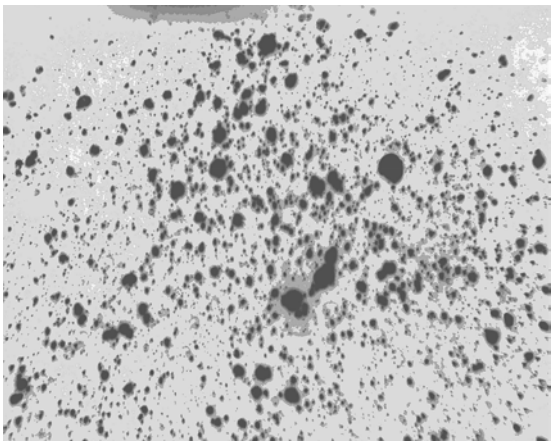

Figure V-7 Image after filtering

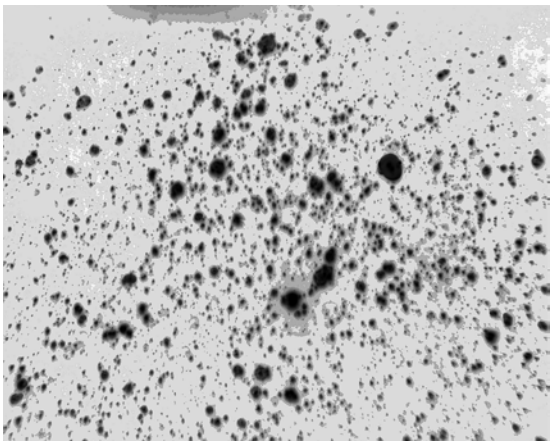

Figure V-8 Filtered image after adjusting the brightness

1 M. Ingels, “Father of Air Conditioning”, Country Life Press, 1952

[1] The approach temperature is the difference in temperature between the coldest fluid entering the coil and the leaving air dry bulb temperature.

---

2 Nagengast, B., “The First 80 Years of Air-Conditioning”, ASHRAE Journal, Vol.34, No.1, pp.S164-S175, 1992.

3 Fleisher, W., “How Air-Conditioning has developed in fifty Years”, Heating Piping and Air-Conditioning, January, pp.120-123, 1950

4 Fluent Incorporated Network Services, 10 Cavendish Court, Lebanon, NH 03766-1442, www.fluent.com.